

Inaugural dissertation  
for  
obtaining the doctoral degree  
of the  
Combined Faculty of Mathematics, Engineering and Natural Sciences  
of the  
Ruprecht - Karls - University  
Heidelberg

Presented by  
Judith Magdalena Derani, M. Sc.  
Born in: Crailsheim, Germany  
Maiden name: Förster  
Oral examination: February 16<sup>th</sup>, 2023



# Combining Radiation and Oncolytic Measles Virus for the Treatment of Refractory Tumors

Referees:

Prof. Dr. Martin Müller

Prof. Dr. Ralf Bartenschlager



# Abstract

Treatment-refractory tumors such as pancreatic ductal adenocarcinoma (PDAC) or head and neck squamous cell carcinoma (HNSCC) remain a major challenge in medical oncology and translational cancer research. Modern radiotherapy techniques are able to achieve maximal tumor damage while trying to limit off-target toxicity. Nevertheless, refractory tumors often show radioresistance. To achieve superior anti-tumor efficacy, this study investigates radiotherapy combined with virotherapy using oncolytic vaccine strain measles virus (MeV). Oncolytic MeVs feature an excellent safety profile and have shown first signs of anti-tumor efficacy in clinical trials. No cross-resistances of MeV with current therapeutic agents have been detected. They infect malignant cells as well as spread within tumors, leading to oncolysis of cancerous cells and induction of an immune response. Thus, MeV represents a promising modality for combination treatments. I hypothesize that the combination of radiotherapy and oncolytic MeV in a radiovirotherapy (RVTx) synergizes in terms of tumoricidal effects and induces a sustained anti-tumor immune response. I tested different dose regimens of radiation as well as oncolytic MeV in a panel of human HNSCC and PDAC cell lines *in vitro*. I assessed cell viability after RVTx treatment and could confirm synergism of RVTx in both tumor entities for specific treatment conditions. Further, I investigated possible mechanisms of action, focusing on the induction of immunogenic cell death (ICD), markers known for DNA damage and viral RNA sensing as well as downstream effects of innate immune activation. The combination treatment induced higher levels of the ICD markers high mobility group box 1 (HMGB1) and calreticulin (CALR) compared to each monotherapy. Further, interferon signaling was induced in RVTx, driven by virotherapy. I established an immunocompetent murine HNSCC model that is susceptible to MeV infection. In an *in vivo* pilot study using this model, I detected increased tumor infiltration of CD8<sup>+</sup> T cells as well as virus-driven immunoreactivity in co-cultures of splenocytes and tumor cells after RVTx treatment. In two human *ex vivo* PDAC tumor models, I analyzed the therapeutic efficacy of RVTx. I could show viral spread in 3D spheroids. Further, RVTx induced virus-driven ICD and interferon- $\beta$  release in patient-derived PDAC cultures. This study identified synergistic therapeutic regimens and provides the proof-of-concept for the induction of an anti-tumor immune response by RVTx. Insights into mechanisms of anti-tumor efficacy were gained in relevant preclinical models. Therefore, this project constitutes important steps towards the development and clinical translation of a state-of-the-art combination treatment modality to achieve sustained improvements for the therapy of refractory tumors.



# Zusammenfassung

Therapie-refraktäre Tumore wie das Pankreaskarzinom (PDAC) oder Kopf-Hals-Tumore (HNSCC) stellen nach wie vor eine große Herausforderung für die medizinische Onkologie und die translationale Krebsforschung dar. Moderne Techniken der Strahlentherapie können den Tumor maximal schädigen und gleichzeitig die Off-Target-Toxizität begrenzen. Dennoch zeigen refraktäre Tumore häufig eine Strahlenresistenz. Um eine bessere Anti-Tumor-Wirksamkeit zu erzielen, wird in dieser Studie Strahlentherapie mit Virotherapie unter Verwendung onkolytischer Masernviren des Impfstammes (MeV) kombiniert. Onkolytische MeV weisen ein ausgezeichnetes Sicherheitsprofil auf und haben in ersten klinischen Studien eine Anti-Tumor-Wirksamkeit gezeigt. Es wurden keine Kreuzresistenzen mit anderen Therapiemodalitäten festgestellt. MeV können maligne Zellen infizieren und sich in Tumoren ausbreiten, was zur Onkolyse der Tumorzellen und Aktivierung einer Immunantwort führt. MeV stellen somit eine vielversprechende Modalität für Kombinationsbehandlungen dar. Dieser Studie liegt die Hypothese zugrunde, dass die Kombination von Strahlentherapie und onkolytischen MeV in einer Radiovirotherapie (RVTx) synergistisch wirkt in Bezug auf tumorizide Effekte und eine anhaltende Anti-Tumor-Immunantwort induziert. In einer Reihe humaner HNSCC- und PDAC-Zelllinien habe ich verschiedene Dosierungen von Bestrahlung und onkolytischen MeV *in vitro* getestet. Ich bestimmte die Viabilität der Zellen nach Kombinationsbehandlung und konnte synergistische Effekte von RVTx in beiden Tumorentitäten für bestimmte Behandlungsschemata bestätigen. Darüber hinaus untersuchte ich mögliche Wirkmechanismen mit Schwerpunkt auf der Induktion von immunogenem Zelltod (ICD), Markern für die Erkennung von DNA-Schäden oder viraler RNA sowie Aktivierung des angeborenen Immunsystems. Die Kombinationsbehandlung induzierte die ICD-Marker HMGB1 und Calreticulin stärker als die Monotherapien. Ausgehend von der Virotherapie wurde eine Interferonsekretion nach RVTx aktiviert. Ich etablierte ein immunkompetentes murines HNSCC-Modell, das für eine MeV-Infektion empfänglich ist. Unter Verwendung dieses Modells in einer *in vivo*-Pilotstudie konnte ich eine erhöhte Infiltration von CD8<sup>+</sup> T-Zellen im Tumor sowie eine virusgetriggerte Immunreaktivität in Ko-Kulturen von Splenozyten und Tumorzellen nach RVTx-Behandlung nachweisen. In zwei humanen *ex vivo* PDAC-Modellen analysierte ich die Wirksamkeit von RVTx. Ich konnte die Virusausbreitung in 3D-Sphäroiden nachweisen. Desweiteren induzierte RVTx durch die MeV-Infektion die Freisetzung von ICD-Markern sowie eine Interferon- $\beta$ -Sekretion in Patienten-abgeleiteten PDAC-Kulturen. In dieser Studie wurden synergistische Therapieschemata identifiziert und der Konzeptnachweis für die Induktion einer Anti-Tumor-Immunantwort durch RVTx erbracht. Einblicke in die Mechanismen der Anti-Tumor-Wirksamkeit in relevanten präklinischen Modellen wurden erzielt. Daher stellt dieses Projekt einen wichtigen Schritt zur Entwicklung und klinischen Umsetzung einer hochmodernen Kombinationsbehandlung dar, mit der sich die Therapie refraktärer Tumore nachhaltig verbessern lässt.



# Contents

<b>Abstract</b>	<b>v</b>
<b>Zusammenfassung</b>	<b>vii</b>
<b>1 Introduction</b>	<b>1</b>
1.1 The ongoing challenge of cancer as a global disease . . . . .	1
1.1.1 Pancreatic ductal adenocarcinoma . . . . .	1
1.1.2 Head and neck squamous cell carcinoma . . . . .	3
1.2 The immune system in the context of cancer . . . . .	4
1.2.1 Interferon-beta mediated innate immune signaling . . . . .	4
1.2.2 Immunogenic cell death . . . . .	6
1.2.3 Principles of adaptive immune responses . . . . .	8
1.3 Ionizing radiation in the context of cancer therapy . . . . .	9
1.4 Measles virus . . . . .	11
1.4.1 Structure and biology of measles virus . . . . .	11
1.4.2 Oncolytic measles virus . . . . .	14
1.5 Role of virotherapy in oncology . . . . .	16
1.6 Combined radiovirotherapy . . . . .	17
<b>2 Aim of the Study</b>	<b>19</b>
<b>3 Materials and Methods</b>	<b>21</b>
3.1 Materials . . . . .	21
3.1.1 Chemicals, buffers and growth media . . . . .	21
3.1.2 Cell lines . . . . .	24
3.1.3 Recombinant viruses . . . . .	26
3.1.4 Plasmids . . . . .	26
3.1.5 Oligonucleotides . . . . .	27
3.1.6 Antibodies . . . . .	28
3.2 Methods . . . . .	29
3.2.1 Cell culture . . . . .	29
3.2.2 Molecular biology methods . . . . .	31
3.2.3 Irradiation . . . . .	32
3.2.4 Recombinant measles virus . . . . .	32
3.2.5 Experimental treatment schedule for radiovirotherapy . . . . .	34
3.2.6 Cell viability assays . . . . .	35
3.2.7 Fluorescence microscopy . . . . .	36
3.2.8 Calculation of synergy . . . . .	36

3.2.9	Characterization of induced mechanisms of action . . . . .	36
3.2.10	Generation of murine tumor models . . . . .	40
3.2.11	<i>In vivo</i> experiments . . . . .	42
3.2.12	Characterization of murine tumor models . . . . .	44
3.2.13	Immune profiling of murine tumors and spleens . . . . .	45
3.2.14	<i>Ex vivo</i> experiments . . . . .	47
3.2.15	Statistical analyses . . . . .	48
<b>4</b>	<b>Results</b>	<b>49</b>
4.1	Evaluation of combination regimens . . . . .	49
4.1.1	Sensitivity of candidate cell lines to monotherapies . . . . .	49
4.1.2	Irradiation of MeV particles . . . . .	51
4.1.3	Viral replication in irradiated tumor cells . . . . .	52
4.2	Dosing and scheduling of radiovirotherapy <i>in vitro</i> . . . . .	53
4.2.1	Analysis of cell viability after radiovirotherapy . . . . .	54
4.2.2	Evaluation and validation of synergy . . . . .	55
4.2.3	Determination of <i>in vitro</i> treatment conditions . . . . .	59
4.3	Detection of immunogenic cell death markers . . . . .	61
4.3.1	Release of HMGB1 and ATP . . . . .	61
4.3.2	Surface-exposed calreticulin . . . . .	62
4.4	Detection of markers for innate immune signaling . . . . .	65
4.4.1	Detection of markers for DNA damage and viral sensing . . . . .	66
4.4.2	Expression and release of interferon-beta . . . . .	67
4.5	Generation of murine tumor models . . . . .	69
4.5.1	Selection and <i>in vitro</i> characterization . . . . .	69
4.5.2	<i>In vivo</i> tumor growth and model characterization . . . . .	71
4.6	Evaluation of radiovirotherapy <i>in vivo</i> . . . . .	76
4.6.1	Efficacy of monotherapies . . . . .	76
4.6.2	Efficacy of combined radiovirotherapy . . . . .	78
4.6.3	Analysis of immune induction and infiltration . . . . .	79
4.7	Analysis of radiovirotherapy <i>ex vivo</i> . . . . .	85
4.7.1	Radiovirotherapy in a 3D PDAC spheroid model . . . . .	85
4.7.2	Radiovirotherapy treatment of patient-derived PDAC cultures . . . . .	86
4.7.3	Induction of ICD and innate immune signaling in PDAC cultures . . . . .	88
<b>5</b>	<b>Discussion</b>	<b>91</b>
5.1	Perspectives of radiovirotherapy . . . . .	91
5.2	Synergistic effects of radiovirotherapy . . . . .	92
5.3	Activation of anti-tumor immune responses . . . . .	95
5.3.1	Induction of immunogenic cell death . . . . .	95
5.3.2	Activation of innate immune signaling pathways . . . . .	97
5.4	Anti-tumor efficacy of radiovirotherapy <i>in vivo</i> . . . . .	100
5.5	Suitability of preclinical models . . . . .	102
5.6	Translational potential of radiovirotherapy . . . . .	105
5.7	Conclusions and outlook . . . . .	107
	<b>Abbreviations</b>	<b>109</b>

<b>Appendix</b>	<b>115</b>
<b>Bibliography</b>	<b>155</b>
<b>List of Figures</b>	<b>187</b>
<b>List of Tables</b>	<b>189</b>
<b>Publications</b>	<b>191</b>
<b>Congress Contributions</b>	<b>193</b>
<b>Acknowledgments</b>	<b>195</b>
<b>Thesis Declaration</b>	<b>197</b>



# 1 Introduction

## 1.1 The ongoing challenge of cancer as a global disease

Although intensive research has been in progress for more than a century, cancer is still one of the leading causes of death worldwide alongside cardiovascular diseases [1, 2]. It is expected that the global cancer burden will rise until 2040 by up to 47% compared to the year 2020 [3]. Research investigations concerning diagnosis and treatment as well as great efforts in cancer prevention have led to improved prognosis for some patients. Although tumor entities such as breast or prostate cancer are among the most common cancer types worldwide, mortality rates are comparably low [4, 5, 6, 7]. Standard treatment options against cancer known as the ‘pillars of cancer therapy’ – chemotherapy, surgery and radiotherapy – have recently been complemented by immunotherapy. By using several approaches such as immune checkpoint blockade (ICB), personalized anti-cancer vaccines or chimeric antigen receptor (CAR) T cells, immunotherapy has become an additional pillar of cancer therapy [8]. In effect, immunotherapy has been a breakthrough and provided great benefits for some cancer patients. However, an unmet high medical need remains for treatment of advanced or refractory tumor entities. Among these, pancreatic ductal adenocarcinoma (PDAC) and head and neck squamous cell carcinoma (HNSCC) are often difficult to treat with established therapies and thus are associated with poor patient prognosis and survival rates [6, 9].

### 1.1.1 Pancreatic ductal adenocarcinoma

Among different pancreatic malignancies, 90% are exocrine tumors with the majority representing adenocarcinomas of the pancreatic duct. PDAC tumors arise from epithelial cells lining the pancreatic duct and harbor driver mutations in the *KRAS* oncogene in the majority of cases [10, 11]. There are several known risk factors among which are tobacco consumption, obesity, chronic pancreatitis and specific germline mutations [12]. With a worldwide incidence of approx. 496,000 and mortality of approx. 466,000 in the year 2020, PDAC is the third leading cause of cancer-related death in men and women combined [5, 6]. The overall median survival time from diagnosis is 10 – 12 months with a 5 year survival rate of only 11% [6, 12].

Reasons for this poor clinical outcome include the time of diagnosis, as early-stage disease is often missed due to the absence of early symptoms and lack of diagnostic procedures for early detection [12, 13]. When diagnosed, 80% of PDAC patients present with advanced, non-resectable stages of disease and 50% already having developed distant metastasis [14]. Only 20% of cancer patients can undergo surgical resection accompanied by adjuvant or neoadjuvant chemotherapy, which represents the only potentially curative therapy so far [15]. In advanced-stage, non-resectable pancreatic cancer, patients are treated palliatively. The standard therapy at this stage is chemotherapy with gemcitabine in combination with albumin-bound paclitaxel or FOLFIRINOX, a combination of folinic acid, 5-fluorouracil, irinotecan and oxaliplatin [14, 15, 16]. Neoadjuvant chemotherapy together with radiotherapy can result in secondary resectability of advanced-staged tumors and increased overall survival [14, 17]. However, PDAC is a great burden for patients due to the high degree of therapy resistance especially to chemo- and radiotherapy, resulting in tumor progression in the course of treatment [12, 15, 18]. Although several genes, such as *KRAS*, *CDKN2A*, *TP53* or *SMAD4*, are mutated in PDAC with high frequencies, there is no approved therapeutic approach available targeting these most common mutations in PDAC [15]. Sotorasib, a drug targeting *KRAS* p.G12C mutations is currently tested in a phase I/II study against different solid tumors including PDAC (NCT03600883) [19, 20]. Novel approaches such as targeted therapies or immunotherapy including immune checkpoint blockade are investigated intensively. Different inhibitors of the mitogen-activated protein kinase (MAPK) signaling pathway targeting MAPK kinase (MEK) or extracellular signal-regulated kinase (ERK) have shown promising preclinical results [21, 22, 23]. Further, erlotinib, a tyrosine kinase inhibitor specific for epidermal growth factor receptor (EGFR), in combination with gemcitabine, is used clinically [24]. Unfortunately, the majority of these compounds did not succeed in clinical trials so far or are still in preclinical stage. Immunotherapy, especially ICB using antibodies against cytotoxic T lymphocyte-associated protein 4 (CTLA-4), programmed death protein 1 (PD-1) and its ligand PD-L1, has changed treatment paradigms and prognosis in certain tumor entities, such as non-small-cell lung cancer and melanoma [25]. However, PDAC remains largely refractory to these therapeutics as early phase clinical trials of ICB therapy reported safety, but only limited efficacy in PDAC patients [25, 26, 27]. Hence, a broad application of ICB in PDAC remains questionable to date [12, 15].

The difficulty of targeting PDAC efficiently is most likely due to its immunosuppressive nature as well as its complexity on genetic, epigenetic and metabolic level [27, 28]. Therefore, there is a high medical need for understanding the mechanisms that lead to insufficient therapeutic responses, improving efficacy as well as finding new druggable targets and therapeutic interventions for PDAC.

### 1.1.2 Head and neck squamous cell carcinoma

Squamous cell carcinomas of the head and neck (HNSCC) were the 6<sup>th</sup> most common type of cancer worldwide with 878,000 new cases and 444,000 deaths reported in 2020 [3, 5]. HNSCC originates from the mucosal epithelium of several sites: oral cavity, nasopharynx, oropharynx, hypopharynx and larynx [29]. These types of cancers are often associated with tobacco consumption, alcohol abuse or infection with human papillomavirus (HPV). HNSCC is typically categorized into HPV-negative and -positive tumors with main differences found in gene expression as well as mutational and immune profiles. Especially oropharyngeal squamous cell carcinoma is associated with prior HPV infection in more than 70% of cases. Moreover, there is a rising incidence of HPV-associated HNSCC tumors worldwide [29, 30, 31]. The typical biomarkers for HPV-positive HNSCC are expression of the viral oncogenes *E6* and *E7*, which are the main drivers for oncogenic transformation of the host cell, as well as upregulation of p16<sup>INK4A</sup> caused indirectly by viral E7 protein [29, 32, 33].

Many HNSCC patients are diagnosed at late stages of the disease and suffer from impairment of fundamental functions such as eating or speaking. Regardless of the HPV status, current standard of care is radiochemotherapy using the radiosensitizer cisplatin given concurrently with radiotherapy at an overall dose of approx. 70 Gy in daily fractions of 2 Gy [34, 35, 36]. According to results of a randomized phase III study in 2006, the FDA approved cetuximab, a monoclonal antibody targeted against EGFR, in combination with radiotherapy as another treatment option for locoregionally advanced HNSCC (NCT00004227) [19, 37]. However, the RTOG 1016 trial as well as the De-ESCALaTE-HPV study implied that this combination might only be suitable for patients that cannot be treated with cisplatin. Cetuximab in combination with radiotherapy was inferior to radiochemotherapy using cisplatin regarding both progression-free and overall survival of patients with HPV-driven oropharyngeal HNSCC (NCT01302834, NCT01874171) [19, 38, 39]. Furthermore, the HPV status has been correlated with radiosensitivity: Several studies have shown that patients with HPV-induced p16 expression respond better to radiotherapy, indicating the prognostic value of the HPV status for HNSCC treatment outcome (e.g. NCT00047008) [19, 40, 41, 42, 43]. In light of the varying treatment response of HNSCC, the emerging immunotherapies have enabled therapy responses regardless of the HPV status [36]. Several clinical trials investigating the effect of immune checkpoint inhibitors nivolumab and pembrolizumab have shown efficacy in second-line treatment of chemotherapy-resistant tumors (NCT02105636, NCT02252042) [19, 44, 45, 46]. Further, the KEYNOTE-048 trial showed prolonged overall survival after pembrolizumab given as monotherapy or in combination with chemotherapy (NCT02358031) [19, 47]. This trial resulted in FDA approval of both immune checkpoint inhibitors for treatment of cisplatin-refractory HNSCC.

Although recent advances have shown promising results in HNSCC treatment, the overall

response rate of recurrent or metastatic HNSCC to current therapeutic options remains infrequent. A median overall survival of about 10 months after initial therapy highlights the requirement of further investigations to improve the current therapeutic landscape of refractory HNSCC [48, 49].

## 1.2 The immune system in the context of cancer

A functional multicellular organism, like the human body, relies on protective measures against exogenous as well as endogenous threats. This protection against infectious agents or toxins and their resulting damage as well as the protection against intrinsic threats from irregular or dying cells is mediated by the immune system [50]. This highly complex and tightly regulated network involves a plethora of cell types and molecules to maintain homeostasis and body defense to prevent harm to the whole organism [50, 51]. Generally, the immune system is categorized into innate and adaptive responses that can be distinguished by their specificity to antigens and characteristic response kinetics [51]. As already stated by Hanahan and Weinberg in 2011, the development of cancer is tightly related to certain mechanisms of immune evasion that are characteristic for tumor cells. These mechanisms need to be overcome by tumor treatment in order to mediate immune activation and enable an immune response specifically directed against the tumor [52]. In the following, I focus on processes of innate and adaptive immune signaling that activate and regulate tumor-targeted responses that are addressed in this study.

### 1.2.1 Interferon-beta mediated innate immune signaling

The innate immune system is the first line of defense against pathogens. Characteristics of innate immunity are fast responses after recognition of pathogen-associated molecular patterns (PAMPs) and danger-associated molecular patterns (DAMPs), molecular signatures of pathogens or host cell damage, respectively [51]. Various signaling pathways associated with innate immune responses lead to transcription of type I interferon (IFN), mostly IFN- $\beta$ , followed by cytokine secretion. Foreign or cell-intrinsic damage-associated molecules presented on the cell surface are recognized by dendritic cells (DCs) or other antigen-presenting cells (APCs) via pattern recognition receptors (PRRs). Together with IFN- $\beta$  secretion, this leads to activation and maturation of these cells and further induction of adaptive immune responses [50, 51].

Two signaling pathways that are further addressed in this study are depicted in Figure 1.1. The induction of double-strand breaks by ionizing radiation (see 1.3 below) leads to release of deoxyribonucleic acid (DNA) fragments into the cytosol. There, it is sensed by the DNA

damage sensor cyclic GMP-AMP synthase (cGAS) which in turn will activate a signaling cascade leading to IFN- $\beta$  secretion [53]. Secondly, infection of cells with viruses harboring a ribonucleic acid (RNA) genome, e.g. measles virus, leads to presence of viral single-stranded RNA in the cytosol. This is sensed by the virus sensor retinoic acid-inducible gene I (RIG-I) that will drive another signaling cascade leading to IFN- $\beta$  secretion [54]. Further details of both pathways are explained in the following.

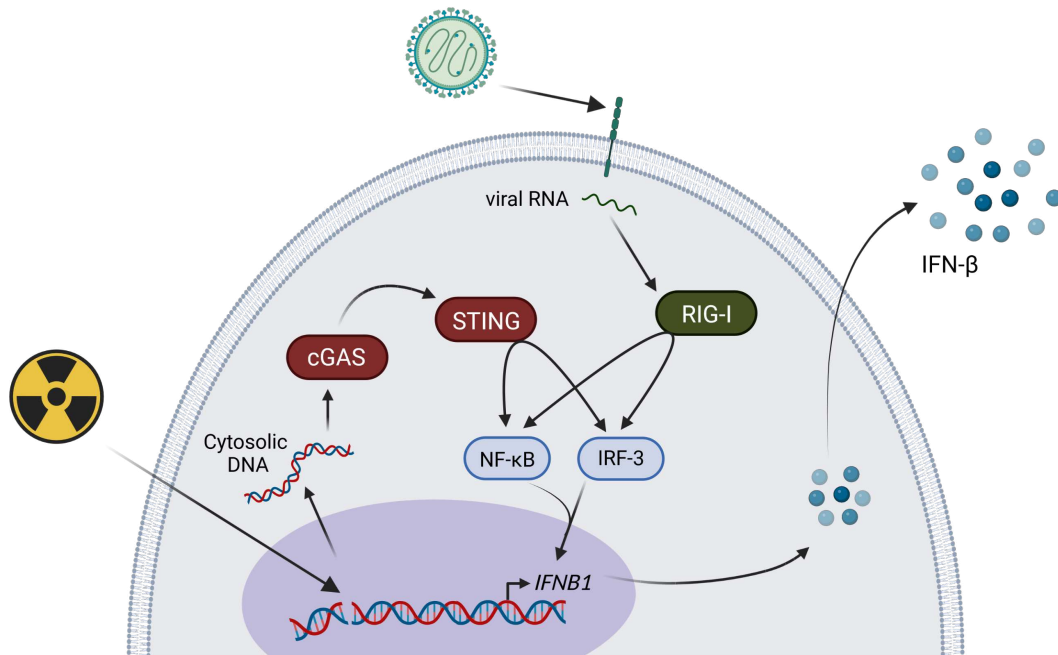


**Figure 1.1: DNA damage and virus sensing activate innate immune signaling.** Ionizing radiation induces DNA damage by double-strand breaks. DNA fragments are transported to the cytosol and sensed by cGAS. This activates a signaling cascade including stimulator of interferon genes (STING) that will lead to expression of IFN- $\beta$  followed by cytokine release. Upon binding of an RNA virus, e.g. measles virus, to surface receptors on the host cell, the viral RNA genome is internalized for replication and sensed by RIG-I. This protein activates another signaling cascade which will also lead to expression of the *IFNB1* gene and release of IFN- $\beta$ . The image was created with BioRender.com.

### 1.2.1.1 The cGAS-STING signaling pathway

The cGAS-STING pathway is well known as the major pathway for sensing double-stranded DNA in the cytosol [55, 56]. The main role of the cytosolic DNA sensor cGAS is surveillance of the cytosol for DNA fragments that can be derived from pathogens such as bacteria or DNA viruses. Further, these fragments can also be of cellular origin after DNA damage, e.g. from ionizing radiation, therefore mimicking viral infection (Figure 1.1) [55, 57]. Upon activation after DNA binding, cGAS synthesizes cyclic guanosine monophosphate–adenosine monophosphate (cGAMP) from adenosine triphosphate (ATP) and guanosine triphosphate (GTP) [58].

The cGAMP molecule serves as ligand for activating STING that is predominantly localized at the endoplasmic reticulum (ER) [53, 55]. STING in turn activates the transcription factors interferon regulatory factor 3 (IRF-3) and nuclear factor  $\kappa$ B (NF- $\kappa$ B) which induce expression of type I IFNs, especially IFN- $\beta$  [57, 59, 60]. Once the cytokine is produced and secreted, IFN- $\beta$  will be detected by DCs. In the following, DCs will mature and present tumor antigens more efficiently. This then induces adaptive immune responses.

### 1.2.1.2 The RIG-I signaling pathway

The most prominent PAMPs of viral infections are viral genome sequences and replication intermediates that are present in the cytosol of the host cell for viral replication. Viruses from the family of *Paramyxoviridae*, including measles virus, and others such as *Flaviviridae* or *Rhabdoviridae* harbor an RNA genome. The RNA helicase RIG-I specifically senses cytosolic RNA derived from such viruses [61, 62]. Once activated, RIG-I induces a downstream signaling cascade including the important adapter protein mitochondrial antiviral signaling (MAVS) that again leads to activation of the transcription factors IRF-3 and NF- $\kappa$ B that will translocate into the nucleus and activate *IFNB1* gene expression as well as cytokine release [54, 55]. Together with the presentation of viral antigens, this will activate a host anti-viral immune response [63].

### 1.2.2 Immunogenic cell death

Besides the direct recognition of foreign particles and substances within a cell as described by the above mentioned immune sensing pathways, Matzinger proposed in 1994 the so-called ‘danger theory’. It states that the immune system is able to distinguish between harmless and dangerous endogenous signals [64, 65]. Injured, stressed or dying cells expose and release different molecules, known as DAMPs or ‘alarmins’, that serve as signal for activating the innate immune system [65, 66, 67]. DAMPs are intracellular molecules with defined functions within the nucleus or cytosol of cells. Upon damage or stress, they are exposed or secreted via non-classical molecular pathways and thereby function as immunostimulants [66, 68]. This process is called immunogenic cell death (ICD). The activation of the immune system is mediated by DCs and other APCs. Released or exposed ICD markers bind to PRRs on the cell surface and induce recruitment as well as maturation of DCs. Then, they promote cross-presentation activity of the latter, hence, leading to downstream initiation of an immune response [66, 69, 70].

To this point, more than 16 different molecules have been identified as markers of ICD [70, 71]. This designation, however, is not reserved to a specific type of cellular component. Quite a broad range of substances are defined as ICD markers: nucleic acids or nucleotides such as

DNA or RNA from viral or cellular origin, different cytokines such as C-X-C motif chemokine ligand 10 (CXCL-10) or chaperones of the ER such as heat shock protein (HSP) 70 or 90 as well as components of bacterial origin such as flagellins or lipopolysaccharides [65, 70, 71]. The most prominent and well-investigated DAMPs serving as ICD markers are released ATP, secreted high mobility group box 1 (HMGB1) and surface-exposed calreticulin (CALR) shown in Figure 1.2 [72, 73].

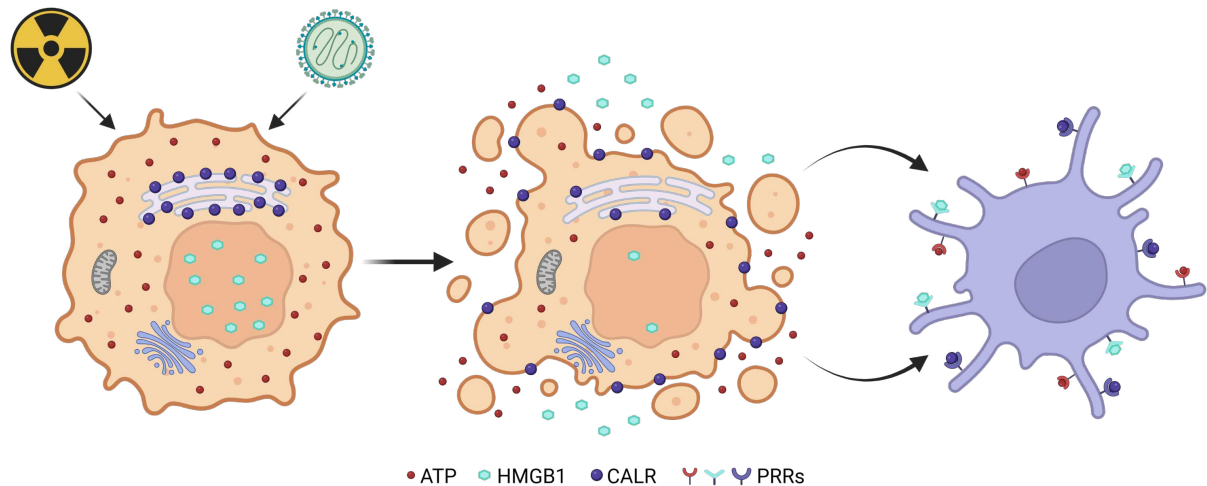


**Figure 1.2: Markers of immunogenic cell death.** The introduction of damage to a cell, e.g. by ionizing radiation or viral infection, leads to release and exposure of several intracellular components, also known as DAMPs. In the course of ICD, these components such as extracellular ATP, released HMGB1 or surface-exposed CALR bind to PRRs on DCs and other APCs and therefore function as inducers of innate immune responses. ATP — adenosine triphosphate; HMGB1 — high mobility group box 1; CALR — calreticulin; PRRs — pattern recognition receptors. The image was created with BioRender.com.

CALR is usually located in the lumen of the ER. It is a soluble protein that serves as a regulator of  $\text{Ca}^{2+}$  homeostasis and as ER chaperone [72, 74]. After exposure to stress and induction of ICD, cells undergo apoptosis [72, 73]. In the early phase of apoptotic cell death after exposure to ICD inducing agents, CALR translocates from the perinuclear ER to the cell surface (see Figure 1.2) [73]. There, it binds to ERp57, another ER chaperone, which is relocalized to the cell surface as well [75]. This CALR-ERp57 complex then serves as an ‘eat me’ signal promoting phagocytosis by DCs, followed by cross-presentation of tumor antigens and secretion of type I IFNs [76, 77, 78]. Further, this process induced by CALR translocation can result in a tumor-specific cytotoxic T cell response.

ATP is well-known as the most important energy source of cells. During the blebbing phase of apoptotic cell degradation, cells secrete ATP via autophagy [73, 79]. Extracellular ATP then serves as chemoattractant or ‘find me’ signal for immature DCs [80]. It triggers purinergic  $\text{P}_2\text{X}_7$  receptors on the surface of DCs, leading to maturation of the latter by

activation of the inflammasome NACHT, LRR and PYD domains-containing protein 3 with apoptosis-associated speck-like protein containing caspase recruiting domain (NALP3-ASC) and secretion of interleukin (IL)  $1\beta$  [73, 81]. This supports subsequent activation of adaptive immunity.

Usually located in the nucleus, HMGB1 serves as a non-histone chromatin binding protein that is constitutively expressed by eukaryotic cells [72]. It has different functions and plays a role in nucleosome stabilization, DNA repair, recombination and transcription [82, 83]. In late stages of apoptosis, HMGB1 is released from the nucleus and accumulates in the extracellular space [84]. By binding to toll-like receptor 4 (TLR-4) on DCs, HMGB1 triggers the TLR-4-myeloid differentiation primary response 88 (MyD88) pathway that mediates tumor antigen processing [73, 85]. Therefore, it plays an important role in activation and antigen presentation of DCs to T cells leading to adaptive immune activation [70, 85, 86].

### 1.2.3 Principles of adaptive immune responses

The above mentioned markers of innate immune sensing and ICD do not harbor cytotoxic functions themselves. They require the downstream activation of immune responses for e.g. pathogen or tumor cell clearance. After priming and maturation of DCs by different pathways of innate immune signaling, they can induce the cascade of adaptive immune responses, especially the activation of T cells [51].

T cells are of the lymphocyte lineage of haematopoietic stem cells and the majority can be divided according to the expression of the T cell receptor (TCR) accessory molecules into  $CD4^+$  and  $CD8^+$  cells [50]. By an interplay of antigen presentation, co-stimulation and expression of inflammatory cytokines such as IFN- $\beta$  or IL-2, DCs and other APCs prime naïve T cells and therefore activate the differentiation into their specific T cell subtype [87].  $CD4^+$  T cells are also known as T helper ( $T_H$ ) cells, as their main function is to assist and regulate the immune response.  $T_H1$  cells are involved in cell-mediated immune responses and elimination of intracellular pathogens. They secrete activating cytokines like IL-2, IFN- $\gamma$  and tumor necrosis factor  $\alpha$  (TNF- $\alpha$ ).  $T_H2$  cells play a role in the elimination of extracellular parasites, bacteria as well as fungi and rather control antibody responses [50, 51, 88]. Another subset of  $CD4^+$  T cells are regulatory T cells ( $T_{reg}$  cells) that have a major immunosuppressive function for regulating T cell-mediated immune responses [89]. A characteristic feature of  $T_{reg}$  cells is expression of the transcription factor forkhead box p3 (Foxp3) [90]. In mediating a feedback-loop for regulating T cell activation,  $T_{reg}$  cells suppress proliferation, differentiation and effector function of a variety of immune cells including T cells, DCs or natural killer (NK) cells and release immunosuppressive cytokines such as IL-10 and transforming growth factor  $\beta$  (TGF- $\beta$ ) [51, 91]. The main effectors of the T cell compartment are  $CD8^+$  T cells, also

called cytotoxic T cells. Once activated, CD8<sup>+</sup> T cells secrete IFN- $\gamma$  for further enhancement of cytotoxicity. They kill target cells in an antigen-specific manner by transferring cytotoxic enzymes such as granzymes into target cells via perforin and secrete molecules that will bind to death receptors of the target cell to eventually mediate apoptosis [50, 51]. In the tumor setting, once this point of tumor cell killing is reached, the entire process begins anew as APCs will internalize and present tumor antigens on their cell surface to activate another round of T cell-mediated immune response. This sequence of processes for tumor cell killing is also known as the cancer-immunity cycle [92].

### 1.3 Ionizing radiation in the context of cancer therapy

The principle behind using ionizing radiation for cancer therapy is the radiation-mediated transfer of energy, also known as linear energy transfer (LET), to cells and tissues [93, 94]. Most common sources for radiation beams are X-rays,  $\gamma$ -rays or charged particles. If radiotherapy is applied systemically, radioactive substances such as iodine are used [93]. The overall effectiveness of radiotherapy depends on LET, the total dose applied together with the number of fractionations as well as the radiosensitivity of target cells and tissues. It is limited by radiation-induced off-target organ toxicity [95].

Generally, the effects of ionizing radiation are classified as direct, indirect or secondary effects. Direct effects are mainly direct cell killing by DNA damage in form of single or double-strand breaks, cross-linking or damage of nucleobases. Indirect effects of radiation also produce DNA damage. Here, the radiolysis of cellular H<sub>2</sub>O and other molecules lead to generation of free radicals such as reactive oxygen species (ROS) which in turn react with the DNA and cause single or double-strand breaks [93, 96]. Further, ionizing radiation also causes damage to other cellular molecules such as enzymes or membrane components and interferes with the cell cycle. Due to DNA damage, cells arrest in G1 phase of the cell cycle and accumulate p53 and p16. This leads to cellular senescence and impaired cell proliferation [97, 98]. In terms of cellular response to effects of ionizing radiation, there are two general responses at play: mechanisms aiming at repairing the induced DNA damage or processes leading to apoptosis. In cancer cells, repair mechanisms are often impaired or act more slowly than in normal, healthy cells. Further, the fast doubling rate of cancer cells causes higher sensitivity to radiation compared to healthy cells and leads to higher vulnerability to possible damage [93, 99].

The secondary effects of ionizing radiation include processes leading to the induction of an anti-tumor immune response. Irradiation of tumor tissue promotes T cell priming by cross-presentation of tumor antigens and leads to reduction of tumor mass by CD8<sup>+</sup> T cell-mediated cell killing [100, 101, 102]. Further, radiotherapy is also able to activate intratumoral

production of IFN- $\beta$  followed by innate immune signaling [53, 63, 103]. This leads to enhanced cross-priming activity of DCs attracting T cells to the tumor site [104]. By local inflammatory reactions after irradiation, a reprogramming of the tumor microenvironment (TME) further enables immune responses by release of tumor antigens and DAMPs [105, 106]. Among these are markers of ICD, most prominently represented by extracellular ATP, release of HMGB1 and surface-exposed CALR (see 1.2.2) [70, 107].

Radiotherapy mainly has effects on a localized target by focusing the radiation beam on a specific tumor site. However, it has shown in rare cases systemic, abscopal effects. Hence, radiotherapy can supposedly induce anti-tumor effects outside of the primary treatment field [108]. The abscopal effect has been reported in several preclinical studies and case reports as delayed therapeutic effects on unirradiated metastatic sites of melanoma, lymphoma, lung adenocarcinoma, hepatocellular carcinoma or Merkel cell carcinoma [109, 110]. It was also observed in one case of metastatic HNSCC after treatment with radiotherapy in combination with ICB using an antibody against PD-1 [111]. Preclinical investigations have shown, that the induction of a systemic anti-tumor immune response is the driving force of the radiation-induced abscopal effect [112]. The activation of the immune system led to migration of T lymphocytes to distant tumor sites mediating tumor cell killing there [109].

With this broad spectrum of biological effects, radiotherapy is in the repertoire of standard treatment for many tumor entities. It is among the four pillars of cancer therapy and more than 50% of patients receive radiotherapy as part of their individual treatment plan [8, 113]. It plays an important role in managing non-resectable or recurrent tumors. Radiotherapy is used in most patients as a treatment with curative intent but is also part of palliative care [93, 114]. In 85% of cases, radiotherapy is applied as external beam radiotherapy (EBRT) and is accompanied by various imaging techniques such as computer tomography for exact positioning of the photon radiation beam on the tumor target [94]. For circumventing radiation damage to sensitive normal tissue, intensity modulated radiotherapy (IMRT) uses several radiation beams that will hit the targeted tumor mass from several directions with varying radiation intensity. In this way, high radiation doses can be delivered to the tumor by sparing surrounding tissue as much as possible [94, 115]. Besides conventional photon radiation, charged particles such as protons or heavy ions have great potential in radiotherapy. By delivering the majority of energy at the end of their range in the so-called ‘Bragg peak’, charged particles provide the opportunity to deliver maximum energy at the intended target site with minimal effect on surrounding tissue [114, 116, 117]. However, costs for purchase and maintenance of suitable machines for conducting particle therapy are about 100 times higher than conventional linear accelerators for photon beam radiotherapy. The availability of particle therapy is therefore limited [94].

Major obstacles for successful tumor treatment with radiotherapy are mechanisms of radioresistance in tumor cells [118]. The hypoxic environment of many tumors prevents the generation of ROS after ionizing radiation [119]. If ROS are still produced, endogenous antioxidant mechanisms such as superoxide dismutases can prevent radiation-induced oxidative stress by converting free oxygen radicals into non-reactive O<sub>2</sub> [120, 121]. Furthermore, the databases of Oncomine and the Cancer Genome Atlas Program have shown that most tumor types have upregulated expression of several genes that are involved in DNA repair mechanisms. Mutations in these specific genes that are common for 10 – 20% of tumors lead to resistance of the tumor to DNA damage and apoptosis [118, 122].

Besides intrinsic mechanisms of radioresistance, many patients struggle with severe side effects of radiotherapy. It is reported that approx. 50% of HNSCC patients experience problems with speaking or swallowing during treatment and even after 10 years, the majority of these patients are still compromised by side effects of radiotherapy [123, 124]. For PDAC currently, radiotherapy is in most cases only an option in the context of palliative treatment due to the high degree of radioresistance and advanced stage of most of the diagnosed tumors. A further obstacle for PDAC is its location within the body surrounded by many radiosensitive organs and tissues [15]. Therefore, further development of this therapy and combinatorial approaches with other treatment modalities are necessary to improve the clinical potential of radiation for cancer therapy.

## 1.4 Measles virus

### 1.4.1 Structure and biology of measles virus

Measles virus belongs to the family of *Paramyxoviridae* within the *Morbillivirus* genus. Viral particles have a size of approx. 100 – 300 nm and contain a single-stranded, non-segmented, negative sense RNA genome with a length of 15,894 nt [125, 126]. The genome encodes six structural and two non-structural proteins flanked by non-coding leader and trailer sequences that contain regulatory elements for transcription and replication (Figure 1.3) [127, 128]. The nucleocapsid enclosing the viral RNA is formed by the nucleoprotein (N) with the large protein (L) and phosphoprotein (P) associated. Further, these proteins also build the RNA-dependent RNA-polymerase complex, also called the ribonucleoprotein (RNP) complex. This is necessary for viral replication within the host cell. The viral envelope is composed of a lipid bilayer derived from of the host cell membrane lined by the matrix protein (M). On the outside, hemagglutinin (H) and fusion (F) proteins are incorporated into the envelope which are essential factors for host cell entry [125, 127, 129].

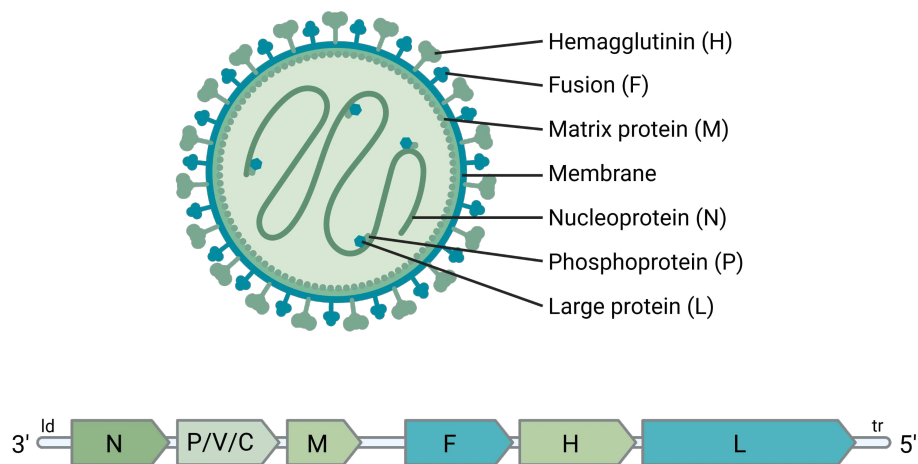


**Figure 1.3: Schematic representation of measles virus particle and genome.** A measles virus particle contains an RNA genome encapsulated by nucleocapsid (N) that is associated with large protein (L) and phosphoprotein (P). Together, they build the RNP complex. This structure is surrounded by a viral envelope of host cell membrane and matrix protein (M) with hemagglutinin (H) and fusion proteins (F) on the surface. All structural and non-structural viral proteins are encoded in the negative sense RNA genome with regulatory elements at the 3' (leader, ld) and 5' (trailer, tr) end. The image was created with BioRender.com.

The genomic sequence of P also contains the genetic information for the two non-structural proteins, V and C (Figure 1.3). An alternative open reading frame (ORF) encodes C. By addition of a non-templated guanosine nucleobase, a frame shift in the sequence leads to transcription of the V protein encoding sequence. Both proteins have an important role in viral replication as well as virulence and modification of the anti-viral response by influencing interferon signaling of the host cell [130, 131, 132, 133, 134].

The human body represents the host for wildtype and vaccine strain measles virus. Non-human primates can also be infected by measles virus, but the overall population size is too small for a sustained transmission of the virus [135]. The entry receptors for wildtype measles virus are signaling lymphocyte-activation molecule family member 1 (SLAMF1), also called CD150, and poliovirus receptor-like 4 (PVRL-4), also known as nectin-4. The former is expressed on lymphocytes and APCs such as DCs, macrophages as well as monocytes, the latter is a component of adherens junctions of epithelial cells, especially alveolar cells [136, 137, 138]. Receptor distribution is a major determinant for the pathogenesis, whereas the route of infection is via the respiratory system [135]. There, the H protein of the viral particles binds to host entry receptors and interacts with F to mediate attachment and fusion with the host cell membrane for viral entry [139, 140]. The RNP complex replicates and transcribes the viral genome in the cytosol [125, 141]. All components of viral particles are produced and transported to the cell membrane. The newly translated H and F proteins are expressed on the outer host cell membrane, new virions are assembled and bud off the host

cell to potentially infect other cells. Remaining H and F proteins on the cell surface mediate fusion with neighboring cells to form the characteristic cytopathic effect of multi-nucleated cells, called syncytia. With ongoing cell fusion upon infection the membrane tension of syncytia rises until they burst. This entails further release of viral particles and thereby fosters infection and spread [142, 143, 144].

With an average incubation time of 10 – 14 days after initial infection via the respiratory system, acute measles disease shows a characteristic maculopapular rash accompanied by further symptoms such as fever, conjunctivitis, coryza, cough and bluish-white Koplik spots on the oral mucosa [125, 145, 146]. In some cases, complications of varying severity arise during disease progression such as otitis media, diarrhoea and laryngotracheobronchitis but also pneumonia or encephalitis [146]. Subacute sclerosing panencephalitis, a neurodegenerative disorder, can arise even 7 – 10 years after infection [147].

Since the development of measles vaccines in the 1960's, the incidence of measles infections dropped to approx. 7.5 million from initially 30 million cases per year and the number of deaths decreased from 2 million to approx. 100,000 deaths per year [135, 148]. The eradication of measles worldwide has not been reached yet due to limited comprehensive vaccine coverage and vaccination campaigns. The first vaccine against measles virus was developed in the 1950's. Enders and Peebles were successful in propagating measles virus from a boy named David Edmonston in tissue cultures [149]. This approach produced a live-attenuated virus with reduced virulence that still infected and replicated in human cells but without losing its immunogenicity important for the capacity as a vaccine. In 1963, the first measles vaccine, Edmonston B, was licensed for vaccination purposes. Further measles vaccine viruses, Moraten and Schwarz, originating from the Edmonston lineage were passaged on chicken embryonic fibroblasts (CEFs) and are still in use for vaccination today [150, 151]. Due to its stable genome without re-appearance of pathogenicity and efficient induction of life-long humoral immunity, the measles vaccine is considered as one of the safest and most efficacious vaccines worldwide and has been given to billions of people over many decades preventing from disease outbreak and severe side effects [125, 152].

For cell entry, the attenuated vaccine strain measles virus (MeV) mainly uses another receptor: the CD46 molecule [137, 153]. It is also known as a co-factor for the serine protease complement factor 1 and is therefore part of the complement system [154, 155]. Further, CD46 is ubiquitously expressed on the surface of most human nucleated cells and is overexpressed in tumor cells of several entities [143, 156]. Thereby, it plays a crucial role in preventing complement-mediated tumor cell lysis [157, 158]. Although this is unfavorable for destruction via the complement system, it is of great advantage for viral infection of tumor cells, pointing towards a natural oncotropism of vaccine strain MeV [159].

## 1.4.2 Oncolytic measles virus

The idea of using measles virus as an anti-cancer agent arose in the last century after several case reports indicating oncolytic activity, i.e. the capability to lyse tumor cells. The most famous case report of a young African boy suffering from Burkitt's lymphoma was documented by Bluming and Ziegler in 1971. The physicians reported complete tumor regression associated with a concurrent measles infection [160]. Other cases reported the same phenomenon in leukemia or Hodgkin's disease [161, 162, 163]. These first insights pointed towards a possible role of measles virus as an oncolytic agent and were the starting point for decades of research developing anti-cancer virotherapy using oncolytic measles virus [164, 165, 166].

The use of measles virus as oncolytic agent requires a high level of safety. Therefore, measles vaccine strain viruses (MeV) are used for the development of a virus-based therapy [167]. Commonly used for vaccination purposes, MeV provides an excellent safety profile and high immunogenicity without genotoxicity. The stable genome and available reverse genetics system provide possibilities for virus engineering and retargeting [166, 168, 169]. However, the increased safety of using a vaccine virus also implies pre-existing antiviral immunity in many patients. Furthermore, as MeV is a human-specific virus, the choice of preclinical models without modification is limited. The investigations of MeV efficacy *in vivo* therefore require the engineering of murine models that are susceptible to viral infection as MeV would not enter murine cells *per se* [170, 171].

Infectivity and tumoricidal efficacy of MeV in several tumor entities was shown in many preclinical studies [166, 167]. In the following, several interesting aspects of MeV retargeting, post-entry targeting as well as the induction of anti-tumor immune responses by MeV are put into focus. Specific engineering of the MeV H protein enables retargeting of viral entry, thereby increasing the specificity of viral infection of tumor cells. Nakamura and colleagues described a pseudoreceptor system that allows the rescue and propagation of fully retargeted MeV to antigens overexpressed on tumor cells and demonstrated specific receptor-mediated anti-tumor activity *in vitro* as well as *in vivo* [172]. This pseudoreceptor system enabled the development of MeV retargeted to CD20, prostate stem cell antigen (PSCA) or EGFR that are frequently overexpressed on lymphoma cells, PDAC or HNSCC. Further, the sequence of a prodrug convertase was inserted in the MeV genome such as purine nucleoside phosphorylase (PNP) derived from *Escherichia coli* or cytosine deaminase/uracil phosphoribosyltransferase (CD/UPRT) that converts 5-fluorocytosine into 5-fluorouracil, a common chemotherapeutic used against many tumor entities including HNSCC. This enabled the development of a combination therapy with chemotherapeutics such as fludarabine or 5-fluorouracil. These chemovirotherapy combinations showed specific infection of tumor cells by MeV with enhanced killing of infected as well as bystander cells *in vitro* and increased

efficacy, tumor growth delay, temporary or complete tumor regression and prolonged survival in xenograft models [173, 174, 175, 176]. Further, post-entry targeting was achieved as another possibility for successful modification of MeV tropism and increasing safety. The insertion of microRNA target sequences into the MeV genome enabled specific viral infection of tumor cells, as the expression of the corresponding microRNAs is lost during tumorigenesis which can be exploited further. Viral infection of and spread in normal tissue was suppressed, as healthy cells express the specific microRNA to a high extent [177]. Following this post-entry targeting strategy, MeVs were generated for specific infection of glioblastoma, hepatocellular carcinoma and PDAC cells without reduced oncolytic efficacy *in vitro* [178, 179, 180]. In corresponding xenograft tumor models, microRNA-sensitive MeV showed tumor growth delay and prolonged survival comparable to unmodified MeV. Investigations in primary human brain tumor explants showed restricted replication and spread of microRNA-sensitive MeV in normal brain tissue [178].

To investigate the possible increase of the anti-tumor efficacy of MeV by inserting immunostimulatory transgenes, several studies were conducted in preclinical models of colon adenocarcinoma and melanoma. Treatment with MeV encoding the immunostimulatory cytokine granulocyte-macrophage colony stimulating factor (GM-CSF) led to delayed tumor progression, prolonged survival as well as induction of an adaptive immune response in an immunocompetent murine colon adenocarcinoma model [181]. Moreover, virotherapy using the GM-CSF-encoding virus induced an enhanced cell-mediated immune response that was specific against tumor as well as virus. The idea of combining ICB with oncolytic MeV led to the generation of MeV vectors encoding antibodies against CTLA-4, PD-1 or PD-L1 [182, 183]. Investigations in immunocompetent murine melanoma models showed oncolytic efficacy as well as delayed tumor progression, increased levels of tumor-infiltrating lymphocytes (TILs), prolonged median overall survival and even complete tumor remission with IFN- $\gamma$  recall responses after tumor rechallenge. Additionally, the established MeV vectors showed tumor cell lysis in patient-derived melanoma tissue. For further development of immunovirotherapy, Veinalde *et al.* and Backhaus *et al.* generated MeV vectors encoding IL-12 fusion protein and an IL-15 superagonist to mediate enhancement of immune responses by T and NK cells [184, 185]. Investigations in murine melanoma and colon adenocarcinoma models showed increased immune cell infiltration and activation as well as upregulation of effector cytokines after treatment with MeV encoding immunomodulators compared to control MeV. Another strategy to recruit T cells to the tumor site and induce anti-tumor immune responses is the use of bispecific T cell engagers (BiTEs), molecules that enable T cell recruitment to the tumor site by simultaneously targeting CD3 as well as a tumor-specific surface antigen. MeVs that encode BiTEs targeting solid tumors such as melanoma or colon adenocarcinoma led to increased T cell infiltration and induction of an anti-tumor immune response in immunocompetent, syngeneic mouse tumor models. Further, in combination with transferred peripheral

blood mononuclear cells (PBMCs), treatment with MeV encoding BiTEs led to prolonged survival in patient-derived xenografts of colorectal cancer [186].

To achieve the induction of an anti-tumor immune response via innate immunity, Li and colleagues generated an attenuated MeV encoding IFN- $\beta$  and conducted investigations in preclinical models of human mesothelioma [187]. The treatment with MeV encoding IFN- $\beta$  was associated with increased infiltration of innate immune cell repertoires in the TME. The study showed delayed tumor growth and prolonged survival in several mesothelioma tumor models after intratumoral injections of MeV encoding IFN- $\beta$ . Moreover, ICD plays an important role in the cancer immunity cycle for induction of an anti-tumor immune response mediated by MeV [188]. The induction of ICD by MeV was first observed by Donnelly *et al.* in 2013. Investigations in human melanoma models showed the release of type I IFNs as well as the ICD marker HMGB1 after treatment with oncolytic MeV [189]. Further, Chen and colleagues showed ICD induction after MeV infection of hepatocellular carcinoma cells by translocation of CALR as well as significantly increased release of ATP and HMGB1 from MeV infected tumor cells [190].

### 1.5 Role of virotherapy in oncology

Many different viruses are tested currently as oncolytic agents for clinical application. Some of these have humans as their natural host and some are genetically engineered. Non-human oncolytic viruses are e.g. of rodent origin [191, 192]. The first oncolytic virus (OV) to achieve limited marketing approval was the genetically modified adenovirus H101 (Oncorine) in China in 2005. It was approved for the treatment of HNSCC [164, 193]. In 2015, talimogene laherparepvec (T-VEC) also known as Imlygic<sup>®</sup>, a herpes simplex virus (HSV) encoding GM-CSF, was approved by the U.S. Food and Drug Administration (FDA) as well as the European Medicines Agency (EMA) for the treatment of non-resectable metastatic melanoma [194]. The type I HSV G47 $\Delta$  (Delytact<sup>®</sup>), was the first oncolytic virotherapy for brain cancer, especially residual or recurrent glioblastoma, and received limited approval in Japan in 2021 [195, 196].

The first clinical trial that was conducted using oncolytic MeV was led by Heinzerling and colleagues in 2005 [197]. The group injected replication competent MeV of the Edmonston Zagreb strain intratumorally into patients with cutaneous T cell lymphoma. The treatment was well-tolerated and paved the way for further clinical studies. Most of the following trials used MeVs encoding carcinoembryonic antigen (CEA) or the human thyroidal sodium-iodine symporter (NIS). CEA represents a common tumor marker and, when encoded by the virus, can be used to monitor MeV replication and deduce viral load from serum levels of CEA [198]. The NIS protein fulfills a dual role in cancer therapy. After application of radioactive

$^{123}\text{I}$  or  $^{131}\text{I}$ , NIS mediates the accumulation of these isotopes in infected tumor cells and provides another possibility for imaging viral gene expression as a surrogate parameter for replication [199]. Further,  $^{131}\text{I}$  can act therapeutically leading to tumor regression after having been concentrated in infected tumor cells via NIS. All in all, 19 phase I or II clinical trials have been conducted so far using oncolytic MeV in various tumor entities such as ovarian cancer, myeloma, tumors of the lung or the gastrointestinal tract as well as HNSCC [167].

The presence of an abscopal effect after oncolytic virotherapy has been reported only occasionally in clinical as well as preclinical studies. A phase II clinical trial reported abscopal effects in malignant melanoma after injecting T-VEC into primary lesions [200]. However, the systemic effect seemed to be limited and would require further therapeutic interventions in combination with T-VEC [201]. In a preclinical study, Havunen and colleagues detected abscopal effects *in vivo* after treating tumor-bearing hamsters with a cytokine-armed adenovirus [202]. After injecting the virus into one tumor lesion the group could detect increased populations of TILs in injected as well as non-injected tumor sites.

The advantages of OVVs are not only based on their lytic capacity. They can also act as vehicles for delivery and expression of several transgenes in the tumor as well as the surrounding TME in order to enhance anti-tumor efficacy and trigger immune responses against tumor antigens [165, 191]. Therefore, they show a high potential as tumoricidal agents for combination with immunotherapy, chemotherapy or radiotherapy in novel approaches of tumor treatment [192, 203, 204].

## 1.6 Combined radiovirotherapy

Combination treatments are an increasing focus of pre-clinical investigations *in vitro* and *in vivo* as well as in clinical trials. For non-resectable PDAC, the combination of radiotherapy with chemotherapy has already become part of the standard of care [14, 15, 16]. The combination of radiotherapy with immunotherapy using ICB has been tested intensively in the past years in several tumor types including HNSCC [205, 206, 207]. ICB inhibits negative regulatory elements that control immune tolerance. The combination of ICB and radiation follows the idea to use the immune activating capacity of radiotherapy to facilitate response of the tumor to immunotherapy [208]. Thereby, an immunologically ‘cold’ tumor can be turned immunologically ‘hot’ and primed for immunotherapy. The same idea is investigated in combinations of OVVs with immunotherapeutic agents [209]. In the clinical setting of oncolytic virotherapy, about one-third of roughly 100 clinical trials so far tested or are currently testing OVVs in combination with other therapeutic regimens. The use of ICB ranks at third place behind chemotherapy and radiotherapy [210]. A famous example of combined

immunovirotherapy is the combination of T-VEC with pembrolizumab, a monoclonal antibody against PD-1. This combination treatment showed strong clinical responses in advanced malignant melanoma [211]. Oncolytic MeV in combination with gemcitabine was investigated by May and colleagues. In a preclinical study, this chemovirotherapy showed strong cell killing of PDAC tumor cells [212]. Interestingly, this effect was achieved using subtherapeutic concentrations of gemcitabine as well as low doses of MeV.

The combination of OVs and radiation has come into focus of preclinical as well as clinical studies. Both therapeutic agents harbor the potential to boost the efficacy of the other: radiation may enhance OV therapy by increasing viral spread and replication. Vice versa, OVs may support radiotherapy by sensitizing the target tissue to radiation [213]. Dai and colleagues showed that oncolytic vaccinia virus in combination with radiotherapy has a synergistic cytotoxic effect with significant increase of apoptosis compared to monotherapy in preclinical PDAC tumor models [214]. Analyses in xenograft tumor models revealed that the combination led to significant tumor growth delay. The combination of the oncolytic parvovirus H1-PV in combination with radiotherapy showed several beneficial effects in glioma cells [215]. Irradiation prior to H1-PV infection led to increased sensitivity to virus infection and enabled killing not only of radiosensitive but also radioresistant cells [216].

Studies exploring a combination of radiation and oncolytic MeV as radiovirotherapy (RVTx) have been conducted for approx. 15 years. Liu and colleagues showed additive or even synergistic anti-tumor effects by increased cell killing after combined RVTx in glioblastoma and prostate cancer cells *in vitro* [217, 218]. Experiments in xenograft models of these tumor entities showed significantly prolonged survival compared to monotherapy or control and even tumor regression after combination therapy. In models for HNSCC and colorectal cancer, the combination of MeV encoding NIS and EBRT together with the radiosensitizing agent SAR-020106, a checkpoint kinase 1 inhibitor, showed synergistic effects in terms of cytotoxicity *in vitro* [219]. *In vivo* experiments in human colorectal xenografts showed anti-tumor efficacy of the combination therapy. Triple combinations of MeV, radiotherapy and chemotherapy were also tested recently by Rajamaran and colleagues [220]. The treatment sequence of chemo-, viro- and radiotherapy showed synergistic effects in different glioma cell lines. Further, the activation of a type I IFN response was detected in primary glioblastoma cultures, indicating a treatment-induced pro-inflammatory phenotype. These previous results of RVTx demonstrated the potential of this combination therapy for further preclinical studies and the achievement of clinical translation.

## 2 Aim of the Study

The urgency to develop safe and successful treatment strategies against cancer is permanently high. Currently, combination therapies encompassing several treatment modalities are frequently employed to develop multi-pronged approaches. The combination of radiotherapy and virotherapy using oncolytic MeV has been studied only for a few tumor entities so far. For refractory tumors such as HNSCC and PDAC, that often show resistance to common treatment approaches, respective data is limited. Further, several studies have shown the induction of innate immune signaling as well as ICD by ionizing radiation or MeV infection, respectively. However, this has not been investigated in a combined approach yet, although both treatment modalities show potential for anti-tumor efficacy when combined.

Based on previous findings in the field of radiation and oncolytic virotherapy, I hypothesize that a combination of both in a radiovirotherapy (RVTx) shows synergistic tumoricidal effects against HNSCC and PDAC models compared to both treatment modalities applied as monotherapies. Further, I hypothesize that RVTx is able to break treatment resistance

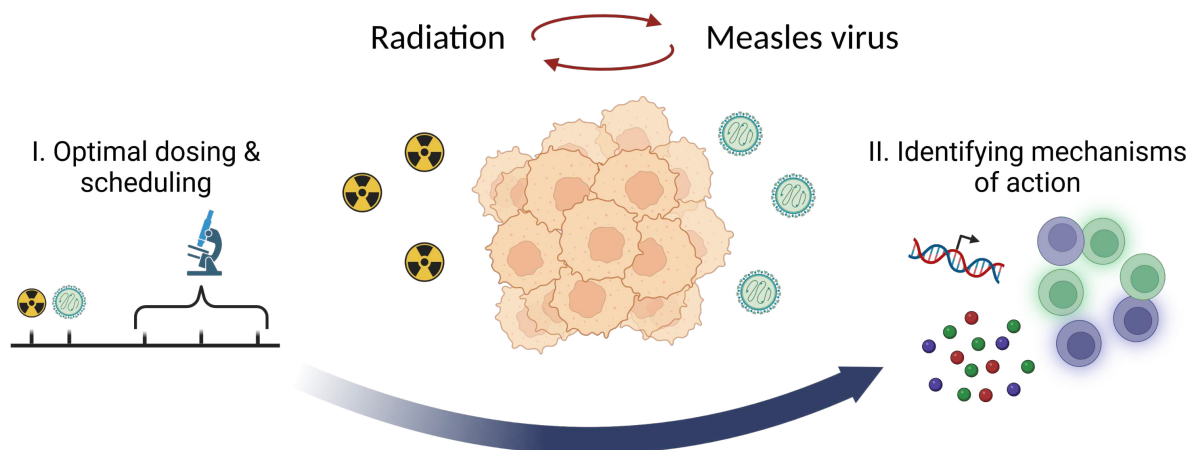


**Figure 2.1: Investigating combined radiovirotherapy (RVTx).** The analysis of RVTx comprises two parts: (I) The evaluation of optimal dosing and scheduling, including analysis of synergistic effects and development of suitable models. (II) A molecular and functional identification of mechanisms of action focusing on cytokine secretion, target gene expression and immune cell characterization for analyzing innate immune signaling and ICD induction. The image was created with BioRender.com.

by inducing a sustained anti-tumor immune response. The aim of this study was therefore a systematic analysis of RVTx in different experimental systems *in vitro*, *in vivo* and *ex vivo* (see Figure 2.1). I used a variety of relevant preclinical models and described all experimental results of this study in this chronological order.

The first part of this study addresses a systematic evaluation of both, radiation and MeV dosing. I investigated synergy of the combination therapy on the basis of a profound cytotoxicity analysis. Further, I developed treatment schedules of RVTx for application in cell culture experiments as well as in animal models. The implementation of *in vivo* experiments also included the development of syngeneic, heterotopic immunocompetent murine models for HNSCC and PDAC. The focus of the second part is the molecular and functional identification of possible mechanisms of action induced by RVTx treatment. I investigated factors of damage sensing, innate and adaptive immune signaling as well as typical markers for ICD induction. Applied methods included analyzing secretion of cytokines and other molecules, target gene expression as well as surface markers and immune cell types. This comprehensive analysis will provide insights into RVTx therapy that will enable moving this treatment strategy further towards clinical application.

# 3 Materials and Methods

## 3.1 Materials

### 3.1.1 Chemicals, buffers and growth media

Chemicals	Catalog no., Manufacturer
Accutase cell detachment solution	423201, BioLegend, San Diego, CA/USA
Agarose, molecular biology grade	A9539, Sigma-Aldrich, Saint Louis, MO/USA
Antibiotic antimycotic solution (ABAM)	A5955, Sigma-Aldrich
ACK lysing buffer	A10492-01, Gibco Life Technologies, Carlsbad, CA/USA
Atipamezol hydrochloride	23554.00.00, Orion Pharma, Espoo, Finland
B-27 <sup>®</sup> supplement	12587-010, Gibco Life Technologies
Bepanthen <sup>®</sup> eyes and nose cream	6029009.00.00, Bayer Vital GmbH, Leverkusen, Germany
$\beta$ -mercapoethanol, purity above 99%	M7522, Sigma-Aldrich
Bovine serum albumin (BSA)	A9418, Sigma-Aldrich
Collagenase type I	17100-17, Gibco Life Technologies
Concanavalin A	C2010-25MG, Sigma-Aldrich
Dako fluorescence mounting medium	S3023, Agilent, Santa Clara, CA/USA
4',6-diamidino-2-phenylindole (DAPI)	D8417, Sigma-Aldrich
Deoxynucleotide triphosphate (dNTP) mix	R0192, Thermo Scientific, Waltham, MA/USA
D-Glucose	15023, Gibco Life Technologies
Dimethyl sulfoxide (DMSO)	D2438-5X, Sigma-Aldrich
Doxorubicin hydrochloride	15007, Cayman Chemical Company, Ann Arbor, MI/USA

<b>Chemicals</b>	<b>Catalog no., Manufacturer</b>
Dulbecco's Modified Eagle's medium (DMEM)	31966, Gibco Life Technologies
DMEM/F12, advanced	12634, Gibco Life Technologies
DMEM/F-12	31331, Gibco Life Technologies
Dulbecco's phosphate-buffered solution (D-PBS)	14190-144, Gibco Life Technologies
Elution buffer (EB)	19086, Qiagen, Hilden, Germany
Epidermal growth factor, human recombinant	01-107, Sigma-Aldrich
ELISA stop solution	SS04, Invitrogen Life Technologies, Waltham, MA/USA
Ethanol, purity above 99.8%	9065.1, Carl Roth, Karlsruhe, Germany
EveryBlot blocking buffer	12010947, Bio-Rad Laboratories, Hercules, CA/USA
Fetal calf serum (FCS)	P40-37500, PAN-Biotech GmbH, Aidenbach, Germany
Fibroblast growth factor 10, recombinant human	100-26, Peprotech, Cranbury, NJ/USA
Fibroblast growth factor basic, recombinant human	233-FB, R&D Systems, Minneapolis, MN/USA
Flumazenil Kabi	M08827/01, Fresenius Kabi, Bad Homburg, Germany
Fugene <sup>®</sup> HD transfection reagent	E231A, Promega, Madison, WI/USA
Fusion inhibitory peptide (FIP) Z-D-Phe-Phe-Gly	C9405, Sigma-Aldrich
Fusion inhibitory peptide (FIP) Z-D-Phe-Phe-Gly-OH	40.157.680.100, Bachem AG, Bubendorf, Switzerland
GeneRuler <sup>™</sup> 1 kb DNA Ladder	SM0311, Thermo Scientific
GeneRuler <sup>™</sup> 100 bp Plus DNA Ladder	SM0321, Thermo Scientific
Gentamicin	15750, Gibco Life Technologies
GlutaMAX <sup>™</sup> supplement	35050, Gibco Life Technologies
H <sub>2</sub> O, sterile, PCR grade	W4502, Sigma-Aldrich
Ham's nutrient mixture F10-F12	sh30026.01, Fisher Scientific, Pittsburgh, PA/USA
Heparin sodium salt	H3149, Sigma-Aldrich
HEPES solution	H0887, Sigma-Aldrich
Hoechst 33342	H1399, Invitrogen Life Technologies
HRP streptavidin for ELISpot	557630, BD Biosciences, San Jose, CA/USA
Human keratinocyte growth supplement (HKGS)	S-001-5, Gibco Life Technologies

<b>Chemicals</b>	<b>Catalog no., Manufacturer</b>
Hydrocortisone	H0135, Sigma-Aldrich
Insulin from bovine pancreas	I6634, Sigma-Aldrich
Iscove's Modified Dulbecco's medium (IMDM)	sh30228.02, Fisher Scientific
Isofluran CP	400806.00.00, CP-Pharma, Burgdorf, Germany
Isopropanol, purity above 99.8%	6752.1, Carl Roth
Kanamycin solution	K0129, Sigma-Aldrich
Laemmli sample buffer (4×)	1610747, Bio-Rad Laboratories
L-Glutamine	25030-081, Gibco Life Technologies
Lipofectamine 2000	11668027, Invitrogen Life Technologies
Matrigel <sup>®</sup> basement membrane matrix	356234, Corning, Corning, NY/USA
MB Taq DNA polymerase	53-1050, Minerva Biolabs, Hackensack, NJ/USA
Medetomidin hydrochloride	401062.00.00, Zoetis Deutschland, Berlin, Germany
Methanol, purity above 99.9%	4627.2, Carl Roth
Midazolam-ratiopharm <sup>®</sup>	N52210.05-Z01, Ratiopharm, Ulm, Germany
Minimal Essential medium Eagle (MEM)	M5650, Sigma-Aldrich
Mitoxantrone hydrochloride	14842, Cayman Chemical Company
Mouse IFN- $\gamma$ ELISpot Pair	551881, BD Biosciences
Nodal protein, recombinant human	3218-ND, R&D Systems
OneTaq <sup>®</sup> DNA polymerase	M0480L, New England Biolabs, Ipswich, MA/USA
OneTaq <sup>®</sup> standard reaction buffer (5×)	B9022S, New England Biolabs
Opti-MEM <sup>™</sup>	51985, Gibco Life Technologies
Oxaliplatin	AG-CR1-3592, AdipoGen Life Science, San Diego, CA/USA
Paraformaldehyde (PFA) solution, 4%	19943, Affymetrix, Santa Clara, CA/USA
Penicillin-streptomycin (P/S)	15070, Gibco Life Technologies
Polybrene infection/transfection reagent	TR-1003, Sigma-Aldrich
Power SYBR <sup>™</sup> Green PCR master mix	4367659, Applied Biosystems, Waltham, MA/USA
Precision Plus <sup>™</sup> protein all blue standards	1610373, Bio-Rad Laboratories

<b>Chemicals</b>	<b>Catalog no., Manufacturer</b>
Protease Inhibitor Cocktail cOmplete™ Ultra tablets	5892970001, Roche, Basel, Switzerland
Puromycin dihydrochloride	A11138-03, Gibco Life Technologies
Purple loading dye (6×)	B7024A, New England Biolabs
RIPA buffer	R0278, Sigma-Aldrich
RNAlater™ RNA stabilization reagent	1017980, Qiagen
RNAprotect® cell reagent	76104, Qiagen
RNase H	M0297L, New England Biolabs
RNase H reaction buffer, 10×	B0297S, New England Biolabs
Roswell Park Memorial Institute (RPMI) 1640	61870, Gibco Life Technologies
ROTI®-Stock, 10× tris-buffered saline-tween (TBST)	1061.1, Carl Roth
Rotiphorese® SDS-PAGE	3060.1, Carl Roth
Skim milk powder, blotting grade	T145.2, Carl Roth
Sodium pyruvate	11360, Gibco Life Technologies
Sodium chloride injection solution, 0.9%, isotonic	2350748, B. Braun SE, Melsungen, Germany
SYBR™ Safe DNA gel stain	S33102, Thermo Scientific
TMB substrate for ELISpot	3651-10, Mabtech, Nacka Strand, Sweden
Trans-Blot Turbo 5× transfer buffer	10026938, Bio-Rad Laboratories
Tris-borate EDTA (TBE) buffer, 10×	15581, Invitrogen Life Technologies
Tris-buffered saline (TBS), 1×, with 1% casein	1610782, Bio-Rad Laboratories
Triton™ X-100	X100, Sigma-Aldrich
Trypan blue solution, 0.4%	T8154, Sigma-Aldrich
Trypsin-ethylenediaminetetraacetic acid (EDTA) solution, 0.05%	25300, Gibco Life Technologies

### 3.1.2 Cell lines

<b>Cell line</b>	<b>Description</b>	<b>Source</b>
AsAn-PaCa	Human pancreatic adenocarcinoma cell line [221]	A. Angelova, Heidelberg, Germany
BxPC-3	Human pancreatic adenocarcinoma cell line [222]	ATCC, Manassas, VA/USA

---

Cell line	Description	Source
HNO210	Human HNSCC cell line derived from the larynx	C. C. Herold-Mende, Heidelberg, Germany
HNO410	Human HNSCC cell line derived from a hypopharyngeal lymph node metastasis	C. C. Herold-Mende, Heidelberg, Germany
mEERL95	Mouse HNSCC cell line established by <i>in vitro</i> transformation of male tonsillar epithelial cells with HPV16 E6-E7-proteins and oncogenic H-ras in a C56BL/6JRj mouse [223]	G. Tolstonog, Lausanne, Switzerland
MOC2	Mouse OSCC cell line [224]	Kerafast, Boston, MA/USA
MRC-5	Human lung fibroblast cell line [225]	ATCC, Manassas, VA/USA
Panc02	Murine pancreatic adenocarcinoma cell line derived from a C57BL/6 mouse [226]	J. Seco, Heidelberg, Germany
PC1	Human pancreatic adenocarcinoma cell culture [227]	C. Ball, Dresden, Germany
PC3	Human pancreatic adenocarcinoma cell culture [227]	C. Ball, Dresden, Germany
PC28	Human pancreatic adenocarcinoma cell culture [227]	C. Ball, Dresden, Germany
PC43	Human pancreatic adenocarcinoma cell culture [227]	C. Ball, Dresden, Germany
PDA30364	Mouse pancreatic adenocarcinoma cell line generated from primary pancreatic tumors in a C57BL/6-Ly5.1 mouse [228]	R. Offringa, Heidelberg, Germany
T3M4	Human pancreatic adenocarcinoma cell line [229]	Z. Raykov, Heidelberg, Germany
Vero	African green monkey kidney epithelial cell line	ATCC, Manassas, VA/USA

---

### 3.1.3 Recombinant viruses

---

Name	Description
MeVac Id-EGFP	Measles Schwarz vaccine strain virus encoding eGFP in ATU downstream of leader [185]
MeVac	Measles Schwarz vaccine strain virus [185]
MV-NIS	Measles Edmonston B strain virus encoding the human thyroiodal sodiom iodide symporter [199]
LV-105 hCD46 BC1	Lentiviral vector encoding human CD46 using a third generation lentiviral vector system [230]; kindly provided by J. P. W. Heidebüchel (Heidelberg, Germany)

---

### 3.1.4 Plasmids

---

Name	Description
pCG-L	Eukaryotic expression vector encoding MeV L protein
pCG-N	Eukaryotic expression vector encoding MeV N protein
pCG-P	Eukaryotic expression vector encoding MeV P protein
pcDI-DsRed2	Eukaryotic expression vector encoding a variant of the <i>Discosoma</i> red fluorescent protein
pcMeVac Id-EGFP	Eukaryotic expression vector encoding MeV Schwarz vaccine strain antigenome encoding eGFP in ATU downstream of leader [184]
pcMeVac	Eukaryotic expression vector encoding MeV Schwarz vaccine strain antigenome [184]
pCAG-Puro-P2A-hCD46-SMARter-NP	Bacterial expression vector produced in <i>Escherichia coli</i> DH5a strain encoding pCAG promoter and human <i>CD46</i> gene [231, 232]
pEF1-Puro-P2A-hCD46-SMARter-NP	Bacterial expression vector produced in <i>Escherichia coli</i> DH5a strain encoding pEF1 promoter and human <i>CD46</i> gene [231, 232]

---

### 3.1.5 Oligonucleotides

All oligonucleotides were designed using Primer-BLAST [233]. I checked primer quality by PCR Primer Stats [234] and UCSC In-Silico PCR [235]. They were synthesized by Eurofins MWG Operon (Ebersberg, Germany) and stored in elution buffer (EB). For primers binding to retinoic acid-inducible gene I (RIG-I), cyclic GMP-AMP synthase (cGAS) and stimulator of interferon genes (STING) the genome position of the first complementary nucleotide is given in the primer name. ‘rev’ or ‘R’ indicates primers hybridizing to the ‘+’ strand DNA/RNA; ‘for’, ‘fwd’ or ‘F’ indicates primers hybridizing to the ‘-’ strand DNA/RNA; h — human; m — murine.

Name	Sequence 5' → 3'
h $\beta$ -actin Ex6 for	TCATTGCTCCTCCTGAGCGCA
h $\beta$ -actin Ex6 rev	CTAGAAGCATTGCGGTGGAC
RIG_I fwd_38017	GAGCAACAGCTGAGAATGTCC
RIG_I rev_38187	ACGGGTGTTGTTTACTAGTGTTG
cGAS fwd_19	GCCAGTAGTGCTTGGTTTCC
cGAS rev_229	GGAGACTCGGTGGGATCCAT
STING fwd_13	CTCCTCCCTCCTAGGTCACA
STING rev_179	CTCAAGCCACCACGATCAAAC
h IFN $\beta$ for	GACGCCGCATTGACCATCTA
h IFN $\beta$ rev	CCTTAGGATTTCCACTCTGACT
h IFNAR-1b for	TGTAAGTGGTGGGATCTGCG
h IFNAR-1b rev	TCAGATGCTTGTACGCGGAG
hCD46_qPCR_F	CTCCTTCTCCGATGCCTGTG
hCD46_qPCR_R	GGTATGTGCCTTTCTTCTTCCTC
m $\beta$ -actin for	AGAGGGAAATCGTGCGTGAC
m $\beta$ -actin rev	CAATAGTGATGACCTGGCCGT
m L13A for	GGCTGCCGAAGATGGCGGAG
m L13A rev	GCCTTCACAGCGTACGACCACC
m IFN $\beta$ for	AAGAGTTACACTGCCTTTGCCATC
m IFN $\beta$ rev	CACTGTCTGCTGGTGGAGTTCATC
m FoxP3 fw	GGCCCTTCTCCAGGACAGA
m FoxP3 rev	GCTGATCATGGCTGGGTTGT

### 3.1.6 Antibodies

All antibodies with respective dilutions for flow cytometry (FC), western blot (WB) and immunofluorescence (IF) analyses I used in this thesis are listed in the table below. Fluorochromes: APC — allophycocyanin; Cy<sup>TM</sup>7 — cyanine 7; PerCP-Cy<sup>TM</sup>5.5 — peridinin chlorophyll protein complex with cyanine 5.5; PE — phycoerythrin; FITC — fluorescein isothiocyanate.

Antibody	Description	Application	Manufacturer
Anti-human calreticulin-Alexa Fluor <sup>®</sup> 647	Mouse IgG2b, clone 681234	FC 1:50	IC38981R, R&D Systems
Anti-calreticulin	Rabbit IgG, clone D3E6	IF 1:100	12238, Cell Signaling Technology
Anti-rabbit IgG (H+L)-Alexa Fluor <sup>®</sup> 594	Goat, secondary antibody	IF 1:200	A11012, Invitrogen Life Technologies
Anti-human CD46-APC	Mouse IgG1, clone TRA-2-10	FC 1:100	352405, BioLegend
Anti-mouse CD3-PE	Rat IgG2b, $\kappa$ , clone 17A2	FC 1:100	100205, BioLegend
Anti-mouse CD4-APC-Cy <sup>TM</sup> 7	Rat IgG2b, $\kappa$ , clone GK1.5	FC 1:100	100413, BioLegend
Anti-mouse CD8a-APC	Rat IgG2a, $\kappa$ , clone 53-6.7	FC 1:100	100711, BioLegend
Anti-mouse CD45.2-PerCP-Cy <sup>TM</sup> 5.5	Mouse (SJL) IgG2a, $\kappa$ , clone 104	FC 1:100	109827, BioLegend
Anti-mouse CD335-FITC	Rat IgG2a, $\kappa$ , clone 29A1.4	FC 1:50	137605, BioLegend
Mouse IgG1, $\kappa$ , APC	Isotype control, clone MOPC-21	FC 1:100	400120, BioLegend
Rat IgG2b, $\kappa$ , PE	Isotype control, clone RTK4530	FC 1:100	400607, BioLegend
Rat IgG2b, $\kappa$ , APC-Cy <sup>TM</sup> 7	Isotype control, clone A95-1	FC 1:100	552773, BD Biosciences
Rat IgG2a, $\kappa$ , APC	Isotype control, clone RTK2758	FC 1:100	400511, BioLegend

Antibody	Description	Application	Manufacturer
Mouse IgG2a, $\kappa$ , PerCP-Cy <sup>TM</sup> 5.5	Isotype control, clone MOPC-173	FC 1:100	400251, BioLegend
Rat IgG2a, $\kappa$ , FITC	Isotype control, clone RTK2758	FC 1:50	400505, BioLegend
Anti-mouse CD16/CD32 (Mouse FC block)	Rat (SD) IgG2b, $\kappa$ , clone 2.4G2	FC 1:100	553142, BD Bio- sciences
Anti-human RIG-I, C-terminus	Rabbit polyclonal	WB 1:1000	06-1041, Merck Millipore, Burling- ton, MA/USA
Anti-human cGAS	Rabbit IgG, clone D1D3G	WB 1:1000	15102, Cell Signal- ing Technology
Anti-human STING	Rabbit IgG, clone D2P2F	WB 1:1000	13647, Cell Signal- ing Technology
Anti-rabbit IgG, HRP-linked	Goat, secondary antibody	WB 1:10,000	7074, Cell Signal- ing Technology

## 3.2 Methods

### 3.2.1 Cell culture

#### 3.2.1.1 Culturing cells

I cultured all cell lines used in this project at 37°C in a humidified atmosphere with 5% CO<sub>2</sub> in Nunc<sup>TM</sup> EasYFlask<sup>TM</sup> cell culture treated flasks with filter caps (Thermo Fisher Scientific). The human head and neck squamous cell carcinoma (HNSCC) cell lines HNO210 and HNO410 as well as Vero cells were cultured in DMEM supplemented with 10% fetal calf serum (FCS). For the murine pancreatic ductal adenocarcinoma (PDAC) cell line PDA30364, also referred to as 30364, I used the same growth medium with addition of 1× penicillin-streptomycin (P/S) and 1× sodium pyruvate. I cultured the human PDAC cell lines AsAn-PaCa, BxPC-3 and T3M4 as well as the murine PDAC cell line Panc02, in RPMI 1640 medium supplemented with 10% FCS. I cultured the MRC-5 cells in MEM supplemented with 10% FCS, 1× sodium-pyruvate, 1× GlutaMAX<sup>TM</sup> and 1× P/S. I cultured the murine cell line mEERL95 in DMEM/F-12 supplemented with 5% FCS, 1× human keratinocyte growth supplement (HKGS) and 1× P/S. As culture medium for the murine cell line MOC2, I used IMDM and Ham's nutrient mixture F10-F12 at a ratio of 2:1 supplemented with 5% FCS, 1× P/S, 5 mg/ml insulin from bovine

pancreas, 400 ng/ml hydrocortisone and 5 ng/ml human recombinant epidermal growth factor. The human PDAC cultures PC1, PC3, PC28 and PC43, I cultured in advanced DMEM/F-12 supplemented with 0.6% D-Glucose, 2 mM L-Glutamine, 12 µg/ml heparin, 5 mM hepes buffer, 1× B-27<sup>®</sup> supplement, 1× P/S, fibroblast growth factors (10 ng/ml rhFGF-basic, 20 ng/ml rhFGF-10) and 20 ng/ml rhNodal. When the cells reached 80 – 100% confluency, I split them at a ratio of 1:5 – 1:100 depending on the growth kinetics of each cell line. For that, I removed the medium, washed the cell layer with D-PBS and added 0.05% trypsin-EDTA solution. After cell detachment (5 – 20 min), I added the respective cell culture medium and split the cells at the required ratio. I performed this subcultivation procedure once or twice per week. To determine the cell number, I mixed the cell suspension with 0.4% trypan blue solution (ratio 1:1) and counted the cells using a Neubauer hemocytometer (Marienfeld).

#### 3.2.1.2 Cryopreservation, storage and thawing of cells

For cryopreservation, I centrifuged the cells at 300×g for 5 min and resuspended the cell pellet with respective cell culture medium supplemented with 5% dimethyl sulfoxide (DMSO). I aliquoted the cells into Nunc<sup>™</sup> CryoTube<sup>™</sup> vials (Thermo Fisher Scientific) at 1·10<sup>6</sup> cells per tube. I kept the tubes in a Stratagene Cryo 1°C Freezing Container (Agilent) at –80°C for 24 h. Afterwards, I transferred them to liquid nitrogen for long-term storage. For thawing the frozen cells, I placed the vials in a 37°C water bath (GFL, Burgwedel, Germany) for 1 min, transferred the cell suspension into a cell culture flask containing the respective culture medium and cultivated them at 37°C, 5% CO<sub>2</sub>. After 24 h, I performed a medium change with fresh medium.

#### 3.2.1.3 Analysis of cell contamination and cell line authentication

To ensure experimental quality, I used the Multiplex Cell Contamination Test [236] and Multiplex Cell Authentication [237]. Both are services provided by Multiplexion (Heidelberg, Germany). For the Multiplex Cell Contamination Test, I prepared cell lysates as follows: I resuspended a cell pellet consisting of 1·10<sup>6</sup> cells in 100 µl D-PBS, incubated at 95°C for 15 min and centrifuged at >10.000×g for 5 min to remove cellular debris. In preparation of the Multiplex Cell Line Authentication, I extracted the genomic DNA of 1·10<sup>6</sup> cells per respective cell line using the DNeasy<sup>®</sup> Blood & Tissue Kit (69504, Qiagen). Additionally, all cell lines were routinely tested for *Mycoplasma* contamination using the Venor<sup>®</sup>GeM Classic Mycoplasma Detection Kit (11-1100, Minerva Biolabs).

## 3.2.2 Molecular biology methods

### 3.2.2.1 Polymerase chain reaction

For the amplification of DNA fragments, I performed a polymerase chain reaction (PCR) using One *Taq*<sup>®</sup> DNA polymerase. For each PCR reaction, I used One *Taq*<sup>®</sup> standard buffer, 200  $\mu$ M deoxynucleotide triphosphate (dNTP) mix, 200 nM of each respective forward and reverse primers (see 3.1.5), 0.625 U DNA polymerase and sterile water together with the respective amount of target DNA fragment. I performed the PCR reactions in a T1 Thermocycler (Biometra, Göttingen, Germany) under the conditions given in Table 3.7. I set the annealing temperature for each primer pair using the T<sub>m</sub> Calculator (New England Biolabs, v1.15.0) [238] and calculated the extension time according to the size of the expected PCR product (60 s per kbp).

**Table 3.7: Polymerase chain reaction (PCR) conditions.** Conditions for PCR with One *Taq*<sup>®</sup> DNA polymerase. X — annealing temperature, y — extension time.

	Temperature [°C]	Time [s]	
Initial denaturation	94	30	
Denaturation	94	30	} 25 – 35×
Annealing	x	30	
Extension	68	y	
Final extension	68	120	

### 3.2.2.2 Agarose gel electrophoresis

For separation of DNA fragments by size, I performed agarose gel electrophoresis. I added Purple Loading dye to the DNA fragments and loaded the mixture on a 1 – 2% agarose gel with SYBR<sup>™</sup> Safe DNA Gel Stain. I used GeneRuler<sup>™</sup> 100 bp or 1 kb DNA Ladder as a molecular weight standard and performed horizontal gelelectrophoresis in a 1× tris-borate EDTA (TBE) buffer at 140 V for 30 – 45 min and visualized the gels under ultraviolet light.

### 3.2.2.3 DNA and RNA isolation

I isolated genomic DNA using the DNeasy<sup>®</sup> Blood & Tissue Kit (69504, Qiagen) according to the manufacturer's instructions. I determined the DNA concentration and purity of the

sample using a spectrophotometer ND-1000 (Nano Drop Technologies, Wilmington, DE/USA) by absorbance measurements at 260 nm wavelength with a quality control using the 260/280 and 260/230 ratios to check purity, i.e. absence of contaminating protein or other substances. For isolation of total RNA, I used the RNeasy® Plus Mini Kit (74134, Qiagen) according to the manufacturer's instructions including additional homogenization using the QIAshredder (79654, Qiagen). Again, I determined the RNA concentration and purity of the sample using a spectrophotometer ND-1000 (Nano Drop Technologies) by absorbance measurements at 260 nm wavelength.

#### 3.2.2.4 Complementary DNA synthesis and reverse transcription PCR

To perform complementary DNA (cDNA) synthesis, I used the Maxima H Minus First Strand cDNA Synthesis Kit (K1652, Thermo Fisher Scientific) using 300 ng total RNA per sample and oligo(dT) primers according to the manufacturer's instructions. Subsequently, I performed RNA digestion using ribonuclease H (RNase H) for 30 min at 37°C before reverse transcription PCR (RT-PCR) using OneTaq® DNA polymerase as described before (see 3.2.2.1).

#### 3.2.3 Irradiation

The irradiation was performed using two different systems: to irradiate virus solutions, I used a linear accelerator (Artiste, Siemens AG, Munich, Germany) with a dose rate of 3 Gy/min. The object to be irradiated was covered with two RW3 slab phantoms (PTW, Freiburg, Germany) as tissue equivalent. For cells and mice, I used the MultiRad 225 system (Faxitron Bioptics, LLC., Tucson, AZ/USA). Depending on the position of cells and mice within the irradiation chamber, the dose rate was at 0.846, 2.151 or 3.182 Gy/min. During mouse irradiation, I covered the animal body completely with a lead shield containing a 13 mm collimator to direct the irradiation beam only onto the tumor.

#### 3.2.4 Recombinant measles virus

##### 3.2.4.1 Rescue

For the generation of recombinant measles virus particles of the viruses MeVac and MeVac Id-EGFP (see 3.1.3), I performed a virus rescue using the RNA polymerase II-dependent system [239]. I seeded Vero cells in a 6-well plate ( $2 \cdot 10^5$  cells/well) incubated them at 37°C, 5% CO<sub>2</sub> for 16 h prior to transfection. The transfection mix contained a plasmid encoding the corresponding measles antigenome (5 µg), the expression plasmids encoding MeVac N, P

and L proteins, pCG-N (500 ng), pCG-P (100 ng) and pCG-L (500 ng), as well as a plasmid encoding a red fluorescent protein, pcDI dsRed (100 ng), as transfection efficiency control topped up to 200  $\mu$ l DMEM or Opti-MEM<sup>TM</sup>. As transfection reagents, I used either 18.6  $\mu$ l Fugene<sup>®</sup> HD (ratio 3:1) or 15.5  $\mu$ l Lipofectamine 2000 (ratio 2.5:1) per 6.2  $\mu$ g input DNA. I slowly added the transfection reagent to the transfection mixing and incubated the mixture at room temperature (RT) for 25 min to allow formation of transfection complexes. During incubation time, I replaced the medium of Vero cells with medium containing DMEM, 2% FCS and 50  $\mu$ g/ml kanamycin (rescue medium). In the following, I added the transfection mixture to the cells, cultivated them at 37°C, 5% CO<sub>2</sub> and monitored the cells daily for syncytia formation.

#### **3.2.4.2 Propagation and storage**

After rescue, I propagated the recombinant virus on Vero cells for up to 4 passages. For the first passage, I seeded  $1.5 \cdot 10^6$  cells in a 10 cm cell culture dish 16 h prior to infection. Once syncytia were visible in the wells of the 6-well plate containing the virus rescue, I scraped the cells in rescue medium using a cell lifter, transferred the cell suspension to a 2 ml tube and vortexed it. After removing culture medium from the prepared Vero cells in the 10 cm culture dish, I pipetted the rescue suspension onto the cells and filled the culture dish with rescue medium up to 5 ml and incubated it at 37°C, 5% CO<sub>2</sub> for 2 – 3 h. Afterwards, I added 5 ml rescue medium and cultivated the cells at 37°C, 5% CO<sub>2</sub> for up to 72 h until syncytia were detectable but had not burst. Subsequently, I removed the culture medium and added 500  $\mu$ l Opti-MEM<sup>TM</sup>. Again, I scraped the cells with a cell lifter, transferred the suspension to a 2 ml tube and vortexed it. I snap-froze the tube in liquid nitrogen and stored it at –80°C for at least 24 h. Next, I thawed the virus preparation in a 37°C water bath, vortexed and centrifuged at 5000 $\times$ g, 4°C for 5 min to remove cellular debris. I aliquoted the supernatant containing virus suspension and stored it at –80°C until further use. To determine the viral titer, I performed a serial dilution titration assay (see 3.2.4.3). For large scale virus propagation in the second and following passages, I seeded  $5 \cdot 10^6$  Vero cells into 15 cm cell culture dishes 24 h prior to infection at a multiplicity of infection (MOI) of 0.03 in 8 ml Opti-MEM<sup>TM</sup> at 37°C, 5% CO<sub>2</sub> overnight. On the next day, I added 8 ml DMEM + 10% FCS to each plate and continued the incubation at 37°C, 5% CO<sub>2</sub> for up to 50 h until syncytia were about to burst. For the harvest of passaged virus, I removed the culture medium completely and scraped the cells with a cell lifter. I collected the virus suspension in a Falcon<sup>TM</sup> tube (Fisher Scientific) and proceeded as described above in order to prepare a clarified virus suspension.

### 3.2.4.3 Titration

To determine the viral titer of the produced virus suspensions, I performed a serial dilution titration assay in octuplicates. In a 1:10 dilution series, I added virus suspension to wells of a 96-well plate containing 90  $\mu$ l DMEM + 10% FCS. Subsequently, I added  $1 \cdot 10^4$  Vero cells in 100  $\mu$ l DMEM to each well and incubated the plate at 37°C, 5% CO<sub>2</sub> for 72 h. Afterwards, I counted the individual syncytia and calculated the titer in cell infectious units (ciu) per milliliter (ciu/ml).

### 3.2.4.4 Multi-step growth curves

To investigate viral proliferation in treated and irradiated cells as well as for virus characterization, I generated multi-step growth curves. I seeded  $1 \cdot 10^5$  human tumor cells (BxPC-3, T3M4, HNO210, HNO410) or Vero cells in 12-well plates. Twenty-four hours later, I treated the cells either with radiovirotherapy or virus alone at an MOI of 0.1 or 0.01 (T3M4) by removing the cell culture-specific medium and inoculating the cells with the respective dose of virus in 300  $\mu$ l Opti-MEM™ in triplicates for each time point. I removed the inoculum after 2 – 3 h, added cell culture-specific medium and incubated the cells at 37°C, 5% CO<sub>2</sub>. At designated time points within four days after treatment, I scraped the cells in culture medium, pooled triplicates and snap-froze the samples in liquid nitrogen. I determined the titers of viral progeny by serial dilution titration assays (see 3.2.4.3) in quadruplicates.

### 3.2.5 Experimental treatment schedule for radiovirotherapy

To analyze synergy and characterize the induced mechanisms of action of radiovirotherapy (RVTx), I defined a specific treatment schedule to be used in all experiments within this thesis. With regard to my previous work in my master's thesis [240], the schedule is as follows: irradiation 24 h prior to virus infection (R24V) (see Figure 3.1). I used this schedule, defined R24V, throughout all experiments of this thesis *in vitro* and *ex vivo* with adjusted doses of radiation and virus according to the specific experiment. Further, I adapted this treatment schedule also to *in vivo* experiments.

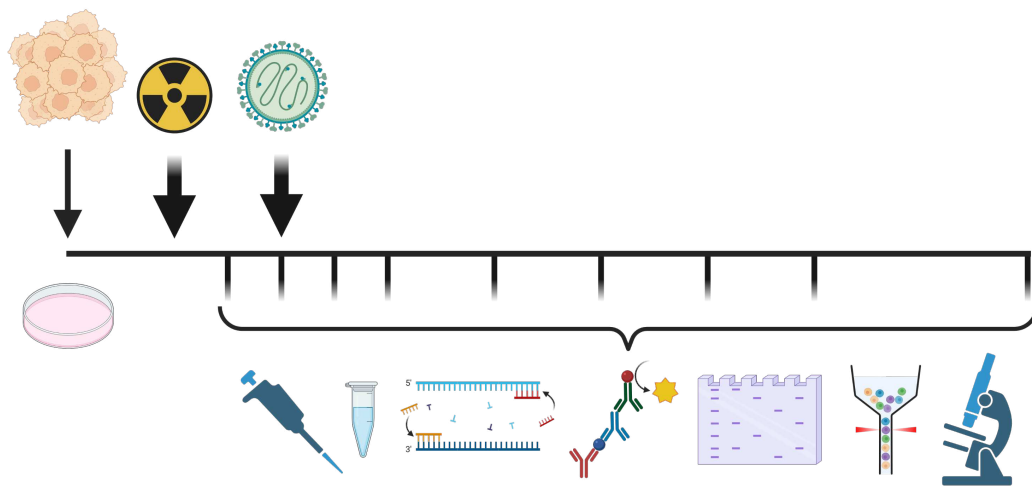


**Figure 3.1: Experimental overview for RVTx analysis *in vitro* and *ex vivo*.** The overall outline of *in vitro* and *ex vivo* experiments in this study was as follows: I seeded tumor cells and irradiated them 24 h later. Another 24 h later, I infected cells with MeVac Id-EGFP (schedule R24V). At specific time points depending on the conducted experiment, I monitored or collected cells and supernatants for several analyses: measuring cell viability or secreted cytokines and other molecules, investigating expression of certain targets on transcriptomic or proteomic level, analysis of cell surface structures as well as fluorescence microscopy. The image was created with BioRender.com.

## 3.2.6 Cell viability assays

### 3.2.6.1 XTT

As one approach for determining cell viability, I performed 2,3-bis-(2-methoxy-4-nitro-5-sulphophenyl)-2H-tetrazolium-5-carboxanilide (XTT) assays using the Colorimetric Cell Viability Kit III (PK-CA20-300-1000, PromoKine, Heidelberg, Germany). This assay is based on the ability of metabolically active cells to reduce the tetrazolium salt XTT into an orange-colored formazan product. This can be quantified using a spectrophotometer. I used the infinite M200 spectrophotometer and i-control software (Tecan, Männedorf, Switzerland). I seeded  $8 \cdot 10^3$  or  $1 \cdot 10^4$  cells into clear 96-well plates and cultivated them for 24 h prior to treatment with radio- or virotherapy alone or the combination according to the R24V schedule. Irradiation of the respective samples was performed as described before (see 3.2.3) at doses of 1, 2, 5 or 8 Gy. Infection of the respective samples with vaccine strain measles virus (MeV) followed 24 h after irradiation. I removed the culture medium from respective wells and inoculated the cells with MeVac Id-EGFP at MOIs ranging from 0.001 to 1, depending on the virus sensitivity of each cell line, in Opti-MEM™ in a total volume of 50  $\mu$ l for 2 – 3 h. Mock-treated samples or samples only receiving irradiation were inoculated with 50  $\mu$ l Opti-MEM™. Afterwards, I substituted the inoculum with 100  $\mu$ l cell culture-specific medium and incubated the cells at 37°C, 5% CO<sub>2</sub>. At the time points 0, 1, 3, 5 and 7 days post treatment (p.tr.), I performed

the XTT assay according to the manufacturer's instructions.

### **3.2.6.2 Intracellular ATP**

To validate the results of the XTT assay, I performed a second cell viability assay measuring intracellular ATP-levels of treated cells. I used the ATPlite 1step Luminescence Assay System (6016731, PerkinElmer, Waltham, MA/USA). I seeded and treated the cells as described above (see 3.2.6.1) but used black 96-well plates (655086, Greiner Bio-One, Kremsmünster, Austria). I performed the assay according to the manufacturer's instructions and measured luminescence using the infinite M200 spectrophotometer and i-control software.

### **3.2.7 Fluorescence microscopy**

To determine cell confluence, morphology or virus infection, I took images by fluorescence microscopy. I used the Axiovert 200 (Carl Zeiss, Oberkochen, Germany) with 5× or 10× objectives in the green fluorescence channel and phase contrast. For image analysis, I used Fiji software [241].

### **3.2.8 Calculation of synergy**

The calculation of synergy of RVTx followed a mathematical analysis using data of both cell viability assays performed as described before (see 3.2.6). I used CompuSyn software (ComboSyn, Inc., Paramus, NJ/USA) developed by Chou and Martin according to the median effect method [242]. Using this software, I calculated a combination index (CI) for each tested treatment schedule of RVTx: A CI of 1 indicates additive effects, above 1 antagonism and a CI below 1 indicates synergy of a combination.

### **3.2.9 Characterization of induced mechanisms of action**

For the identification and characterization of different mechanisms of action induced by RVTx, I seeded  $1 \cdot 10^5$  cells of the human tumor cell lines BxPC-3, T3M4, HNO210 and HNO410 into wells of 12-well plates in triplicates for each treatment condition 24 h prior to treatment according to the R24V schedule. I irradiated respective cells with doses of 2 or 5 Gy photon irradiation as described before (see 3.2.3) followed by virus infection using MeVac Id-EGFP 24 h later. To this end, I removed the cell culture medium and replaced it by 300  $\mu$ l virus inoculum at an MOI of 0.1 or 0.01 (T3M4) in Opti-MEM™. Mock-treated samples or cells only receiving irradiation were inoculated with 300  $\mu$ l Opti-MEM™. After 2 – 3 h, I replaced

the inoculum by 1 ml cell culture-specific medium per well and incubated the cells at 37°C, 5% CO<sub>2</sub>. At specific time points after treatment, I collected the cells and supernatants for various analyses.

### **3.2.9.1 Enzyme-linked immunosorbent assays**

To detect different cytokines released after RVTx-treatment, I performed an enzyme-linked immunosorbent assay (ELISA) using supernatant of treated cells. I cleared the supernatant from cellular debris by centrifugation at 5000×g for 5 min at 4°C and froze aliquots at -80°C until further use. I detected the extracellular release of the immunogenic cell death (ICD) marker high mobility group box 1 (HMGB1) using HMGB1 ELISA (ST51011) or HMGB1 express ELISA (30164033, both IBL international, Hamburg, Germany) according to the manufacturer's instructions. For the detection of secreted cytokine interferon (IFN) β, I used the VeriKine-HS™ Human IFN Beta Serum ELISA Kit (41415, PBL Assays Science, Piscataway, NJ/USA) according to the manufacturer's instructions. I measured the absorbance at 450 nm using the infinite M200 spectrophotometer and i-control software.

### **3.2.9.2 Measurement of extracellular ATP**

I analyzed levels of extracellular ATP from supernatants of treated cells. To this end, I transferred 50 μl of supernatant from treated cells into respective wells of a 96-well V bottom plate (3894, Corning) and centrifuged at 500×g for 5 min at 4°C to clear from cellular debris. Next, I transferred the supernatant into black 96-well plates (655086, Greiner Bio-One) and performed a luminescence-based ATP assay using the ATP Determination Kit (A22066, Thermo Fisher) according to the manufacturer's instructions. I measured the luminescence at 1000 millisecond integration time using the infinite M200 spectrophotometer and i-control software.

### **3.2.9.3 Flow cytometric analysis of surface calreticulin**

The relocation of calreticulin (CALR) from the endoplasmic reticulum (ER) to the cell surface was the third marker of ICD that I analyzed in this project. As one approach, I detected CALR on the cell surface via flow cytometry (FC). To this end, I seeded and treated the cells as described above (see 3.2.9). When performing media change after virus infection, I added 12.5 μg/ml fusion inhibitory peptide (FIP) to infected wells. FIP prevents virus fusion with the plasma membrane and thereby inhibits virus spread and syncytia formation. Yet, the latter would be destroyed during sample processing. Therefore, FIP is necessary to ensure

the detection of infected cells *per se*. Forty-eight hours p.t.r., I pooled the supernatant of triplicate samples into a 5 ml tube, washed the wells with 500  $\mu$ l D-PBS, also collected the wash in the respective 5 ml tubes. Collecting all liquids from the experiment should prevent loss of cells. Subsequently, I added 200  $\mu$ l accutase to the wells for cell detachment. Once the cells had detached, I resuspended them in 1 ml supernatant-wash-solution and centrifuged at 500 $\times$ g for 5 min at RT. I discarded the supernatant and resuspended the cells in 200  $\mu$ l D-PBS. I transferred the cells into wells of a 96-well V-bottom plate. For unstained controls, I added 100  $\mu$ l of respective samples into specific wells of the V-bottom plate. I centrifuged the plate (500 $\times$ g, 5 min, RT) and incubated the cells in plain D-PBS or with 100  $\mu$ l Zombie Violet dye (1:1000 in D-PBS, Zombie Violet™ Fixable Viability Kit, 423113, BioLegend) for live-dead cell discrimination for 15 min at RT in the dark. Afterwards, I added 200  $\mu$ l FC buffer (D-PBS + 1% FCS) and centrifuged at 500 $\times$ g for 5 min at RT. I resuspended the cells in 50  $\mu$ l FC buffer, added 1  $\mu$ l of an Alexa Fluor® 647-conjugated anti-calreticulin antibody to the corresponding wells and incubated for 45 min at RT in the dark. Subsequently, I added 150  $\mu$ l FC buffer and centrifuged at 500 $\times$ g for 5 min at RT. I washed the cells once with 200  $\mu$ l D-PBS, resuspended the cells in 100  $\mu$ l 1% paraformaldehyde (PFA) and incubated for 15 min at RT in the dark for fixation. Afterwards, I centrifuged (500 $\times$ g, 5 min, RT) and resuspended the pellets in 200  $\mu$ l FC buffer. I transferred the cells to Falcon™ Round-Bottom Polystyrene Test Tubes with Cell Strainer Snap Cap (352235, Fisher Scientific) (FC tubes) and acquired 10,000 events per sample on a BD LSRFortessa™ (BD Biosciences) with FACS Diva software version 8.0.1 and analyzed the data with FlowJo V10 (Tree Star Inc., La Jolla, CA/USA).

#### 3.2.9.4 Immunofluorescence

In addition to FC, I performed immunofluorescence (IF) stainings to detect CALR relocation. I seeded  $2 \cdot 10^5$  cells on cover slips (631-0125, VWR, Radnor, PA/USA) in 6-well plates. Twenty-four hours later, I treated the cells according to the R24V schedule and added FIP to all infected cells when performing media change after virus inoculation. I incubated the plates for another 48 h at 37°C, 5% CO<sub>2</sub>. Subsequently, I removed the medium, washed the wells twice with 1 ml D-PBS and fixed the cells by adding 600  $\mu$ l 4% PFA per well and incubating for 15 min at RT. After fixation, I washed 3 $\times$  with 1 ml D-PBS and blocked the cells for 60 min at RT by adding 1 ml blocking buffer (2% bovine serum albumin (BSA) + 0.1% Triton™ X-100 in D-PBS). Subsequently, I removed the blocking buffer and added 20  $\mu$ l of anti-CALR primary antibody in antibody dilution buffer (1% BSA + 0.1% Triton™ X-100 in D-PBS) drop-wise directly onto the cover slips. Control wells received antibody dilution buffer only. I covered the cover slips with parafilm cutouts. In order to provide a humidified chamber for incubation and prevent draining, I added water to the space between

the wells of the 6-well plate, elevated the lid using toothpicks and sealed the 6-well plates with parafilm. I incubated the cells at 4°C for at least 16 h. The next day, I removed the parafilm cutouts and washed the wells 3× with 1 ml D-PBS before applying the secondary antibody. I added 20 µl of the Alexa Fluor® 594-conjugated secondary antibody diluted in antibody dilution buffer drop-wise directly onto the cover slips, covered the cover slips with parafilm cutouts and incubated the plates for 90 min at RT in the dark. Afterwards, I washed 3× with 1 ml D-PBS and added 1 ml Hoechst 33342 (1:500 in D-PBS) to the cells and incubated for 15 min in the dark. I washed 3× with 1 ml D-PBS and mounted the cover slips upside down onto microscope slides (630-1985, VWR). I stored the slides at 4°C protected from light. For readout, I used the Zeiss Cell Observer or the Zeiss Axio Scan.Z1 and the ZEN 2011 (blue edition) software (all Carl Zeiss).

### **3.2.9.5 Protein extraction and determination of concentration**

To analyze protein expression in RVTx-treated cells, I collected cell samples after treatment. I removed the supernatant, washed the cells with 1 ml D-PBS and detached the cells by adding 200 µl trypsin-EDTA. Subsequently, I pooled the triplicates into 1.5 ml tubes, pelleted the cells by centrifuging at 300×g for 5 min and washed the pellet with 1 ml D-PBS. Subsequently, I removed the supernatant completely and performed cell lysis by adding 100 µl cold RIPA buffer containing cOmplete™ Ultra Protease Inhibitor Cocktail for 5 min on ice. I pelleted the cell debris by centrifugation at 2000×g for 5 min at 4°C and froze the supernatant at −20°C until further use.

To determine the protein concentration, I diluted each sample 1:10 in D-PBS and performed a bicinchoninic acid (BCA) assay using the BCA Protein Assay Kit (71285-3, Merck Millipore) according to the manufacturer's instructions. I measured the absorbance at 562 nm using the infinite M200 spectrophotometer and i-control software.

### **3.2.9.6 Sodium dodecyl sulphate-polyacryl-amide gel electrophoresis**

To separate the extracted proteins by size, I performed a sodium dodecyl sulphate-polyacrylamide gel electrophoresis (SDS-PAGE). I mixed the samples with 4× Laemmli buffer at a ratio of 3:1 and incubated at 95°C for 5 min. Subsequently, I loaded the samples on a precast polyacrylamide gel (Any kD™ Mini-PROTEAN® TGX Stain-Free™ Protein Gel, 4568126, Bio-Rad) in running buffer (10× SDS-PAGE in deionized water (ddH<sub>2</sub>O)). I used Precision Plus™ Protein All Blue Standards as molecular weight standard and performed electrophoresis for approx. 15 – 20 min at 300 V. For total protein quantification, I activated the gel according to the manufacturer's instructions using a ChemiDoc Imaging System (Bio-Rad).

#### 3.2.9.7 Western blot

After SDS-PAGE, I transferred the proteins onto a methanol-activated low-autofluorescent polyvinylidene fluoride (PVDF) membrane using the Trans-Blot Turbo RTA Transfer Kit (1704275, Bio-Rad) according to the manufacturer's instructions. After the transfer, I used the ChemiDoc Imaging System to take images of the membrane for total protein quantification. To block unspecific binding sites, I incubated the membrane using EveryBlot Blocking Buffer for 5 min at RT on an orbital shaker. Afterwards, I discarded the blocking buffer and incubated the membrane with primary antibody solution (15 ml 5% skim milk or BSA in tris-buffered saline-tween (TBS-T) containing the respective antibody, see 3.1.6) for 2 h at RT on an orbital shaker. Subsequently, I washed the membrane 3× with 1× tris-buffered saline (TBS) + 1% casein before adding the secondary antibody (1.5 µl horseradish peroxidase (HRP)-linked antibody in 15 ml 5% skim milk in TBS-T). I incubated the secondary antibody solution for 2 h at RT on an orbital shaker. Afterwards, I washed the membrane 3× with 1× TBS + 1% casein. For chemiluminescent imaging, I used the Clarity Max™ Western ECL Substrate Kit (1705062, Bio-Rad) according to the manufacturer's instructions. I recorded signals using the ChemiDoc Imaging System and used Image Lab software version 6.1.0 (Bio-Rad) for total protein normalization and quantification.

#### 3.2.10 Generation of murine tumor models

##### 3.2.10.1 Generation of human CD46-expressing murine tumor cells

To generate suitable murine tumor models for HNSCC and PDAC in the context of RVTx, I transfected four murine tumor cell lines with vectors encoding the human *CD46* gene. I seeded two murine HNSCC (MOC2, mEERL95) and two murine PDAC (Panc02, 30364) cell lines in 6-well plates ( $2 \cdot 10^5$  cells/well). Twenty-four hours later, I transfected the cells with 1 µg of the nanovectors pCAG-Puro-P2A-hCD46-SMARter-NP or pEF1-Puro-P2A-hCD46-SMARter-NP. Both encode the human *CD46* gene as well as a puromycin resistance gene [243] (see 3.1.4), using Lipofectamine 2000 as transfection reagent (see 3.2.4.1).

Additionally, I transduced the mEERL95 cells with the lentiviral vector LV-105 hCD46 BC1 [230] (see 3.1.3). I seeded the cells in 6-well plates ( $2 \cdot 10^5$  cells/well) and transduced the cells 24 h later. To this end, I washed the cells once with D-PBS and added 700 µl cell culture-specific medium to the wells. I prepared different dilutions of lentivirus (1:100 – 1:10,000) in cell culture-specific medium + 9 µg/ml polybrene and added 100 µl of each to respective wells. I incubated the plate at 37°C, 5% CO<sub>2</sub> and performed medium change the next day.

### 3.2.10.2 Puromycin selection

In order to select for human CD46 (hCD46) expressing cells, I performed puromycin selection for transfected MOC2, Panc02 and 30364 cells. I had determined the cell-specific puromycin concentration for selection beforehand according to the puromycin sensitivity of the cell lines. Two days after transfection, I changed the medium of each well and added the corresponding concentration of puromycin: 2 µg/ml for Panc02 and 5 µg/ml for MOC2 and 30364. For mEERL95 cells, selection using puromycin was not possible as the parental cells already contained the puromycin resistance gene. Subsequently, I cultured the transfected and transduced cells further and expanded the cultures in cell culture flasks until sorting.

### 3.2.10.3 Fluorescence-activated cell sorting

For the preparation of fluorescence-activated cell sorting (FACS), I pelleted the cells (500×g, 5 min) and resuspended in 100 µl D-PBS. I blocked the Fc receptors by adding 1 µl mouse FC block and stained the respective cell samples with 1 µl APC-conjugated anti-human CD46 antibody or APC-conjugated mouse IgG1,κ isotype control for 30 min at RT in the dark and washed the cells with D-PBS subsequently. For live-dead cell discrimination, I resuspended the cells in 0.1 µg/ml DAPI for 5 min in the dark. After washing, I transferred the stained cells and controls into FC tubes and acquired the samples using a BD FACSAria™ II (BD Biosciences) with FACS Diva software version 8.0.1. For each transfected or transduced cell line, I performed single cell as well as bulk population sorting. Single cells were sorted into 96-well cell culture plates containing 200 µl cell culture-specific medium + 10 – 30% FCS + 1× antibiotic antimycotic solution (ABAM). The bulk population was sorted into FC tubes containing 2 ml medium. I pelleted these cells at 300×g for 10 min and cultured them in culture flasks in cell culture-specific medium containing twice the amount of FCS, compared to normal culture conditions. For transduced mEERL95, in addition to single cell sorting I sorted the bulk population into wells of a 96-well plate at 500 – 1000 cells/well. I incubated the plates and flasks at 37°C, 5% CO<sub>2</sub> until colonies needed to be transferred into larger culture dishes or were analyzed further.

### 3.2.10.4 Analysis of hCD46 expression, cell clone selection and expression stability

Once the sorted cells had reached a sufficient number, I analyzed them for hCD46 expression by FC analysis. I pelleted the cells (500×g, 5 min) and resuspended in 100 µl FC buffer. I blocked the Fc receptors by adding 1 µl mouse FC block and stained the respective cell samples with 1 µl APC-conjugated anti-human CD46 antibody or APC-conjugated mouse IgG1,κ

isotype control for 30 min at RT in the dark and washed the cells subsequently using FC buffer. For live-dead cell discrimination, I resuspended the cells in 0.1 µg/ml DAPI and incubated for 5 min in the dark. After washing, I transferred the stained cells and controls into FC tubes, acquired the samples using a BD LSRFortessa™ with FACS Diva software version 8.0.1 and analyzed the data with FlowJo V10. According to the hCD46 expression analyzed by FC, I selected 3 – 5 clones from each transfected/transduced cell line and pooled them to generate heterogenous cell populations from single sorted cells. I cultivated the newly generated hCD46 expressing murine tumor cell lines in cell culture-specific medium with the respective amount of puromycin at 37°C, 5% CO<sub>2</sub>. To analyze the stability of hCD46 expression, I performed FC analysis as described above. For 2 – 3 weeks, I cultivated half of the cells from each cell line with the respective amount of puromycin and the other half without. Afterwards, I performed a second FC analysis as described above.

#### 3.2.10.5 Infection of hCD46 expressing murine tumor cells

To investigate virus susceptibility of the newly generated hCD46 murine tumor cell lines, I infected the cells at different MOIs of MeVac Id-EGFP. I seeded  $1 \cdot 10^5$  cells in 12-well plates 24 h prior to virus infection. For this, I removed the cell culture-specific medium and replaced it with 300 µl virus inoculum at MOIs of 0.03, 0.3 or 3 in Opti-MEM™. Mock-treated cells were inoculated with 300 µl Opti-MEM™. After 2 – 3 h, I replaced the inoculum by 1 ml cell culture-specific medium per well and incubated the cells at 37°C, 5% CO<sub>2</sub>. At 24, 48 and 72 h post infection (p.i.), I performed fluorescence microscopy using the Axiovert 200 with a 10× objective, took images in the green fluorescence channel as well as phase contrast and analyzed the images using Fiji software.

#### 3.2.11 *In vivo* experiments

All experimental procedures involving animals were approved beforehand by the Animal Protection Officer at the German Cancer Research Center (Heidelberg, Germany) and the regional council according to the German Animal Protection Law. I used 6 – 8 weeks old C57BL/6J mice, both male and female at a ratio of 1:1. The mice were bred externally by Janvier Labs (Saint Berthevin Cedex, France).

##### 3.2.11.1 Implantation

For *in vivo* experiments, I used the murine hCD46 cell lines MOC2-hCD46 pEF1 single (MOC2-hCD46) and 30364-hCD46 pCAG single (30364-hCD46) transfected with hCD46 encoding nanovectors as described above (see 3.2.10.1). When reaching 70 – 80% confluency,

I detached and collected low passage tumor cells from cell culture flasks as described before (see 3.2.1). I washed the cells with D-PBS and prepared cell suspensions for implantation: MOC2-hCD46 in D-PBS at a final concentration of  $5 \cdot 10^6$  cells/ml and 30364-hCD46 in D-PBS-Matrigel (ratio 1:1) at a final concentration of  $1 \cdot 10^7$  cells/ml. I kept the cell suspension on ice until use. I shaved the left thigh of the animals and injected  $100 \mu\text{l}$  ( $5 \cdot 10^5$  cells for MOC2-hCD46 or  $1 \cdot 10^6$  cells for 30364-hCD46) of the prepared cell suspensions per mouse subcutaneous (s.c.) into the shaved region using 1 ml syringes (720-2561, VWR) and 26 G needles (194211002, Neolab, Heidelberg, Germany). During implantation into the thigh, I anesthetized the mice via inhalation narcosis using isoflurane (1.5 – 2.5 vol%). During narcosis, I covered the eyes of the mice using Bepanthen<sup>®</sup> eye and nose cream. In case of implanting a secondary MOC2-hCD46 tumor, I also shaved the right flank of the mice and implanted  $2.5 \cdot 10^5$  MOC2-hCD46 cells in  $100 \mu\text{l}$  D-PBS 2 days after implanting the primary tumor.

### 3.2.11.2 Monitoring

I monitored the mice every second to third day by examining physical well-being, overall weight and tumor volumes. To determine the tumor volume, I measured the largest and smallest diameter with a caliper and calculated the volume using the formula: largest diameter  $\times$  (smallest diameter)<sup>2</sup>  $\times$  0.5. I sacrificed mice when tumor volumes exceeded  $1000 \text{ mm}^3$ , a tumor diameter exceeded 15 mm, ulceration occurred or animals were moribund. For mice harboring two tumors, I added both tumor volumes as total tumor volume.

### 3.2.11.3 Treatment

The tumor treatment started once the mean tumor volume reached 100 – 150  $\text{mm}^3$ . Before starting the treatment, I allocated the animals to respective treatment groups to ensure similar mean tumor volumes within the groups. For virus treatment, I used the S1-classified measles virus vaccine strain MeVac. Immediately prior to treatment, I thawed the respective amount of virus suspension and prepared a concentration of  $1 \cdot 10^7$  ciu/ml in D-PBS. I applied intratumoral (i.t.) injections with  $100 \mu\text{l}$  virus suspension (1 ml syringes, 26 G needles) once or on 3 to 4 consecutive days (see specific experimental treatment schedules). Mice not receiving MeVac (mock or radiation only) received i.t. injections with  $100 \mu\text{l}$  D-PBS. I performed the irradiation of mice using the MultiRad 225 system as described before (see 3.2.3) with a dose of 5 Gy irradiation on 3 to 4 consecutive days. Before radiation treatment, I anesthetized the mice with antagonizable injection narcosis applying intraperitoneal (i.p.) injections of  $100 \mu\text{l}$  midazolam (500  $\mu\text{g}/\text{ml}$ ) + medetomidin-hydrochloride (50  $\mu\text{g}/\text{ml}$ ) in 0.9% sodium chloride per mouse. After irradiation, I antagonized the narcosis by injecting  $100 \mu\text{l}$

atipamezol-hydrochloride (250 µg/ml) + flumazenil (50 µg/ml) in 0.9% sodium chloride per mouse into the nuchal fold. The mice in groups not receiving irradiation (mock or virus only) were anesthetized but not irradiated.

## 3.2.12 Characterization of murine tumor models

### 3.2.12.1 Isolation of murine tumor cells

I isolated tumors aseptically using a scalpel and kept them in D-PBS on ice until further processing. I minced the tumors in small pieces and incubated the samples in digestion buffer (RPMI 1640 + 5% FCS + 200 U/ml collagenase type I) for 30 min in a 37°C waterbath. Subsequently, I passed the pieces through a 100 µm nylon cell strainer (352360, Neolab) into digestion buffer, pelleted the cells (300×g, 5 min, RT) and washed them once with D-PBS. I counted the cells as described before (see 3.2.1.1) and kept the cells on ice until further use.

### 3.2.12.2 Analysis of hCD46 surface expression

To analyze hCD46 surface expression of freshly explanted tumor cells, I performed antibody staining and FC analysis as described before (see 3.2.10.4). Additionally, I cultured the cells in cell culture-specific medium without puromycin. After approx. 2 weeks, I performed a second analysis of hCD46 surface expression in order to check expression stability.

### 3.2.12.3 Tests for virus sensitivity and puromycin sensitivity

I analyzed virus sensitivity of the explanted tumor cells after *ex vivo* culture for approx. 2 weeks in cell culture-specific medium + 1× ABAM + 100 µg/ml gentamicin for removing murine fibroblasts following the same protocol as described for the newly generated and sorted murine tumor cells (see 3.2.10.5). To examine vector-encoded genes in the explanted tumor cells, I analyzed the sensitivity to puromycin. I seeded  $1 \cdot 10^5$  cells in 12-well plates and cultivated them for 24 h in cell culture-specific medium without puromycin. Subsequently, I added the respective amount of the selection reagent into each well and cultivated the cells further. I monitored cell confluence by microscopy using the Axiovert 200 with a 10× objective and took images in phase contrast 24 h after adding puromycin. I analyzed the images using Fiji software.

#### 3.2.12.4 Expression of hCD46 on genomic and transcriptomic level

To analyze hCD46 expression on the genomic as well as transcriptomic level, I used freshly explanted tumor cells or cultured tumor cells stored either in RNeasy Protect™ RNA Stabilization Reagent or RNeasy Protect® Cell Reagent. I performed DNA and RNA isolation, cDNA synthesis and PCR or RT-PCR, respectively, followed by agarose gel electrophoresis as described before (see 3.2.2). For the PCR reaction, I used the hCD46\_qPCR\_F and hCD46\_qPCR\_R primers (see 3.1.5) according to the protocol described in 3.2.2.1.

### 3.2.13 Immune profiling of murine tumors and spleens

#### 3.2.13.1 Intratumoral expression of immune markers

To analyze RNA expression of different immune markers *in vivo*, I sacrificed mice two days after completion of RVTx treatment (see 3.2.11.3 and Figure 4.20). I extracted the tumors aseptically and stored one piece of tumor per mouse in RNeasy Protect® Cell Reagent at  $-80^{\circ}\text{C}$ . I thawed the tumor pieces on ice, transferred them to a new 1.5 ml tube and weighed them, respectively. I used up to 30 mg tumor tissue for the analysis, homogenized with a micro pestle (CXH7.1, Carl Roth) and performed the subsequent steps of RNA isolation including in-solution DNase digest using the RNase-Free DNase Set (79254, Qiagen) and cDNA synthesis as described above (see 3.2.2) using 500 ng RNA, respectively.

For quantitative PCR (qPCR) analysis of the murine *Ifnb1* and *Foxp3* genes encoding IFN- $\beta$  and forkhead box p3 (Foxp3), I mixed 10  $\mu\text{l}$  of Power SYBR™ Green PCR Master Mix with 1  $\mu\text{l}$  of each 30  $\mu\text{M}$  forward and reverse primer, ddH<sub>2</sub>O up to 20  $\mu\text{l}$  total reaction volume and added the mixture to wells of a white 96 well PCR TW-MT plate (712282, Biozym Scientific, Hessisch Oldendorf, Germany). I used the primer pairs m IFNb for and rev as well as m FoxP3 fw and rev (see 3.1.5). As housekeeping controls, I amplified murine *Rpl13a* and *Actb* encoding L13a and  $\beta$ -actin using m L13A for and ref as well as m  $\beta$ -actin for and rev primer pairs. I added 2  $\mu\text{l}$  cDNA template or ddH<sub>2</sub>O to respective wells. I performed the qPCR using the CFX96 Touch Real-Time PCR Detection System (BioRad). The reaction conditions were as follows: 15 min initial denaturation at  $95^{\circ}\text{C}$ , followed by 40 cycles of 15 s denaturation at  $95^{\circ}\text{C}$ , 30 s annealing at  $55^{\circ}\text{C}$  ( $\beta$ -actin) or  $60^{\circ}\text{C}$  (IFN- $\beta$ , Foxp3 and L13a), fluorescence detection and extension at  $70^{\circ}\text{C}$  for 30 s. This was followed by a melting curve analysis at  $65 - 95^{\circ}\text{C}$ . ‘No template’ and ‘no reverse transcriptase’ controls were run in parallel. I analyzed the qPCR data using the Bio-Rad CFX Maestro 1.1 software (version 4.1, Bio-Rad) and Microsoft Excel. I checked the technical quality of each qPCR run by examining melting and amplification curves and calculated relative expression of *Ifnb1* and *Foxp3* as  $2^{-\Delta\text{Cq}}$  by normalizing the quantification cycle (Cq) values of target genes against the mean of the two

housekeeping genes.

#### 3.2.13.2 Isolation of murine splenocytes

I isolated spleens aseptically using a scalpel and kept them in D-PBS on ice until further processing. I passed the spleens through a 100  $\mu\text{m}$  nylon cell strainer into 8 ml D-PBS and pelleted the cells (500 $\times$ g, 5 min, RT). I resuspended the pellets in 1 ml ACK lysing buffer for red blood cell lysis, incubated 10 min at RT, added 9 ml D-PBS and pelleted the remaining cells (500 $\times$ g, 5 min, RT). I resuspended the pellets in 10 ml D-PBS, counted the cells as described before (see 3.2.1.1) and kept the cells on ice until further use within the next hours.

#### 3.2.13.3 Tumor- and virus-specific immune memory recall

To determine T cell activation, I performed an enzyme-linked immune absorbent spot (ELISpot) assay detecting the release of IFN- $\gamma$  nine days after the final treatment of mice with RVTx (see 3.2.11.3 and Figure 4.20). One day prior to setting up the co-cultures, I activated the ELISpot plates (MSIPS4W10, Merck Millipore) with 35% ethanol (EtOH), washed the plates with sterile ddH<sub>2</sub>O and coated them with Mouse IFN- $\gamma$  ELISpot Pair capture antibody at 4°C overnight according to the manufacturer's instructions. The next day, I washed the plates with D-PBS and blocked the wells with assay specific medium (RPMI 1640 medium supplemented with 10% FCS, 1 $\times$  GlutaMAX™ and 1 $\times$  P/S) for 2 h at RT. Subsequently, I set up different co-cultures in order to determine anti-tumoral or anti-viral responses. I isolated the splenocytes as described above (see 3.2.13.2) and co-cultivated them in a 2-fold serial dilution (1 $\cdot$ 10<sup>6</sup>, 5 $\cdot$ 10<sup>5</sup>, 2.5 $\cdot$ 10<sup>5</sup>) with 1 $\cdot$ 10<sup>5</sup> MOC2-hCD46 cells from cell culture, respectively, in assay-specific medium. To detect virus-induced IFN- $\gamma$  release, I cultivated 1 $\cdot$ 10<sup>6</sup> splenocytes with MeVac virus suspension at MOI = 1. Adding 10  $\mu\text{g}/\text{ml}$  concanavalin A (Con A) to the culture medium served as positive control. I let the co-cultures incubate at 37°C, 5% CO<sub>2</sub> for approx. 36 hrs before I developed the ELISpot. After incubation, I transferred the supernatant to fresh 96-well plates and stored it for further analyses via ELISA (see below). I washed the ELISpot plates 3 $\times$  with D-PBS, once with ddH<sub>2</sub>O and again 3 $\times$  with D-PBS before I added Mouse IFN- $\gamma$  ELISpot Pair detection antibody according to the manufacturer's instructions. After incubation for 2 h at RT in the dark, I washed the plates again 5 $\times$  with D-PBS and added HRP Streptavidin according to the manufacturer's instructions and incubated for 1.5 h at RT in the dark. After 5 wash steps with D-PBS, I added TMB substrate according to the manufacturer's instructions and incubated for 10 min at RT in the dark. Afterwards, I washed the plates 4 $\times$  with ddH<sub>2</sub>O and let the plates dry in the dark. For readout, I used a CTL ELISpot reader (Cellular Technology Limited, Shaker

Heights, OH/USA).

As mentioned above, I performed ELISAs from supernatants of the IFN- $\gamma$  ELISpot to investigate secretion of IFN- $\gamma$ , interleukin (IL) 2 and IL-10 after co-culture of murine splenocytes with tumor cells or virus. I thawed the samples on ice and cleared the supernatant from cellular debris by centrifugation at 5000 $\times$ g for 5 min at 4°C. For detection of the respective cytokines, I used IFN gamma Mouse Uncoated ELISA Kit with Plates (88-7314-22), IL-2 Mouse Uncoated ELISA Kit with Plates (88-7024-22) or IL-10 Mouse Uncoated ELISA Kit with Plates (88-7105-22, all Invitrogen) including the additional ELISA Stop Solution according to the manufacturer's instructions. I measured the absorbance at 450 nm with reference wavelength at 570 nm using the infinite M200 spectrophotometer and i-control software.

#### **3.2.13.4 Flow cytometry of tumor-infiltrating lymphocytes**

Nine days after treatment completion, I performed the analysis of tumor-infiltrating lymphocytes (TILs) in RVTx-treated tumors. I sacrificed the mice, extracted tumors aseptically and prepared single-cell suspensions as described above (see 3.2.12.1). Subsequently, I performed antibody staining and FC analysis using 2 $\cdot$ 10<sup>6</sup> cells per sample. For controls, I used a splenocyte mixture from extracted spleens of all analyzed mice at 1 $\cdot$ 10<sup>6</sup> cells for each control sample. I pelleted the cells (500 $\times$ g, 5 min) and resuspended in 100  $\mu$ l D-PBS. I blocked the Fc receptors by adding 1  $\mu$ l mouse FC block for 15 min at RT and stained the respective samples and controls with antibodies against murine leukocyte subpopulation markers: 1  $\mu$ l CD45.2-PerCP-Cy<sup>TM</sup>5.5, 1  $\mu$ l CD3-PE, 1  $\mu$ l CD4-APC-Cy<sup>TM</sup>7, 1  $\mu$ l CD8a-APC, 1  $\mu$ l CD335-FITC. For isotype controls, I replaced the respective antibodies with the corresponding isotypes (see 3.1.6). I incubated the cells for 30 min at RT in the dark and subsequently washed the cells using D-PBS. For live-dead cell discrimination, I resuspended the cells in 0.1  $\mu$ g/ml DAPI and incubated for 5 min in the dark. After washing, I transferred the stained cells and controls into FC tubes and acquired 50,000 events per sample using a BD LSRFortessa<sup>TM</sup> with FACS Diva software version 8.0.1 and analyzed the data with FlowJo V10.

### **3.2.14 Ex vivo experiments**

#### **3.2.14.1 Monitoring morphology and ICD induction in PDAC spheroids**

The PDAC spheroids serving as a 3D *ex vivo* model were generated using AsAn-PaCa and MRC-5 cells in 96-well U-bottom plates filled with RPMI 1640 as described before [221]. Twenty-four hours after generation of spheroids, I treated them according to the R24V schedule (see 3.2.5) with irradiation at 2 or 5 Gy. For virus infection, I used MeVac ld-EGFP

at an MOI of 0.3 referring to the number of tumor cells within the spheroid and added the virus suspension drop-wise on top of the spheroids that remained in their culture medium. At 24, 48 and 72 h p.tr., I took images using the Axiovert 200 with a 10× objective in the green fluorescence channel and phase contrast and analyzed the images using Fiji software. At the last time point, I collected the supernatant of each spheroid into tubes, centrifuged (5000×g, 5 min, 4°C) and stored them at −80°C until further use. To investigate the induction ICD after RVTx, I analyzed the extracellular release of HMGB1 as described before (see 3.2.9.1).

#### 3.2.14.2 Effects of RVTx treatment on patient-derived PDAC cultures

As a second *ex vivo* model, I used the patient-derived PDAC cultures PC1, PC3, PC28 and PC43 that were generated by Ehrenberg *et al.* [227]. To analyze the effect of RVTx on these cultures, I performed different experiments treating them according to the R24V schedule using irradiation doses of 2 and 5 Gy and virus infection with MeVac ld-EGFP at MOI = 1. To investigate the effects of RVTx on cell viability, I conducted XTT assay and fluorescence microscopy as described above (see 3.2.6.1 and 3.2.7). To check for potential induction of ICD and innate immune activation after RVTx treatment, I performed experiments to investigate surface CALR (see 3.2.9.3) as well as HMGB1 and IFN-β release (see 3.2.9.1) as described before. Additionally, I performed RNA isolation, cDNA synthesis and PCR (see 3.2.2) to analyze RNA expression of the *IFNB1* gene using the h IFNβ for and h IFNβ rev primers (see 3.1.5), followed by agarose gel electrophoresis (see 3.2.2.2).

#### 3.2.15 Statistical analyses

I performed the statistical analyses within this thesis using Microsoft Excel V14 (Microsoft Corp., Redmond, WA/USA) and GraphPad Prism version 9.3.1 (GraphPad, San Diego, CA/USA). I analyzed ELISA, WB and FC results by one-way analysis of variance (ANOVA) with Tukey's multiple comparison post-hoc-test. Multiplicity-adjusted p-values were reported for data analyzed with ANOVA. I considered results statistically significant if p-values were below 0.05. Survival curves of *in vivo* experiments were analyzed by log-rank (Mantel-Cox) test with Bonferroni correction for multiple comparisons. I considered the results statistically significant if the p-value was lower than the corrected threshold after Bonferroni correction.

# 4 Results

## 4.1 Evaluation of combination regimens

The combination of radiotherapy and virotherapy using oncolytic measles virus (MeV) has not been tested in pancreatic ductal adenocarcinoma (PDAC) or head and neck squamous cell carcinoma (HNSCC) before. This project is based on the hypothesis that a combined radiovirotherapy (RVTx) will show synergistic anti-tumor effects when compared to both treatment regimens used as monotherapies. For optimal implementation of both therapies in combination, I analyzed the sensitivity of tumor cell lines against radio- as well as virotherapy. This was followed by an investigation of MeV replication after irradiation of virus solutions themselves and viral growth in irradiated tumor cells in order to determine whether irradiation might have a negative impact on MeV in the combination regimen.

### 4.1.1 Sensitivity of candidate cell lines to monotherapies

As a crucial aspect for combining radio- and virotherapy, I first determined the sensitivity of the candidate tumor cell lines, BxPC-3 and T3M4 (both PDAC) as well as HNO210 and HNO410 (both HNSCC), to each treatment modality. I treated the cells with several doses of photon radiation or oncolytic MeV and performed 2,3-bis-(2-methoxy-4-nitro-5-sulfophenyl)-2H-tetrazolium-5-carboxanilide (XTT) assays.

The cell lines showed different sensitivities to radio- and virotherapy (Figure 4.1 and Figure 4.2). Compared to mock (cell viability set at 100%), low radiation doses such as 1 and 2 Gy only showed minor (approx. 80% compared to mock) to moderate (approx. 60%) effects on cell viability, whereas the higher radiation doses of 5 and 8 Gy led to a strong reduction of cell viability over the course of the experiment, especially for BxPC-3 (29% and 24% at day 5 post irradiation (p.r.)), HNO210 (33% and 16%) and HNO410 (27% and 22%) (Figure 4.1). For T3M4, I observed the strongest reduction in cell viability for irradiation with 8 Gy (38%) on day 5 p.r.. Again, lower radiation doses, also including 5 Gy, showed only minor effect on cell viability of this cell line. However, for most treatment conditions, remaining cells regained

proliferative capacity on day 7 p.r. leading to no further reduction in cell viability after a single dose of radiation at the beginning of the experiment.

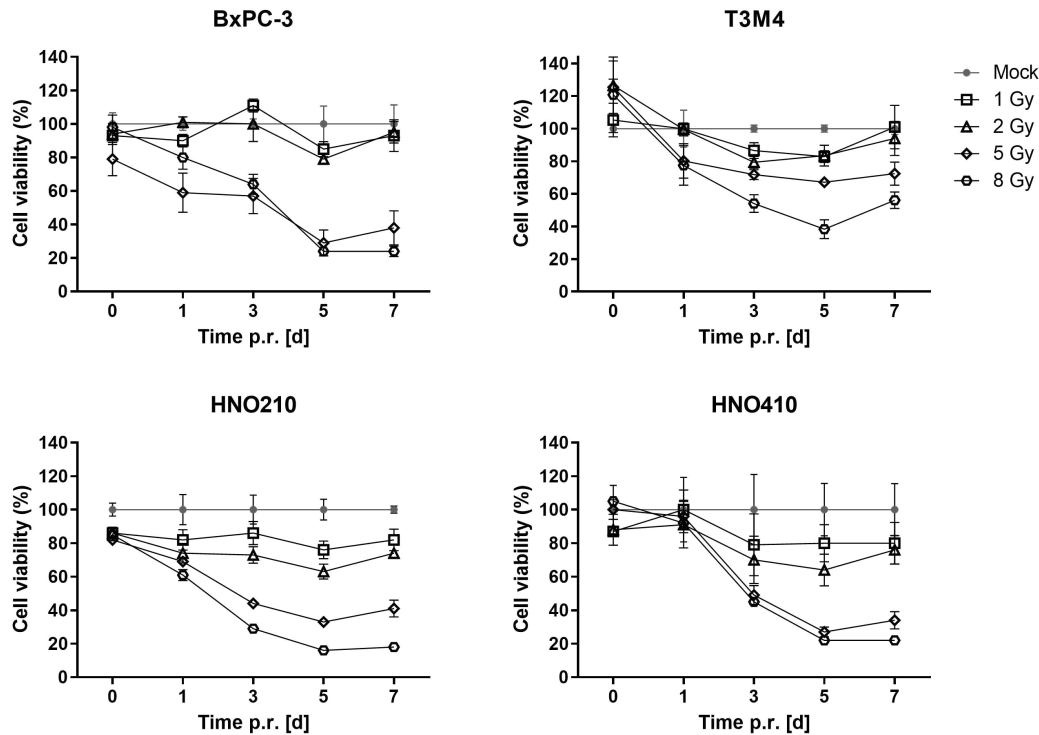


**Figure 4.1: Radiosensitivity of human tumor cell lines.** To analyze the effect of radiation alone, I tested the sensitivity of human tumor cell lines to ionizing radiation. I measured cell viability via XTT assay at indicated time points after irradiation with doses ranging from 1 to 8 Gy. The data was normalized to mock set at 100%. Mean and SD of triplicate samples are shown of a representative experiment of  $n = 3$  independent experiments. p.r. — post irradiation; d — days.

Regarding virus sensitivity, both HNSCC cell lines showed a strong reduction of cell viability after MeV infection at a multiplicity of infection (MOI) of 0.1 (29% or 30% at day 7 post infection (p.i.) or 1 (both 11%) compared to mock, shown in Figure 4.2. The PDAC cell line BxPC-3 showed only minor virus sensitivity at MOI = 0.1 (81% at day 7) and only moderate reduction of cell viability at MOI = 1 (56%). As T3M4 cells were previously known to be sensitive to MeV infection [240], I chose MOIs ranging from 0.001 to 0.1, leading to comparable results as seen for BxPC-3. There was only a minor reduction of cell viability after infection at an MOI of 0.01 (88% at day 7) and moderate reduction at MOI = 0.1 (53%).

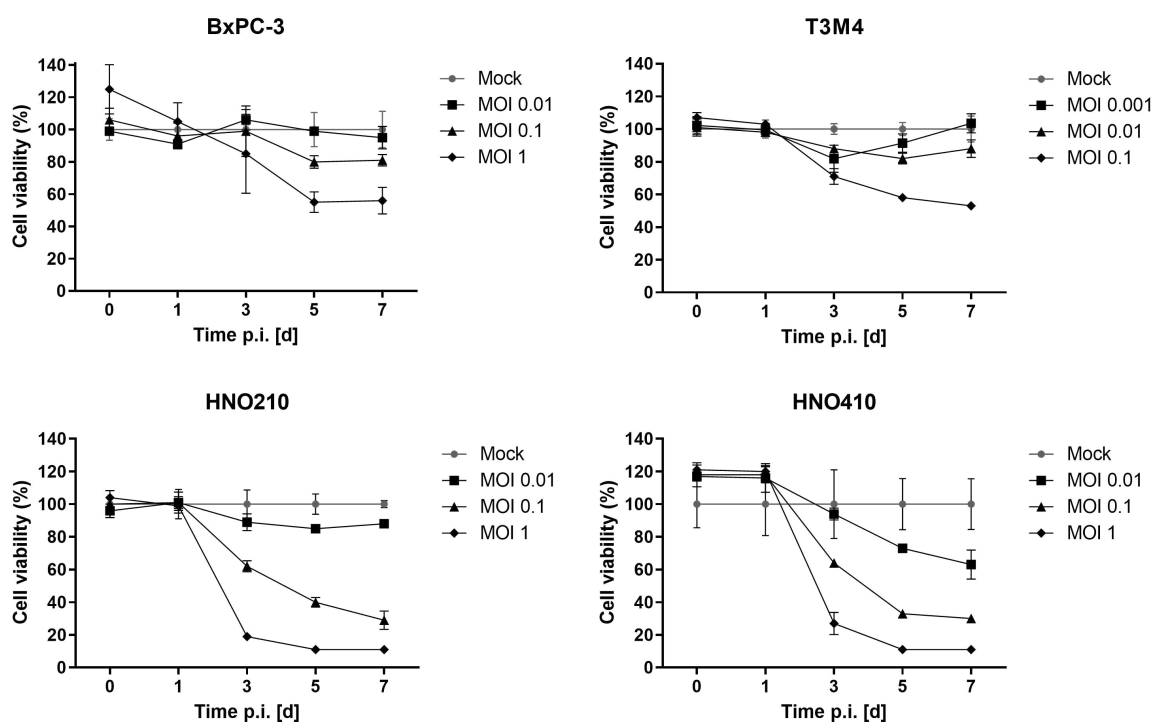


**Figure 4.2: Virus sensitivity of human tumor cell lines.** To analyze the effect of virus alone, I tested the sensitivity of human tumor cell lines to MeV infection and measured cell viability via XTT assay at indicated time points after viral infection at different MOIs ranging from 0.1 to 1 (0.001 to 0.1 for T3M4). The data was normalized to mock set at 100%. Mean and SD of triplicate samples are shown of a representative experiment of  $n = 3$  independent experiments. MOI — multiplicity of infection; p.i. — post infection; d — days.

All in all, these experiments showed the heterogeneity of tumor cell lines regarding their specific therapeutic sensitivity. Additionally, they identified suitable dose ranges for both treatment modalities in further experiments.

#### 4.1.2 Irradiation of MeV particles

To determine replication capability of MeV within the RVTx treatment, I first analyzed whether irradiation had a direct impact on the virus. Therefore, I irradiated virus solutions of both MeV variants used in this project, MeVac Id-EGFP and unmodified MeVac, as well as clinical grade MV-NIS for comparison with radiation doses ranging from 2 to 50 Gy. Subsequently, I analyzed virus infectivity via serial dilution titration assays. Independent of the applied radiation dose, irradiated MeV solutions showed the same titers of virus progeny when infecting Vero cells as unirradiated virus within the tested conditions (Figure 4.3). Even high radiation doses such as 50 Gy did not affect the infectivity of different viruses.

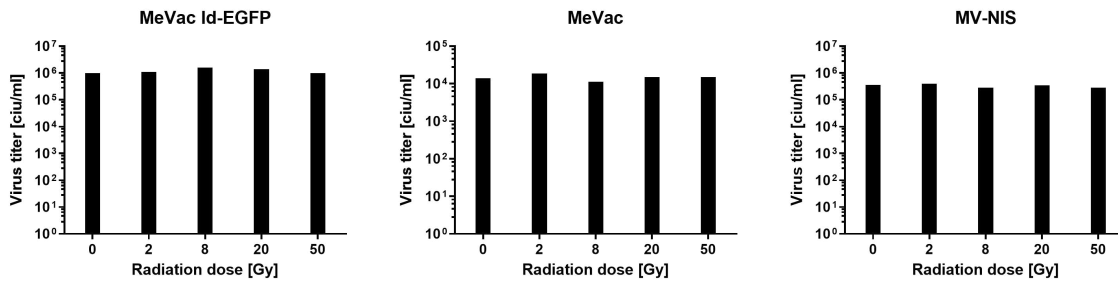


**Figure 4.3: Irradiation of MeV solutions.** I investigated whether irradiation has a direct impact on viral replication by irradiating virus solutions of MeVac Id-EGFP, MeVac and MV-NIS with radiation doses ranging from 2 to 50 Gy followed by serial dilution titration assays. The graphs show representative data of progeny titers of  $n = 2$  independent experiments.

### 4.1.3 Viral replication in irradiated tumor cells

Besides investigating whether irradiation had a direct effect on MeV, I also analyzed viral replication in irradiated tumor cells to test whether cell damage induced by irradiation would have an impact on replication of the virus. To this end, I irradiated tumor cells with doses ranging from 1 and 8 Gy and infected them with MeVac Id-EGFP 24 h after irradiation. I generated multi-step growth curves including viral progeny titers at several time points after treatment to determine replication kinetics (Figure 4.4). In both PDAC cell lines, BxPC-3 and T3M4, viral replication was not reduced by prior cell irradiation as the growth curves matched the unirradiated control. For HNO210 and HNO410, higher radiation doses such as 5 and 8 Gy impacted viral replication as titers of progeny particles dropped by at least one log over time compared to the unirradiated control. However, this was probably also due to strong reduction of viable cells in these samples impairing proper viral replication.

Taken together, these results showed that irradiation only has a minor impact on MeV infectivity and replication. Therefore, both treatment modalities could be tested further as a combination treatment.

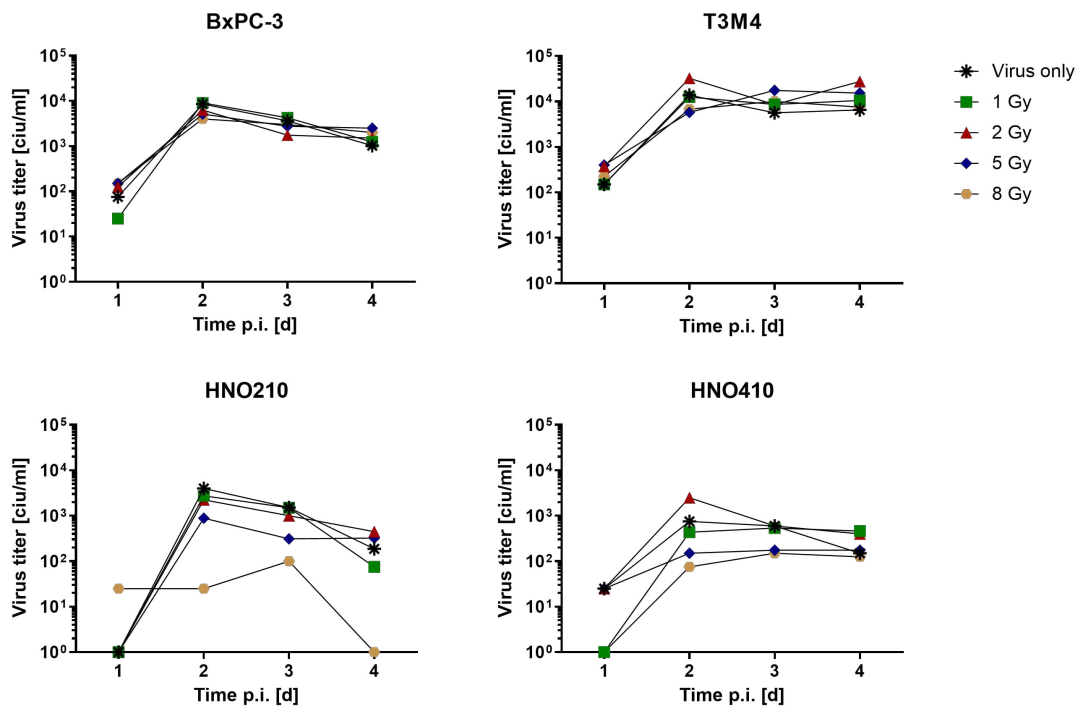


**Figure 4.4: Multi-step growth curves after RVTx treatment.** By determining progeny titers in irradiated tumor cells, I investigated the impact of irradiation on viral replication in human tumor cells. I generated multi-step growth curves of cells treated with different radiation doses in combination with a medium virus MOI (0.1 for BxPC-3, HNO210 and HNO410, 0.01 for T3M4) at indicated time points followed by serial dilution titration assay. The graphs show representative data of pooled technical replicates per sample of  $n = 2$  independent experiments. MOI — multiplicity of infection; p.i. — post infection; d — days.

## 4.2 Dosing and scheduling of radiovirotherapy *in vitro*

After evaluating both monotherapies regarding their individual effect on cell viability of candidate cell lines as well as MeV replication efficiency, I analyzed cell viability after combination treatment using the following schedule: irradiation 24 h prior to virus infection (R24V) as shown in Figure 3.1. Subsequently, I systematically combined several treatment doses of radio- as well as virotherapy and analyzed cell viability of candidate cell lines using two different assays: XTT and ATPlite assay. This data then served as the basis for calculating synergy of the combination therapy, determining an *in vitro* treatment schedule for further analyses of RVTx. I used the schedule R24V for all experiments analyzing RVTx *in vitro* and also *ex vivo*.

### 4.2.1 Analysis of cell viability after radiovirotherapy

In a first approach, I combined radio- and virotherapy and analyzed cell viability over a period of 7 days by XTT assay. Figure 4.5 shows representative data of combining 2 or 5 Gy irradiation with an intermediate virus MOI for each tested cell line according to analysis of virus sensitivity conducted before (see 4.1.1). Complete results are shown in Figure A1 (see Appendix). For all four cell lines, RVTx led to reduction of cell viability in comparison to monotherapies. The latter mostly showed minor to moderate cell killing whereas combination of both treatment modalities strongly decreased cell viability. For BxPC-3, the combination of 2 or 5 Gy irradiation with intermediate virus MOI resulted in 54% or 32% cell viability on day 5 post treatment (p.tr.), for T3M4 54% or 43%, HNO210 21% or 12% and for HNO410 16% or 9% compared to mock. Again, seven days after treatment, I observed a slight increase in cell viability, possibly due to regrowth of cells as the RVTx treatment was only applied once in this experiment.

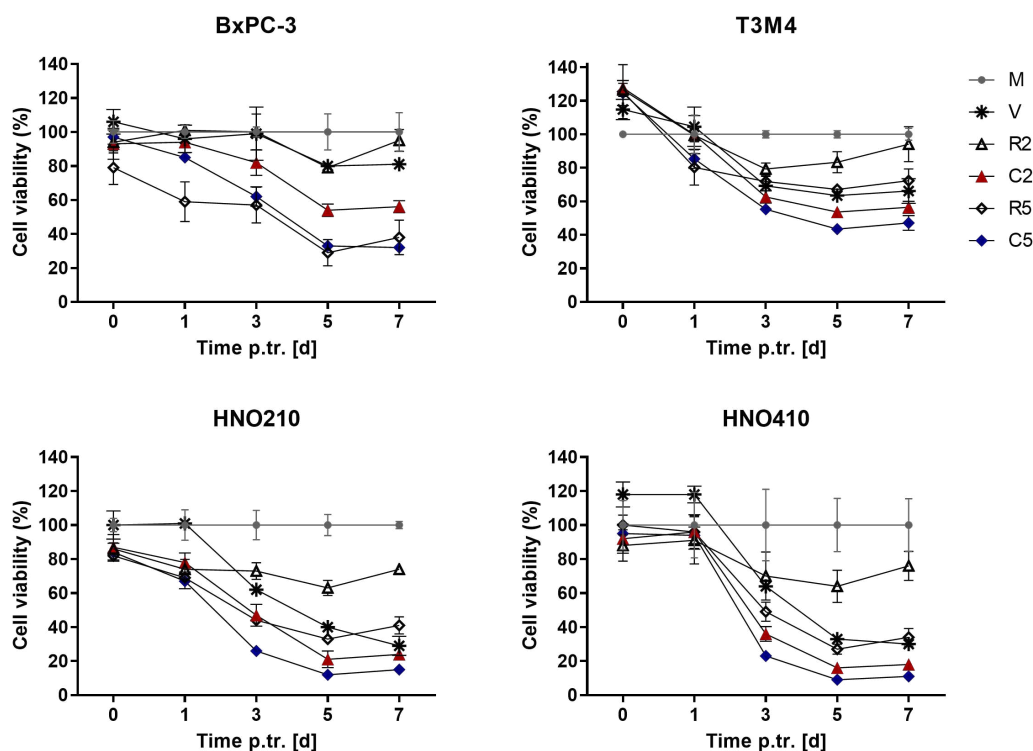


**Figure 4.5: Cell viability after RVTx *in vitro*.** To analyze the effect of RVTx on cell viability, I performed XTT assay, measuring cell viability at indicated time points after treatment with RVTx or monotherapies infecting cells with MeV at MOIs of 0.1 for BxPC-3, HNO210 and HNO410 and 0.01 for T3M4, respectively. The data was normalized to mock set at 100%. The graphs show representative mean and SD from triplicate samples of  $n = 2$  independent experiments. M — mock; V — virus; R2, R5 — radiation with 2 or 5 Gy; C2, C5 — combination with 2 or 5 Gy irradiation; p.tr. — post treatment; d — days.

### 4.2.2 Evaluation and validation of synergy

Combined RVTx showed enhanced reduction of cell viability in the tested human tumor cell lines compared to both monotherapies, especially between three and seven days p.tr. (see Figure 4.5). In order to investigate synergistic effects of RVTx *in vitro*, I performed a systematic analysis of cell viability in the mentioned time period after combination treatment using XTT and ATPlite assay for cross-checking the validity of results.

Altogether, I combined four different radiation doses, 1, 2, 5, and 8 Gy, with three different MeV doses (for each cell line individually determined virus MOIs for a low, medium and high MOI). Figure 4.6 shows exemplary data for BxPC-3 from three independent cell viability analyses using ATPlite assay. The complete results for all tested human tumor cell lines and both cell viability assays are shown in Figures A2 to A8 (see Appendix). For BxPC-3, low irradiation and low virus dose (top left diagram in Figure 4.6) showed hardly any cytotoxic effect, neither as monotherapies nor in combination. Increasing radiation dose but maintaining a low virus dose (left column of diagrams) led to reduction in cell viability mediated by irradiation without additional effect of MeV infection. Likewise, the combination of low irradiation with increasing virus dose (top row) led to a virus-mediated cytotoxic effect over the course of the experiment. When combining the highest radiation dose of 8 Gy with increasing virus doses (bottom row), the treatment efficacy was no longer dominated by the effect of radiation, but was also influenced by virotherapy. Again, I could observe a similar effect when combining increasing radiation dose with the highest virus dose (right column) as the reduction in cell viability was primarily virus-mediated until, with higher radiation doses, both treatment modalities showed an impact on cell viability.

The cell viability after RVTx treatment dropped to almost 0% at day 7 p.tr. when I applied both treatment modalities at their highest dose (diagram bottom right). Although this combination showed the best result in the experiment, the combined effect of radiation and MeV at high doses might be too strong. While this dose combination leads to increased cell killing, it might also increase toxicity when translated to the clinical setting. Therefore, reduced doses of combined treatment modalities might be more tolerable. Further, high doses of irradiation might not induce immunogenic effects such as immunogenic cell death (ICD) or innate immune activation as observed before [244, 245]. However, the induction of an anti-tumor immune response is a prerequisite for an optimal combinatorial effect of radiation and oncolytic MeV according to the hypothesis of this study.

Focussing on intermediate radiation as well as virus doses, such as 2 or 5 Gy combined with a medium virus MOI, I could observe cytotoxicity for both treatment modalities as indicated by reduced cell viability. Furthermore, the combination led to an enhanced reduction in cell viability as I could already show before (see Figure 4.5 in 4.2.1). Given the results of the

RVTx combination, the next step was to test whether these effects were more than additive, i.e. synergistic.

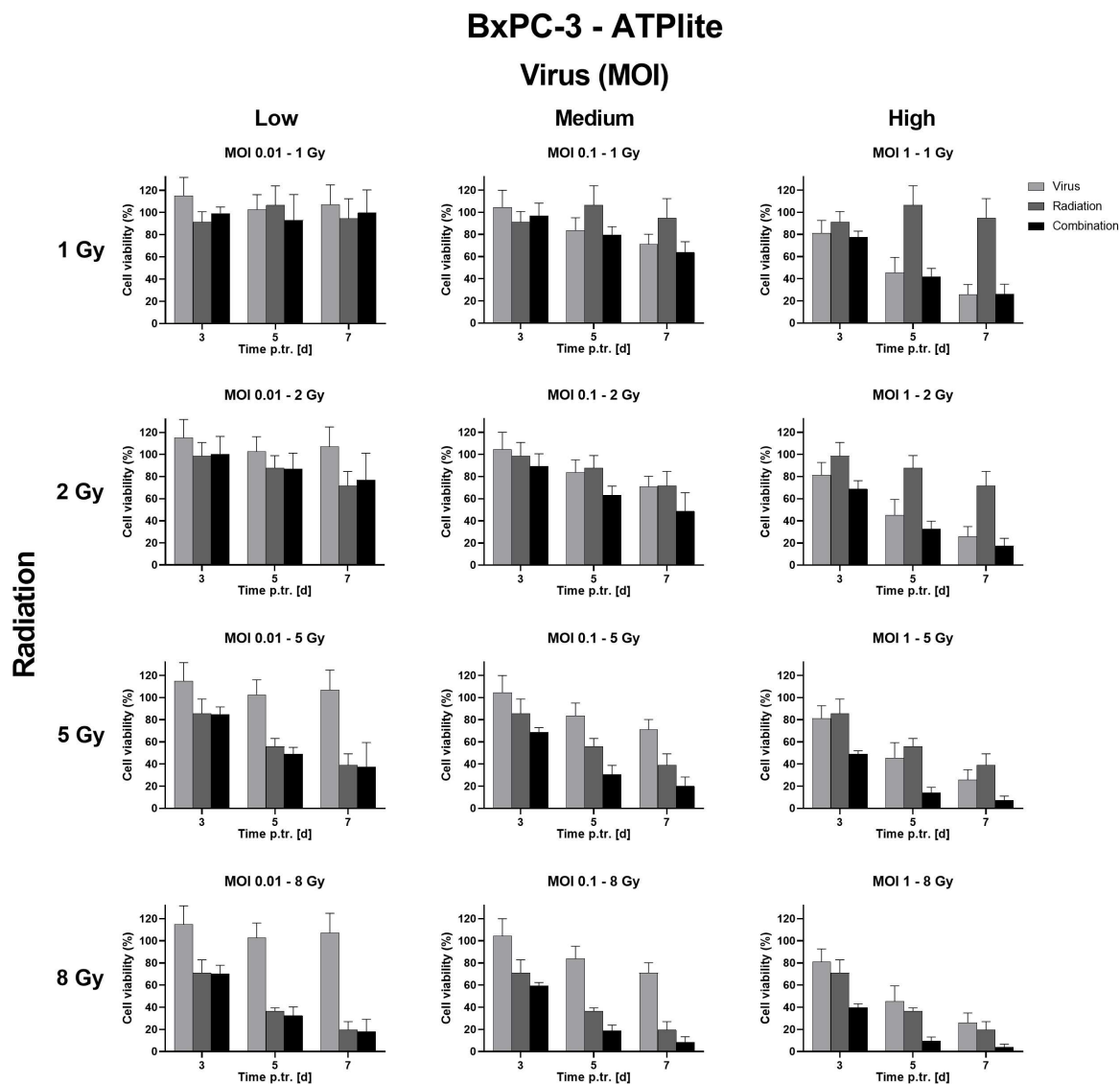


**Figure 4.6: Cell viability of BxPC-3 after RVTx treatment in ATPlite assay.** I evaluated synergy of RVTx by systematically combining both monotherapies. I seeded cells in 96 well-plates and determined cell viability via ATPlite assay at indicated time points after RVTx using different radiation and virus doses as indicated. The data was normalized to mock set at 100%. The figure shows mean and SD for data of  $n = 3$  independent experiments. MOI — multiplicity of infection; p.tr. — post treatment; d — days.

The data of this systematic evaluation of cell viability after RVTx served as basis for detecting synergistic effects of the combination therapy on candidate tumor cell lines. I used the CompuSyn software (ComboSyn, Inc.) for calculating synergy. It is based on the median effect method by Chou and Talalay [242] and calculates a combination index (CI) value for

each tested treatment condition. A CI of 1 indicates an additive effect of the used doses of radiation and virus, a CI-value above 1 indicates antagonism and CI below 1 indicates synergy of the specific doses of radiation and virus used for RVTx treatment. As I analyzed cell viability between days 3 and 7 p.tr. in the underlying experiment, I also analyzed synergy for each time point within this time period. Thus, I was able to analyze whether synergy was consistently observed over several time points or only for a single time point. Figure 4.7 shows a heatmap representation of CI values of the different dose combinations tested in candidate tumor cell lines using ATPlite assay. The corresponding heatmap showing CI values of the data from XTT assay is shown in Figure A9, an overview of all CI values is given in Table A1 (see Appendix).

As could be anticipated when considering the low effect in cell viability, the combination of low irradiation with low virus MOI was not synergistic but rather showed an antagonistic effect in the analysis of CI values (top left in each heatmap) over the course of the experiment. Increasing the dose of one component but keeping a low dose of the other, such as combining increasing radiation doses with a low virus MOI (left column of each heatmap), often showed only additive or even antagonistic effects of the specific combination. Interestingly, combining the highest radiation dose with a high virus dose led to CI values below 1 and indicated synergy of this dose combination. However, it is important to consider the CI values together with the results of the originating cell viability analysis (see above). The cytotoxic effect of this combination might be too strong to induce further anti-tumor immune responses and the result should therefore be evaluated with caution. Focusing on the combination of intermediate doses of radiation and MeV, these combinations showed synergy at all three analyzed time points in ATPlite as well as XTT assay for most cell lines. Taking this data together with the reduction in cell viability observed in both assays using intermediate dosing conditions, these might be suitable treatment schedules for further *in vitro* experiments.

Therefore, using this systematic analysis of cell viability and synergy combining several dosing conditions of radiation and oncolytic MeV, I could show that RVTx mediates a synergistic effect at specific treatment conditions in all tested human tumor cell lines. To determine a suitable treatment schedule for subsequent analyses of RVTx *in vitro* a comprehensive assessment of the tested dosing condition was required considering cell viability as well as the calculated CI values.

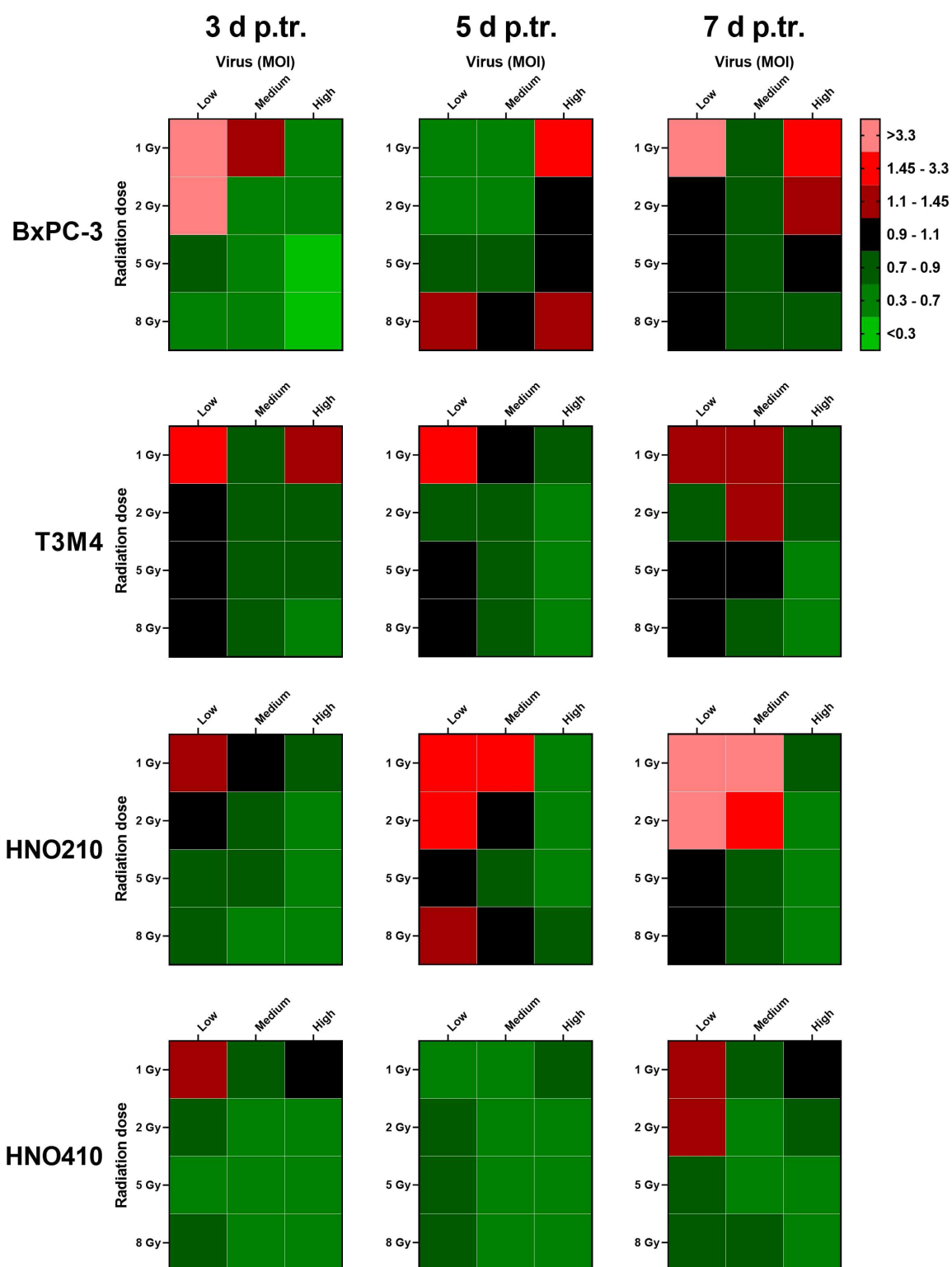


**Figure 4.7: Heatmap of synergy analysis of RVTx in ATPlite assay.** Using CompuSyn software, I calculated the synergy of all tested RVTx combinations determined by ATPlite assay. The corresponding CI values are given in Table A1. Values indicating antagonism are shown in red coloring, additive in black and synergistic in green coloring. d p.tr. — days post treatment; MOI — multiplicity of infection.

### 4.2.3 Determination of *in vitro* treatment conditions

The results of the cell viability experiments and synergy calculation shown above revealed a variety of dosing conditions that might be suitable as a uniform treatment schedule for further investigations, but the results did not overlap completely. However, in order to make an informed decision on a treatment schedule, it is necessary to assess the results of both analyses equally. It is a requirement that a specific dosing of the combination regimen shows a sustained synergistic effect over the course of the experiment. It is equally important that it leads to reduction in cell viability but it should still give the opportunity of inducing an anti-tumor immune response. Therefore, I developed a scoring system in order to assess different dosing conditions concerning their synergistic effect as well as resulting in cell viability reduction shown in Table 4.1. Using this scoring system, I aimed at selecting one or two specific treatment schedules for all candidate cell lines in follow-up *in vitro* experiments characterizing RVTx.

**Table 4.1: Categories for treatment schedule assessment.** To select a specific treatment schedule for further RVTx *in vitro* experiments, I developed a scoring system that equally considers synergy and the cytotoxic effect of a specific dosing condition. To assess performance of the treatment conditions in cell viability assays, I set a cut-off at 20% (of mock) as lowest and 80% as highest value on day 7 p.tr..

Scoring category	Scoring value
Synergy on all days	2
Synergy on two days	1
Cell viability of combination between 20 and 80% on day 7 p.tr.	2
Cell viability of both monotherapies between 20 and 80% on day 7 p.tr.	1

Using this scoring system, I assessed each tested dosing condition for all cell lines. I added the values concerning synergy and cell viability from ATPlite as well as XTT assay following Table 4.1 to obtain cell line-specific schedule counts as shown in Table A2, heatmap representation shown in Figure 4.8. For all cell lines, especially for BxPC-3 and HNO210, combination of intermediate dosing conditions such as 2 or 5 Gy irradiation with medium virus MOI showed the highest count. Additionally, for T3M4, a schedule combining 8 Gy irradiation with medium virus MOI and for HNO410, a combination of 2 Gy irradiation with low virus MOI showed a high count. Further, I summed up the schedule counts of all cell lines in a total count (heatmap on the right). This heatmap shows the most suitable treatment schedule for all cell lines in this panel. Therefore, I could determine a combination of 2 or 5 Gy irradiation with a medium MOI of MeV as treatment schedule for following *in vitro* experiments investigating RVTx.

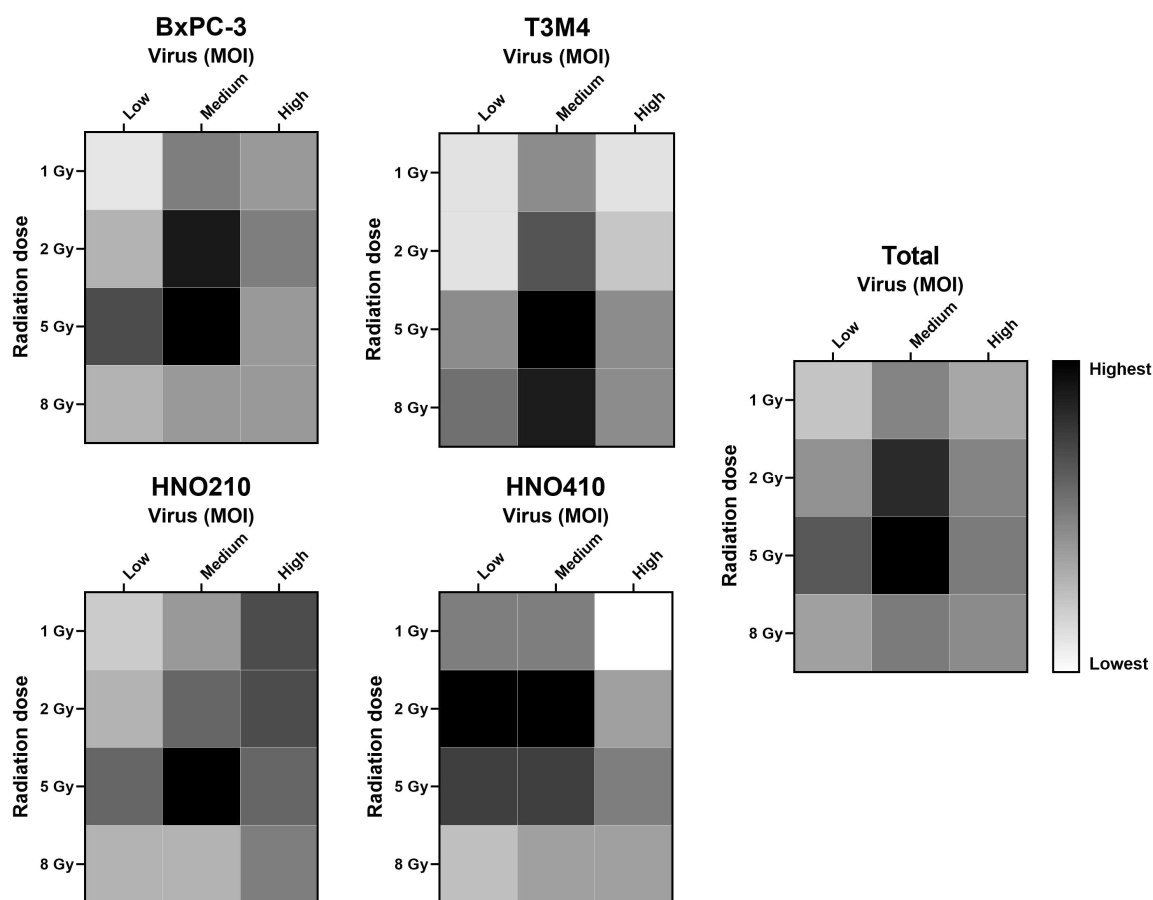


**Figure 4.8: Heatmap of schedule counts for analysis of RVTx treatment schedules.** To evaluate the performance of each treatment schedule in cell viability assays and synergy analyses, I developed a scoring system with cut-off at 20 and 80% for cell viability data to determine a treatment schedule for further analyses of RVTx *in vitro*. Score values correspond to the given color code showing lowest score in white and highest in black. The summary of schedule scoring is given in Table A2. MOI — multiplicity of infection.

In order to confirm this schedule, I analyzed a second set of cut-off percentages to assess cell viability. The effect of RVTx as well as monotherapies should range between 25 and 75% on the last day of the experiment. This would consider combination as well as monotherapies more strictly, resulting in cell viability above 75% and below 25% as unsuitable for further investigations. The given reduction in cell viability would be too weak or too strong, respectively. As shown in Table A3 and Figure A10 (see Appendix), changing the cut-off values for cell viability slightly changed the schedule counts for each cell line. However, the total count still revealed a combination of 2 or 5 Gy irradiation with a medium virus MOI as the most suitable treatment schedule for further experiments, confirming the results of the previous scoring cut-offs.

## 4.3 Detection of immunogenic cell death markers

Having determined suitable treatment dosing conditions for investigating RVTx *in vitro*, I continued with a molecular and functional characterization of potential mechanisms of action. As one aspect, I investigated the induction of ICD by RVTx. It has been hypothesized for several years that localized radiotherapy induces ICD and this could be confirmed in various tumor entities [106, 107]. In the context of oncolytic MeV, Donnelly and colleagues demonstrated the induction of ICD after MeV infection in human melanoma [189]. Among many different factors currently known as ICD markers [70], I focused my analyses on the release of the nucleoprotein high mobility group box 1 (HMGB1) as well as ATP and the expression of the endoplasmic reticulum (ER)-associated protein calreticulin (CALR) on the cell surface. These markers are commonly used to verify ICD induction [73].

### 4.3.1 Release of HMGB1 and ATP

Secretion of HMGB1 as well as ATP represent two important ICD markers as they promote the maturation and cross-presentation capacity of antigen-presenting cells (APCs) and therefore play an important role in the initiation of an adaptive immune response [70, 73]. For the detection of released HMGB1, I performed an enzyme-linked immunosorbent assay (ELISA) using supernatants of RVTx-treated cells 72 h p.tr.. As shown in Figure 4.9, I could detect an increase in HMGB1 release in samples treated with the combination therapy compared to monotherapies. This was statistically significant for BxPC-3, HNO210 as well as HNO410. A high radiation dose of 5 Gy (R5) was associated with increased release of HMGB1 compared to the lower radiation dose of 2 Gy (R2) but the combination using the respective radiation dose (C2 or C5) showed even higher HMGB1 release than irradiation alone. T3M4 showed a high baseline level of released HMGB1 in mock-treated samples. Radio- as well as virotherapy led to elevated HMGB1 levels in the cell supernatant. Again, although the increase was statistically not significant, I detected highest release after combination treatment (C2, C5). In general, the different cell lines varied in regard to the concentration of released HMGB1 which can be ascribed to differences in the baseline level of mock-treated cells. The fact, however, that combination of radio- and virotherapy was most potent in terms of HMGB1 release was true for all cell lines.

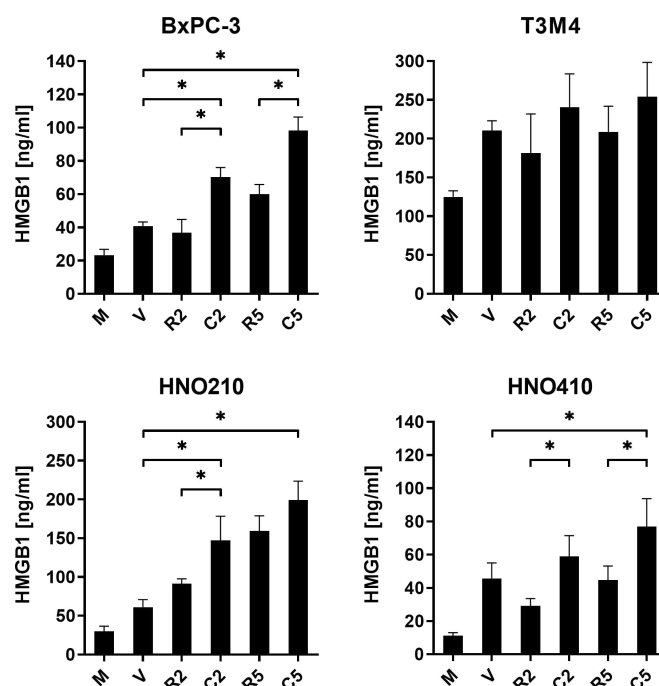


**Figure 4.9: HMGB1 release after RVTx *in vitro*.** I treated PDAC and HNSCC cells with RVTx, collected supernatants 72 h p.tr. and detected released HMGB1 by ELISA. Statistical analysis was performed using one-way ANOVA with Tukey correction for multiple comparison testing. The graphs show mean and SD of triplicate samples from one representative experiment of  $n = 3$  independent experiments.  $p < 0.05$ : \*; M — mock; V — virus; R2, R5 — radiation with 2 or 5 Gy; C2, C5 — combination with 2 or 5 Gy irradiation.

To measure ATP release, I also used supernatants of treated cells and performed a luminescence-based assay. Investigating several time points after treatment, I could not detect changes in levels of released ATP or produce reproducible data when repeatedly performing independent experiments in any tested human tumor cell line (data not shown). Furthermore, the detection limit of the assay provided an additional constraint. Therefore, the investigation of potential ATP release after RVTx treatment as another ICD marker was not possible under the given circumstances.

### 4.3.2 Surface-exposed calreticulin

Another typical ICD marker is CALR, which promotes the phagocytosis of dying cells by APCs as an ‘eat me’ signal [70, 76]. While under physiological conditions, CALR is located at the ER and functions as a chaperone, it becomes a distinct marker for ICD after relocation to the cell surface upon ICD-inducing cell damage. To detect CALR relocation after RVTx treatment, I performed flow cytometry (FC) analysis and immunofluorescence (IF) stainings of treated cells. Both represent common approaches to detect this marker on the cell surface

*in vitro* as well as in clinical samples [246, 247].

I performed the detection of surface-exposed CALR by FC 48 h after treating the cells with RVTx or monotherapies. The corresponding gating strategy is shown in Figure A11 (see Appendix). Overall, the CALR expression on the cell surface was low in the tested cells but the data still showed increased expression, especially after RVTx combining 5 Gy irradiation with MeV (C5) in BxPC-3, HNO210 and HNO410 cells (Figure 4.10). For the latter, the increase of exposed CALR was statistically significant when comparing different combinations with respective monotherapies. I could detect the same for HNO210 when comparing the combination C5 with virus alone. Further, when I determined the population of CALR<sup>+</sup> cells directly from the single cell population, I could detect a population of dead but CALR-expressing cells that were possibly stained for intracellular CALR due to membrane permeability. This indicated that a precise gating strategy was an important prerequisite to determine the percentage of cells that expressed CALR on the cell surface as a marker for ICD induction.

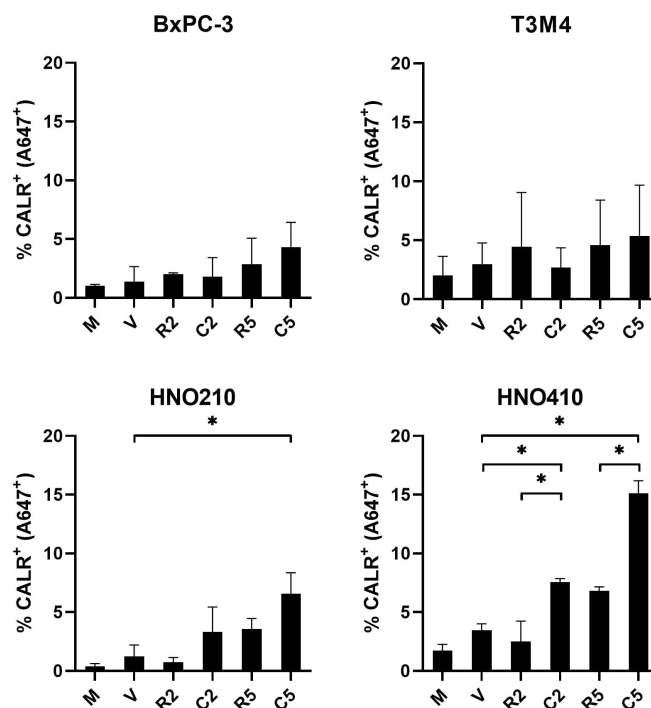


**Figure 4.10: Surface-exposed CALR after RVTx *in vitro*.** I treated PDAC and HNSCC cells with RVTx and detected surface-CALR 48 h p.tr. by FC. Statistical analysis was performed using one-way ANOVA with Tukey correction for multiple comparison testing. The graphs show mean and SD of  $n = 2$  independent experiments.  $p < 0.05$ : \*; CALR — calreticulin; M — mock; V — virus; R2, R5 — radiation with 2 or 5 Gy; C2, C5 — combination with 2 or 5 Gy irradiation.

As I used an eGFP-encoding MeV, I could also detect infected cells by FC. Interestingly, the percentage of double-positive cells, indicating concurrent virus infection and CALR exposure, was very low. Representative data is shown for HNO410 (see Figure A11). The majority of live CALR<sup>+</sup> cells did not emit a signal of the green fluorescent protein (GFP) and most cells expressing virus-encoded genes (GFP<sup>+</sup>) did not expose CALR on their cell surface.

Due to these findings in the FC analysis of CALR, I also performed IF to visualize the surface-exposed ICD marker. As the expression levels seemed to be very low and had to be discriminated carefully from background fluorescence, a reasonable detection of CALR signal by IF was only possible for HNO410 (Figure 4.10). In accordance with the results of the FC analysis, I could detect only a few CALR<sup>+</sup> cells after all types of treatment (see white arrows, Figure 4.11). Due to the addition of fusion inhibitory peptide (FIP), which prevents viral spread, I detected only local infection sites of single cells expressing eGFP and no formation of syncytia. This, however, prevented rupture of the latter during sample processing and ensured the detection of infected cells *per se*. With increasing radiation dose, it seemed that there was an increasing number of CALR<sup>+</sup> cells detectable which peaked in the combination of 5 Gy irradiation with MeV, showing many cells stained with the Alexa Flour<sup>®</sup> 594-conjugated CALR-antibody (bottom right). However, as already seen in FC, there were no cells present showing CALR as well as eGFP signal.

All in all, the investigation of ICD markers showed a robust induction of HMGB1 release as well as elevated levels of surface-exposed CALR after RVTx treatment in the panel of human PDAC and HNSCC tumor cell lines.

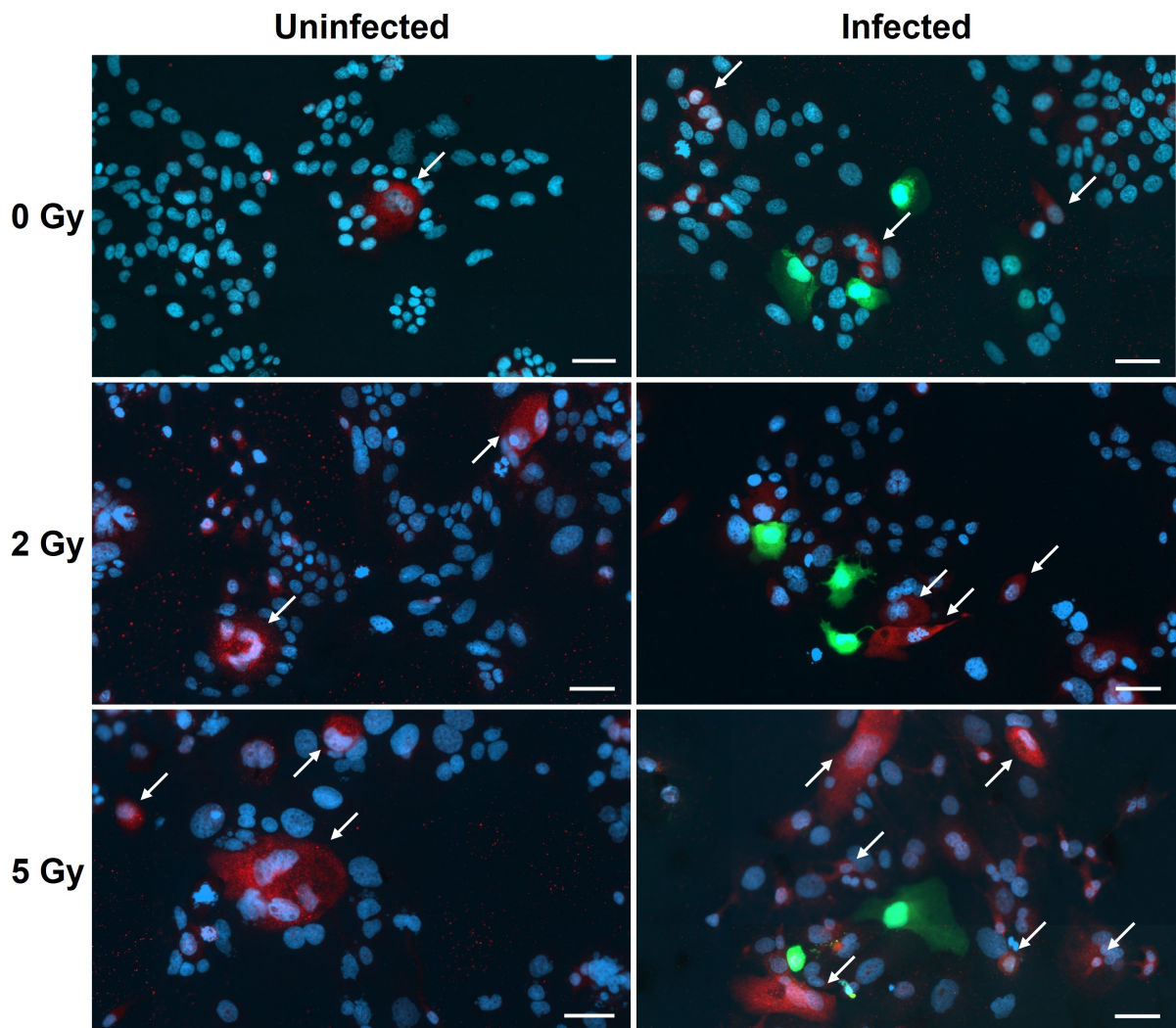


**Figure 4.11: Surface-exposed CALR in HNO410 after RVTx visualized by IF.** After having treated HNO410 cells with RVTx, I performed IF staining 48 h p.tr. using an Alexa Flour<sup>®</sup> 594-conjugated antibody to detect CALR on the cell surface (red, highlighted by white arrows). As an eGFP-encoding MeV was used, infected cells could be detected in the green fluorescence channel. I added FIP after treatment to maintain local infection sites and prevent rupture of syncytia due to mechanical stress during sample processing. Nuclei were stained with Hoechst 33342. Representative images of  $n = 2$  independent experiments are shown. Scale bar: 50  $\mu\text{m}$ .

## 4.4 Detection of markers for innate immune signaling

Ionizing radiation as well as viral infection are factors well known to activate innate immunity. By triggering different innate immune sensors, both induce type I interferon (IFN) signaling [63, 248]. The irradiation of cells not only leads to DNA double-strand breaks but also to release of DNA into the cytosol. This is sensed by the cyclic GMP-AMP synthase (cGAS) which activates the adapter protein stimulator of interferon genes (STING). The following signaling cascade leads to induction of IFN-related genes and the secretion of IFN- $\beta$  [53, 55].

The presence of 5'-triphosphorylated single-stranded RNA in the host cell cytosol upon MeV infection is sensed by the protein retinoic acid-inducible gene I (RIG-I), which in turn activates a downstream signaling cascade leading to IFN- $\beta$  expression and release [54, 55]. Thus, after having detected the RVTx-mediated induction of ICD, I analyzed whether the combination therapy has the potential to activate innate immune signaling.

### 4.4.1 Detection of markers for DNA damage and viral sensing

In order to investigate whether RVTx induces innate immune signaling, I analyzed protein expression of cGAS, STING as well as the virus sensor RIG-I via sodium dodecyl sulphate-polyacrylamide gel electrophoresis (SDS-PAGE) and western blot (WB). I also quantified target protein expression by normalizing respective WB signals to total protein content of treated cells. For the DNA damage sensor cGAS, I could only detect minor changes in protein expression over time compared to mock (see Figure A12 in Appendix). Furthermore, there was no trend for altered expression induced by either irradiation or MeV infection. The signal intensity in WB was strongest for cGAS at an early time point (12 h p.r.). At later time points (12 and 24 h p.tr.), it was very weak and required long exposure times for visualization (see Figure A13A). Especially for T3M4, HNO210 and HNO410, I detected the signal only using long exposure times between approx. 430 and 1050 seconds. The detection of STING showed strong protein expression but hardly any change over time after RVTx treatment compared to mock (see Figure A13B and Figure A14). The PDAC cell line T3M4 did not show any expression of STING on protein level although the gene was present in the genome detected by polymerase chain reaction (PCR) before (Schlue, unpublished).

Besides investigating cGAS and STING as factors for DNA damage sensing after irradiation, I analyzed the protein expression of RIG-I as a marker for viral RNA sensing 48 h after RVTx treatment. Although statistically not significant, I could detect a clear trend of increased RIG-I protein expression due to MeV infection shown in Figure 4.12 and A15. When normalizing the data to mock, I observed an increase in protein expression between 10- and 16-fold in samples of all human tumor cell lines treated with MeV compared to corresponding mock. Irradiation alone did not induce RIG-I expression. Only for HNO210 cells, I could detect an increase after 5 Gy irradiation (R5). However, regarding the combination treatment, RVTx seemed to further increase RIG-I expression only for HNO210 and HNO410. This was especially apparent for the combination of 5 Gy irradiation with MeV.

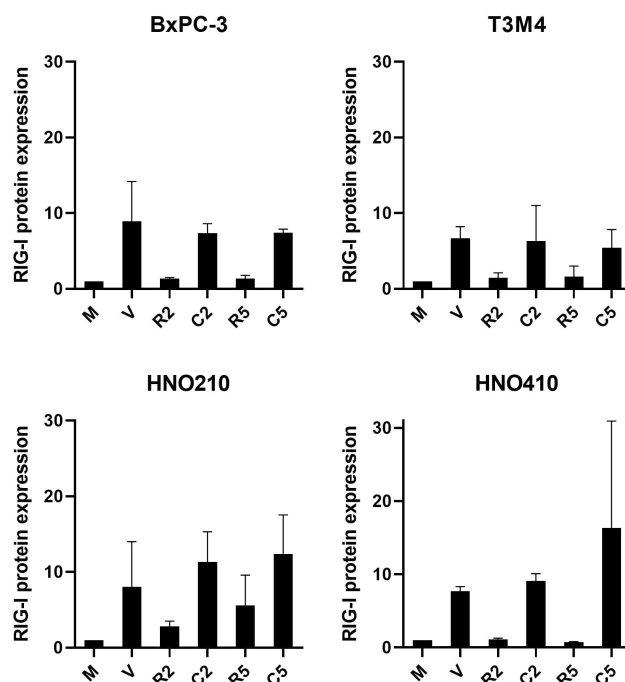


**Figure 4.12: Protein expression of RIG-I after RVTx.** To investigate RIG-I protein expression, I collected cell lysates 48 h p.tr. and performed SDS-PAGE followed by WB. For quantification, I normalized the detected signal to total protein content followed by normalization to mock. Statistical analysis was performed using one-way ANOVA with Tukey correction for multiple comparison testing. The graph shows mean and SD of  $n = 2$  independent experiments. M — mock; V — virus; R2, R5 — radiation with 2 or 5 Gy; C2, C5 — combination with 2 or 5 Gy irradiation.

According to this data, I could observe a virus-mediated induction of RIG-I expression after RVTx treatment. However, neither irradiation nor viral infection mediated a clear induction of cGAS or STING.

#### 4.4.2 Expression and release of interferon-beta

As shown in Figure 1.1 (see 1.2.1), RIG-I and cGAS-STING pathways lead to IFN- $\beta$  secretion and the activation of other interferon stimulated genes (ISGs). Therefore, I analyzed secretion of this cytokine as well as expression of the *IFNB1* gene on RNA level 24 h after RVTx treatment. The quantification of secreted cytokine by ELISA showed differences between PDAC and HNSCC cell lines (Figure 4.13). For HNO210 and HNO410, I could detect increasing levels of IFN- $\beta$  in the supernatant of samples treated with virus alone (V) or in combination with radiation (C2, C5). For HNO210, irradiation with 2 or 5 Gy (R2, R5) also led to increased levels of IFN- $\beta$  in the supernatant compared to mock. Especially in this cell line, the difference when comparing monotherapies with RVTx was statistically significant.

For both PDAC cell lines, however, I could not detect IFN- $\beta$  in the supernatant as the signal was below the detection limit of the assay.

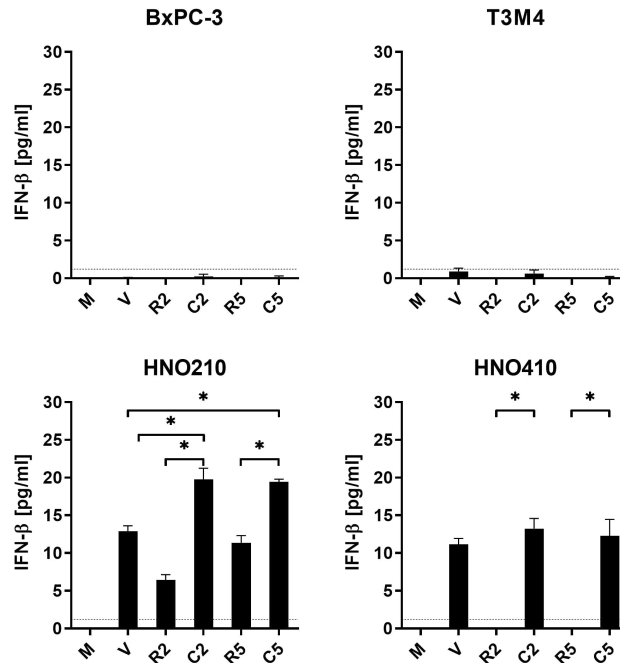


**Figure 4.13: IFN- $\beta$  release after RVTx *in vitro*.** I treated PDAC and HNSCC cells with RVTx, collected supernatants 24 h p.tr. and detected released IFN- $\beta$  by ELISA. Statistical analysis was performed using one-way ANOVA with Tukey correction for multiple comparison testing. The graphs show representative mean and SD of  $n = 3$  independent experiments. The dotted line indicates the detection limit of the assay.  $p < 0.05$ : \*; M — mock; V — virus; R2, R5 — radiation with 2 or 5 Gy; C2, C5 — combination with 2 or 5 Gy irradiation.

Despite the strong differences in IFN- $\beta$  secretion between the different treatment conditions, the expression of the *IFNB1* gene on transcriptomic level was detectable via reverse transcription PCR (RT-PCR) in HNSCC as well as PDAC cell lines in MeV- and RVTx-treated samples (Figure A16 in Appendix). For the PDAC cell lines, I could even observe a faint signal in mock or samples treated with radiation alone. T3M4 cells from cell culture showed baseline RNA levels of *IFNB1*. It seems that the process between the expression of the gene on RNA level and secretion of the cytokine might be impaired in the analyzed PDAC cell lines. T3M4 showed higher virus sensitivity than other PDAC cell lines before [240]. This might correlate with the finding of impaired IFN- $\beta$  secretion indicating reduced host-cell anti-viral defense.

In summary, I could observe activation of RIG-I signaling mediated by MeV infection and the release of IFN- $\beta$  leading to activation of innate immune signaling in HNSCC but not in PDAC cell lines. Looking at the entire spectrum of investigated mechanisms of action within

this study, RVTx induced at least one component of the parallel pathways of ICD signaling and innate immune sensing in all candidate cell lines. This would eventually lead to immune activation.

## 4.5 Generation of murine tumor models

The preceding *in vitro* findings of this study showed synergy of RVTx as well as induction of ICD and an innate immune response. Therefore, I aimed at investigating RVTx in heterotopic, syngeneic mouse tumor models of HNSCC and PDAC. Humans are the natural host of measles virus and express the necessary entry receptors for wildtype as well as vaccine strains — CD150, nectin-4 or CD46 — on some cells [136, 138, 153]. Mice are consequently not a natural host as murine cells do not express suitable receptors for viral entry. Thus, the virus is not able to enter murine cells *per se* [171] and *in vivo* investigations of RVTx require the establishment of murine tumor cells expressing an MeV entry receptor, e.g. human CD46 (hCD46). I generated cell lines of murine HNSCC and PDAC tumors stably expressing hCD46 and performed a characterization focusing on virus susceptibility *in vitro*, tumor growth and hCD46 expression before investigating the effects of the combination therapy *in vivo*.

### 4.5.1 Selection and *in vitro* characterization

To establish murine tumor cells of HNSCC and PDAC that stably express hCD46, I selected four cell lines of these entities with a murine C57BL/6J origin: MOC2 and mEERL95 for HNSCC, 30364 and Panc02 for PDAC [223, 224, 226, 228].

Before generating hCD46 expressing murine tumor cells, I analyzed the radiosensitivity of non-transfected, parental cells. I irradiated them with different doses of radiation ranging from 1 to 8 Gy and performed an XTT assay to monitor cell viability (see Figure A17 in Appendix). In all cell lines, the cell viability did not change over time after irradiation compared to untreated control. It seemed that these tumor cells were resistant to ionizing radiation. Only the MOC2 cell line showed intermediate sensitivity to irradiation as cell viability dropped to 69% at 5 Gy and 48% at 8 Gy irradiation.

After analyzing radiosensitivity of parental murine tumor cells, I transfected or transduced them with two different types of vectors: I used either nanovectors (expression vectors produced in *E. coli* encoding *CD46* controlled by promoters pEF1 or pCAG) or I used a lentiviral vector (see 3.2.10.1). I selected the transfected cells for hCD46 expression by puromycin challenge (see 3.2.10.2) and performed fluorescence-activated cell sorting (FACS) to generate hCD46 expressing murine cell lines from single or bulk sorted cell populations.

By FC analysis, I selected clones from single cell sorted populations and combined them to generate heterogenous cell populations for each tumor model. Once the newly generated cell lines had grown to sufficient cell numbers, I analyzed susceptibility to MeV infection as well as surface expression of hCD46. In light of these selection criteria, Figure 4.14 and Figure A18 show the most promising candidates of the four murine tumor models: MOC2-hCD46 pEF1 single designated as MOC2-hCD46, 30364-hCD46 pCAG single as 30364-hCD46, mEERL95-hCD46 lenti single as mEERL95-hCD46 and Panc02-hCD46 pEF1 single as Panc02-hCD46.

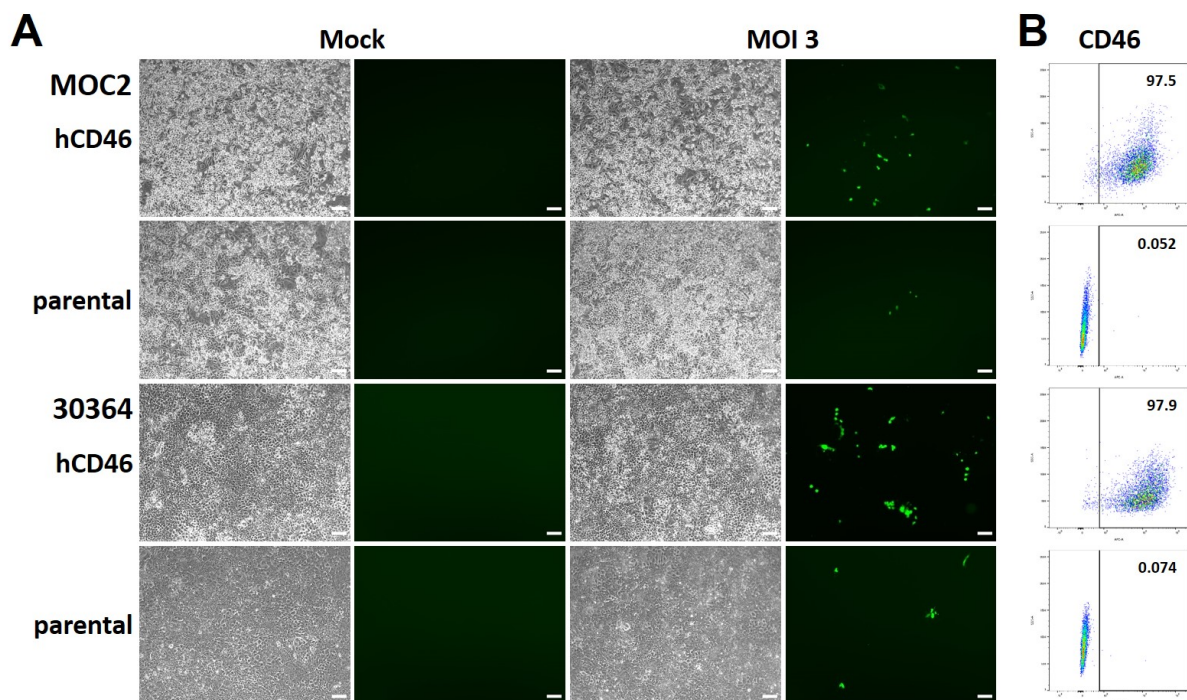


**Figure 4.14: *In vitro* characterization of newly generated murine tumor cells.** After hCD46-transfection and FACS, (A) I analyzed susceptibility of MOC2-hCD46 and 30364-hCD46 cells to MeV. I infected cells with MeVac Id-EGFP at MOI = 3 and monitored virus infection and syncytia formation at 72 h p.i. by fluorescence microscopy in phase contrast and green fluorescence channel. (B) Secondly, I performed an FC analysis to investigate hCD46 surface expression. Non-transfected, parental cells served as negative control. hCD46 — cell line transfected with hCD46 encoding vector; parental — non-transfected cells. Scale bar: 100  $\mu$ m.

MOC2-hCD46 and 30364-hCD46 showed virus infection as indicated by green fluorescent cells and formation of small syncytia 72 h after infection with MeV at MOI = 3 (Figure 4.14A). Parental cells showed minor viral infection and less GFP signal than hCD46 transfected cells. For the transduced or transfected mEERL95-hCD46 and Panc02-hCD46, however, I could hardly observe any infected cells at 72 h p.i. (Figure A18A). Concerning the surface expression of hCD46, I detected a shift of the entire cell population of MOC2-, 30364- and Panc02-hCD46

cells in FC analysis showing strong expression of the transfected receptor compared to parental cells (Figure 4.14B and Figure A18B). The cell population of the lentivirally transduced mEERL95-hCD46 showed heterogenous expression of hCD46. Although the majority of transduced cells were hCD46-positive, the intensity of surface expression seemed to vary in this cell line and no homogenous population was visible via FC analysis.

After analyzing hCD46 surface expression, I cultivated them with or without the selection reagent puromycin for 2 – 3 weeks in order to monitor receptor expression stability and performed another FC analysis. Comparing the results before and after this cultivation period, I did not observe differences in hCD46 surface expression between cells being cultivated with or without puromycin (data not shown). The hCD46 gene seemed to be stably expressed leading to constant surface expression of hCD46 on murine tumor cells.

According to these findings, especially the differing virus susceptibility of the newly generated murine tumor cell lines, MOC2-hCD46 and 30364-hCD46 were deemed the most suitable candidates as murine HNSCC and PDAC tumor models for further investigations of RVTx *in vivo*.

### 4.5.2 *In vivo* tumor growth and model characterization

After generation of the murine tumor models MOC2-hCD46 and 30364-hCD46 followed by *in vitro* characterization, I analyzed tumor growth kinetics as well as transgene expression *in vivo* to ensure that tumor treatment with oncolytic MeV is possible.

First, I analyzed whether the newly generated tumor cell lines showed consistent tumor growth after subcutaneous (s.c.) implantation. I injected  $5 \cdot 10^5$  MOC2-hCD46 or  $1 \cdot 10^6$  30364-hCD46 cells s.c. into the left thigh of 6 – 8 weeks old C57BL/6J mice. On the day of each implantation, I routinely analyzed the expression level of hCD46 of the implanted cells in order to ensure correct experimental conditions (see Figure A19). In this first animal experiment, I monitored tumor growth of both tumor models over the course of 50 days (Figure 4.15).

All mice that received MOC2-hCD46 cells showed successful tumor engraftment and tumor growth (Figure 4.15, left). Once the tumors were established, some developed ulceration at an early time point which led to sacrifice of the mice before reaching a maximum tumor volume of  $1000 \text{ mm}^3$ . In following animal experiments using MOC2-hCD46 as tumor model, I could observe equally consistent tumor growth. Early ulceration of tumors was only present for some mice. For 30364-hCD46, the tumors grew larger and did not ulcerate as quickly as in the MOC2-hCD46 model in this first experiment (Figure 4.15, right). However, I could not observe tumor formation in all mice and the overall growth kinetics varied between the animals. Some tumors grew rapidly whereas others entered the exponential growth phase

with delayed kinetics. Follow-up experiments using 30364-hCD46 as tumor model showed similar tumor growth kinetics: in a fraction of mice the tumor did not develop, while others showed delayed tumor growth (see Figure A20).

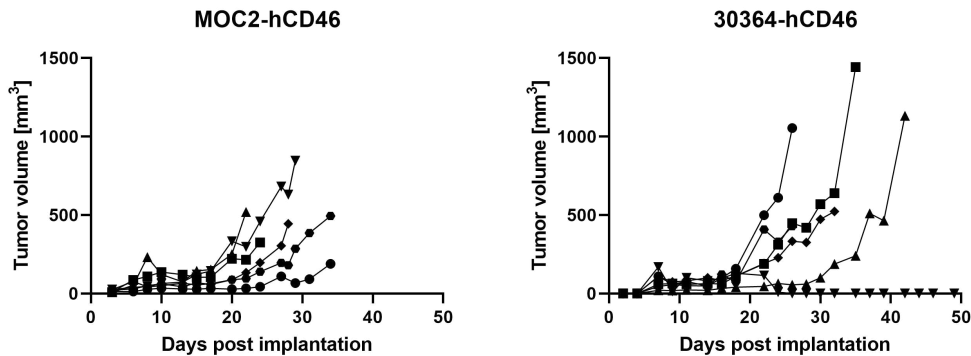


**Figure 4.15: Growth of transgenic murine tumors *in vivo*.** To analyze tumor growth kinetics *in vivo*, I implanted  $5 \cdot 10^5$  MOC2-hCD46 and  $1 \cdot 10^6$  30364-hCD46 cells s.c. into the left thigh of 6 – 8 weeks old C57BL/6J mice. Over the course of 50 days, I monitored tumor growth by measuring tumor volumes every second to third day. The graphs show individual tumor growth curves of  $n = 6$  animals per group.

Besides analyzing tumor growth kinetics, I aimed at analyzing the hCD46 status of established tumors *in vivo* in order to ensure that, once the tumors received MeV injections during treatment, the virus would be able to enter tumor cells. To this end, I characterized the transgene expression and virus susceptibility of established tumors in mice.

After having implanted MOC2-hCD46 and 30364-hCD46 cells s.c. into mice, I monitored tumor growth. Again in case of 30364-hCD46, the tumors in different mice did not show similar growth kinetics or consistent development among the animals (see Figure A20). Once the tumors of both models reached sizes of 100 – 200 mm<sup>3</sup>, I performed intratumoral (i.t.) injections of  $1 \cdot 10^6$  cell infectious units (ciu) of MeVac, the unmodified measles virus vaccine strain. Two days after this single virus dose, I explanted the tumors and generated single cell suspensions. I co-cultured them with Vero cells and monitored syncytia formation. However, I could not detect any syncytia as no infectious virus seemed to be present in the tumor cell suspensions (data not shown). Further, I analyzed hCD46 surface expression of freshly explanted tumor cells (Figure A21A and C). For both tumor models, I could hardly detect any hCD46 signal on live tumor cells in cell suspensions of explanted tumor samples. Only for the sample of mouse #1 of 30364-hCD46, I detected a small population of 6.89% hCD46-positive of all live tumor cells. Fourteen to eighteen days after cultivating the single cell suspension in cell-specific medium without puromycin, I performed a second FC analysis to examine whether the hCD46 receptor expression was detectable after the

cultivation period. In fact, for explanted MOC2-hCD46 tumor cells, I could detect hCD46 again on 66.7 to 79.3% of all live cells, almost reaching the level of MOC2-hCD46 cells from cell culture (Figure A21B). For 30364-hCD46, however, there was no hCD46-positive cell population detectable. Even sample #1 showed only 0.89% tumor cells expressing hCD46 on their cell surface.

Although it remains to be investigated why hCD46 surface expression was not detectable on freshly explanted tumor cells and only detectable on MOC2-hCD46 cells after *in vitro* culture, these findings raised the question whether the tumor cell samples were still susceptible to viral infection and resistant to puromycin. Therefore, I infected explanted tumor samples

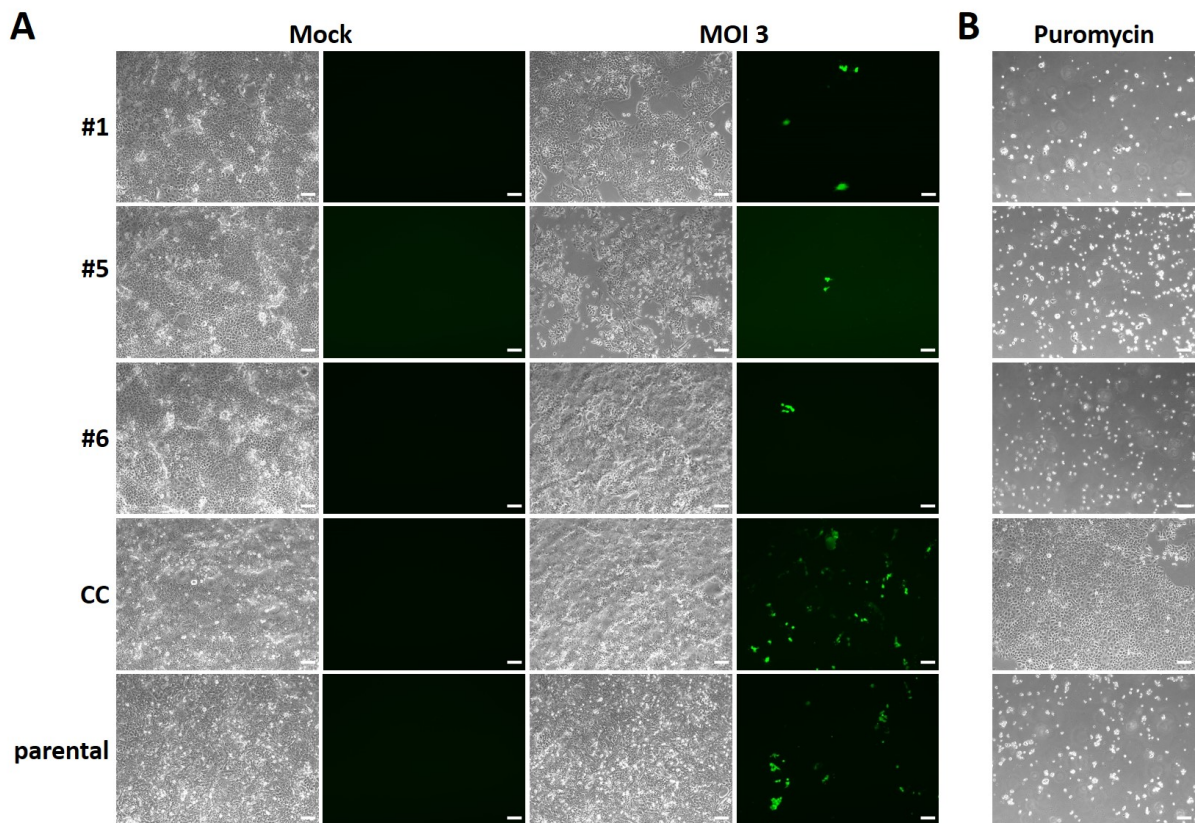


**Figure 4.16: Analysis of virus susceptibility and puromycin resistance of 30364-hCD46 tumor samples.** (A) To characterize murine *in vivo* tumor models, I infected 30364-hCD46 tumor samples cultivated after explantation with MeVac Id-EGFP at MOI = 3 and monitored viral infection as well as syncytia formation at 72 h p.i. by fluorescence microscopy in phase contrast and green fluorescence channel. (B) Additionally, I tested puromycin resistance by challenging tumor cells with 5  $\mu\text{g}/\text{ml}$  puromycin for 24 h and investigated cell confluence by microscopy. Transfected cells from cell culture (CC) and non-transfected, parental cells served as positive and negative control, respectively. Representative images of triplicate samples of selected tumor samples are shown. MOI — multiplicity of infection; CC — *in vitro* tumor cells from cell culture; parental — non-transfected cells. Scale bar: 100  $\mu\text{m}$ .

with MeVac Id-EGFP at an MOI of 3 and monitored cell infection by fluorescence microscopy for 72 h. Further, I challenged tumor cells with puromycin at the previously determined concentrations (see 3.2.10.2) and monitored cell confluence 24 h later by microscopy. The infection of 30364-hCD46 tumor cells confirmed the findings of the preceding FC analysis: I could only detect single infected cells, which was comparable to unspecific infection of parental, non-transfected 30364 cells (Figure 4.16A). Especially tumors from mice #5 and #6 showed very little infection. Regarding puromycin resistance, again, the result was comparable to parental cells after challenging 30364-hCD46 tumor cells with puromycin for 24 h. All cells were dead and had detached in wells containing explanted tumor cells (Figure 4.16B). For MOC2-hCD46, all explanted tumor cells from mice showed virus susceptibility and infection comparable to the positive control (see Figure A22A). The negative control, non-transfected MOC2 cells, did not show infection events. After challenging the cells with puromycin for 24 h, the cell confluence of explanted tumor cells was comparable with the positive control, MOC2-hCD46 from cell culture (see Figure A22B). Therefore, it seemed that although the MOC2-hCD46 cells did not show transgene expression after explantation, the nanovector was still present and hCD46 detectable after *in vitro* culture. For 30364-hCD46, the question remained whether the cells had only silenced the expression of hCD46 and the puromycin resistance gene or whether they had lost the entire transfected nanovector. This was investigated in the following.

For further characterization of the expression of the human *CD46* gene in the MOC2-hCD46 and 30364-hCD46 tumor models, I tested *CD46* expression on genomic and transcriptomic level. Therefore, I isolated DNA or RNA from cell pellets and performed complementary DNA (cDNA) synthesis for the latter followed by PCR or RT-PCR and gel electrophoresis. I detected the genomic presence of *CD46* in all samples of MOC2-hCD46 (Figure 4.17A). For 30364-hCD46, samples #1 and #6 showed faint bands of *CD46* compared to the positive control (Figure 4.17B). Considering the transgene expression on transcriptomic level (Figure 4.17C and D), again all samples of MOC2-hCD46 showed a signal originating from present RNA. For 30364-hCD46, however, I could not detect any PCR signal from amplified cDNA. The expression of the murine *Actb* gene encoding  $\beta$ -actin as a housekeeping control showed consistent expression across all samples (see Figure A23) ensuring absence of technical issues in the assay.

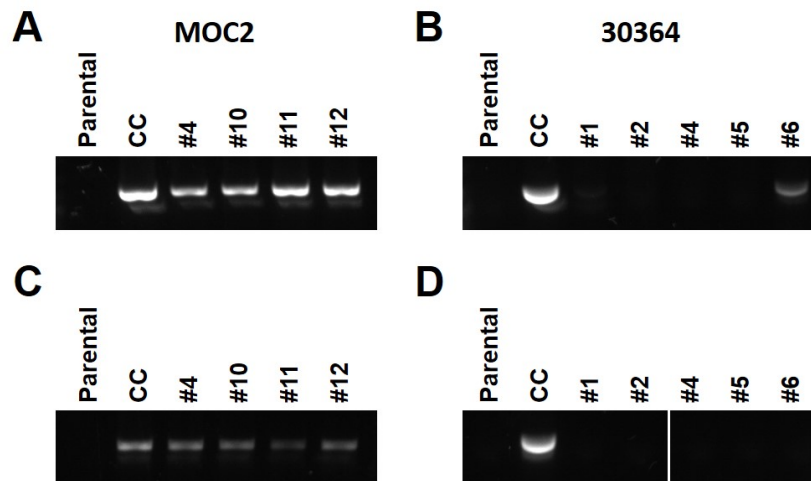


**Figure 4.17: Expression of *CD46* in murine tumors on genomic and transcriptomic level.** I isolated DNA and RNA from tumor samples of MOC2-hCD46 and 30364-hCD46 and performed cDNA synthesis to analyze expression of the human *CD46* gene on (A, B) genomic and (C, D) transcriptomic level by RT-PCR and gel electrophoresis. Expression of the housekeeping gene *Actb* as technical control is shown in Figure A23. Parental — non-transfected cells; CC — *in vitro* tumor cells from cell culture.

All in all, the *in vivo* characterization of both tumor models showed that MOC2-hCD46 stably expressed the viral entry receptor that is necessary for MeV infection of murine tumors. Therefore this tumor model was suitable for further *in vivo* investigations of RVTx. 30364-hCD46, however, did not show stable expression of the transgene and seemed to have lost the vector at the starting time point of possible tumor treatment. Therefore, I continued the *in vivo* work of this study using the MOC2-hCD46 model representing HNSCC.

The investigations of RVTx *in vivo* also aimed at exploring possible abscopal effects of the combination therapy. Therefore, the *in vivo* model characterization included the determination of a suitable cell number for implanting secondary tumors. According to the previous findings, I conducted this experiment only for MOC2-hCD46. I implanted  $5 \cdot 10^5$  cells s.c. into the left thigh of C57BL/6J mice to induce primary tumors. Two days after injecting this primary tumor, I injected cells into the right flank as secondary tumors. The mice were divided into three groups: the first group received the same number of cells as for the primary tumor ( $5 \cdot 10^5$  cells), the second group received half ( $2.5 \cdot 10^5$  cells) and the third group received one fifth of the primary tumor ( $1 \cdot 10^5$  cells). The aim was to determine a tumor cell number for secondary tumors that would guarantee consistent but delayed tumor growth compared to the primary tumor, mimicking metastatic growth. Over the course of 32 days, I monitored the size of both tumors. The mice reached experimental endpoint once the size of both tumors added up to a volume of  $1000 \text{ mm}^3$ . The tumor growth of secondary tumors depended on the tumor cell number, shown in Figure A24A and C (see Appendix), whereas primary tumors on the

thigh did not differ between the groups (Figure A24A, left and B). In group 1, that received the same number of MOC2-hCD46 cells in the flank as on the thigh, growth of the secondary tumor was comparable to the primary (Figure A24, black). Group 2 showed delayed growth of the secondary tumor in all mice (red). In group 3, only two out of six mice developed secondary tumors (blue). According to this data, the implantation of  $2.5 \cdot 10^5$  cells into the right flank would lead to optimal growth of primary as well as secondary tumors to analyze a possible abscopal effect of RVTx *in vivo*.

### 4.6 Evaluation of radiovirotherapy *in vivo*

The identification of different mechanisms of action of RVTx *in vitro* showed the potential of this combination therapy to induce an anti-tumor immune response. As a next step towards clinical translation, the evaluation of RVTx in immunocompetent murine models in terms of therapeutic efficacy was essential. After successful development and characterization of the HNSCC tumor model MOC2-hCD46, I analyzed the efficacy of radio- and virotherapy as monotherapies in order to determine a suitable treatment schedule for examining the combination therapy *in vivo*. Subsequently, I investigated RVTx efficacy in terms of survival and abscopal effects. Furthermore, I analyzed the induction of an anti-tumor immune response as well as key players driving innate and adaptive anti-tumor immunity.

#### 4.6.1 Efficacy of monotherapies

The analysis of radio- and virotherapy as monotherapies *in vivo* should contribute to establishing a schedule for treating tumor-bearing immunocompetent mice with RVTx. Therefore, I monitored tumor growth and survival of mice that received one of the treatment modalities either three or four times. As shown in Figure 4.18A, I implanted MOC2-hCD46 cells into the left thigh of C57BL/6J mice. Once the tumors reached an average volume of  $100 - 150 \text{ mm}^3$ , the treatment was initiated: the tumors were irradiated three or four times (5 Gy per session) or were injected i.t. with  $1 \cdot 10^6$  ciu MeVac on three or four consecutive days. Animals in the mock group received corresponding mock treatment (see 3.2.11.3).

The irradiation of murine tumors *in vivo* led to delayed tumor growth and prolongation of survival which was statistically significant, independent of the treatment schedule (Figure 4.18B and D). Individual tumor growth curves also showed a decrease in tumor volume after irradiation (see Figure A25A). For one mouse of the group receiving three doses of irradiation, I could observe complete tumor remission after treatment. For virotherapy alone, I could not observe an impact on tumor growth or survival (Figure 4.18C and E). The tumor growth of treated mice corresponded to the untreated group and there was no impact on survival

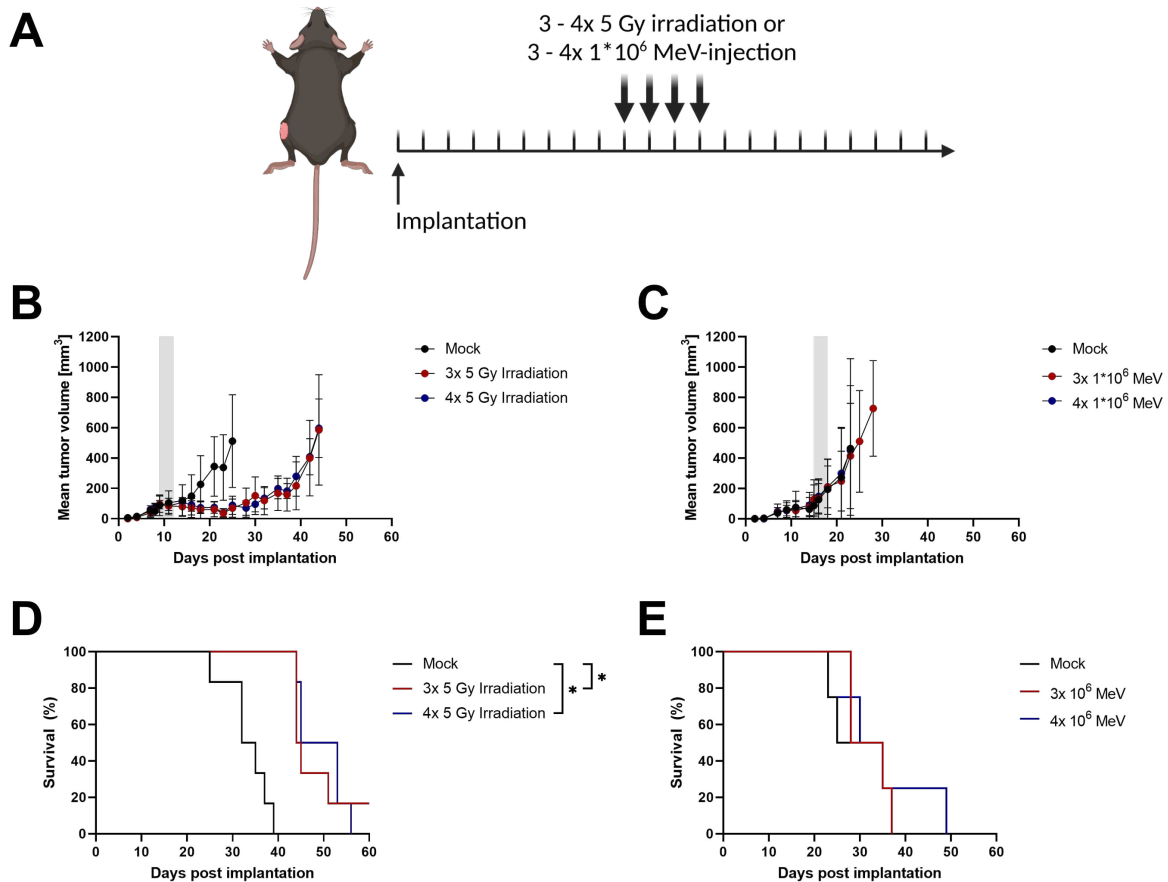


**Figure 4.18: Efficacy of radio- or virotherapy *in vivo*.** I analyzed both treatment modalities as monotherapies. (A) According to the treatment schedules, I implanted  $5 \cdot 10^5$  MOC2-hCD46 cells s.c. into the left thigh of C57BL/6J mice and treated with 3 or 4 doses of either 5 Gy irradiation (total irradiation dose of 15 or 20 Gy per mouse) or i.t. injections of  $1 \cdot 10^6$  ciu MeVac once the tumors reached mean tumor volumes of 100 – 150 mm<sup>3</sup>. I monitored tumor growth and survival after (B, D) radio- or (C, E) virotherapy to evaluate treatment efficacy. The mean tumor volume (B, C) of the group is shown until the first mouse was sacrificed. The grey area in tumor growth curves indicates the time frame of the corresponding treatment. I used Kaplan-Meier analysis and log rank (Mantel-Cox) test to assess survival data.  $p < 0.05$ : \*. The graphs show data of  $n = 6$  animals per group for radiotherapy and  $n = 4$  for virotherapy. The image in (A) was created with BioRender.com.

detectable. However, due to unequal tumor growth, only four animals per group reached inclusion criteria for this experiment (see Figure A25B).

According to the findings for radio- and virotherapy *in vivo*, I chose a treatment schedule for the combination therapy as follows: tumors on the left thigh of mice should be treated with three doses of 5 Gy irradiation (a total of 15 Gy per mouse) and three i.t. injections of  $1 \cdot 10^6$  ciu of MeVac on consecutive days, respectively. Referring to the *in vitro* treatment schedule R24V, I started the sequence of virus treatment one day after the first dose of irradiation (see Figure 4.19A).

### 4.6.2 Efficacy of combined radiovirotherapy

After examining the individual effects of radio- and virotherapy *in vivo*, I analyzed the efficacy of RVTx combination in terms of tumor growth and survival. Based on the results of preceding monotherapy experiments, I determined a suitable treatment schedule for RVTx *in vivo* (Figure 4.19A).

According to the previous evaluation of radiation efficacy *in vivo* (4.6.1), irradiation of MOC2-hCD46 tumors led to tumor growth delay and significant prolongation of survival compared to mock and virotherapy alone (Figure 4.19B and C). The latter showed minor improvement in both analyzed categories compared to mock. Mice receiving combination therapy showed similar tumor growth delay and prolongation of survival compared to the group receiving radiotherapy. The difference between each, radiation alone and combination treatment, compared to mock and virotherapy alone was statistically significant. Individual tumor growth curves showed again, that MeV delayed tumor growth only to a minor extent in the MOC2-hCD46 tumor model, whereas radiotherapy had a strong impact on

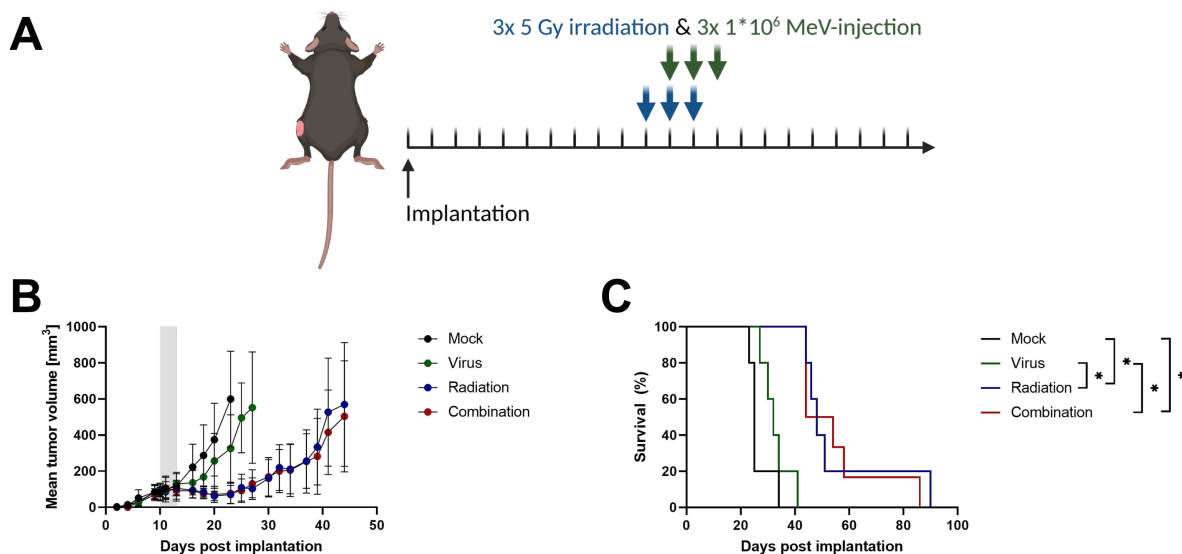


**Figure 4.19: Efficacy of radiovirotherapy *in vivo*.** (A) According to the treatment schedule, I implanted  $5 \cdot 10^5$  MOC2-hCD46 cells into the left thigh of C57BL/6J mice and treated with 3 doses of 5 Gy irradiation, 3 i.t. injections of  $1 \cdot 10^6$  ciu MeVac or the combination of both once the tumors reached average tumor volumes of  $100 - 150 \text{ mm}^3$ . I monitored (B) tumor growth and (C) survival after mock (black), monotherapies (blue, green) or RVTx treatment (red). The mean tumor volume (B) of the group is shown until the first mouse was sacrificed. The grey area in (B) indicates the time frame of the corresponding treatment. I used Kaplan-Meier analysis and log rank (Mantel-Cox) test to assess survival data.  $p < 0.05$ : \*. The graphs show data of  $n = 5$  animals per group for mock, radio- and virotherapy and  $n = 6$  for combination. The image in (A) was created with BioRender.com.

tumor growth kinetics as monotherapy as well as in combination with virotherapy (see Figure A26).

After analyzing the effect of RVTx on primary tumors, I aimed at investigating possible abscopal effects of the combination therapy as they have been described for both radiotherapy and virotherapy in general before [108, 202]. Therefore, I injected MOC2-hCD46 cells on the left thigh as well as two days later on the right flank of C57BL/6J mice using the previously determined cell number (see 4.5.2). I treated primary tumors with RVTx as described before (see Figure 4.19) and monitored tumor growth and survival. However, due to insufficient growth of MOC2-hCD46 tumors on the left thigh, I could only include four animals per treatment group. The primary tumors grew unequally and even some mock-treated animals lost the tumor over the course of the experiment (see Figure A27A). Further, I could not detect any difference in growth of secondary tumors on the flank (Figure A27B). The data of this experiment could not be evaluated and it remains to be determined whether RVTx can induce an abscopal anti-tumor response.

Nevertheless, the combination of radiation and oncolytic MeV showed significant tumor growth delay and prolongation of survival, which was mainly driven by irradiation. In order to extend the evaluation of RVTx *in vivo*, I investigated different factors of innate and adaptive immunity in the following.

### 4.6.3 Analysis of immune induction and infiltration

The efficacy of an anti-tumor therapy determines the survival outcome and is dependent on the tumor composition, direct anti-tumor toxicity as well as activation of intrinsic anti-tumor defense. As RVTx showed the potential to activate several innate immune pathways *in vitro*, that possibly trigger an immune response, I aimed at investigating multiple factors of anti-tumor response pathways *in vivo* at two different time points after RVTx treatment: a first time point focusing mainly on innate immunity and a second, late time point covering mainly factors of adaptive immunity. The experimental outline is shown in Figure 4.20. Two days after treatment, I analyzed the expression of target genes by quantitative PCR (qPCR): *Ifnb1* for activation of innate immune pathways and *Foxp3* as marker of immune regulation. The analysis of the second time point, nine days after treatment, focused on intratumoral levels of tumor-infiltrating lymphocytes (TILs) and certain cytokines for T cell activation or regulation by FC analysis, enzyme-linked immune absorbent spot (ELISpot) and ELISA.

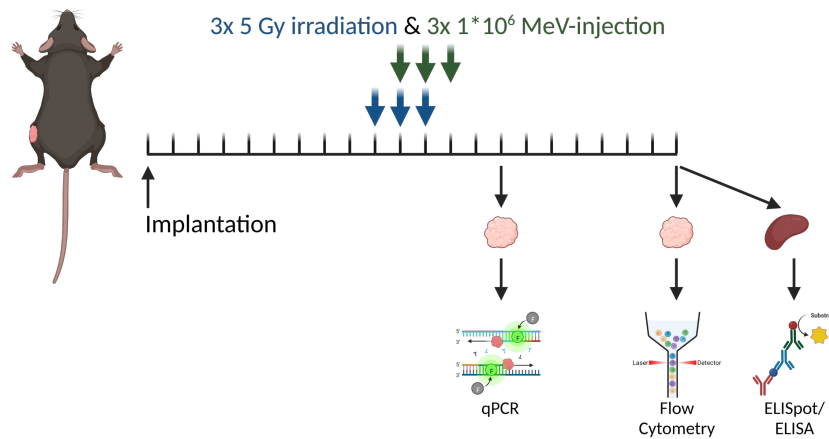


**Figure 4.20: Treatment overview for RVTx immune analysis.** To analyze the induction of an anti-tumor immune response by RVTx, I implanted  $5 \cdot 10^5$  MOC2-hCD46 cells into the left thigh of C57BL/6J mice. Once the developed tumors reached mean volumes of  $100 - 150 \text{ mm}^3$ , I treated them with 3 doses of 5 Gy irradiation, 3 i.t. injections of  $1 \cdot 10^6$  ciu MeVac or the combination of both, starting on day 9 post implantation. Two days after the last virus injection, I explanted tumors for analysis of several target genes on transcriptomic level by qPCR. Seven days later, I explanted tumors and spleens to analyze TILs by FC as well as secretion of several cytokines by ELISpot and ELISA. The image was created with BioRender.com.

The first part of the immune analysis of RVTx *in vivo* focused on transcriptional expression of target genes. Regarding the expression of the human *Ifnb1* gene and IFN- $\beta$  secretion *in vitro* shown before (see 4.4.2), I analyzed the expression of the murine gene via qPCR two days after final treatment of tumors with RVTx. Calculating  $\Delta\text{-C}_q$  values from IFN- $\beta$  and mean of both housekeeping genes, *Rpl13a* and *Actb* encoding L13a and  $\beta$ -actin, showed upregulation of *Ifnb1* expression in tumors treated with radiation alone or RVTx combination (Figure 4.21). The upregulation in irradiated tumors was statistically significant compared to tumors treated with MeVac alone. Consideration of  $\text{C}_q$  values from each analyzed gene (see Figure A28) showed that IFN- $\beta$  was also upregulated in the group treated with virotherapy alone compared to mock. The corresponding amplification and melting curves are shown in Figure A29. Virus treatment, however, seemed to upregulate metabolic activity of infected cells as both housekeeping genes, *Rpl13a* and *Actb*, showed decreased  $\text{C}_q$  values in this group compared to all other groups. Therefore, the relative expression of the *Ifnb1* gene for IFN- $\beta$  was only upregulated in mice receiving irradiation or RVTx.

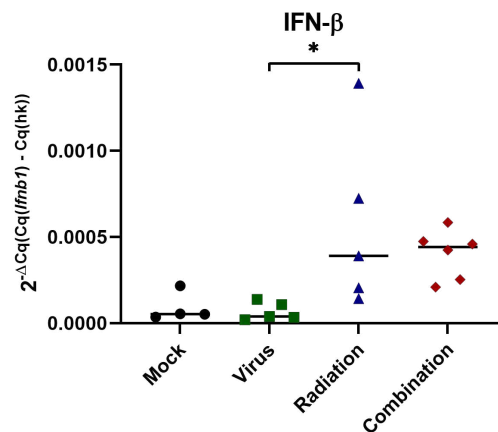


**Figure 4.21: *In vivo* expression of *Ifnb1* after RVTx.** To analyze innate immune activity, I investigated the expression of IFN- $\beta$  on transcriptomic level in tumors of animals two days after the final treatment. The treatment overview is shown in Figure 4.20. After RNA extraction and cDNA synthesis, I performed qPCR analysis of the *Ifnb1* gene. *Rpl13a* as well as *Actb* served as housekeeping controls. Statistical analysis was performed using one-way ANOVA with Tukey correction for multiple comparison testing.  $p < 0.05$ : \*. The graph shows mean data of technical replicates per mouse of  $n = 4$  animals per group for mock,  $n = 5$  for radio- as well as virotherapy and  $n = 6$  for combination. Cq — quantification cycle; hk — mean of housekeeping controls.

In the further immune analysis of RVTx *in vivo*, I focused on factors of adaptive immune responses and performed FC analysis of TILs, IFN- $\gamma$  ELISpot and several ELISAs to analyze cytokine release after co-culture of extracted splenocytes from treated mice with MOC2-hCD46 tumor cells from cell culture or MeVac virus solution (see Figure 4.20).

The FC analysis of treated MOC2-hCD46 tumors evaluated differences in TILs as mediators for an adaptive immune response *in vivo* (Figure 4.22). The corresponding gating strategy is shown in Figure A30. Whereas populations of lymphocytes and natural killer (NK) cells did not differ between the treatment groups, I detected a slight increase of non-lymphocytes, comprising CD45<sup>+</sup> leukocytes, such as dendritic cells (DCs), monocytes or granulocytes. Moreover, I observed a significant increase in the T cell population in RVTx-treated mice with on average 62.4% of CD3<sup>+</sup> cells in the leukocyte population compared to all other groups with CD3<sup>+</sup> T cell populations on average ranging between 21.3 and 41.5%. Discriminating the T cell population further, I detected a smaller population of CD4<sup>+</sup> T cells in tumors treated with radiation alone or RVTx combination with on average 36.6% and 24.1% CD4<sup>+</sup> lymphocytes of CD3<sup>+</sup> T cells. The difference between this smaller cell population in the RVTx-treated group compared to mock or virus treatment alone (on average 54.7% and 55% CD4<sup>+</sup> of CD3<sup>+</sup> T cells) was statistically significant. Considering CD8<sup>+</sup> T cells, I observed an opposite trend showing a larger population in irradiated and RVTx-treated tumors (on average 58.6% and 73.1% CD8<sup>+</sup> of CD3<sup>+</sup> T cells) compared to mock or virus alone (on

average 32.1% and 35.4%). Again, the difference between RVTx, mock or MeVac alone was statistically significant.

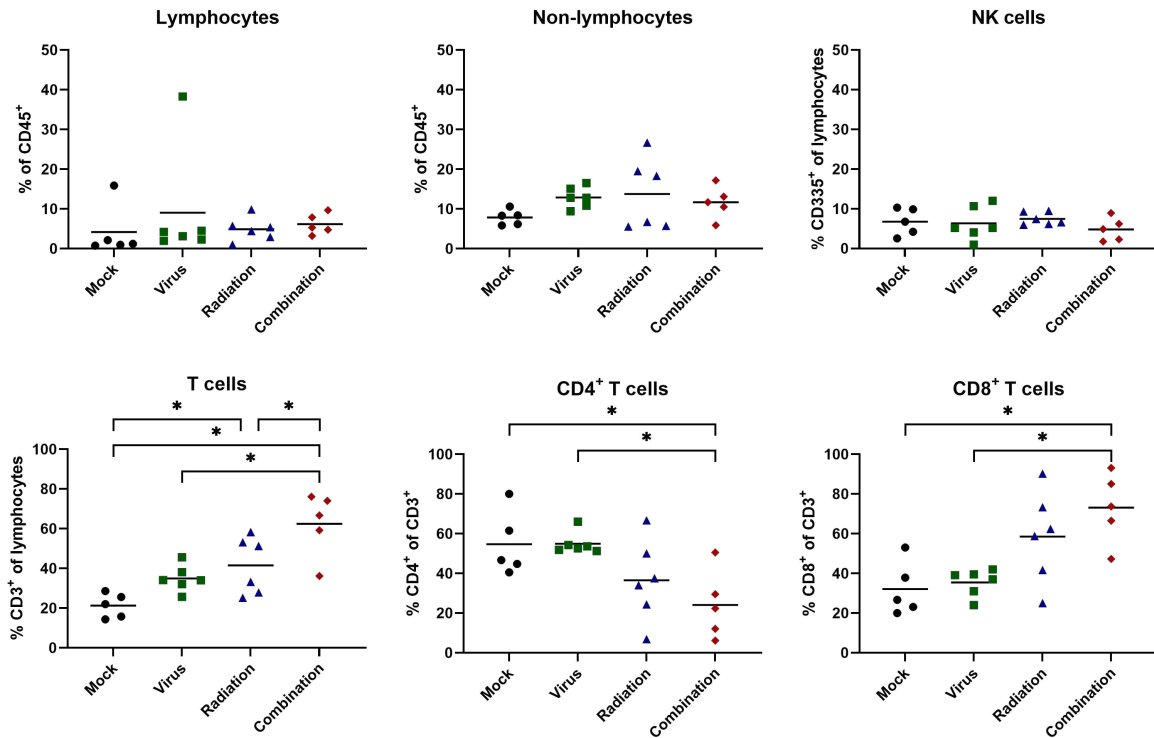


**Figure 4.22: Analysis of tumor-infiltrating lymphocytes in treated tumors.** After explanting MOC2-hCD46 tumors from C57BL/6J mice, I prepared single cell suspensions and performed antibody staining to analyze TILs by FC. The gating strategy is shown in Figure A30. Statistical analysis was performed using one-way ANOVA with Tukey correction for multiple comparison testing.  $p < 0.05$ : \*. The graphs show data of  $n = 5$  animals per group for mock and combination,  $n = 6$  for radio- as well as virotherapy.

To investigate early mechanisms for regulation of possible T cell responses, I assessed expression levels of the *Foxp3* gene encoding the regulatory protein forkhead box p3 (Foxp3) (see Figure A31). At this early time point after treatment, the relative expression of this target gene was not substantially altered in any group compared to mock. Cq values as well as amplification and melting curves (see Figure A28 and Figure A29) showed that signals from many samples were below the detection threshold given by no template and no reverse transcriptase controls. Therefore, it seemed that regulation of the T cell response by Foxp3 was not present at this early time point after RVTx treatment.

After detecting a significant increase of CD8<sup>+</sup> T cells after tumor treatment with RVTx, I investigated tumor- or virus-stimulated cytokine release by an adaptive anti-tumor and anti-viral immune response. Therefore, I co-cultured splenocytes from treated animals with MOC2-hCD46 tumor cells from cell culture or MeVac virus solution and performed IFN- $\gamma$

ELISpot and several ELISAs (see Figure 4.20 and 3.2.13.3).

Considering the detection of IFN- $\gamma$  release (Figure 4.23A), I observed only a small increase in co-cultures of splenocytes from mice of the RVTx treatment group with MOC2-hCD46 tumor cells from cell culture in the ELISpot assay. For virus-induced cytokine release, IFN- $\gamma$  secretion did not differ between groups measured by ELISpot (Figure 4.23B). However, it has to be considered that the detection of MeV antigen-specific IFN- $\gamma$  release in the ELISpot assay was insufficient as the used ELISpot reader was not suitable to detect the signal correctly due to signal saturation.

After performing ELISA from supernatants of the ELISpot assay, I could observe IFN- $\gamma$  release from splenocytes co-cultured with MeVac virus solution specifically from mice that received treatment including virotherapy (Figure 4.23B, right). Tumor-induced IFN- $\gamma$  release was only detectable from splenocytes of a few individual animals, but there was no trend visible for one specific treatment group. For interleukin (IL) 2, another T cell-activating cytokine, I detected a slight increase of cytokine release in response to tumor stimulation after combination therapy compared to mock or monotherapies (Figure 4.23C, left). The difference was statistically significant between the RVTx-treated group and mock as well as virus alone. MeV antigen-specific IL-2 release from splenocytes was strongly increased in virus- as well as RVTx-treated animals and was statistically significant compared to mock or radiation alone. The regulatory cytokine IL-10 was not secreted from splenocytes co-cultured with MOC2-hCD46 cells (Figure 4.23D, left). The signal was absent in all treatment groups. For MeV antigen-mediated secretion, however, I could detect increased levels of IL-10 in animals treated with virus or combination (Figure 4.23D, right). For the latter, the increase was statistically significant compared to mock or radiation alone.

All in all, I could observe an adaptive immune response after RVTx *in vivo* by increased levels of CD8<sup>+</sup> TILs. Further, virotherapy seemed to induce anti-viral responses associated with IFN- $\gamma$  and IL-2 release. Nine days after initial RVTx treatment, *de novo* challenge of splenocytes with MeV also induced secretion of IL-10.

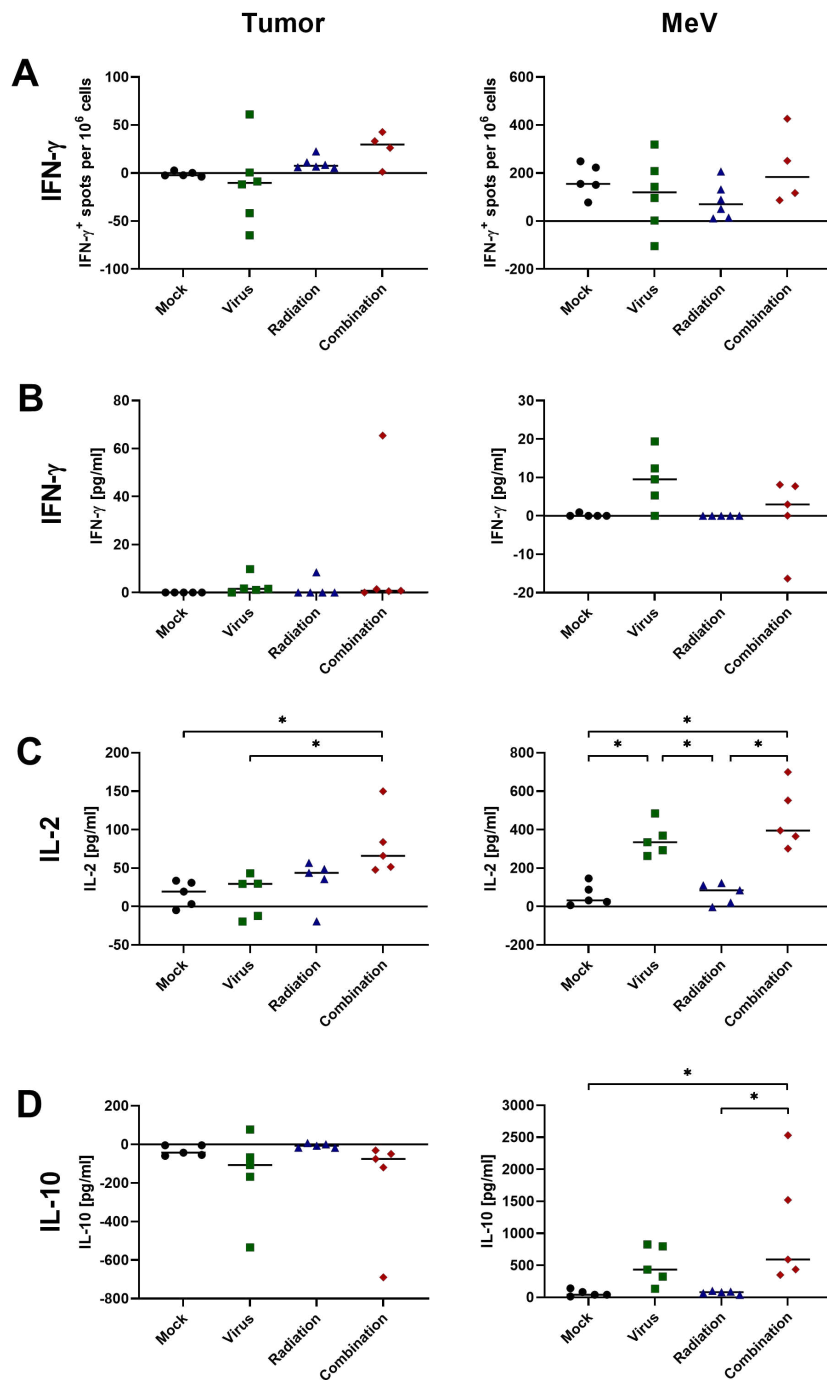


**Figure 4.23: Analysis of cytokine release after RVTx *in vivo*.** I investigated tumor- and virus-induced release of cytokines by splenocytes from RVTx-treated animals. After explanting spleens from tumor-bearing C57BL/6J mice, I prepared single cell suspensions and co-cultured splenocytes with MOC2-hCD46 tumor cells from cell culture or MeVac virus solution in plates coated with an IFN- $\gamma$  capture antibody. After 36 h incubation, I performed (A) an IFN- $\gamma$  ELISpot and used supernatants of co-cultures for ELISAs detecting (B) IFN- $\gamma$ , (C) IL-2 and (D) IL-10 cytokine release. Statistical analysis was performed using one-way ANOVA with Tukey correction for multiple comparison testing.  $p < 0.05$ : \*. The graphs show mean data of triplicate samples per mouse of  $n = 4 - 6$  animals per group normalized to medium only control.

## 4.7 Analysis of radiovirotherapy *ex vivo*

Besides the analysis and characterization of RVTx in cell culture and animal models, I also aimed at investigating the combination therapy in more clinically relevant, *ex vivo* tumor models. To this end, I chose two different models: a three-dimensional (3D) PDAC spheroid model and patient-derived PDAC cultures. I treated both models with RVTx according to the R24V schedule (see 3.2.5 and 4.2) and analyzed virus susceptibility, cell viability as well as induction of ICD and innate immune signaling.

### 4.7.1 Radiovirotherapy in a 3D PDAC spheroid model

A 3D spheroid provides the opportunity to study a therapy in a defined 3D structure *ex vivo*. In this project, I used a PDAC spheroid model generated by the hanging drop technique [249] comprising the human PDAC cell line AsAn-PaCa [221] and MRC-5 [225], a human lung fibroblast cell line. This enabled the investigation of a possible impact of fibroblasts in the surrounding tumor microenvironment (TME) on RVTx treatment.

First, I investigated virus susceptibility and morphological changes of PDAC spheroids after RVTx treatment. I irradiated and infected them according to the R24V schedule using MeVacId-EGFP at  $\text{MOI} = 0.3$ . Figure 4.24 shows morphology and infection of spheroids 72 h after treatment. Two aspects seemed to have changed in morphology after treatment: firstly, I could detect a decrease in overall size of the treated spheroids compared to mock (Figure 4.24, top left). Especially spheroids that received combination treatment showed a reduction in size (middle and bottom right). Secondly, the spheroid cells started to grow on the well-bottom and the compact 3D structure disintegrated faster for treated than untreated spheroids. Besides morphological changes, I could monitor viral infection in the 3D structure of the spheroid via GFP fluorescence in productively infected cells. I detected GFP<sup>+</sup> areas in several layers of the spheroid as well as infected cells in the surrounding, indicating viral spread over time. However, I did not observe differences between irradiated and non-irradiated samples by fluorescence microscopy.

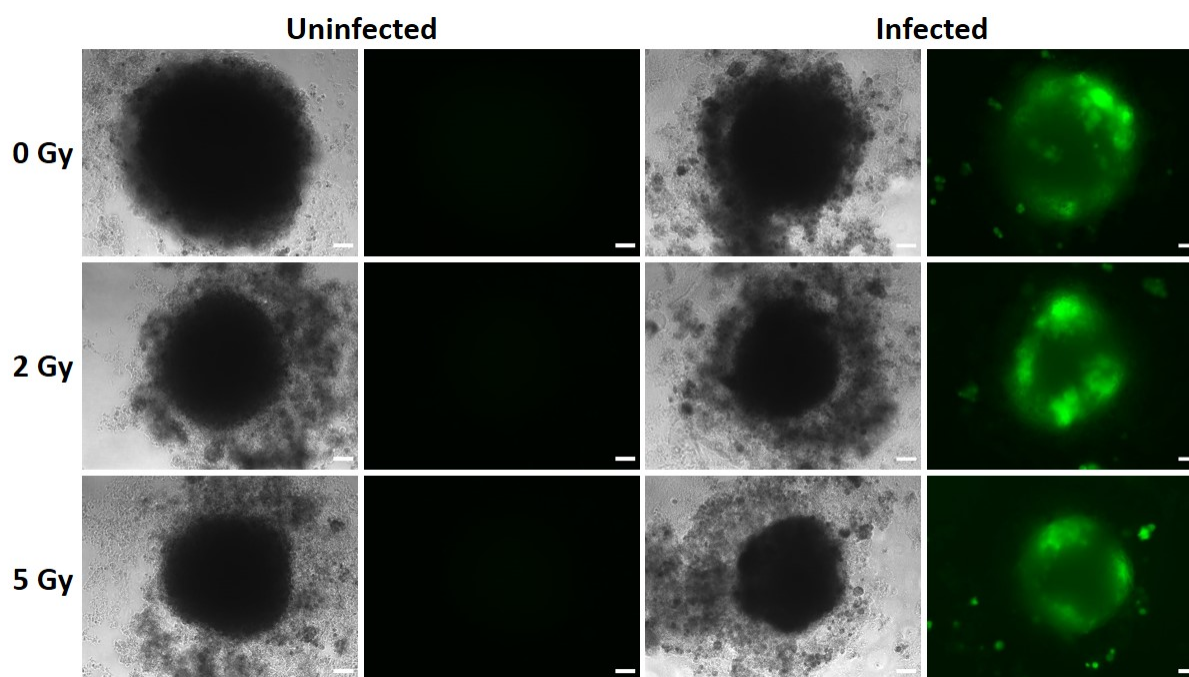


**Figure 4.24: RVTx treatment of 3D PDAC spheroids.** To investigate RVTx *ex vivo*, I used a 3D spheroid model of PDAC containing tumor cells as well as fibroblasts. Generated using the hanging drop technique, I irradiated spheroids with 2 or 5 Gy prior to infection with MeVac Id-EGFP at MOI = 0.3. Seventy-two hours p.tr., I analyzed virus susceptibility and changes in spheroid morphology via fluorescence microscopy. Images were taken in phase contrast and green fluorescence channel. The images show representatives of  $n = 3$  independent experiments. Scale bar: 100  $\mu\text{m}$ .

Furthermore, I investigated ICD induction after RVTx treatment of the PDAC spheroids. In a preliminary experiment, I pooled supernatants of treated spheroids 72 h p.tr. and performed an HMGB1 ELISA (Figure A32, see Appendix). Considering the overall low values of optical density (OD) in the assay, there were only minor changes visible between treated samples and mock control that were not statistically significant. However, there still seemed to be a trend towards increased HMGB1 levels in samples treated with the combination (C2, C5) compared to monotherapies.

#### 4.7.2 Radiovirotherapy treatment of patient-derived PDAC cultures

Besides 3D PDAC spheroids, I also used patient-derived primary cell cultures from PDAC patient tumors as a second *ex vivo* model to study the effects of RVTx. These cultures were established by Ehrenberg and colleagues via xenotransplantation to be used as *ex vivo* preclinical models to study PDAC [227]. I chose four different cultures that showed differences in virus susceptibility in previous work (Schaefer *et al.*, under review): the cultures were resistant, partly sensitive or very sensitive to MeV infection.

In a first experiment, I analyzed cell viability after RVTx treatment by XTT assay over a period of seven days after treatment using MeVac Id-EGFP at MOI = 1. Additionally, I observed viral infection over the same time period via fluorescence microscopy. The XTT assay revealed heterogeneity regarding responsiveness of the tested PDAC cultures to RVTx (Figure 4.25). The patient-derived culture PC1 (top left) showed strong sensitivity to virus and the reduction in cell viability of samples treated with the combination was mainly driven by MeV infection. I observed the opposite for PC28 (bottom left), as this culture seemed to be resistant to virus infection and the effect of RVTx was mainly due to irradiation. A third culture in this panel, PC43 (bottom right), seemed to be resistant to radiation as well as MeV infection, since cell viability was comparable to mock over the course of the experiment. Only PC3 (top right) showed intermediate sensitivity to both treatment modalities in monotherapies and further reduction in cell viability after combination treatment, pointing towards a synergistic effect of RVTx in this culture.

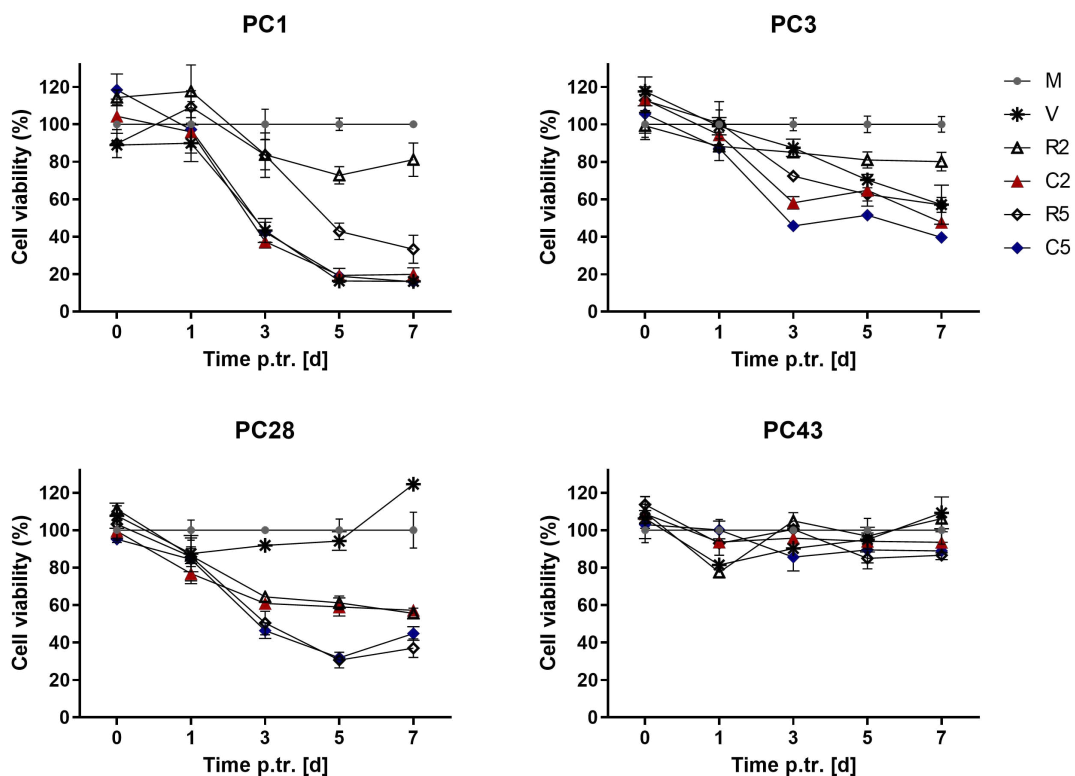


**Figure 4.25: Cell viability of patient-derived PDAC cultures after RVTx.** I treated PDAC cultures with RVTx according to the R24V schedule, irradiation (2 or 5 Gy) prior to infection with MeVac Id-EGFP (MOI = 1) and assessed cell viability over a period of seven days by XTT assay. The data was normalized to mock set at 100%. Mean and SD of technical triplicates are shown of one experiment. p.tr. — post treatment; d — days; M — mock; V — virus; R2, R5 — radiation with 2 or 5 Gy; C2, C5 — combination with 2 or 5 Gy irradiation.

In parallel to cell viability, I monitored virus infection of cells by fluorescence microscopy, shown in Figure A33. For PC1 and PC3, I observed productive infection as indicated by green fluorescent cells and syncytia formation in samples treated with MeVac ld-EGFP (V, C2, C5). Although PC1 showed stronger reduction of cell viability in response to infection (Figure 4.25), the green fluorescence signal was stronger in PC3. The PDAC culture PC28 did not show infected cells, confirming the results of the XTT assay. For PC43, I observed very few individual cells infected with MeV but no syncytia formation, again confirming the findings of the XTT assay that this culture is rather resistant to the applied treatment.

### 4.7.3 Induction of ICD and innate immune signaling in PDAC cultures

Following the findings of the cell viability analysis, I focused the *ex vivo* investigations of RVTx on the induction of ICD and innate immune signaling. As described for RVTx *in vitro* (4.3 and 4.4), I analyzed the release of HMGB1, surface expression of CALR, *IFNB1* gene expression as well as release of IFN- $\beta$ .

To detect HMGB1 release, I collected supernatants of PDAC cultures 72 h after treatment with RVTx or corresponding monotherapies and performed an ELISA. The baseline release of HMGB1 in mock-treated samples was very low in all tested cultures (Figure 4.26). The PDAC cultures that had been shown to be sensitive to virus before, PC1 and PC3, showed elevated levels of this ICD marker in samples that were infected with MeVac ld-EGFP. The differences between combination (C2, C5) and radiation alone (R2, R5) were statistically significant, whereas the overall level of released protein was almost six times higher for PC3 compared to PC1. For PC28 and PC43 that had been shown to be resistant to virus before, I detected lower levels of HMGB1 in the sample supernatant. However, conditions that include virus infection still led to higher, statistically significant, levels of HMGB1 release compared to samples not treated with MeV. For the radiosensitive culture PC28, irradiation seemed to mediate ICD induction as well. Although the overall level of HMGB1 release was low, I observed the highest level of released HMGB1 in RVTx-treated samples compared to the corresponding monotherapies.

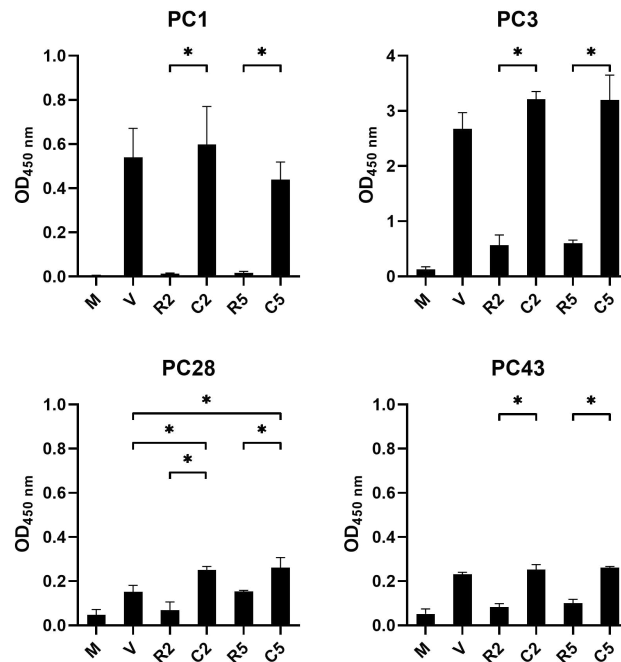


**Figure 4.26: HMGB1 release after RVTx *ex vivo*.** Patient-derived PDAC cultures were treated with RVTx. Seventy-two hours later, I collected supernatants and detected released HMGB1 by ELISA. Statistical analysis was performed using one-way ANOVA with Tukey correction for multiple comparison testing. The graphs show mean and SD of triplicate samples originating from one experiment.  $p < 0.05$ : \*; OD<sub>450 nm</sub> — optical density at 450 nm; M — mock; V — virus; R2, R5 — radiation with 2 or 5 Gy; C2, C5 — combination with 2 or 5 Gy irradiation.

In a next step, I analyzed the expression of surface-bound CALR by FC analysis as a second marker for ICD induction in two of the four PDAC cultures, PC3 and PC28 (see Figure A34). For the former, I could detect higher expression of CALR on cells treated with any RVTx combination (C2 or C5) compared to mock and monotherapies. For PC28, I did not observe differences or a specific trend in the CALR expression of cells from the different samples. This ICD marker did not seem to be induced by RVTx in this PDAC culture.

As a second part of the molecular and functional characterization of RVTx *ex vivo*, I investigated the induction of an innate immune response in terms of *IFNB1* expression on transcriptomic level as well as IFN- $\beta$  release. For the former, I observed highest expression of the *IFNB1* gene in all PDAC cultures treated with virus alone or RVTx (V, C2, C5) 24 h after treatment (Figure 4.27A). This result was in line with the findings *in vitro* (see 4.4.2). Interestingly, PDAC cultures PC28 and PC43, that seemed to be rather resistant to MeV infection, showed baseline expression of *IFNB1* as well as elevated levels of the transcript after being irradiated with 2 or 5 Gy (R2, R5).

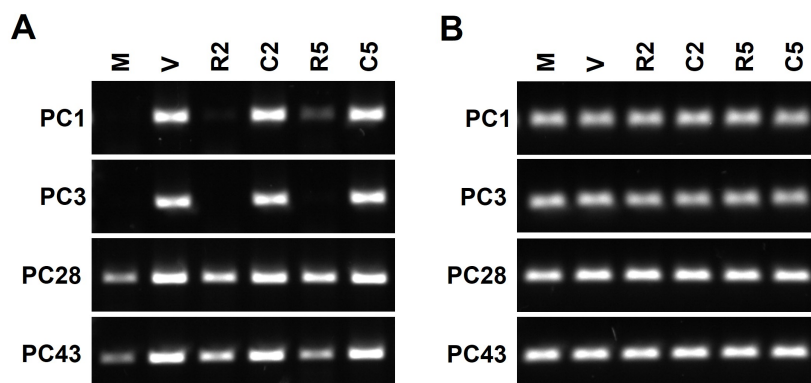


**Figure 4.27: Expression of *IFNB1* on transcriptomic level in PDAC cultures.** Twenty-four hours after treating patient-derived PDAC cultures with RVTx and corresponding monotherapies, I analyzed expression of (A) *IFNB1* encoding IFN- $\beta$  and (B) *ACTB* encoding  $\beta$ -actin via RT-PCR followed by gel electrophoresis. The images show data of a single experiment. M — mock; V — virus; R2, R5 — radiation with 2 or 5 Gy; C2, C5 — combination with 2 or 5 Gy irradiation; CC — cell culture control.

Further, I investigated IFN- $\beta$  release 24 h p.tr. by ELISA (see Figure A35). While I detected *IFNB1* transcript not only in virus-infected samples of the analyzed PDAC cultures but also to some extent in irradiated samples, the released cytokine was only present in samples that were infected with MeVac Id-EGFP. Moreover, the cultures showed differences in the concentration of released IFN- $\beta$ . Indicated by the low OD value, PC3 and PC28 showed only low cytokine levels. PC43 showed higher IFN- $\beta$  release. For the virus sensitive culture PC1, I measured higher IFN- $\beta$  levels as indicated by OD values in the analyzed supernatants compared to PC3 or PC43.

All in all, I observed an impact of RVTx treatment in patient-derived PDAC cultures in terms of cell viability as well as induction of ICD and innate immune signaling. The heterogeneity of the analyzed cultures was not only apparent with regards to the sensitivity to both treatment modalities of RVTx. I could also observe heterogeneity in the analyzed downstream effects of ICD induction and innate immune activation. Thus, the efficacy of RVTx treatment may be patient-specific and would require a personalized approach encompassing patient-specific biomarkers when applied in the clinical context.

# 5 Discussion

## 5.1 Perspectives of radiovirotherapy

Radiovirotherapy (RVTx) combines two promising treatment modalities for cancer therapy: radio- and virotherapy. Radiotherapy, i.e. applying ionizing radiation for induction of tumor cell damage, has been among the ‘pillars of cancer therapy’ for decades and belongs to the standard-of-care treatment plan for many tumor entities. It is used in cancer therapy with curative intent as well as in palliative care [8, 93, 113]. Virotherapy is still rather new in the clinical landscape of cancer therapy, although research has been going on since decades [164]. Nevertheless, several preclinical and clinical studies have shown the potential of oncolytic viruses in the context of cancer treatment [192, 210, 250]. The greatest success so far was the approval of the oncolytic herpes simplex virus (HSV) talimogene laherparepvec (T-VEC) by the U.S. Food and Drug Administration (FDA) and European Medicines Agency (EMA) in 2015 for the treatment of non-resectable metastatic melanoma [194].

Both treatment modalities feature beneficial characteristics for combined application as RVTx, especially through the induction of an anti-tumor immune response via innate immune sensing or induction of immunogenic cell death (ICD) [57, 106, 166, 189]. Furthermore, radio- as well as virotherapy are able to promote anti-tumor effects of the respective other treatment modality [213]. Although several studies showed that irradiation did not lead to increased expression of the respective viral receptor, it was shown to enhance viral replication in target tumor cells [217, 218, 251, 252]. Further, irradiation can induce the upregulation of viral as well as transgene expression and improve the therapeutic efficacy [217, 252, 253, 254]. Vice versa, oncolytic viruses can interfere with DNA damage signaling pathways by interacting with cellular factors that are involved in DNA damage repair or cell cycle progression and drive the cells into apoptosis [213, 255]. Therefore, they may act as radiosensitizing agents.

Oncolytic measles virus (MeV) vaccines have shown safety and efficacy in several preclinical studies and early clinical trials [165, 166]. In many of these investigations, a vaccine strain MeV encoding the sodium-iodine symporter (NIS) was employed. Expression of virally delivered NIS enables uptake of systemically administered radioiodine isotopes and therefore allows real-time non-invasive monitoring of viral infection. Further, this combination also showed

therapeutic effects as radioiodine plus MeV-NIS led to tumor regression and local bystander effects [199, 256, 257]. In current clinical phase I and II studies, MeV-NIS is combined with chemotherapy or immune checkpoint inhibition while the NIS transgene is used for virus monitoring [165, 167]. In preclinical studies, the combination of MeV with external beam radiotherapy (EBRT) as RVTx showed synergistic anti-tumor effects in glioblastoma and prostate carcinoma cells as well as tumor regression and prolonged survival in respective xenograft models [217, 218]. A triple combination of chemo-, viro- and radiotherapy showed synergistic effects in glioblastoma as well as initiation of a type I interferon (IFN) response and expression of downstream interferon stimulated genes (ISGs) by RNA sequencing *in vitro* [220]. The evaluation of suitable treatment conditions for RVTx considering synergistic and cytotoxic effects combined as well as the induction of an anti-tumor immune response in immunocompetent models *in vivo* has not been investigated so far, especially not for head and neck squamous cell carcinoma (HNSCC) and pancreatic ductal adenocarcinoma (PDAC) [167].

This study focused on the investigation of RVTx using EBRT and an unmodified or eGFP-encoding MeV vaccine strain in HNSCC and PDAC models. A systematic evaluation of different treatment conditions that considered synergy as well as cytotoxic effects was conducted. This yielded a suitable treatment schedule for *in vitro* or *ex vivo* studies of RVTx. The induction of ICD and innate immune responses had been demonstrated for both treatment modalities before but not for combined RVTx [73, 106, 189, 248]. I investigated several ICD markers and factors for innate immune sensing and activation to define possible mechanisms of action of RVTx, both in established cell cultures of the tumor entities *in vitro* as well as in patient-derived tumor models *ex vivo*. To assess the possible activation of an adaptive immune response *in vivo*, I generated syngeneic immunocompetent murine tumor cell lines expressing the human *CD46* gene to enable viral entry into murine tumor cells. The pilot study analyzing the therapeutic efficacy of RVTx *in vivo* covered the analysis of survival after RVTx treatment, a characterization of tumor-infiltrating lymphocytes (TILs) as well as inflammatory cytokines in co-culture experiments. In the following, I will discuss the synergistic effect and the activation of anti-tumor immune responses by RVTx as well as the suitability of preclinical models and will review the translational potential of this combination therapy.

## 5.2 Synergistic effects of radiovirotherapy

The combination of radiotherapy applied as EBRT and virotherapy using different oncolytic viruses such as MeV, vaccinia virus, adenovirus, reovirus or HSV has been studied preclinically in several tumor entities including brain, prostate, pancreas or head and neck cancer [214,

217, 218, 219, 220, 258, 259, 260, 261, 262, 263, 264, 265]. The efficacy of a combination therapy was determined either based on cytotoxicity or on the synergistic effect of a treatment condition. The respective candidate tumor cell lines were treated with a single dose of irradiation as well as virus in varying order. For the analysis of cytotoxicity or cell viability after RVTx treatment, the aforementioned studies mainly applied 3-(4,5-dimethylthiazol-2-yl)-2,5-diphenyltetrazolium bromide (MTT) assay [258, 260, 261, 263, 265] or lactate dehydrogenase (LDH) release assay [214, 219, 259, 262]. The assays are based on either measuring the metabolic activity of live cells or the amount of cytosolic enzyme released upon cell lysis. Some studies also measured the proliferative capacity of treated tumor cells by clonogenic assay [217, 264].

In the present project, I also applied the RVTx combination only once with varying doses of irradiation or MeV to the candidate cell lines of PDAC and HNSCC – BxPC-3, T3M4, HNO210 and HNO410 – and measured cell viability over the course of seven days post treatment (p.tr.). I observed that treatment conditions applying low doses of RVTx showed only minor effects on cell viability whereas high doses of irradiation and MeV led to strong cell killing, leading to death of almost all cells at the end of the experiment. Intermediate doses led to a reduction of cell viability, which was stronger in the combination compared to both modalities applied as monotherapies but cell viability never reached 0%. Although combining high doses of radiation and MeV showed the highest cytotoxicity, the resulting off-target toxicity might be too strong when translated to the clinical setting. Lower doses may be superior for inducing anti-tumor immunity as I hypothesized in this study for the RVTx combination. In fact, Vanpouille-Box and colleagues showed that the application of high radiation doses led to the induction of a DNA exonuclease that would degrade cytosolic DNA and therefore attenuate radiation-induced immunogenicity by downregulating the DNA damage sensor cyclic GMP-AMP synthase (cGAS) and the downstream pathway leading to secretion of IFN- $\beta$  [244, 245]. Therefore, the combination of intermediate doses of both treatment modalities was deemed more suitable for further experiments.

The evaluation of potential synergistic effects of an RVTx combination was considered in some of the above mentioned studies and was based on measuring cell viability. The determination of synergy, additivity or antagonism was often performed by dose-response curve analysis with the calculation of a combination index (CI) for each treatment condition by the median effect method of Chou and Talalay [214, 217, 220, 242, 265]. Other analyses used the isobologram method based on the IC<sub>50</sub> value, defined as the concentration of drugs that produce 50% cytotoxicity [258, 260, 266].

Strikingly, the measurement of cytotoxicity as well as the determination of synergy was performed in most studies only at one specific time point at the end of the experiment. However, an aspect that was not addressed in the aforementioned studies was the possibility

of cell regrowth in the performed *in vitro* experiments. In this project, I observed an increase in viability at later experimental time points when observing cell viability over seven days after RVTx treatment (see Figure 4.5). A single dose of both treatment modalities might not be sufficient to eradicate the entire treated cell population and the remaining cells had started to grow again. A fractionated combination therapy, applying several doses of irradiation and MeV, would possibly suppress cell growth at this point. Importantly, in light of this relevant finding, it was necessary to consider the progression of cell viability also in the evaluation of synergy. Therefore, I calculated the CI values of all tested treatment conditions at three consecutive experimental time points, 3, 5 and 7 days p.tr., using the CompuSyn software applying the median effect method to determine synergy, additivity or antagonism. I observed that some treatment conditions showed synergy at just one experimental time point whereas other conditions showed synergy on all days, especially the combination of intermediate and high doses of RVTx (see Figure 4.7 and Figure A9).

The determination of the *in vitro* efficacy of a specific treatment combination in the aforementioned studies was usually either based on cell viability data or on the calculated synergistic effect. Both aspects were never considered equally. In regard of the above mentioned findings in cell viability and synergy analyses in this project, I developed a scoring system to assess the tested treatment conditions in consideration of specific categories that would evaluate both results: the synergy of a specific combination as well as the cytotoxicity of a combination and the corresponding monotherapies (see Table 4.1). This scoring system of RVTx treatment conditions resulted in a clear preference towards intermediate treatment conditions of combining 2 or 5 Gy irradiation with a cell line-specific intermediate dose of MeV. The high cytotoxicity of treatment conditions with high doses of irradiation and MeV was put into perspective of the applied scoring system. Thus, the results of the scoring indicated that the intermediate dose were the most beneficial treatment regimens.

All in all, the systematic analysis of RVTx treatment conditions evaluated both, cytotoxicity and synergy, on several experimental time points and considered both equally to determine a suitable treatment schedule for investigating possible underlying mechanisms of action of RVTx *in vitro* and *ex vivo*.

The treatment schedule of RVTx was first evaluated in established cell lines, followed by an analysis in *ex vivo* patient-derived PDAC cultures. The result showed a strong heterogeneity between the four tested cultures (see Figure 4.25). Only one culture showed increased reduction of cell viability after the combination treatment compared to monotherapies. The other cultures were resistant to one or even both treatment modalities. This result might serve as a good representation for present heterogeneity among tumor patients and the varying response to an applied anti-tumor treatment. The translation of *in vitro* experiments using well-established and stably-growing tumor cell lines to patient-derived

models and even extrapolated to the clinical setting will therefore have to be handled with caution.

## 5.3 Activation of anti-tumor immune responses

Immunotherapy is the ‘fourth pillar’ of contemporary cancer therapies [8]. The aim of many current preclinical and clinical studies is the activation of the host immune system to mediate a sustained anti-tumor immune response. A variety of pathways and markers have been described as targets to achieve this aim. In this study, I hypothesized that RVTx would induce an anti-tumor immune response and focused the identification of possible mechanisms of action on ICD, innate immune signaling as well as the activation of an adaptive immune response investigating several models *in vitro*, *in vivo* and *ex vivo*.

### 5.3.1 Induction of immunogenic cell death

Immunogenic cell death (ICD) is described as a specific type of apoptotic cell death that is characterized by the exposure of danger-associated molecular patterns (DAMPs) [267]. Among these DAMPs are calreticulin (CALR), ATP and high mobility group box 1 (HMGB1) which represent the most common markers of ICD [72, 73]. In the context of cancer, relocation or release of these molecules lead to activation and maturation of dendritic cells (DCs) and further to induction of a T cell-mediated anti-tumor immune response [267, 268].

Radiotherapy as well as virotherapy have been shown to induce ICD. Ionizing radiation has been shown to trigger HMGB1 release as well as relocation of CALR to the cell surface in tumor cells *in vitro* and in established tumors in immunocompetent mice [269, 270, 271]. This was associated with cross-presentation of tumor antigens to CD4<sup>+</sup> and CD8<sup>+</sup> T cells and subsequent immune activation *in vivo* [85]. Additionally, radiotherapy can induce autophagy [101]. This mechanism is required for ATP release and mediates the induction of this mode of ICD in irradiated mammary and prostate carcinoma cells [79, 272, 273]. Several studies have demonstrated the induction of ICD by oncolytic viruses. Treatment of melanoma cells with T-VEC leads to release of HMGB1 and ATP as well as CALR translocation *in vitro* [274]. MeV promotes ICD in melanoma as well as hepatocellular carcinoma cells by release of HMGB1 and ATP [189, 190]. Further, the oncolytic parvovirus H1-PV induces ICD by HMGB1 release in several PDAC cell lines *in vitro* [275].

The induction of ICD in combined RVTx treatment has not been investigated so far. In this study, I analyzed the relocation and release of CALR, ATP and HMGB1 in different candidate tumor cell lines of PDAC and HNSCC *in vitro* as well as patient-derived PDAC

cultures *ex vivo*. I treated the cells with RVTx using 2 or 5 Gy radiation doses combined with a respective intermediate dose of MeV.

I could detect surface-exposed CALR after RVTx on all candidate cell lines by flow cytometry (FC) analysis *in vitro*. Although the percentage of CALR<sup>+</sup> cells only ranged between approx. 5 to 15% of viable cells at 48 h p.tr., there was a distinct difference between RVTx-treated cells and cells that were only irradiated or infected (see Figure 4.10). The difference was statistically significant in the HNSCC cell lines HNO210 and HNO410. Especially the latter showed strong upregulation of surface-CALR after RVTx with 5 Gy radiation dose. Visualization of this ICD marker by immunofluorescence (IF) staining confirmed the upregulation of CALR on the surface of HNO410 cells treated with RVTx with 5 Gy irradiation (see Figure 4.11). Interestingly, virus-infected cells, detectable via GFP encoded by the applied MeVac Id-eGFP virus, hardly showed CALR on their surface as detected via FC analysis and IF stainings. There were hardly any double-positive cells detectable in the cell population. A double-positive population was only detectable among dead cells. However, it is very likely that the CALR signal of dead cells originated from intracellular staining of this marker. Measles virus is known to alter the host cell metabolism and circumvent the interferon response in favor of viral replication [133, 276]. It seems that the viral infection impaired or suppressed the exposure of CALR to circumvent induction of ICD. This phenomenon has not yet been described in literature. The above mentioned studies used unmodified MeV expressing no marker such as GFP for the detection of viral infection or did not investigate CALR expression [189, 190]. Thus, a distinction between infected and non-infected cells was not possible in the cell population that was analyzed for CALR exposure in those studies. Nevertheless, I detected cells expressing CALR on their surface in the surroundings of virus-infected, GFP<sup>+</sup> cells. It seems that MeV infection had a bystander effect of inducing ICD in neighboring, uninfected cells (see Figure 4.11). It remains to be investigated whether the surface exposure of CALR in these cells was actually mediated by MeV infection or rather due to irradiation. In the *ex vivo* patient-derived PDAC cultures, I could investigate CALR relocation only in two of the four cultures due to difficulties with culturing this *ex vivo* model. PC3, the PDAC culture that showed higher cytotoxicity after combination therapy compared to monotherapies showed strong expression of CALR on the cell surface after RVTx compared to monotherapies or mock control (see Figure A34). In PC28 cells, which were rather resistant to treatment, I could not observe changes among the different conditions. Again, the heterogeneity in treatment response among different tumors was also visible here.

Compared to previous studies of ICD induction after virotherapy showing ATP release, I could not detect this ICD marker after RVTx *in vitro*. In the course of trouble-shooting for this experiment, I tested several commercially available products for detection of ATP levels in luminescence-based assays. The same products were used in previous studies to

measure extracellular levels of ATP in the context of ICD induction [190, 274, 275]. However, I did not obtain reproducible data on released ATP using these products neither after RVTx treatment nor after application of known ICD inducers such as doxorubicin or mitoxantrone [66]. It has to be considered, though, that the majority of ATP-detecting assays are designed for the detection of intracellular ATP levels. These are of course manifold higher than the extracellular levels and ATP may be released, but the levels may be below the detection limit of current assays.

The detection of HMGB1 release as the third ICD marker tested in this study was successful in all candidate tumor cell lines *in vitro* and cultures *ex vivo*. I detected an increase of HMGB1 in supernatants of RVTx treated cells compared to monotherapy or mock in all tested human tumor cell lines of PDAC and HNSCC (see Figure 4.9). Except for T3M4, the increase was statistically significant. This PDAC cell line, though, showed high HMGB1 release already in mock-treated samples compared to the other candidate tumor cell lines and a strong trend towards even more elevated HMGB1 release after RVTx was detectable. The patient-derived PDAC cultures showed a clear virus-mediated HMGB1 release after virotherapy or RVTx (see Figure 4.26). Although the amount of released HMGB1 differed between the cultures, the difference between RVTx treatment and irradiation alone was statistically significant in all cultures. HMGB1 plays an important role in the nucleus of eukaryotic cells, stabilizing the nucleosome and maintaining genome stability [82, 83]. As an ICD marker, it plays an important role in the maturation of DCs and the following cross-presentation of tumor antigens to T cells [277, 278].

Therefore, the robust expression of HMGB1 as an ICD marker after combination treatment in all cell lines *in vitro* and patient-derived tumor cultures *ex vivo* might indicate HMGB1 release as a key component for possible induction of an anti-tumor immune response by RVTx. This might be accompanied by surface exposure of CALR and further attraction of DCs to the tumor site especially in HNSCC tumors.

### 5.3.2 Activation of innate immune signaling pathways

Factors of the innate immune system represent the first line of defense against external as well as internal threats. Different immune sensing pathways that are specialized to detect possible invading microorganisms or dangerous substances enable the activation of a rapid innate immune response followed by the induction of a specific adaptive immune response [50]. In case of RVTx, certain cellular sensing mechanisms are relevant to detect DNA damage induced by ionizing radiation as well as viral entry: cGAS and retinoic acid-inducible gene I (RIG-I). Upon damage of the DNA by irradiation in form of double-strand breaks, DNA fragments translocate to the cytosol and are sensed by cGAS [55]. This protein in turn

activates a signaling cascade involving stimulator of interferon genes (STING) that leads to expression of the *IFNB1* gene and further secretion of IFN- $\beta$  for activation and maturation of DCs as well as a downstream activation of an adaptive immune response [51, 58, 59]. RIG-I is a cytosolic sensor protein for single or double-stranded 5'-triphosphorylated RNA mainly originating from viruses harboring an RNA genome such as measles virus [279]. Upon sensing viral RNA in the cytosol, RIG-I activates a downstream signaling pathway that also leads to expression and secretion of IFN- $\beta$  inducing an immune response mediated by DCs and other antigen-presenting cells (APCs) [54, 63].

Previous preclinical studies have shown that the activation of the cGAS-STING signaling pathway in tumor cells is essential for inducing an anti-tumor immune response mediated by IFN- $\beta$  secretion [280, 281]. The detection of cGAS and STING expression in this study, however, did not indicate an activation of this signaling pathway through RVTx. On the western blot (WB) membrane, the cGAS protein was hardly detectable and there were no changes visible between the different treatment modalities. A single dose of 2 or 5 Gy irradiation might not be enough to induce cGAS expression. STING on the other hand was stably expressed in BxPC-3, HNO210 and HNO410 cells independent of the applied treatment. In T3M4 cells, I could not detect STING although the *STING1* gene could be detected on genomic level in all cell lines (Schlue, unpublished). Suter and colleagues showed that cGAS-STING signaling can be suppressed by the janus kinase 2 (JAK2)-signal transducer and activator of transcription (STAT3) pathway in prostate cancer cells that fail to induce type I IFN expression triggered with cyclic guanosine monophosphate-adenosine monophosphate (cGAMP) or IFN stimulating DNA [282]. Potentially, this could also be the case in the candidate tumor cell lines tested in this study and remains to be investigated.

As mentioned above, RIG-I is described in literature as a sensor for viral RNA [61, 62]. Upon viral infection of the candidate tumor cells in this study, I detected RIG-I protein in all cell samples that received virus alone or RVTx combination. Irradiation did not seem to induce RIG-I by itself or downregulate the virus-induced protein expression in the combination treatment. Therefore, RVTx led to robust RIG-I signaling *in vitro*.

The induction of type I IFN signaling as well as cytokine release is a well-known downstream effect of cGAS-STING as well as RIG-I signaling [53, 54]. Besides the presentation of tumor-antigens, the expression of IFN- $\beta$  is a major factor for activation and maturation of DCs mediating the downstream activation of the adaptive immune system. Tumor cell-mediated IFN- $\beta$  release is therefore a major driver of anti-tumor directed immune responses [63]. In the context of viral infection, type I IFNs have shown to induce selective apoptosis in infected cells [283]. Type I IFNs also regulate the transcription of many downstream genes, ISGs, such as the chemokine C-X-C motif chemokine ligand 10 (CXCL-10) or the antiviral protein myxovirus resistance 1 (MX1) [284]. In the context of cancer therapy, a higher expression of ISGs is often

associated with improved patient outcome and survival [285]. The use of recombinant type I IFNs as a stand-alone systemic anti-tumor immunotherapy against melanoma was the first approved human immunotherapeutic agent [63, 285]. However, toxicities and adverse effects limited the direct administration of recombinant type I IFNs as cancer immunotherapy [286]. Nowadays, recombinant type I IFNs are administered in combination with other therapeutic agents such as oncolytic viruses, immune checkpoint blockade (ICB) or chemotherapy [63]. Alternatively, anti-cancer therapies are applied that specifically induce the production of type I IFNs in tumor cells. Both, radio- and virotherapy have been shown to induce a type I IFN-mediated immune response in cancer therapy [248, 287].

In this study, I detected elevated levels of released IFN- $\beta$  in treated HNO210 or HNO410 cells. This was mainly mediated by viral infection and the differences of RVTx combination to irradiation alone were statistically significant (see Figure 4.13). The PDAC cell lines BxPC-3 and T3M4, however, did not show cytokine release although I detected expression of the *IFNB1* gene in treated cells. As mentioned above, T3M4 cells did not show expression of STING protein, however, both PDAC cell lines should nevertheless be able to induce IFN- $\beta$  release via RIG-I signaling as both showed virus-mediated upregulation of RIG-I protein expression. It remains to be determined whether the deficiency in IFN- $\beta$  release was due to impaired release mechanisms or cytokine production. Investigations of the *IFNB1* gene expression and cytokine release upon RVTx treatment of patient-derived PDAC cultures showed virus-mediated *IFNB1* induction as well as IFN- $\beta$  release. This might point to a functional RIG-I signaling pathway and induction of an anti-viral immune response after RVTx treatment of this *ex vivo* model. Interestingly, investigating *Ifnb1* gene expression in RVTx-treated murine MOC2-hCD46 tumors showed upregulation of *Ifnb1* after combination as well as radiotherapy (see Figure 4.21). It seemed that two days after tumor treatment with RVTx, radiation-induced IFN- $\beta$  expression, possibly induced via cGAS-STING signaling, was activated *in vivo*, presumably due to the administration of several radiation doses or by non-tumor cells in the surrounding. Thus, although I did not detect radiation-induced IFN- $\beta$  expression *in vitro* or *ex vivo* after single-dose irradiation of cells and cultures, RVTx might still be able to activate the cGAS-STING axis and induce a radiation-mediated activation of type I IFN signaling.

In general, type I IFN signaling can be viewed as a double-edged sword. Especially in the context of virotherapy and RVTx, the induction of type I IFN signaling might lead to an anti-tumor immune response, boosting the effect of the combination therapy on the one hand. On the other hand, it might also lead to a strong anti-viral immune response that would dampen the oncolytic effect of virotherapy [248]. However, the benefits of MeV treatment may lie beyond direct oncolytic effects. MeV infection did not have an impact on cell viability after treatment in tumors that only allow low levels of viral infection, as it was seen for the murine

tumor model MOC2-hCD46 (see Figure 4.14), or even seem to be virus resistant, as the PDAC patient-derived cultures PC28 and PC43 (see Figure 4.25). However, MeV infection might serve as an adjuvant attracting DCs to the tumor site in the course of an anti-viral response. In this way, tumor antigens might be recognized leading to the desired anti-tumor immune response. Secondly, the induction of an anti-viral immune response might serve as an important safety mechanism for virotherapy. It may ensure systemic viral clearance, preventing unwanted toxicity and side effects in the clinical setting.

Further, even if an anti-viral response would not lead to activation of an anti-tumor immune response, the RVTx combination features the advantage of a second treatment modality. Radiotherapy might trigger the immune system via the cGAS-STING axis mediating IFN- $\beta$  induction. Lastly, the induction of ICD in RVTx-treated tumors might overcome possible deficiencies in innate immune sensing. Both, radio- and virotherapy have been shown to upregulate the expression of ISGs in tumor cells via ICD induction [267, 288, 289]. The robust induction of ICD via HMGB1 release might bypass the deficiency of tumor cells to secrete type I IFNs. It may trigger IFN- $\beta$  production by DCs after binding to toll-like receptor 4 (TLR-4) [60, 85]. This may in turn lead to cross-presentation of tumor antigens to attracted T cells and induce a tumor-directed adaptive immune response. RVTx triggers two different pathways of innate immune signaling. Thus, a possible defect within the tumor cells might be compensated by the combination therapy. RVTx might induce innate immune signaling, independent of the deficient IFN signaling pathway, that would lead to activation of adaptive immune responses.

### 5.4 Anti-tumor efficacy of radiovirotherapy *in vivo*

In this study, I used the murine tumor model MOC2-hCD46 to analyze the efficacy and immunological effects of RVTx *in vivo*. First, I determined the schedule for *in vivo* assessment of the combination therapy. RVTx *in vivo* consisted of three radiation doses of 5 Gy each combined with three injections of  $1 \cdot 10^6$  ciu MeVac on consecutive days starting the virotherapy on the day of the second irradiation. Although I detected a significant tumor growth delay and prolonged survival after RVTx compared to mock or virus alone, the combination therapy did not show beneficial effects compared to radiation alone (see Figure 4.19). The tumor irradiation seemed to be the main driver for the efficacy of the combination therapy as the administration of MeVac at the chosen dose showed only minor effects in terms of tumor growth and survival in this tumor model. However, tumor regression was only transient. In the RVTx-treated group, it seemed that at the time point of tumor regrowth the effect of virotherapy was not detectable anymore and the virus might have been cleared from the system. A modulation, i.e. higher doses of MeVac, or repetition of the treatment sequence

might increase anti-tumor efficacy. Applying the MeVac injections after completion of tumor irradiation might increase viral entry and spread as a result of prior damage by a total dose of 15 Gy irradiation ( $3 \times 5$  Gy). This might increase the sensitivity of tumor cells to viral infection [213].

As innate immune signaling and ICD will not eliminate tumor cells *per se* but rather mediate downstream effects to eventually induce immune responses, I analyzed activation of adaptive anti-tumor and anti-viral immunity. I analyzed the abundance of TILs in tumors nine days after completion of RVTx and detected increased abundance of CD3<sup>+</sup> T lymphocytes in tumors after combination treatment. This difference was statistically significant compared to the other treatment groups. Further analysis showed that the cell population mainly consisted of CD8<sup>+</sup> T cells. Importantly, RVTx seemed to attract T cells, especially cytotoxic T cells, to the tumor site. Further, I analyzed tumor- and virus-mediated cytokine release from splenocytes of treated mice. The splenocytes were co-cultured beforehand with MOC2-hCD46 cells from cell culture or MeVac virus solution to assess different triggers of an adaptive immune response. The detection of IFN- $\gamma$  after co-culture of virus with splenocytes from mice treated with MeVac indicated induction of an anti-viral response. The co-culture of splenocytes with tumor cells did not indicate a tumor-specific immune response. For interleukin (IL) 2, an immune activating cytokine released by T<sub>H</sub>1 cells, however, I detected a statistically significant increase of cytokine release in co-cultures of tumor cells and virus with splenocytes from RVTx-treated mice compared to other treatment groups. This implied the presence of T lymphocytes of the T<sub>H</sub>1 type responding to tumor and virus after RVTx. Further, I detected secretion of IL-10 after co-culture of virus with splenocytes from mice treated with MeVac alone or RVTx. This cytokine has shown immunosuppressive as well as -stimulatory function [290, 291]. The former might indicate the activation of an immune regulating feedback loop due to the presence of regulatory T cells (T<sub>reg</sub> cells) attracted to the tumor after viral infection. T<sub>reg</sub> cells are well characterized by the secretion of IL-10 as well as the expression of the transcription factor forkhead box p3 (Foxp3) [91, 106, 292]. To investigate the presence of T<sub>reg</sub> cells in murine tumors, I analyzed the expression of the *Foxp3* gene from RNA extracted early after RVTx treatment. However, I did not detect elevated levels of *Foxp3* expression in treated tumors compared to mock. Therefore, a conclusive statement concerning the presence of T<sub>reg</sub> cells possibly inducing the regulation of an immune response was not possible at this early time point after RVTx treatment. Nevertheless, the co-culture of extracted splenocytes with MeV led to increased release of IL-10. This might indicate the induction of a regulatory feedback loop that might also limit immune responses *in vivo*. In fact, tumors that received RVTx or radiation treatment started to grow again approx. 10 days after treatment (see Figure 4.19).

In summary, the possible induction of ICD and innate immune signaling detected after

RVTx treatment *in vitro* might activate an adaptive anti-tumor and anti-viral response as observed *in vivo*. However, RVTx treatment did not only induce immune activation, but also suppression. To circumvent downregulation of the adaptive immune response against the tumor, an extension of the RVTx treatment sequence might be beneficial. Introducing a second series of virus injections approx. 10 days after initial RVTx treatment might further boost the present immune response. The MOC2 tumor model was described as an aggressive and immunosuppressive tumor before, associated with the infiltration of T<sub>reg</sub> cells [224, 293, 294]. Thus, as an alternative approach, a triple combination of RVTx with ICB might boost the effect of the combination therapy additionally and circumvent induction of immunosuppression. Oweida and colleagues showed that the combination of radiotherapy and ICB led to significant tumor growth delay, improved survival as well as decreased levels of T<sub>reg</sub> cells in the tumor microenvironment (TME) of MOC2 tumors [295]. A triple combination including RVTx and ICB might further boost the induced anti-tumor immune response and therefore create a possible combination treatment especially for refractory, treatment-resistant tumor types such as HNSCC or PDAC.

### 5.5 Suitability of preclinical models

The experimental investigations of novel cancer therapeutics and their combinations such as RVTx require suitable preclinical models to assess the efficacy as well as safety and potential toxicity prior to first clinical trials. In this study, I analyzed the efficacy of RVTx and induction of potential mechanisms of action in several preclinical models of HNSCC and PDAC. I used established human tumor cell lines of PDAC and HNSCC – BxPC-3, T3M4, HNO210 and HNO410 – to analyze the efficacy and synergy of RVTx as well as factors of ICD, innate immune sensing and activation *in vitro*. Further, I generated and applied immunocompetent murine tumor models modified to enable MeV entry *in vivo* and used different *ex vivo* models to investigate RVTx in a setting that resembles the patient tumor more closely.

The analysis of possible anti-tumor and anti-viral immunity after application of RVTx requires suitable immunocompetent tumor models. Measles virus is a human-specific virus which will not enter murine cells without prior modification [135, 170, 171]. For the development and study of vaccines against measles virus, human *CD46*-transgenic mice are used that harbor a knockout of the interferon-alpha/beta-receptor (IFNAR) [296]. These mice show virus replication and spread similar to the human host and are therefore also applied in studies of oncolytic MeV vaccines [166, 297]. However, it remains to be investigated whether the genetic modification influences virotherapy in this model. Thus, syngeneic immunocompetent mouse tumor models are more commonly used than IFNAR knockout mice. They are implanted either

orthotopically or heterotopically depending on the tumor location and the implementation of a possible treatment [188, 293, 295].

In this project, I used syngeneic, heterotopic immunocompetent murine tumor models to analyze the efficacy of RVTx. I implanted tumor cells on the left thigh of mice. The location of the tumor allowed effective shielding, minimizing off-tumor effects of radiation. First, I generated murine PDAC or HNSCC cell lines expressing the human *CD46* gene using a lentiviral vector for stable integration of *CD46* into the genome or episomal, non-integrating nanovectors that have been shown to resist epigenetic silencing and allow stable transgene expression [230, 231]. Further, the latter enabled cell selection via additional expression of a puromycin resistance gene. From originally four candidate cell lines, I was able to generate a murine tumor model expressing hCD46 for each tumor entity – 30364-hCD46 for PDAC and MOC2-hCD46 for HNSCC – both using the nanovector system. The mEERL95 cell line, representing an HPV-positive tumor, was transduced lentivirally as the pre-existing puromycin resistance made the nanovectors unsuitable. Unfortunately, the transduced cells did not show virus susceptibility. 30364-hCD46 as well as MOC2-hCD46 showed *CD46* gene expression and viral infection in cell culture experiments. The conducted *in vivo* experiments, however, revealed that 30364-hCD46 did not maintain stable transgene expression once the cells were implanted into the mouse. Contrary to previous findings of stable transgene expression and resistance to epigenetic silencing, it is possible that the human *CD46* gene was silenced in the implanted tumor cells [231, 243]. A complete loss of the transfected vector might be more likely, though, as the puromycin resistance of the transfected cells was lost as well. Without the continuous selection pressure the episomal nanovector of approx. 7 kb in size might be lost *in vivo* over time [298]. The MOC2-hCD46 model, representing an HPV-negative tumor, showed stable transgene expression over the course of the conducted *in vivo* experiments. As already described before, MOC2-hCD46 showed its aggressive phenotype and high treatment resistance in survival experiments. The virus susceptibility and sensitivity of the murine cells, though, was reduced compared to human tumor cells and therefore might have been insufficient for MeV infection *in vivo*. Lentiviral transduction of murine tumor cell lines had shown stable expression of hCD46 as well as sufficient virus susceptibility and permissiveness *in vitro* as well as *in vivo* before [183, 186]. A change of the vector system for 30364 and MOC2 cells from nano- to lentiviral expression vectors might enable stable transgene expression and provide enhanced susceptibility of these murine cells to MeV infection.

In order to move a promising new treatment approach from the preclinical setting to clinical use, the gap between artificial, experimental environments and clinical reality needs to be closed with suitable three-dimensional (3D) tumor models of human origin. Different approaches of *ex vivo* models use spheroid cultures, tumor slice cultures or patient-derived tumor explants to investigate different anti-tumor treatments in tumor models that better resemble the actual

clinical setting [299, 300, 301]. A great benefit of these models is the ability to generate or maintain the cellular composition of individual tumors [302]. In HNSCC research, tumor slice cultures and organotypic tumor explants have been established successfully. They have been used to investigate the patient-specific tumor properties concerning mutational burden as well as responsiveness to different treatment modalities including radiotherapy or oncolytic virotherapy [299, 300, 303, 304]. Due to the resemblance to the clinical setting, I attempted in this study to investigate RVTx in some of these *ex vivo* models.

In the context of PDAC, Angelova and colleagues developed a 3D PDAC spheroid model comprising PDAC tumor cells and fibroblasts using the hanging drop technique to form a 3D tumor structure [221, 249]. Using this model, human tumor cell lines can be investigated in a more realistic setting than in monolayer cell culture. To test the efficacy of RVTx against PDAC, I employed the 3D spheroid model of AsAn-PaCa cells and fibroblasts and analyzed morphology as well as virus susceptibility after combination treatment. I detected a reduction in size after treatment as well as viral infection and spread within the spheroid over time. The irradiation did not seem to inhibit viral infection. However, a quantitative assessment of emitted GFP fluorescence would be necessary to determine differences between combination and monotherapies. Further, the short time-span for conducting experiments with the spheroids of approx. 7 days and the small cell number of only 25,000 cells overall to generate the model limit the possibilities of feasible experiments. I was not able to monitor cell viability as performed *in vitro* and could not analyze possible induction of ICD or innate immune signaling. Hence, the further analysis of RVTx in this *ex vivo* model would require additional experimental methods such as live cell analysis, histology or immunohistochemistry as shown before [249]. A second *ex vivo* PDAC model applied in this study were patient-derived tumor cultures. Originating from PDAC tumors, Ehrenberg and colleagues xenotransplanted surgically resected tumors into immunodeficient mice and expanded the tumor cell culture *in vivo*. After explantation of these xenograft tumors the cultivation was continued *in vitro* generating semi-adherent PDAC cultures maintaining the heterogeneous character of patient tumors [227]. Models like these can be used to investigate the specific biology of a patient tumor and support the decision for further anti-tumor treatment [305]. I treated four different PDAC cultures with RVTx and monitored cell viability as well as induction of ICD and innate immune signaling. I detected a heterogeneous response of the PDAC cultures to the combination treatment in terms of sensitivity or resistance representing the varying efficacy a cancer therapy can have in the clinical setting. Interestingly, all PDAC cultures showed a virus-mediated release of HMGB1 and expression as well as secretion of IFN- $\beta$  independently of the cytotoxic potential of RVTx. This points towards a high potential of RVTx to induce anti-tumor or anti-viral immune responses. However, the overall efficacy might be quite patient-specific and would require individual analysis to assess the therapeutic benefit for the individual case. Further, using these patient-derived cultures in this preclinical setting showed

the difficulty of reproducibility to validate results. This *ex vivo* model should rather be viewed as primary tissue that can be cultured for a limited time span rather than as a permanent cell culture. Additionally, the longer the PDAC cultures were maintained, the more they were prone to lose their intrinsic heterogeneity. Therefore, these aspects have to be considered when conducting experiments as well as interpreting data that include patient-derived tumor cultures. Further, these models do not recapitulate the immune environment. Efforts to generate and use such models are underway [306, 307].

Conclusively, in this study, I applied several preclinical models of HNSCC and PDAC to investigate the efficacy of RVTx inducing a possible anti-tumor response from different preclinical perspectives. Each model has its limitations and thus the data has to be interpreted with caution. Nonetheless, the collective data of *in vitro*, *in vivo* and *ex vivo* experiments performed in this study indicate immune activation and a possible benefit of RVTx in the treatment of refractory tumors.

## 5.6 Translational potential of radiovirotherapy

In recent years, the concept of RVTx has been studied clinically in various tumor entities including HNSCC and PDAC. The combination therapy often comprised an oncolytic virus together with EBRT as well as additional chemotherapy. Whereas HNSCC had been a target tumor entity in several clinical trials investigating an RVTx combination, the number of trials including PDAC patients remains small.

A phase I/II clinical study investigated the combination of an oncolytic HSV encoding granulocyte-macrophage colony stimulating factor (GM-CSF) with radiochemotherapy using cisplatin in patients with stage III/IV HNSCC. It showed no dose-limiting toxicity as well as locoregional recurrence and disease-specific survival of 82.4% with a median follow-up of 29 months [308]. In a phase I dose escalation study, patients with different advanced-stage tumors such as melanoma, HNSCC, tumors in the lung, ovaries or colorectal tract as well as PDAC were treated with palliative radiotherapy in combination with intratumoral injections of an oncolytic reovirus. The combination therapy was well tolerated without dose-limiting toxicity and a considerable fraction of patients had a partial response or stable disease [309]. Mell and colleagues conducted a phase I clinical trial combining intravenous viral therapy using the oncolytic vaccinia virus GL-ONC1 with chemoradiation using cisplatin and intensity modulated radiotherapy (IMRT) for the treatment of locoregionally advanced HNSCC (NCT01584284) [19, 310]. The combination therapy was well tolerated in patients and the two year overall survival was at 69.2%. These trials point towards the safety and potential efficacy of using radiation and virotherapy in combination for treating HNSCC.

Clinical trials using oncolytic MeV often use a virus encoding NIS. This enables non-

invasive monitoring as well as cellular uptake of radioiodine isotopes [165]. Further, the combination of both has induced beneficial therapeutic effects in terms of tumor regression and bystander effects in preclinical as well as clinical investigations [165, 256, 311, 312]. An ongoing phase I/II dose escalation study investigates oncolytic virotherapy in patients with recurrent or metastatic HNSCC or metastatic breast cancer (NCT01846091) [19]. However, the combination of oncolytic MeV and radiotherapy applied as EBRT has not been tested so far in the clinical setting.

Overall, the combination of radiotherapy and oncolytic virotherapy has not been broadly investigated in clinical trials, although both have shown promising anti-tumor effects also in combination with other therapeutic modalities. Radiotherapy is broadly applied in combination with chemotherapeutics as a standard treatment for several tumor types across different tumor stages also in HNSCC [106]. The combination of radiotherapy and immunotherapy using ICB is tested in several clinical trials in recurrent or metastatic HNSCC as well as for curative treatment [34, 313]. Radiotherapy has shown the potential to induce an anti-tumor immune response by triggering CD8<sup>+</sup> T cell responses mediated by antigen presentation by DCs [313]. This can be boosted even further with immunotherapy [207]. Further, immunotherapy using ICB was combined with different oncolytic viruses for treating recurrent or metastatic HNSCC [314]. Although oncolytic viruses can activate innate immunity and recruit inflammatory cells, clinical trials for treating HNSCC showed adverse events against the combination with ICB and no superior treatment efficacy compared to ICB immunotherapy alone (NCT02626000) [19, 315]. Moreover, the HPV status of the tumor has been shown to affect treatment outcome as HPV-driven HNSCC tumors have shown enhanced sensitivity, e.g. to radiation treatment [316]. This is often correlated with improved treatment outcome of patients with HPV-positive tumors. In the present study, RVTx therapy induced increased abundance of TILs in the TME as well as increased cytokine release in the HPV-negative tumor model MOC2-hCD46 compared to monotherapies. This might point towards RVTx, using ionizing radiation in combination with oncolytic MeV, as a beneficial anti-tumor therapy to induce an anti-tumor immune response independent of the HPV status.

For PDAC tumors, curative treatment options are very limited. Surgery and chemotherapy are common treatment modalities that are accompanied by radiotherapy in the palliative setting of advanced stage or recurrent tumors [317, 318]. Due to a strong treatment resistance, radiotherapy is usually not applied as standard treatment. Immunotherapy as a novel treatment approach for PDAC has often remained ineffective due to the immunosuppressive TME and low level of immune cell infiltration in the tumor, making it an immunologically ‘cold’ tumor [319]. Clinical trials applying ICB therapy against PDAC resulted in a poor outcome when applied as monotherapy and with no added benefit when combined with chemotherapy (NCT01473940) [19, 26, 320]. The combination of chemotherapy, checkpoint inhibition and

oncolytic viruses showed clinical benefit, as PDAC patients experienced stable disease or even regression of injected lesions (NCT02620423, NCT02045589) [19, 321, 322]. Oncolytic viruses may harbor the ability to ‘warm up’ the PDAC tumor by infection of tumor cells and activation of an immune response [318]. In a preclinical study conducted by May and colleagues, the combination of oncolytic MeV and chemotherapy showed reduction of tumor mass [212]. In the study presented here, the combination of oncolytic MeV and ionizing radiation led to synergistic tumor cell killing and induction of ICD in several preclinical PDAC tumor models. This might point towards the activation of immune response pathways including a possible radiosensitization of PDAC due to viral infection.

In conclusion, preclinical and clinical research has led to success in therapeutic responses and the number of possible combinations is endless. Nevertheless, the clinical need for an effective therapy of refractory HNSCC and PDAC remains high. RVTx provides promising features to induce a sustained anti-tumor immune response. The clinical translation of RVTx however still requires further preclinical investigations until a suitable combination of radiation and oncolytic virotherapy may be developed.

## 5.7 Conclusions and outlook

This study investigated the combination of ionizing radiation and oncolytic MeV as RVTx for the treatment of refractory HNSCC and PDAC tumors. I could show that irradiation of cells or virus did not reduce MeV infection and replication in tumor cells. In a systematic *in vitro* evaluation of different RVTx treatment conditions, I could show synergy of the combination therapy and determined a treatment schedule using intermediate radiation doses combined with an intermediate virus dose. The activation of pathways involved in anti-tumor immunity was shown by the detection of significantly increased levels of HMGB1 release and CALR surface expression as markers for ICD induction *in vitro*. Further, MeV was sensed via RIG-I signaling and induced IFN- $\beta$  secretion, enabling the activation of an adaptive immune response. For *in vivo* investigations of RVTx, I successfully developed an immunocompetent murine tumor model representing HPV-negative tumors. The RVTx combination therapy led to delayed tumor growth and prolonged survival compared to mock or virotherapy treatment. Although it did not show a benefit compared to radiation alone in terms of tumor growth and survival, I detected increased levels of CD8<sup>+</sup> TILs in the TME after RVTx treatment, which was statistically significant compared to the monotherapies or mock. Further, the combination therapy induced cytokine secretion due to an anti-tumor as well as anti-viral vaccination effect of splenocytes. Additionally, RVTx induced morphological changes and viral spread as observed in 3D PDAC spheroids and showed cytotoxic effects in some patient-derived PDAC cultures *ex vivo*. This model represents the heterogenous therapy response of PDAC tumors

in the clinical setting. Despite only limited toxicity, RVTx induced ICD by HMGB1 release as well as activated innate immune signaling due to IFN- $\beta$  secretion, both mediated by MeV infection.

Based on these findings, the rational development of RVTx for potential clinical use can be continued. Using clonogenic assays, a possible radiosensitizing effect of MeV in the context of RVTx is investigated (Günther *et al.*, in preparation). Further, to assess suitability of RVTx in the individual tumor setting, Günther and colleagues have developed a transcriptome-based ICD signature. This signature might serve as a predictive tool for the therapeutic efficacy of RVTx or other treatment approaches. RVTx *in vivo* should be further investigated with a refined treatment schedule to benefit from possible immune responses induced by MeV. The *in vivo* analysis of the combination therapy also still requires the investigation in a suitable murine PDAC tumor model. To ensure stable expression of the viral entry receptor hCD46, lentiviral transduction of murine PDAC tumor cells might be the preferred choice compared to transfection of nanovectors. Further, the *in vivo* analysis of RVTx against HNSCC should include HPV-positive as well as HPV-negative tumor models to enable the comparison of the therapeutic efficacy in both HNSCC subtypes. In cooperation with the Heidelberg University Hospital, patient tumor explant models of HNSCC are currently developed for investigating virotherapy and other treatment modalities *ex vivo* (Günther, Szczeponik, *et al.*, unpublished). The *ex vivo* analysis of RVTx will greatly benefit from the establishment of this novel preclinical model as it will give insights into the responsiveness of patient-derived HPV-positive as well as HPV-negative HNSCC tumors to the combination treatment. Lastly, the investigation of RVTx in this study showed successful proof-of-concept for this novel treatment approach. A rational modification of both therapeutic regimens such as arming MeV for increased viral efficacy, the use of protons or carbon ions to improve the therapeutic quality of radiotherapy in the combined approach or an additional combination of RVTx with immune checkpoint inhibition will move radiovirotherapy towards the development of a state-of-the-art cancer therapy with the goal of improved efficacy in otherwise treatment-refractory tumors.

# Abbreviations

<b>3D</b>	three-dimensional
<b>30364-hCD46</b>	30364-hCD46 pCAG single
<b>ABAM</b>	antibiotic antimycotic solution
<b>ANOVA</b>	analysis of variance
<b>APC</b>	allophycocyanin
<b>APCs</b>	antigen-presenting cells
<b>ATP</b>	adenosine triphosphate
<b>BCA</b>	bicinchoninic acid
<b>BiTEs</b>	bispecific T cell engagers
<b>BSA</b>	bovine serum albumin
<b>CALR</b>	calreticulin
<b>CAR</b>	chimeric antigen receptor
<b>cDNA</b>	complementary DNA
<b>CD/UPRT</b>	cytosine deaminase/uracil phosphoribosyltransferase
<b>CEA</b>	carcinoembryonic antigen
<b>CEFs</b>	chicken embryonic fibroblasts
<b>cGAMP</b>	cyclic guanosine monophosphate–adenosine monophosphate
<b>cGAS</b>	cyclic GMP-AMP synthase
<b>CI</b>	combination index
<b>ciu</b>	cell infectious units
<b>Con A</b>	concanavalin A
<b>Cq</b>	quantification cycle
<b>CTLA-4</b>	cytotoxic T lymphocyte-associated protein 4
<b>CXCL-10</b>	C-X-C motif chemokine ligand 10

<b>Cy</b>	cyanine
<b>DAMPs</b>	danger-associated molecular patterns
<b>DAPI</b>	4',6-diamidino-2-phenylindole
<b>DCs</b>	dendritic cells
<b>ddH<sub>2</sub>O</b>	deionized water
<b>DMEM</b>	Dulbecco's Modified Eagle's medium
<b>DMSO</b>	dimethyl sulfoxide
<b>DNA</b>	deoxyribonucleic acid
<b>dNTP</b>	deoxynucleotide triphosphate
<b>D-PBS</b>	Dulbeccos's phosphate-buffered solution
<b>EB</b>	elution buffer
<b>EBRT</b>	external beam radiotherapy
<b>EDTA</b>	ethylenediaminetetraacetic acid
<b>EGFR</b>	epidermal growth factor receptor
<b>ELISA</b>	enzyme-linked immunosorbent assay
<b>ELISpot</b>	enzyme-linked immune absorbent spot
<b>EMA</b>	European Medicines Agency
<b>ER</b>	endoplasmic reticulum
<b>ERK</b>	extracellular signal-regulated kinase
<b>EtOH</b>	ethanol
<b>F</b>	fusion
<b>FACS</b>	fluorescence-activated cell sorting
<b>FC</b>	flow cytometry
<b>FCS</b>	fetal calf serum
<b>FDA</b>	Food and Drug Administration
<b>FIP</b>	fusion inhibitory peptide
<b>FITC</b>	fluorescein isothiocyanate
<b>Foxp3</b>	forkhead box p3
<b>GFP</b>	green fluorescent protein
<b>GM-CSF</b>	granulocyte-macrophage colony stimulating factor

<b>GTP</b>	guanosine triphosphate
<b>H</b>	hemagglutinin
<b>hCD46</b>	human CD46
<b>HKGS</b>	human keratinocyte growth supplement
<b>HMGB1</b>	high mobility group box 1
<b>HNSCC</b>	head and neck squamous cell carcinoma
<b>HPV</b>	human papillomavirus
<b>HRP</b>	horseradish peroxidase
<b>HSP</b>	heat shock protein
<b>HSV</b>	herpes simplex virus
<b>ICB</b>	immune checkpoint blockade
<b>ICD</b>	immunogenic cell death
<b>IF</b>	immunofluorescence
<b>IFN</b>	interferon
<b>IFNAR</b>	interferon-alpha/beta-receptor
<b>IL</b>	interleukin
<b>IMDM</b>	Iscove's Modified Dulbecco's medium
<b>IMRT</b>	intensity modulated radiotherapy
<b>i.p.</b>	intraperitoneal
<b>IRF-3</b>	interferon regulatory factor 3
<b>ISGs</b>	interferon stimulated genes
<b>i.t.</b>	intratumoral
<b>JAK2</b>	janus kinase 2
<b>L</b>	large protein
<b>LDH</b>	lactate dehydrogenase
<b>LET</b>	linear energy transfer
<b>M</b>	matrix protein
<b>MAPK</b>	mitogen-activated protein kinase
<b>MAVS</b>	mitochondrial antiviral signaling
<b>mEERL95-hCD46</b>	mEERL95-hCD46 lenti single

<b>MEK</b>	MAPK kinase
<b>MEM</b>	Minimal Essential medium Eagle
<b>MeV</b>	measles virus
<b>MOC2-hCD46</b>	MOC2-hCD46 pEF1 single
<b>MOI</b>	multiplicity of infection
<b>MTT</b>	3-(4,5-dimethylthiazol-2-yl)-2,5-diphenyltetrazolium bromide
<b>MX1</b>	myxovirus resistance 1
<b>MyD88</b>	myeloid differentiation primary response 88
<b>N</b>	nucleoprotein
<b>NALP3-ASC</b>	NACHT, LRR and PYD domains-containing protein 3 with apoptosis-associated speck-like protein containing caspase recruiting domain
<b>NF-<math>\kappa</math>B</b>	nuclear factor $\kappa$ B
<b>NIS</b>	sodium-iodine symporter
<b>NK</b>	natural killer
<b>OD</b>	optical density
<b>ORF</b>	open reading frame
<b>OV</b>	oncolytic virus
<b>P</b>	phosphoprotein
<b>PAMPs</b>	pathogen-associated molecular patterns
<b>Panc02-hCD46</b>	Panc02-hCD46 pEF1 single
<b>PBMCs</b>	peripheral blood mononuclear cells
<b>PCR</b>	polymerase chain reaction
<b>PDAC</b>	pancreatic ductal adenocarcinoma
<b>PD-1</b>	programmed death protein 1
<b>PD-L1</b>	programmed death ligand 1
<b>PE</b>	phycoerythrin
<b>PerCP-Cy</b>	peridinin chlorophyll protein complex with cyanine
<b>PFA</b>	paraformaldehyde
<b>p.i.</b>	post infection

<b>PNP</b>	purine nucleoside phosphorylase
<b>p.r.</b>	post irradiation
<b>PRRs</b>	pattern recognition receptors
<b>P/S</b>	penicillin-streptomycin
<b>PSCA</b>	prostate stem cell antigen
<b>p.tr.</b>	post treatment
<b>PVDF</b>	polyvinylidene fluoride
<b>PVRL-4</b>	poliovirus receptor-like 4
<b>qPCR</b>	quantitative PCR
<b>R24V</b>	irradiation 24 h prior to virus infection
<b>RIG-I</b>	retinoic acid-inducible gene I
<b>RNA</b>	ribonucleic acid
<b>RNP</b>	ribonucleoprotein
<b>ROS</b>	reactive oxygen species
<b>RPMI</b>	Roswell Park Memorial Institute
<b>RT</b>	room temperature
<b>RT-PCR</b>	reverse transcription PCR
<b>RVTx</b>	radiovirotherapy
<b>s.c.</b>	subcutaneous
<b>SD</b>	standard deviation
<b>SDS-PAGE</b>	sodium dodecyl sulphate-polyacrylamide gel electrophoresis
<b>SLAMF1</b>	signaling lymphocyte-activation molecule family member 1
<b>STAT3</b>	signal transducer and activator of transcription
<b>STING</b>	stimulator of interferon genes
<b>TBE</b>	tris-borate EDTA
<b>TBS</b>	tris-buffered saline
<b>TBS-T</b>	tris-buffered saline-tween
<b>TCR</b>	T cell receptor
<b>TGF-<math>\beta</math></b>	transforming growth factor $\beta$
<b>T<sub>H</sub></b>	T helper

<b>TILs</b>	tumor-infiltrating lymphocytes
<b>TLR-4</b>	toll-like receptor 4
<b>TME</b>	tumor microenvironment
<b>TNF-<math>\alpha</math></b>	tumor necrosis factor $\alpha$
<b>T<sub>reg</sub> cells</b>	regulatory T cells
<b>T-VEC</b>	talimogene laherparepvec
<b>WB</b>	western blot
<b>XTT</b>	2,3-bis-(2-methoxy-4-nitro-5-sulfophenyl)-2H-tetrazolium-5-carboxanilide

# Appendix

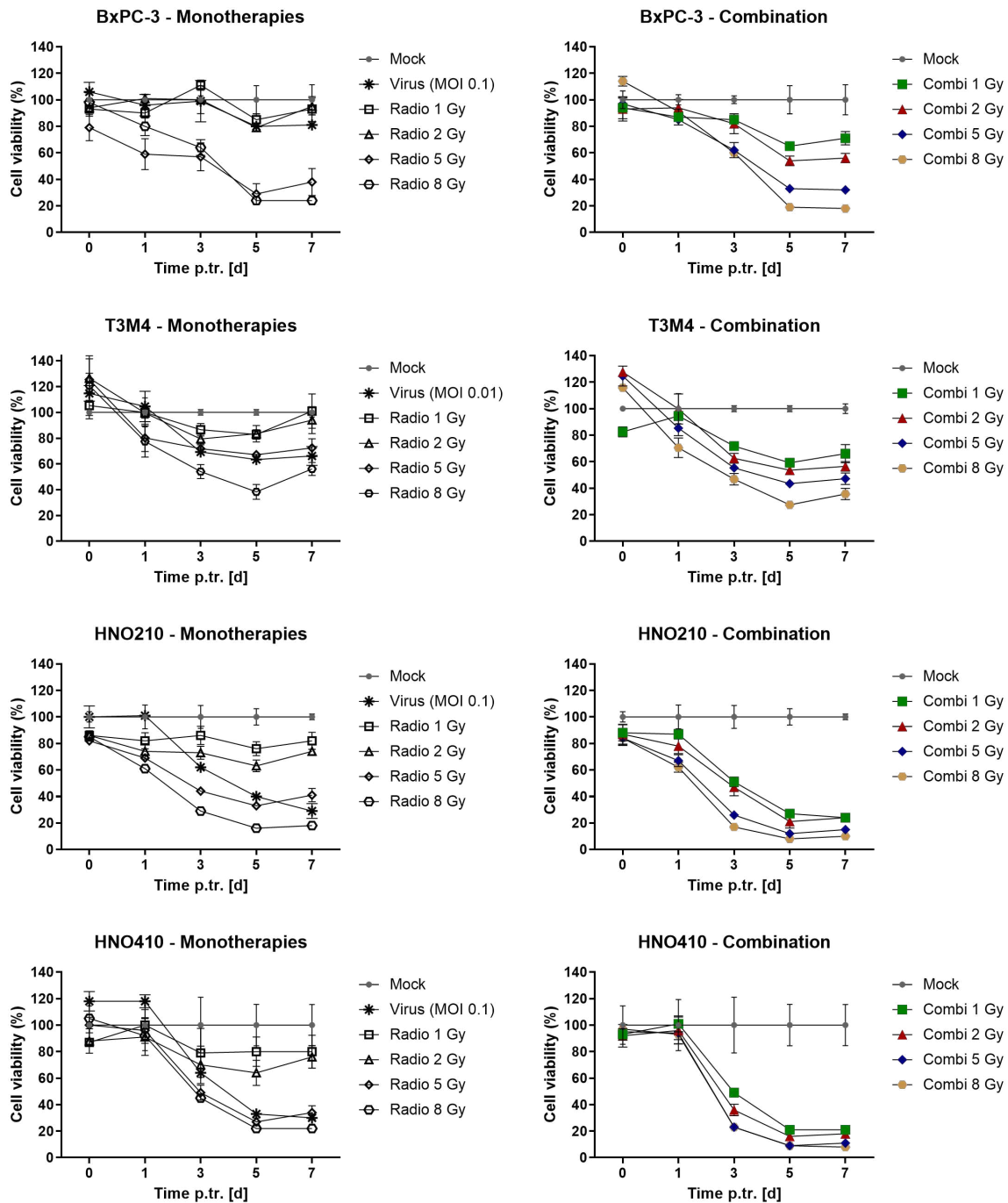


**Figure A1: Cell viability after RVTx *in vitro*.** This complete data set for determining cell viability after RVTx treatment of human tumor cells shows all tested combinations of a radiation dose range with intermediate virus MOI. I performed XTT assays as described for Figure 4.5 and normalized the data to mock set at 100%. The graphs show representative mean and SD from technical replicates per sample of  $n = 2$  independent experiments. MOI — multiplicity of infection; Radio — radiation; Combi — combination; p.tr. — post treatment; d — days.

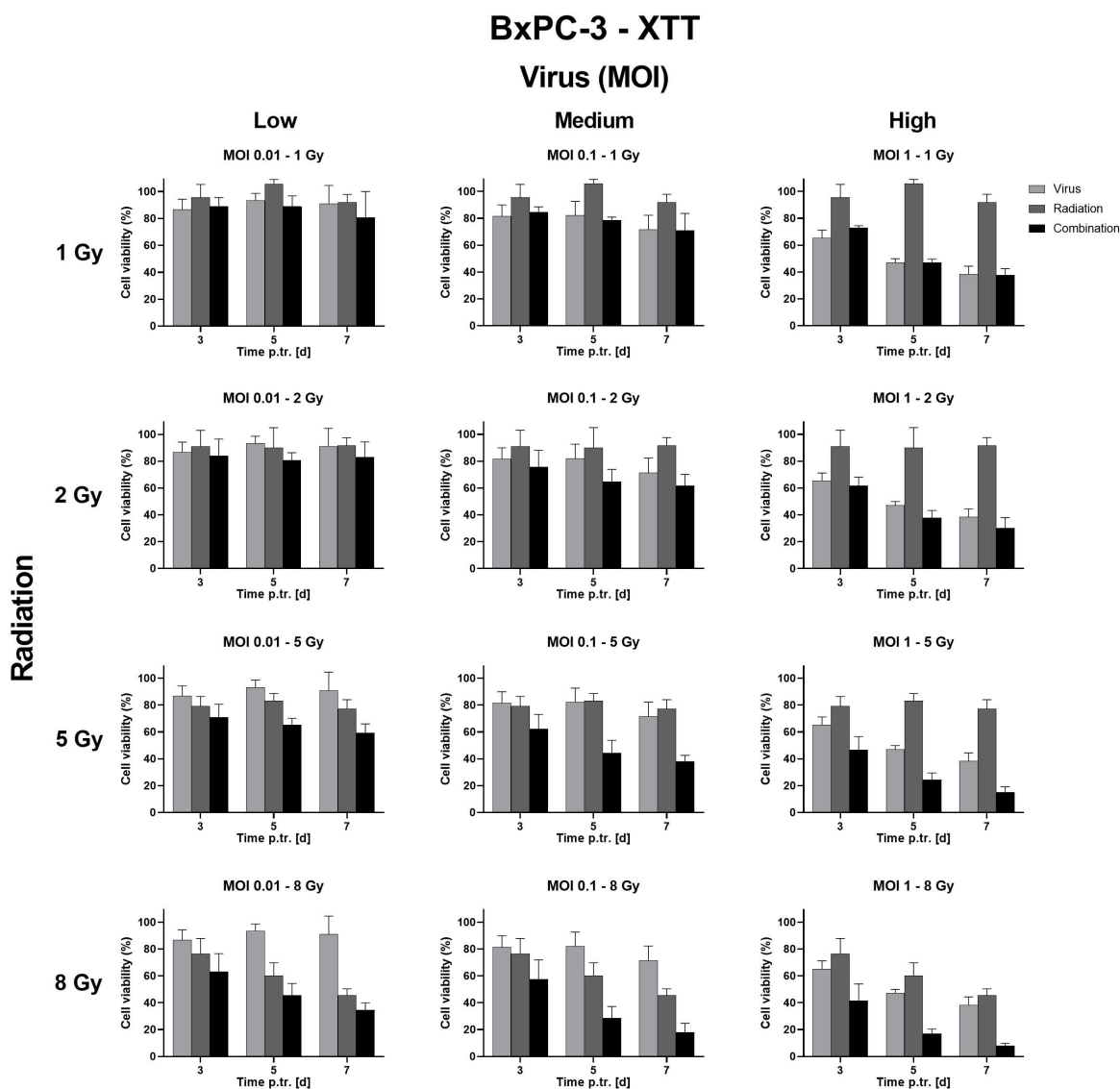


**Figure A2: Cell viability of BxPC-3 after RVTx treatment in XTT assay.** I evaluated synergy of RVTx by systematically combining both monotherapies. I seeded cells in 96 well-plates and determined cell viability via XTT assay at indicated time points after RVTx using different radiation and virus doses as indicated. The data was normalized to mock set at 100%. The figure shows mean and SD for data of  $n = 3$  independent experiments. MOI — multiplicity of infection; p.tr. — post treatment; d — days.

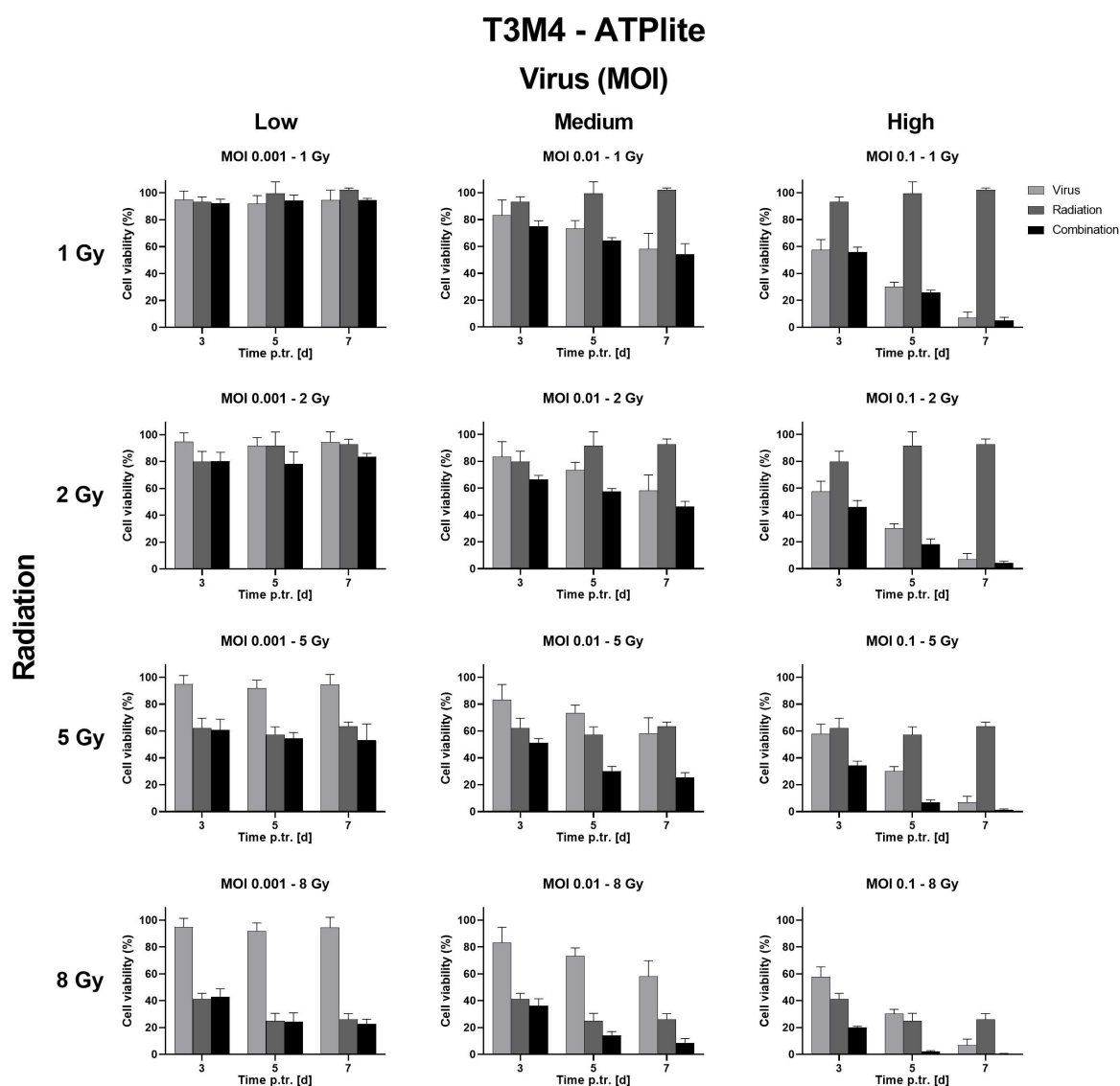


**Figure A3: Cell viability of T3M4 after RVTx treatment in ATPlite assay.** I evaluated synergy of RVTx by systematically combining both monotherapies. I seeded cells in 96 well-plates and determined cell viability via ATPlite assay at indicated time points after RVTx using different radiation and virus doses as indicated. The data was normalized to mock set at 100%. The figure shows mean and SD for data of  $n = 3$  independent experiments. MOI — multiplicity of infection; p.tr. — post treatment; d — days.

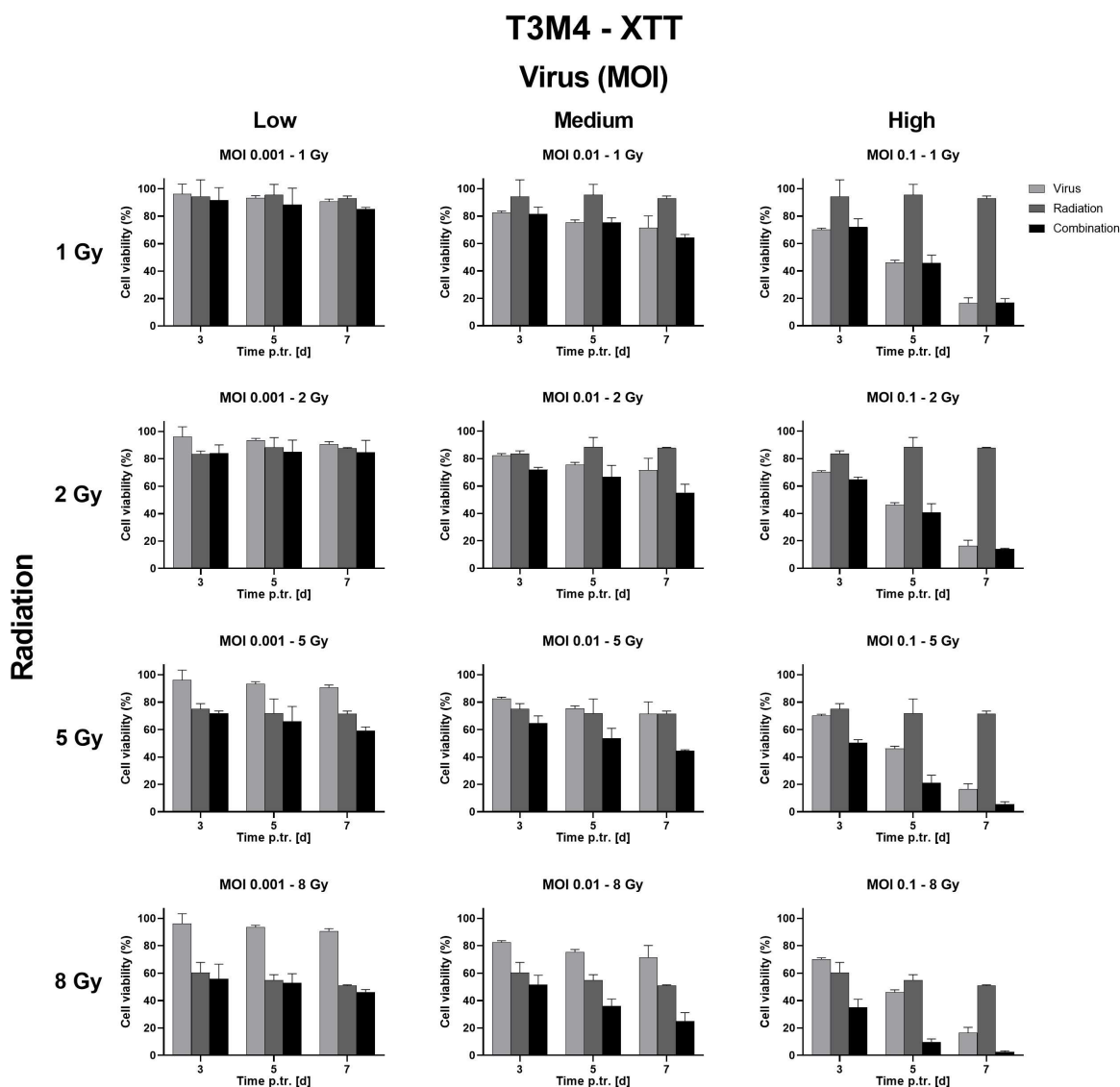


**Figure A4: Cell viability of T3M4 after RVTx treatment in XTT assay.** I evaluated synergy of RVTx by systematically combining both monotherapies. I seeded cells in 96 well-plates and determined cell viability via XTT assay at indicated time points after RVTx using different radiation and virus doses as indicated. The data was normalized to mock set at 100%. The figure shows mean and SD for data of  $n = 3$  independent experiments. MOI — multiplicity of infection; p.tr. — post treatment; d — days.

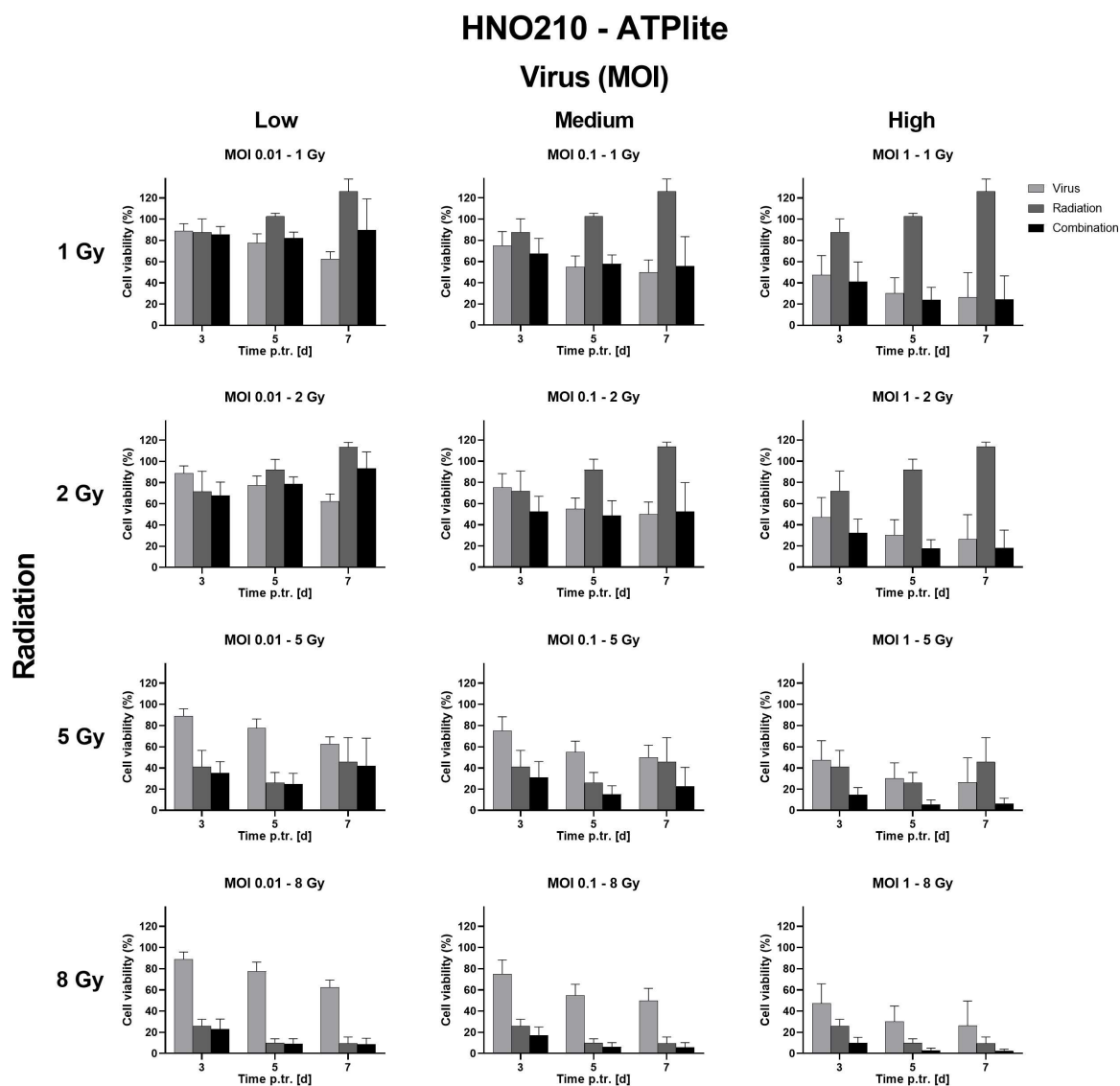


**Figure A5: Cell viability of HNO210 after RVTx treatment in ATPlite assay.** I evaluated synergy of RVTx by systematically combining both monotherapies. I seeded cells in 96 well-plates and determined cell viability via ATPlite assay at indicated time points after RVTx using different radiation and virus doses as indicated. The data was normalized to mock set at 100%. The figure shows mean and SD for data of  $n = 3$  independent experiments. MOI — multiplicity of infection; p.tr. — post treatment; d — days.

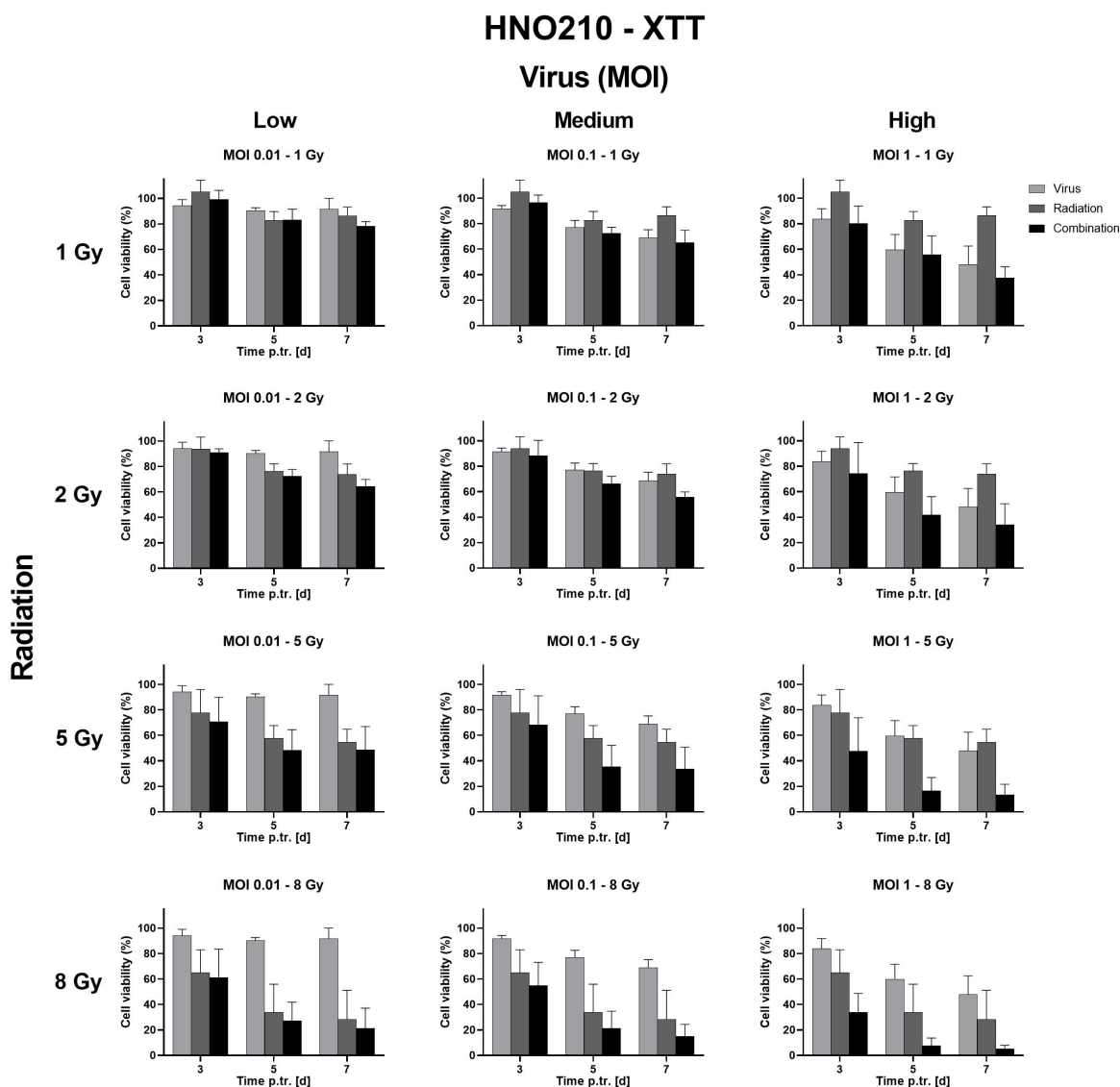


**Figure A6: Cell viability of HNO210 after RVTx treatment in XTT assay.** I evaluated synergy of RVTx by systematically combining both monotherapies. I seeded cells in 96 well-plates and determined cell viability via XTT assay at indicated time points after RVTx using different radiation and virus doses as indicated. The data was normalized to mock set at 100%. The figure shows mean and SD for data of  $n = 3$  independent experiments. MOI — multiplicity of infection; p.tr. — post treatment; d — days.

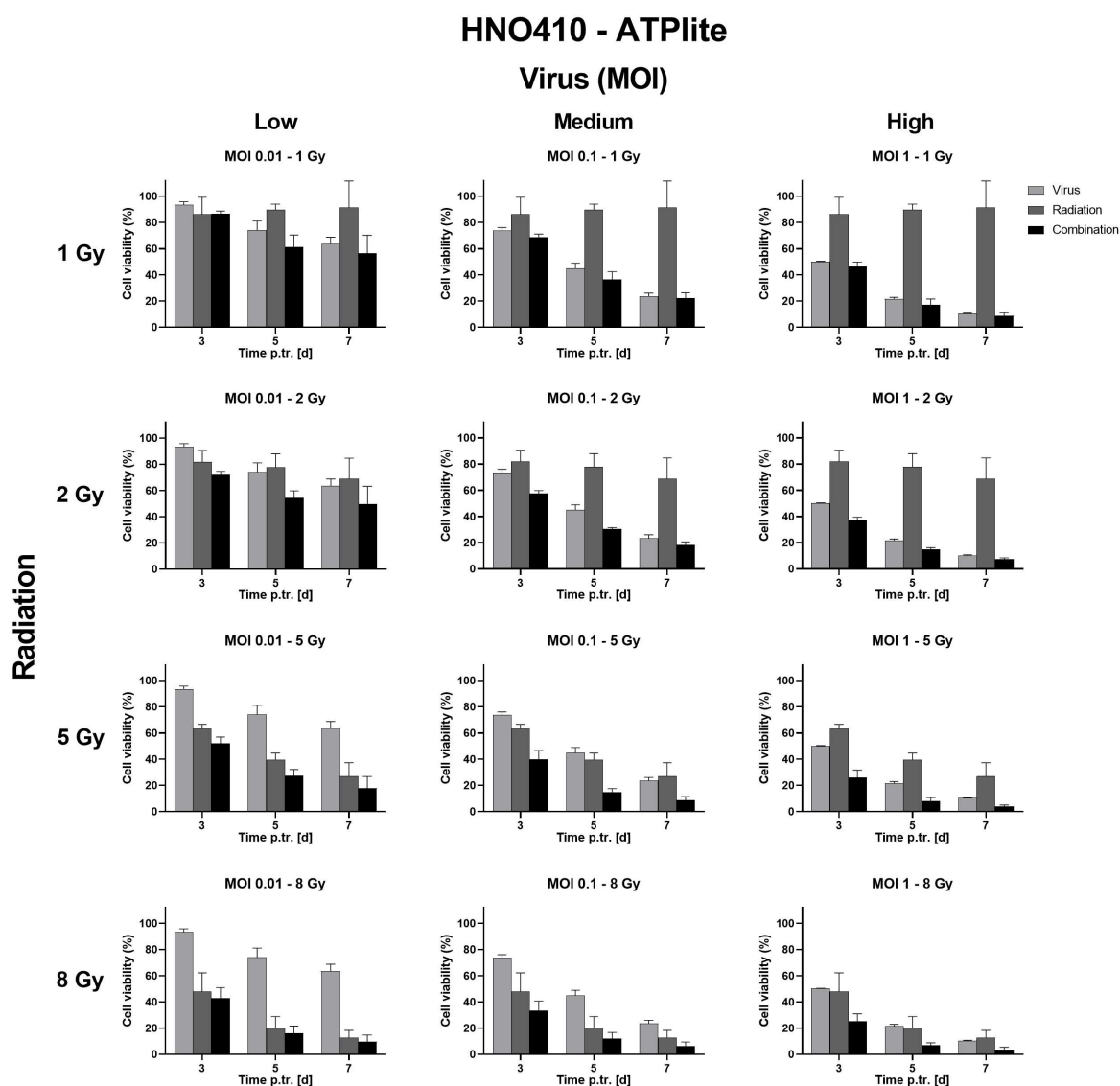


**Figure A7: Cell viability of HNO410 after RVTx treatment in ATPlite assay.** I evaluated synergy of RVTx by systematically combining both monotherapies. I seeded cells in 96 well-plates and determined cell viability via ATPlite assay at indicated time points after RVTx using different radiation and virus doses as indicated. The data was normalized to mock set at 100%. The figure shows mean and SD for data of  $n = 3$  independent experiments. MOI — multiplicity of infection; p.tr. — post treatment; d — days.

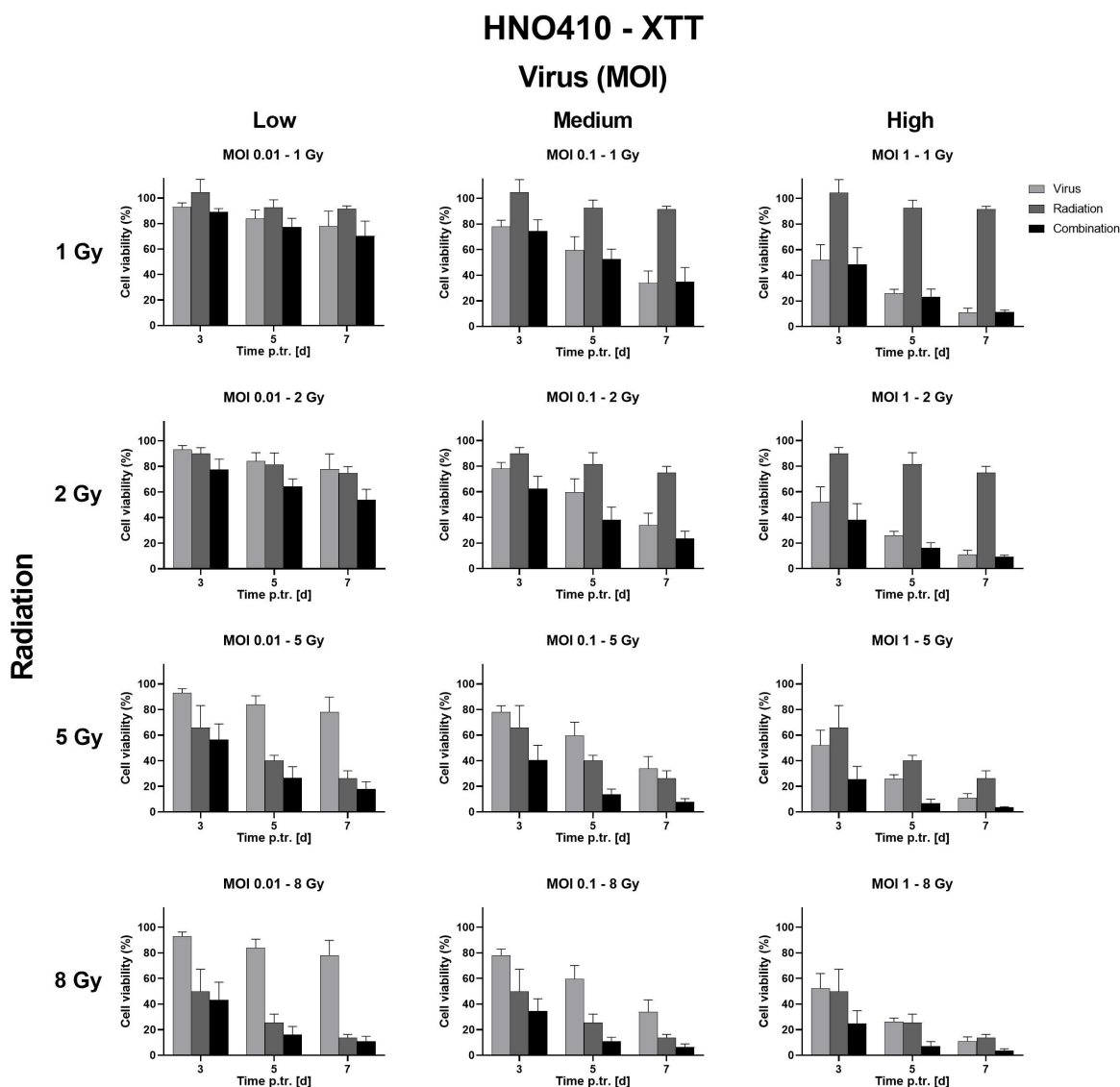


**Figure A8: Cell viability of HNO410 after RVTx treatment in XTT assay.** I evaluated synergy of RVTx by systematically combining both monotherapies. I seeded cells in 96 well-plates and determined cell viability via XTT assay at indicated time points after RVTx using different radiation and virus doses as indicated. The data was normalized to mock set at 100%. The figure shows mean and SD for data of  $n = 3$  independent experiments. MOI — multiplicity of infection; p.tr. — post treatment; d — days.

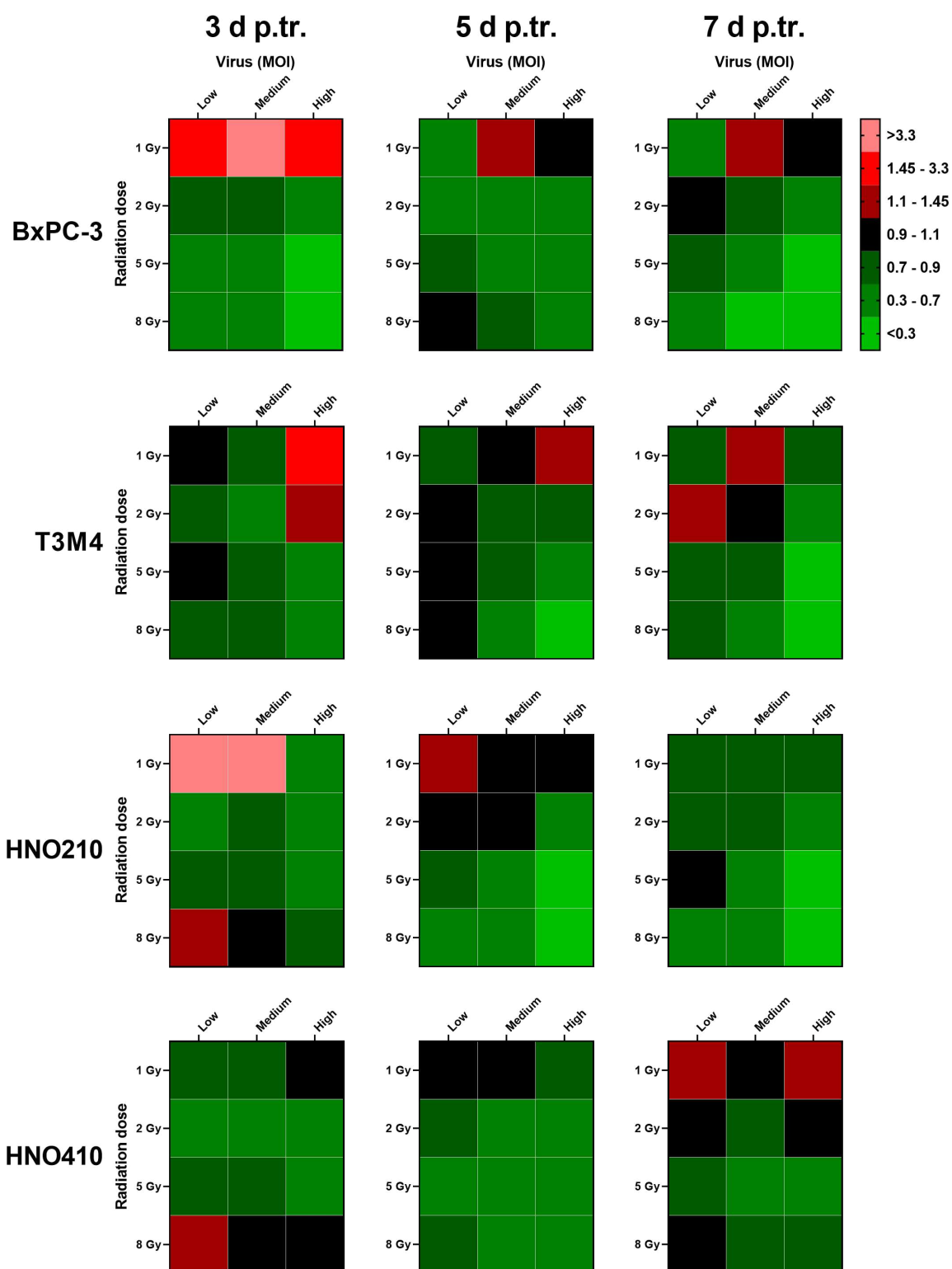


**Figure A9: Heatmap of synergy analysis of RVTx in XTT assay.** Using CompuSyn software, I calculated the synergy of all tested RVTx combinations determined by XTT assay. The corresponding CI values are given in Table A1. Values indicating antagonism are shown in red coloring, additive in black and synergistic in green coloring. d p.tr. — days post treatment; MOI — multiplicity of infection.

**Table A1: Combination indices of synergy analysis.** Calculated CI values for all tested RVTx combinations based on the data of ATPlite and XTT assay indicating synergy, antagonism or additivity of a combination. The data of BxPC-3, T3M4, HNO210 and HNO410 presented here serve as basis for the heatmap representations shown in Figure 4.7 and Figure A9. MOI — multiplicity of infection; d p.tr. — days post treatment.

BxPC-3	ATPlite	Virus dose (MOI)								
		Low			Medium			High		
	d p.tr.	3	5	7	3	5	7	3	5	7
Radiation dose [Gy]	1	5.239	0.473	5.572	1.271	0.662	0.723	0.678	1.490	1.649
	2	79.13	0.678	1.01	0.633	0.65	0.77	0.568	1.1	1.344
	5	0.877	0.897	1.034	0.36	0.793	0.774	0.276	1.029	0.983
	8	0.586	1.154	0.99	0.37	0.989	0.705	0.268	1.116	0.846
BxPC-3	XTT	Virus dose (MOI)								
		Low			Medium			High		
	d p.tr.	3	5	7	3	5	7	3	5	7
Radiation dose [Gy]	1	2.067	0.603	0.564	4.168	1.126	1.176	2.972	0.984	1.016
	2	0.824	0.53	1.042	0.751	0.597	0.78	0.563	0.663	0.65
	5	0.549	0.801	0.721	0.392	0.639	0.434	0.221	0.571	0.249
	8	0.579	0.932	0.485	0.469	0.733	0.251	0.243	0.632	0.149
T3M4	ATPlite	Virus dose (MOI)								
		Low			Medium			High		
	d p.tr.	3	5	7	3	5	7	3	5	7
Radiation dose [Gy]	1	1.452	1.924	1.352	0.783	0.91	1.172	1.17	0.793	0.77
	2	0.946	0.756	0.9	0.733	0.863	1.103	0.777	0.584	0.781
	5	1.087	1.032	1.023	0.878	0.793	1.006	0.701	0.465	0.507
	8	1.015	1.027	1.052	0.85	0.838	0.848	0.509	0.446	0.426
T3M4	XTT	Virus dose (MOI)								
		Low			Medium			High		
	d p.tr.	3	5	7	3	5	7	3	5	7
Radiation dose [Gy]	1	1.029	0.873	0.873	0.796	1.1	1.254	1.838	1.142	0.846
	2	0.852	1.003	1.278	0.56	0.784	0.935	1.149	0.9	0.675
	5	1.001	0.904	0.802	0.816	0.762	0.854	0.685	0.353	0.241
	8	0.831	0.94	0.783	0.732	0.604	0.483	0.448	0.198	0.106

HNO210	ATPlite	Virus dose (MOI)								
		Low			Medium			High		
	d p.tr.	3	5	7	3	5	7	3	5	7
Radiation dose [Gy]	1	1.411	2.221	124.0	0.955	1.551	3.624	0.747	0.671	0.709
	2	0.921	1,821	526.3	0.704	1.047	2.705	0.552	0.538	0.457
	5	0.852	0.914	0.934	0.763	0.806	0.766	0.406	0.623	0.539
	8	0.895	1.108	0.926	0.695	1.004	0.839	0.46	0.834	0.685
HNO210	XTT	Virus dose (MOI)								
		Low			Medium			High		
	d p.tr.	3	5	7	3	5	7	3	5	7
Radiation dose [Gy]	1	2228	1.102	0.762	96.08	0.936	0.827	0.484	0.961	0.706
	2	0.669	1.0	0.746	0.871	0.943	0.747	0.423	0.455	0.694
	5	0.832	0.888	1.059	0.801	0.536	0.678	0.588	0.204	0.297
	8	1.146	0.585	0.619	1.042	0.420	0.446	0.773	0.138	0.176
HNO410	ATPlite	Virus dose (MOI)								
		Low			Medium			High		
	d p.tr.	3	5	7	3	5	7	3	5	7
Radiation dose [Gy]	1	1.175	0.669	1.113	0.735	0.641	0.755	0.999	0.712	1.001
	2	0.716	0.778	1.114	0.535	0.587	0.696	0.601	0.616	0.836
	5	0.666	0.764	0.804	0.444	0.517	0.618	0.38	0.431	0.543
	8	0.718	0.813	0.881	0.489	0.685	0.747	0.473	0.534	0.678
HNO410	XTT	Virus dose (MOI)								
		Low			Medium			High		
	d p.tr.	3	5	7	3	5	7	3	5	7
Radiation dose [Gy]	1	0.721	0.919	1.117	0.864	0.921	1.085	0.957	0.859	1.349
	2	0.547	0.811	0.918	0.592	0.6	0.756	0.628	0.532	1.084
	5	0.85	0.67	0.77	0.723	0.439	0.542	0.668	0.330	0.53
	8	1.132	0.747	0.907	1.028	0.587	0.735	0.978	0.507	0.751

**Table A2: Summary of schedule assessment with cut-off at 20 and 80% for RVTx *in vitro*.** Values of schedule assessment according to results for cell viability and CI analyses for each tested RVTx combination in human tumor cell lines and the total count, summarizing the schedule counts for all cell lines. For evaluating the performance of treatment schedules in cell viability assays, I set a scoring cut-off at 20% of mock as lowest and 80% as highest value that needs to be reached. MOI — multiplicity of infection.

<b>BxPC-3</b>	<b>Virus dose (MOI)</b>			<b>T3M4</b>	<b>Virus dose (MOI)</b>		
<b>Radiation dose [Gy]</b>	Low	Medium	High	<b>Radiation dose [Gy]</b>	Low	Medium	High
<b>1</b>	1	5	4	<b>1</b>	1	4	1
<b>2</b>	3	9	5	<b>2</b>	1	6	2
<b>5</b>	7	10	4	<b>5</b>	4	9	4
<b>8</b>	3	4	4	<b>8</b>	5	8	4
<b>HNO210</b>	<b>Virus dose (MOI)</b>			<b>HNO410</b>	<b>Virus dose (MOI)</b>		
<b>Radiation dose [Gy]</b>	Low	Medium	High	<b>Radiation dose [Gy]</b>	Low	Medium	High
<b>1</b>	2	4	7	<b>1</b>	4	4	0
<b>2</b>	3	6	7	<b>2</b>	8	8	3
<b>5</b>	6	10	6	<b>5</b>	6	6	4
<b>8</b>	3	3	5	<b>8</b>	2	3	3

<b>Total</b>	<b>Virus dose (MOI)</b>		
<b>Radiation dose [Gy]</b>	Low	Medium	High
<b>1</b>	8	17	12
<b>2</b>	15	29	17
<b>5</b>	23	35	18
<b>8</b>	13	18	16

**Table A3: Summary of schedule assessment with cut-off at 25 and 75% for RVTx *in vitro*.** Values of schedule assessment according to results for cell viability and CI analyses for each tested RVTx combination in human tumor cell lines and the total count, summarizing the schedule counts for all cell lines. For evaluating the performance of treatment schedules in cell viability assays, I set a scoring cut-off at 25% of mock as lowest and 75% as highest value that needs to be reached. MOI — multiplicity of infection.

<b>BxPC-3</b>	<b>Virus dose (MOI)</b>			<b>T3M4</b>	<b>Virus dose (MOI)</b>		
<b>Radiation dose [Gy]</b>	Low	Medium	High	<b>Radiation dose [Gy]</b>	Low	Medium	High
<b>1</b>	1	5	4	<b>1</b>	1	4	1
<b>2</b>	3	9	5	<b>2</b>	1	6	2
<b>5</b>	7	7	3	<b>5</b>	4	9	4
<b>8</b>	3	4	4	<b>8</b>	3	6	4
<b>HNO210</b>	<b>Virus dose (MOI)</b>			<b>HNO410</b>	<b>Virus dose (MOI)</b>		
<b>Radiation dose [Gy]</b>	Low	Medium	High	<b>Radiation dose [Gy]</b>	Low	Medium	High
<b>1</b>	0	4	5	<b>1</b>	4	2	0
<b>2</b>	3	6	7	<b>2</b>	7	5	3
<b>5</b>	6	8	6	<b>5</b>	5	5	4
<b>8</b>	1	3	5	<b>8</b>	2	3	3

<b>Total</b>	<b>Virus dose (MOI)</b>		
<b>Radiation dose [Gy]</b>	Low	Medium	High
<b>1</b>	6	15	10
<b>2</b>	12	26	17
<b>5</b>	22	29	17
<b>8</b>	9	16	16

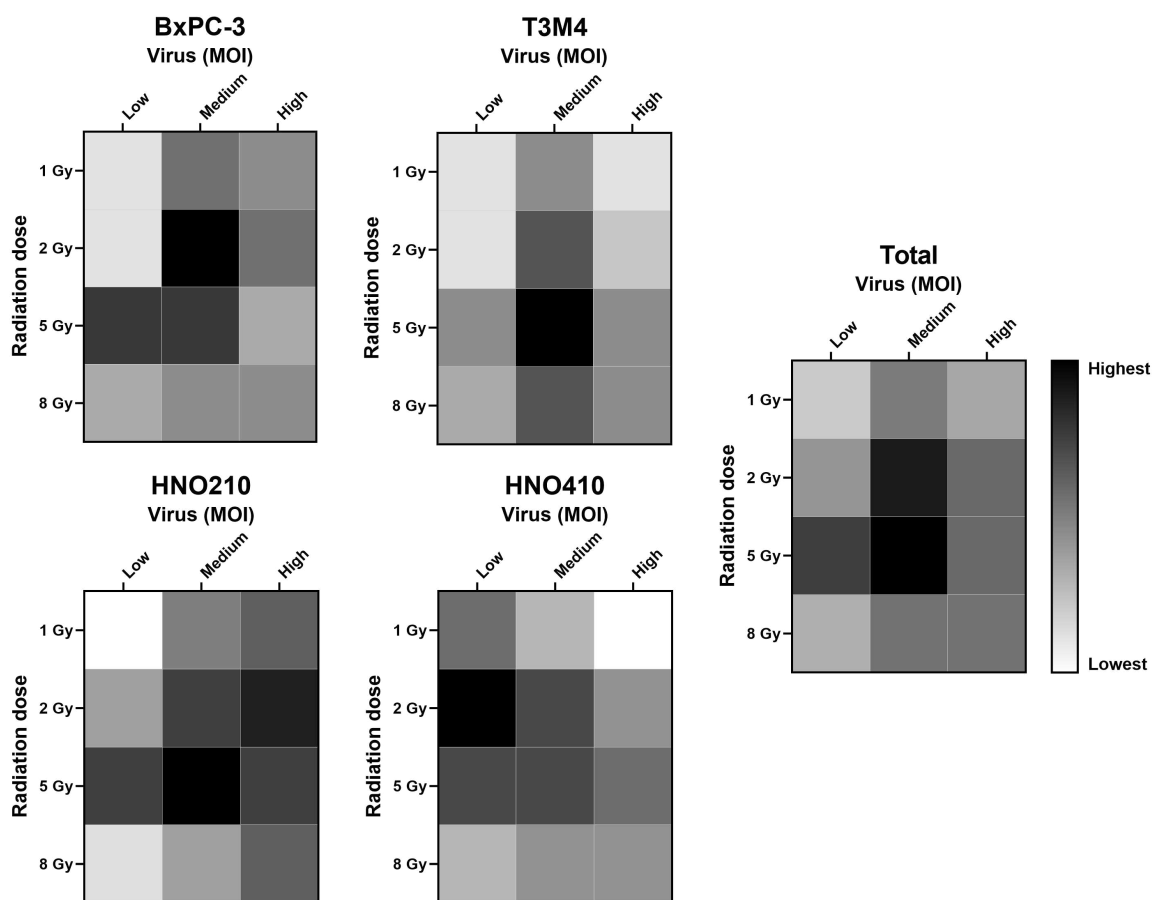


**Figure A10: Heatmap of schedule counts for analysis of RVTx treatment schedules.** To evaluate the performance of each treatment schedule in cell viability assays and synergy analyses, I developed a scoring system with cut-off at 25 and 75% for cell viability data to determine a treatment schedule for further analyses of RVTx *in vitro*. Score values correspond to the given color code showing lowest score in white and highest in black. The summary of schedule scoring is given in Table A3. MOI — multiplicity of infection.

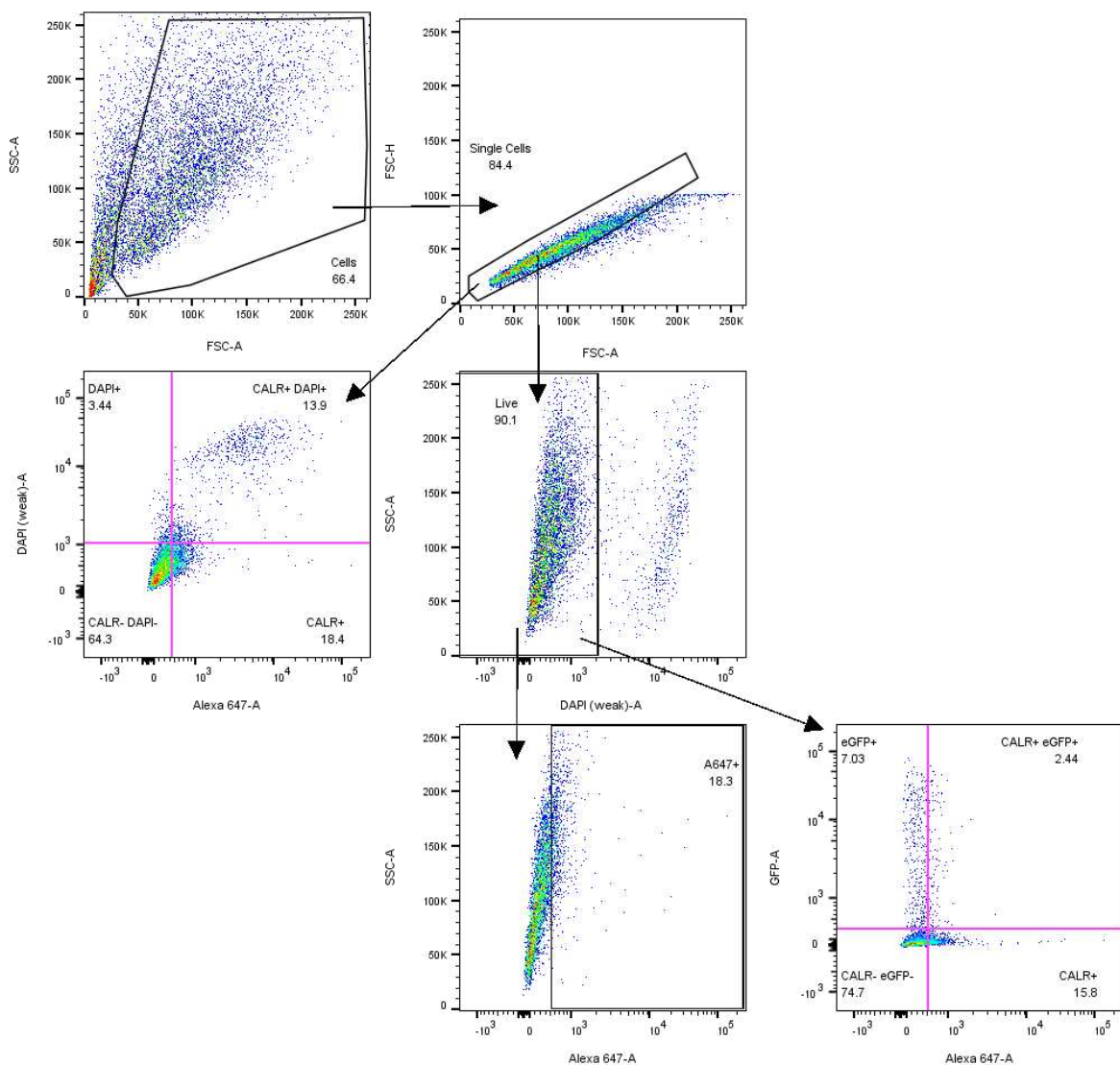


**Figure A11: Gating strategy for analysis of surface-exposed CALR after RVTx.** To identify the single cell population of interest, I used the forward (FSC-A, -H) and side scatter (SSC-A) parameters. By DAPI-staining, I discriminated live from dead cells and identified CALR<sup>+</sup> cells among all single cells and live cells. From the live cell population I also gated for double-positive CALR<sup>+</sup> and eGFP<sup>+</sup> cells with the GFP signal indicating productive virus infection.

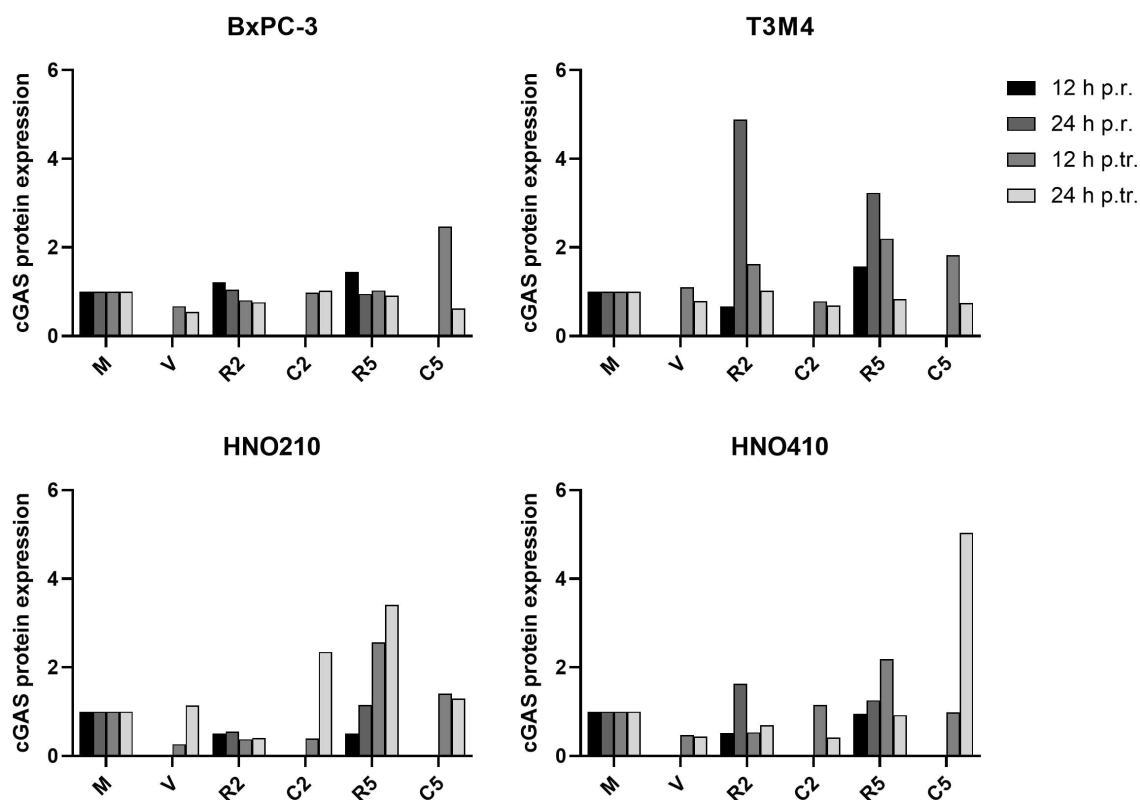


**Figure A12: Protein expression of cGAS after RVTx.** To investigate cGAS protein expression, I collected cell lysates at indicated time points after treatment and performed SDS-PAGE followed by WB. For quantification, I normalized the detected signal to total protein content followed by normalization to mock. Data of a single experiment is shown. h p.r. — hours post radiation; h p.tr. — hours post treatment; M — mock; V — virus; R2, R5 — radiation with 2 or 5 Gy; C2, C5 — combination with 2 or 5 Gy irradiation.

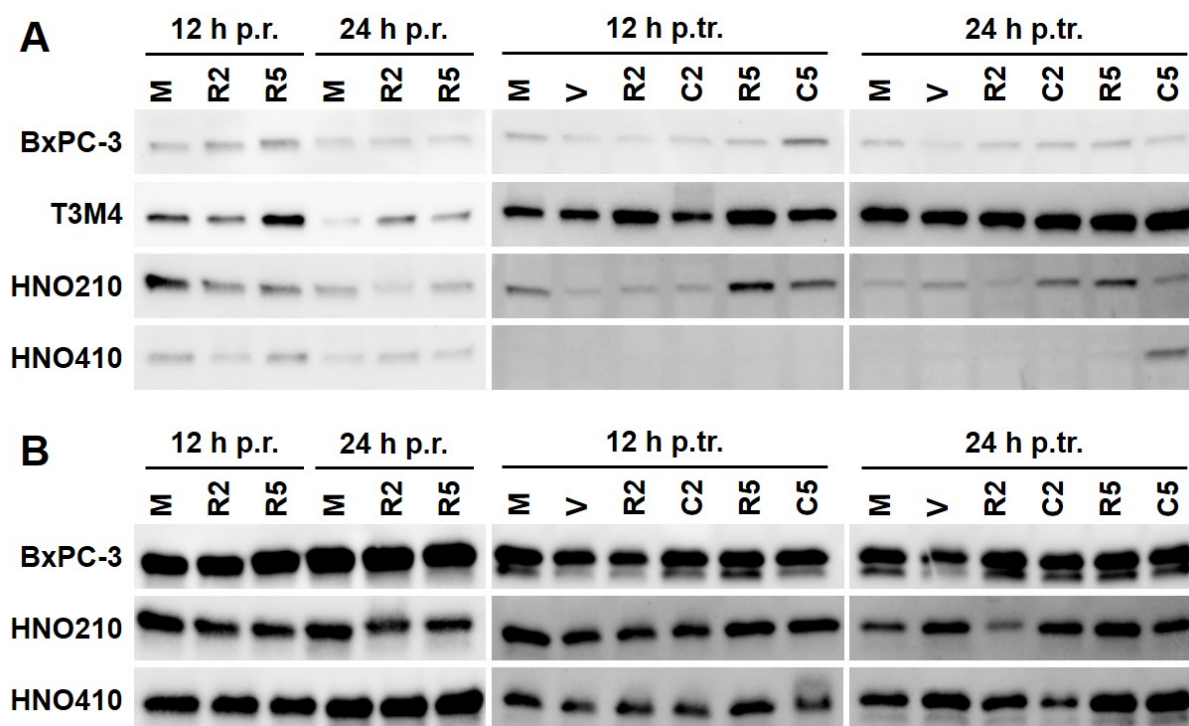


**Figure A13: Western blot of cGAS and STING.** I detected protein expression of (A) cGAS and (B) STING by SDS-PAGE and WB in cell lysates at indicated time points after irradiation or RVTx. The experiment was conducted once. h p.r. — hours post radiation; h p.tr. — hours post treatment; M — mock; V — virus; R2, R5 — radiation with 2 or 5 Gy; C2, C5 — combination with 2 or 5 Gy irradiation.

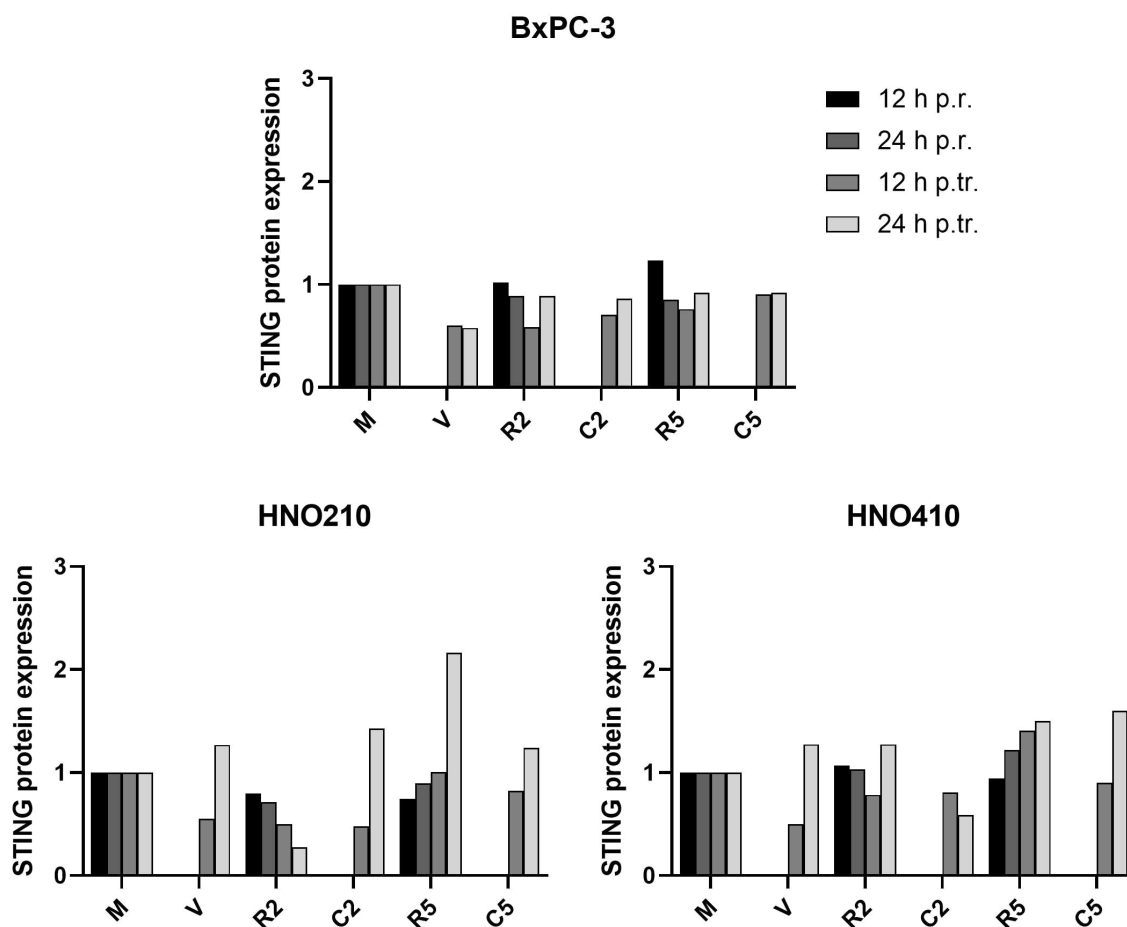


**Figure A14: Protein expression of STING after RVTx.** To investigate STING protein expression, I collected cell lysates at indicated time points after treatment and performed SDS-PAGE followed by WB. For quantification, I normalized the detected signal to total protein content followed by normalization to mock. Data of a single experiment is shown. h p.r. — hours post radiation; h p.tr. — hours post treatment; M — mock; V — virus; R2, R5 — radiation with 2 or 5 Gy; C2, C5 — combination with 2 or 5 Gy irradiation.

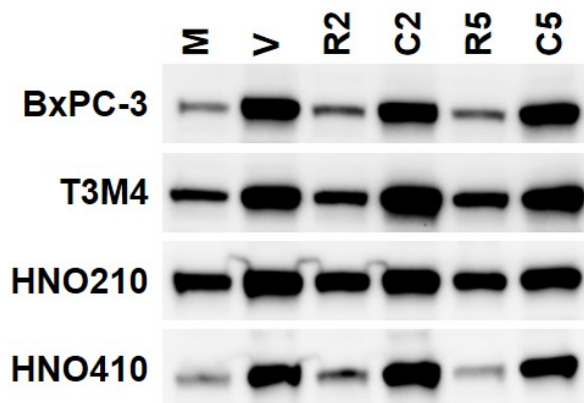


**Figure A15: Western blot of RIG-I.** I detected protein expression of RIG-I by SDS-PAGE and WB in cell lysates 48 h p.tr. with RVTx. A representative image of  $n = 2$  independent experiments is shown. M — mock; V — virus; R2, R5 — radiation with 2 or 5 Gy; C2, C5 — combination with 2 or 5 Gy irradiation.

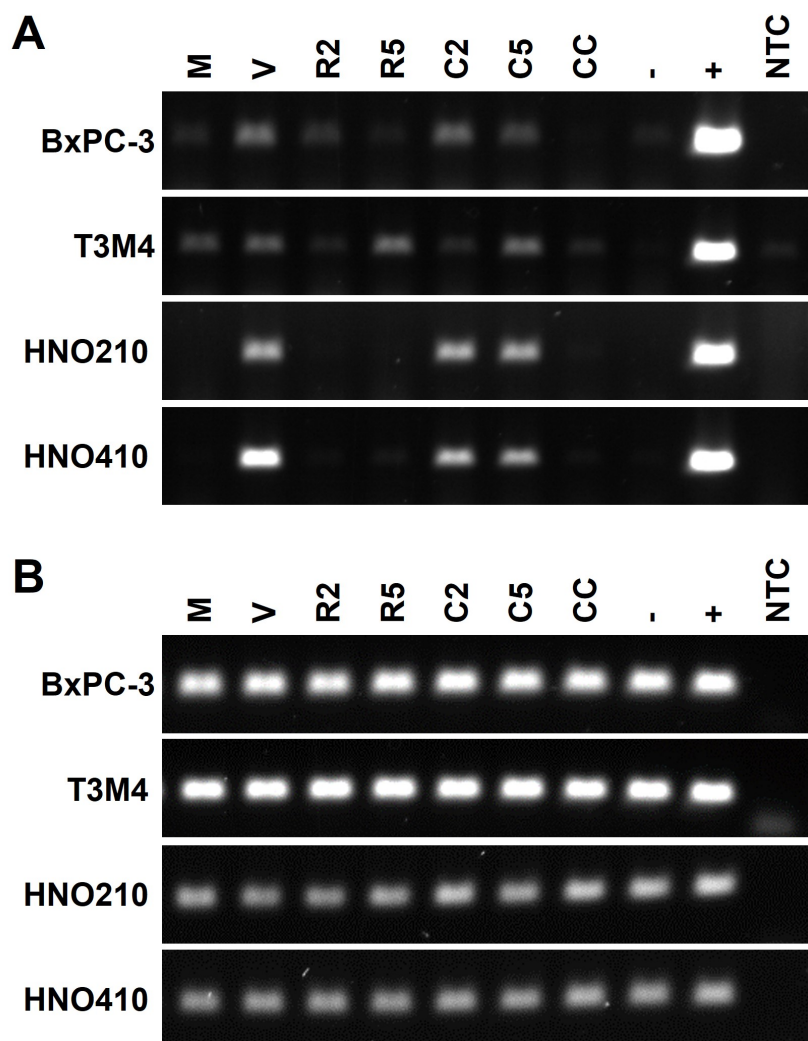


**Figure A16: Expression of *IFNB1* after RVTx.** In parallel with detection of cytokine release, I analyzed expression of the genes encoding (A) IFN- $\beta$  (*IFNB1*) and (B)  $\beta$ -actin (*ACTB*) on transcriptomic level via RT-PCR of PDAC and HNSCC cells 24 h p.tr.. Lysates from routine cell culture (CC) showed baseline expression. MeV-infected and uninfected SW982 cells served as positive and negative control. Representative data of  $n = 2$  independent experiments is shown. M — mock; V — virus; R2, R5 — radiation with 2 or 5 Gy; C2, C5 — combination with 2 or 5 Gy irradiation; CC — cell culture control; -, + — negative, positive control; NTC — non-template control.

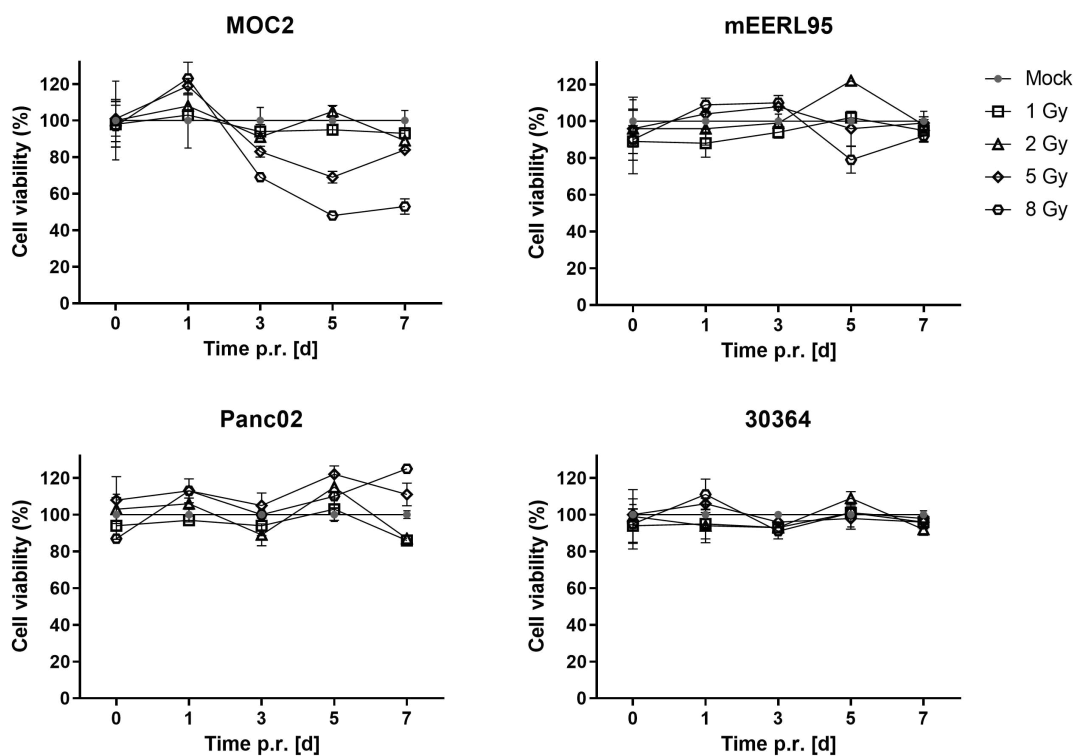


**Figure A17: Radiosensitivity of murine tumor cell lines.** To analyze the effect of radiation alone, I tested the sensitivity of non-transfected murine tumor cell lines to ionizing radiation. I seeded the cells in 12 well-plates and performed XTT assay at indicated time points to monitor cell viability after irradiation with doses ranging from 1 to 8 Gy. The data was normalized to mock set at 100%. The graphs show mean and SD of triplicate samples from one representative of  $n = 2$  independent experiments. p.r. — post irradiation; d — days.

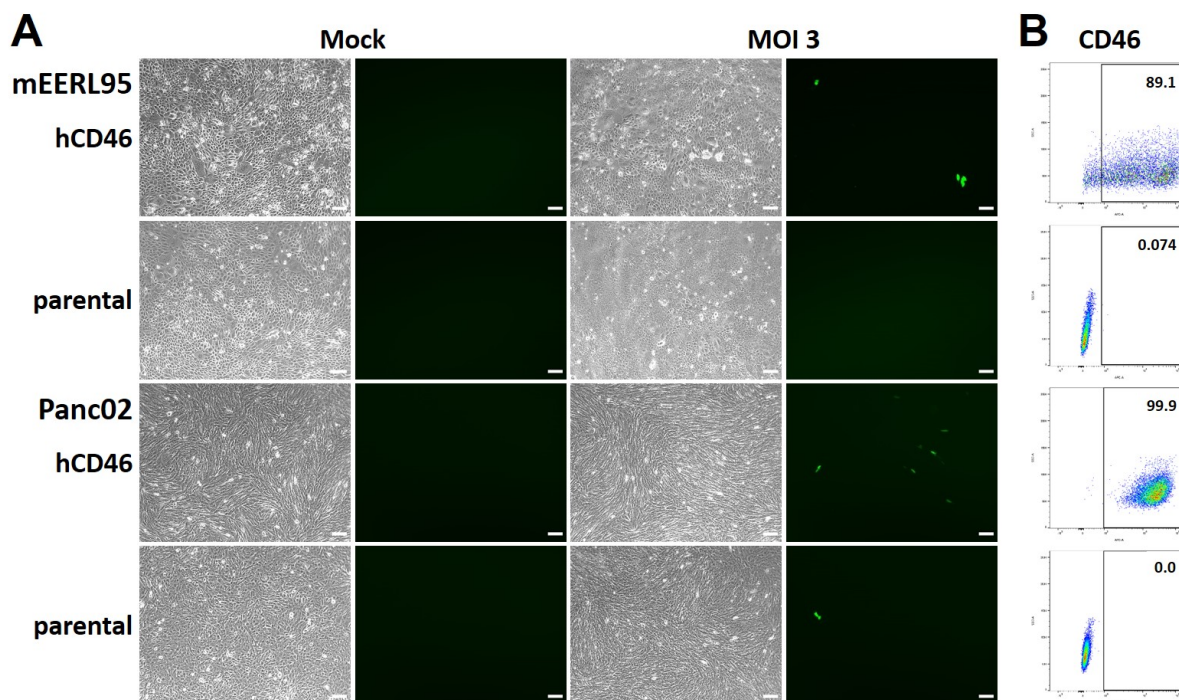


**Figure A18:** *In vitro* characterization of newly generated murine tumor cells. After hCD46-transduction or -transfection and FACS, (A) I analyzed susceptibility of mEERL95-hCD46 and Panc02-hCD46 cells to MeV. I infected cells with MeVac Id-EGFP at MOI = 3 and monitored virus infection and syncytia formation at 72 h p.i. by fluorescence microscopy in phase contrast and green fluorescence channel. (B) Secondly, I performed FC analysis to investigate hCD46 surface expression. Untransduced or non-transfected, parental cells served as negative control. hCD46 — cell line transduced/transfected with hCD46 encoding vector; parental — untransduced/non-transfected cells. Scale bar: 100  $\mu$ m.

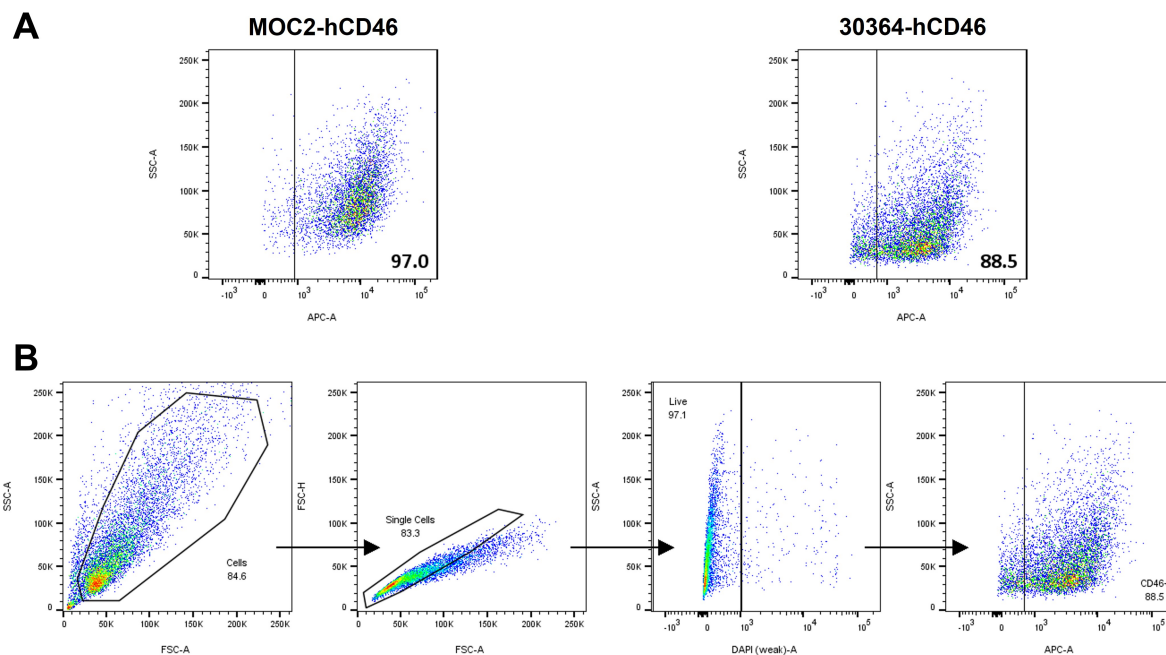


**Figure A19: Surface expression of hCD46 at tumor implantation and gating strategy.** (A) In the course of each tumor implantation, I routinely tested the surface expression of hCD46 via FC analysis on MOC2-hCD46 and 30364-hCD46 cells used for implantation. Here, a representative experiment is shown. (B) For correct gating of the cell population, I used the forward (FSC-A, -H) and side scatter (SSC-A) parameters. By DAPI-staining, I discriminated live from dead cells and identified hCD46<sup>+</sup> cells by an APC-conjugated antibody.

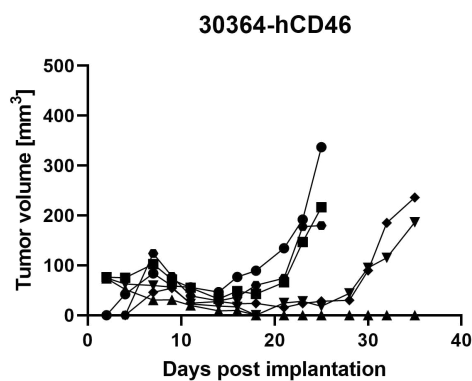


**Figure A20: Growth of 30364-hCD46 tumors *in vivo*.** In the course of analyzing hCD46 expression in 30364-hCD46 tumors (see 4.5.2), I implanted  $1 \cdot 10^6$  cells s.c. into the left thigh of 6 – 8 weeks old C57BL/6J mice. Once the tumors reached a size of 150 – 200 mm<sup>3</sup>, I injected  $1 \cdot 10^6$  ciu of MeVac into the tumor. Two days later, I sacrificed the mice, explanted tumors and performed several experiments to analyze transgene expression in murine tumor cells. The graphs show individual tumor growth curves of  $n = 6$  animals.

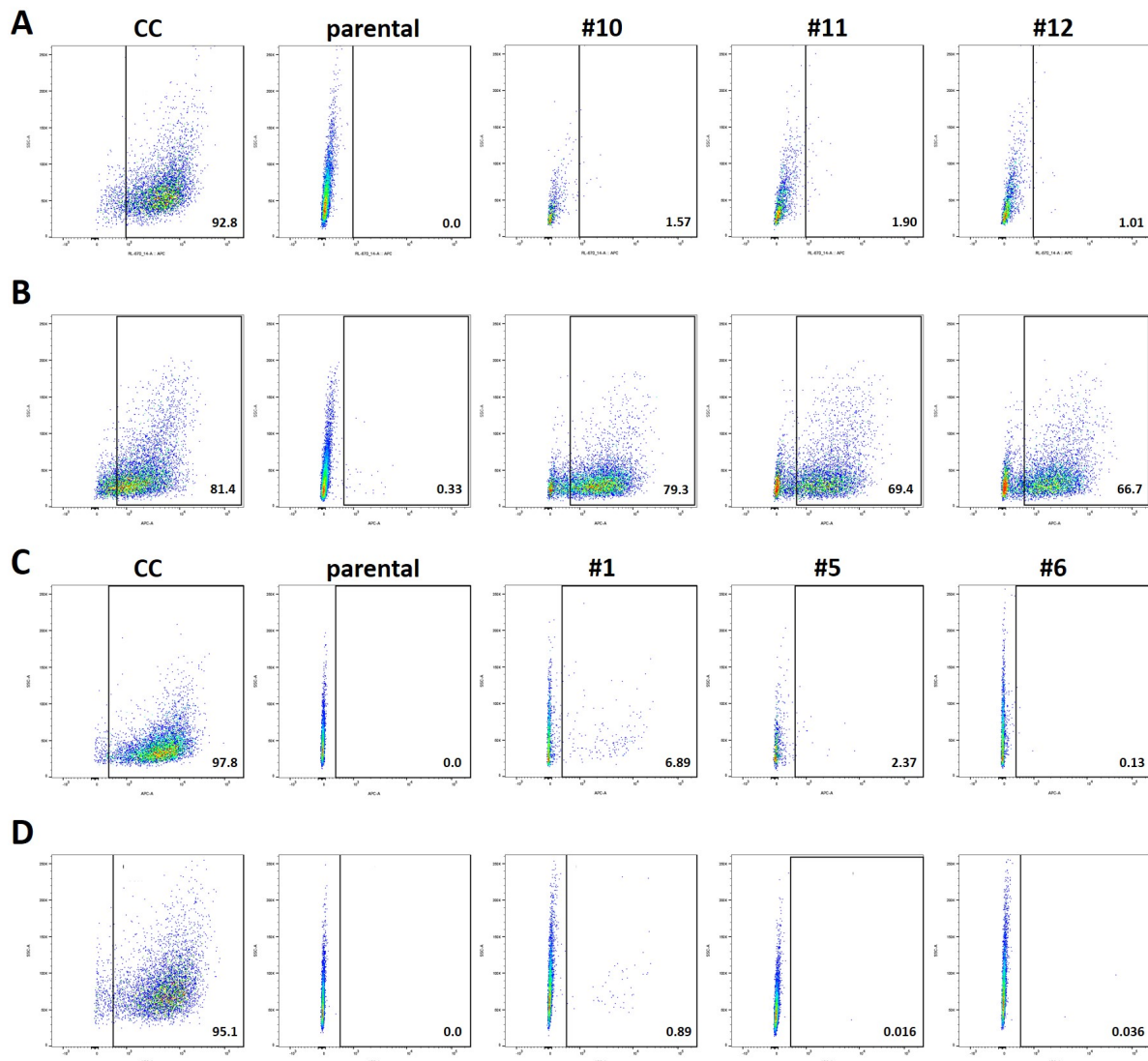


**Figure A21: Human CD46 expression in murine tumors.** In the course of model characterization, I explanted tumor cells from mice that were treated with  $1 \cdot 10^6$  ciu of MeVac i.t. two days before and prepared single cell suspensions. I analyzed hCD46 surface expression on freshly explanted (A) MOC2-hCD46 and (C) 30364-hCD46 cells and 2 weeks after culturing single cell suspensions without puromycin (B, D) by FC analysis. Tumor cells from cell culture (CC) and parental murine cells served as positive and negative control. The images show data of representative tumor samples. CC — *in vitro* tumor cells from cell culture; parental — non-transfected tumor cells.

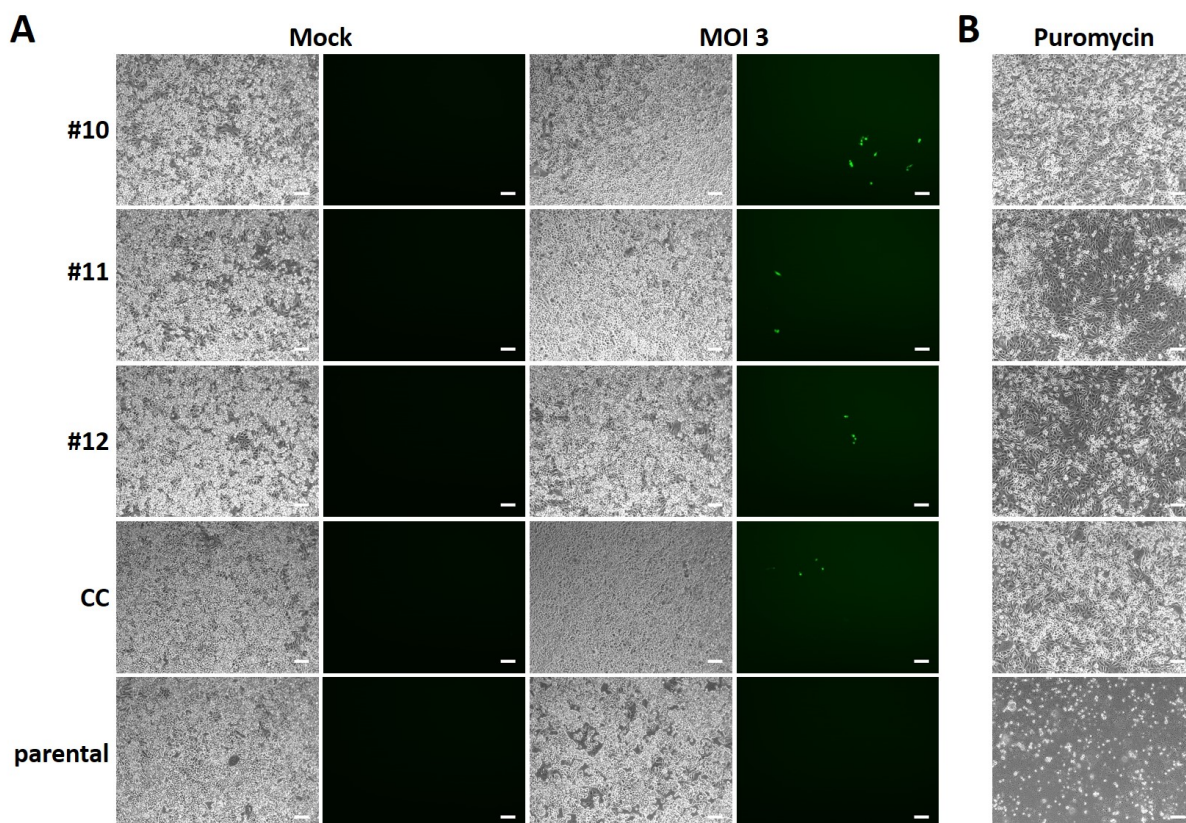


**Figure A22: Analysis of virus susceptibility and puromycin resistance of MOC2-hCD46 tumor samples.** (A) I infected MOC2-hCD46 tumor samples cultivated after explantation with MeVac Id-EGFP at MOI = 3 and monitored virus infection as well as syncytia formation at 72 h p.i. by fluorescence microscopy in phase contrast and green fluorescence channel. (B) Additionally, I tested puromycin resistance by challenging tumor cells with 5  $\mu\text{g}/\text{ml}$  puromycin for 24 h and investigated cell confluence by microscopy. Transfected cells from cell culture (CC) and non-transfected, parental cells served as positive and negative control, respectively. Representative images of triplicate samples of selected tumor samples are shown. MOI — multiplicity of infection; CC — *in vitro* tumor cells from cell culture; parental — non-transfected cells. Scale bar: 100  $\mu\text{m}$ .

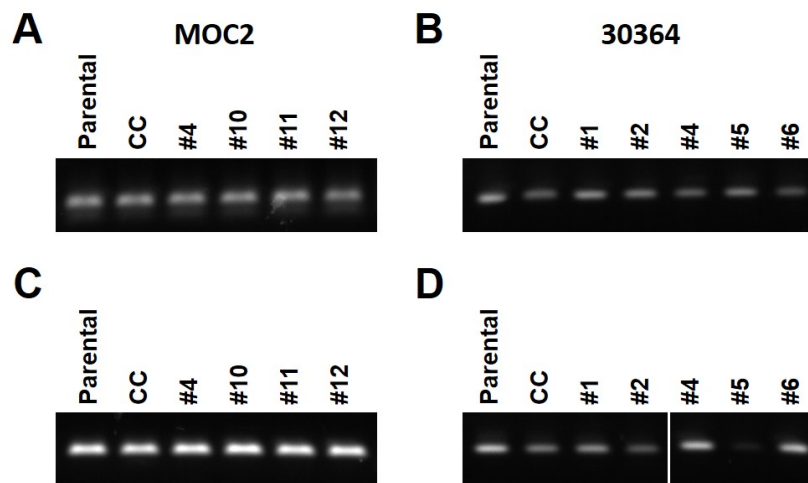


**Figure A23: Expression of *Actb* in murine tumors on genomic and transcriptomic level.** In the course of analyzing the expression of the human *CD46* gene on genomic and transcriptomic level as described in 4.5.2, I amplified *Actb* encoding murine  $\beta$ -actin as housekeeping control from DNA and cDNA of (A, C) MOC2-hCD46 and (B, D) 30364-hCD46 cells. Expression of *CD46* is shown in Figure 4.17. Parental — non-transfected cells; CC — *in vitro* tumor cells from cell culture.

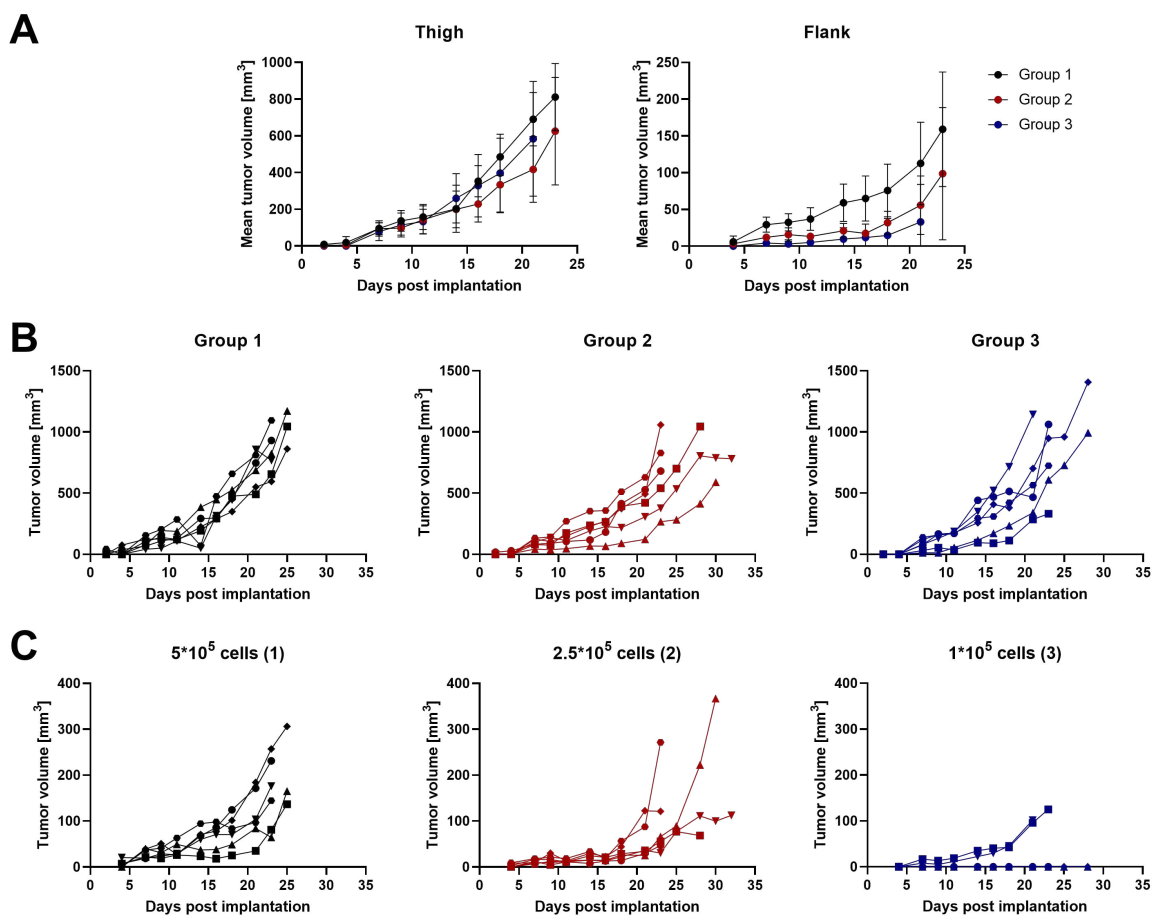


**Figure A24: Assessment of secondary tumor growth *in vivo*.** To investigate possible abscopal effects of RVTx *in vivo*, I determined a suitable cell number to induce secondary tumor growth in mice. Two days after injecting the primary tumor on the left thigh of C57BL/6J mice, I injected either  $5 \cdot 10^5$  (group 1, black),  $2.5 \cdot 10^5$  (group 2, red) or  $1 \cdot 10^5$  MOC2-hCD46 cells (group 3, blue) s.c. into the right flank and monitored tumor growth. (A) Mean tumor volumes as well as individual growth curves of (B) primary tumors on the thigh and (C) secondary on the flank are shown. The graphs show data of  $n = 6$  animals per group.

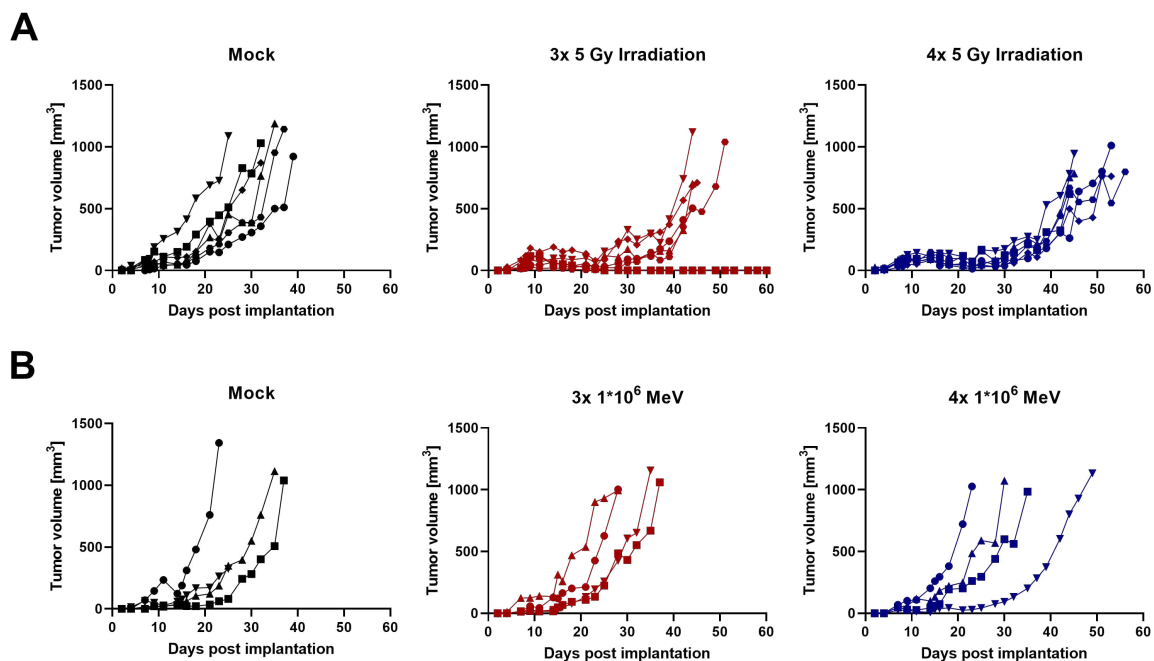


**Figure A25: Tumor growth after radio- or virotherapy *in vivo*.** The investigation of RVTx *in vivo* required analysis of both treatment modalities as monotherapies beforehand. Once the injected MOC2-hCD46 tumors s.c. on the left thigh of C57BL/6J mice reached a mean tumor volume of 100 – 150 mm<sup>3</sup>, the mice were allocated to three groups. They received either mock treatment or 3 or 4 treatment doses of either (A) 5 Gy irradiation (total irradiation dose of 15 or 20 Gy per mouse) or (B) 3 or 4 i.t. injections of 1·10<sup>6</sup> ciu MeVac (see Figure 4.18A). I monitored tumor volumes and survival to evaluate treatment efficacy. The graphs show individual tumor growth curves of n = 6 animals per group for radiotherapy and n = 4 for virotherapy.

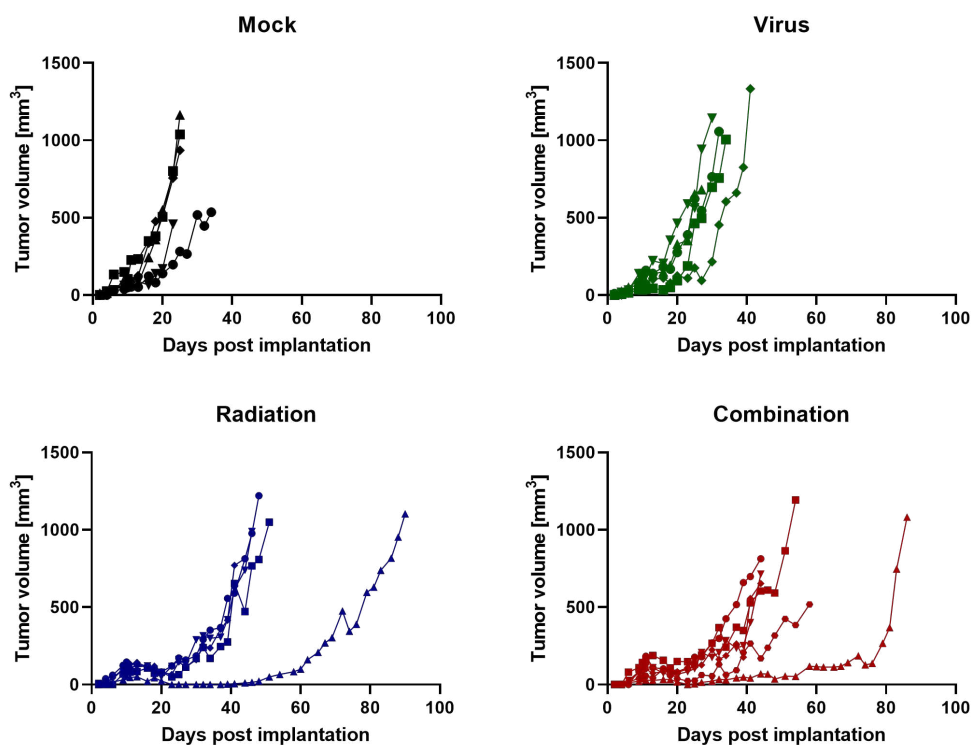


**Figure A26: Tumor growth after radiovirotherapy *in vivo*.** Once the injected MOC2-hCD46 cells s.c. on the left thigh of C57BL/6J mice grew to tumors of a mean volume of 100 – 150 mm<sup>3</sup>, the mice were allocated to four groups. They received either mock treatment (black), 3 doses of 5 Gy irradiation (blue), 3 i.t. injections of 1·10<sup>6</sup> ciu MeVac (green) or the RVTx combination (red) according to the treatment schedule (see Figure 4.19A). I monitored tumor volumes and survival to evaluate treatment efficacy. The graphs show individual tumor growth curves of n = 5 animals per group for mock, radio- and virotherapy and n = 6 for combination.

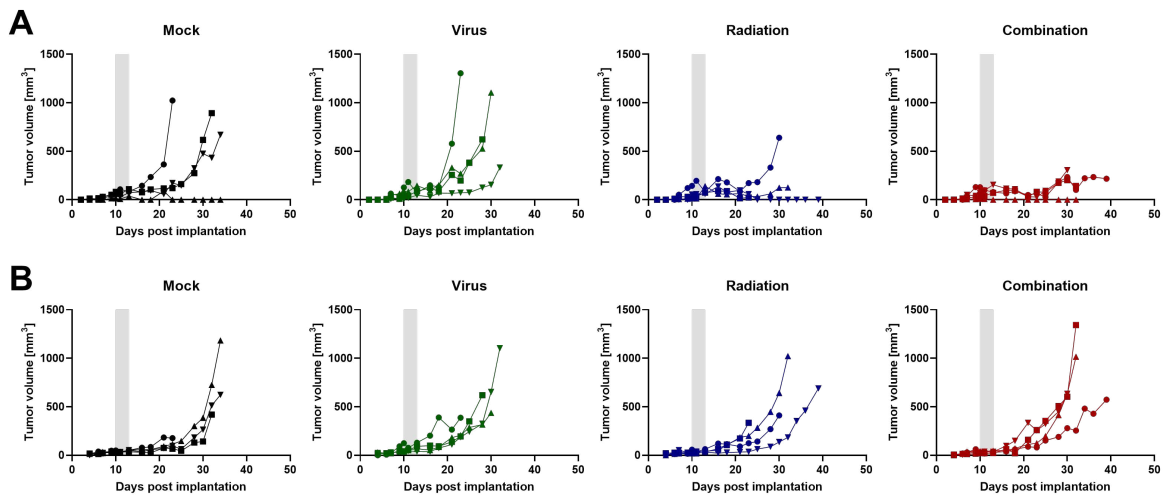


**Figure A27: Analysis of abscopal effects after RVTx *in vivo*.** To investigate an abscopal effect of RVTx, I injected secondary MOC2-hCD46 tumors on the right flank of C57BL/6J mice two days after primary tumors on the left thigh. Once the primary tumors reached a mean tumor volume of  $100 - 150 \text{ mm}^3$ , mice were allocated to four groups. They received either mock-treatment (black), 3 doses of 5 Gy irradiation (blue), 3 i.t. injections of  $1 \cdot 10^6$  ciu MeVac (green) or the RVTx combination (red) according to the treatment schedule (see Figure 4.19A). I monitored tumor volumes of (A) primary tumors on the thigh and (B) secondary on the flank. The grey area in the tumor growth curves indicate the time frame of the corresponding treatment. The graphs show individual tumor growth curves of  $n = 4$  animals per group.

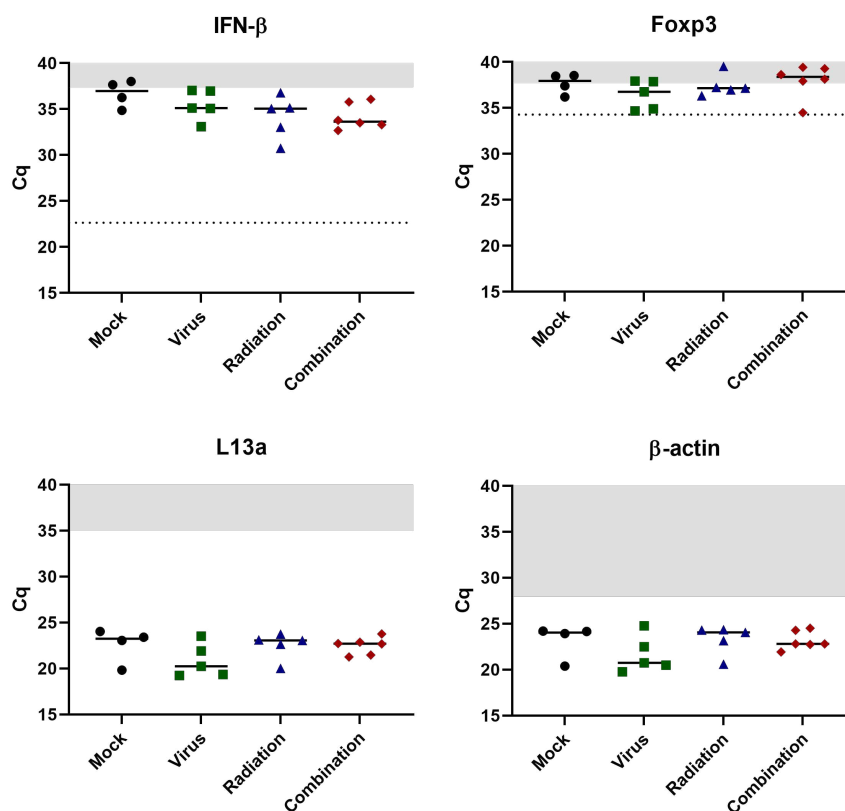


**Figure A28:** Cq values for *in vivo* analysis of IFN- $\beta$  and Foxp3 after RVTx. I analyzed the expression of the murine *Ifnb1* and *Foxp3* genes on transcriptomic level from treated MOC2-hCD46 tumors by qPCR. Murine *Rpl13a* and *Actb* encoding L13a and  $\beta$ -actin served as housekeeping controls. The grey area indicates the technical limit of each qPCR experiment corresponding to signals of no template or no reverse transcriptase control. The graphs show mean data of triplicate samples per mouse of  $n = 4$  animals per group for mock,  $n = 5$  for radio- as well as virotherapy and  $n = 6$  for combination. Cq — quantification cycle.

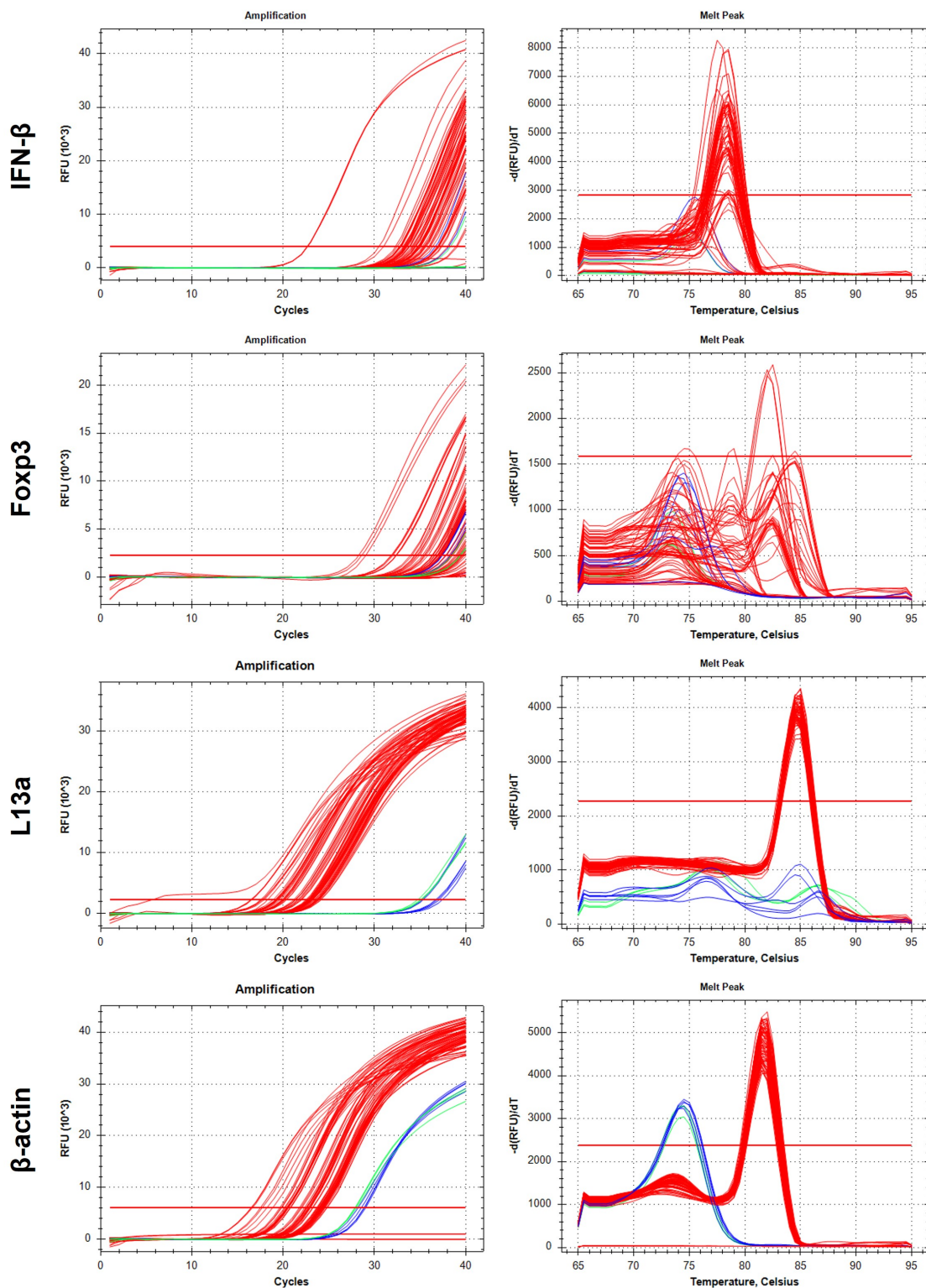


**Figure A29: Amplification and melting curves for qPCR analysis of IFN- $\beta$  and Foxp3 after RVTx.** After treatment of MOC2-hCD46 tumors in mice with RVTx, I analyzed the expression of the murine *Ifnb1* and *Foxp3* genes by qPCR. *RPL13a* and *Actb* served as housekeeping controls. Amplification (left) and melting curves (right) of triplicates for each sample are shown in red, no template controls in green and no reverse transcriptase controls in blue.

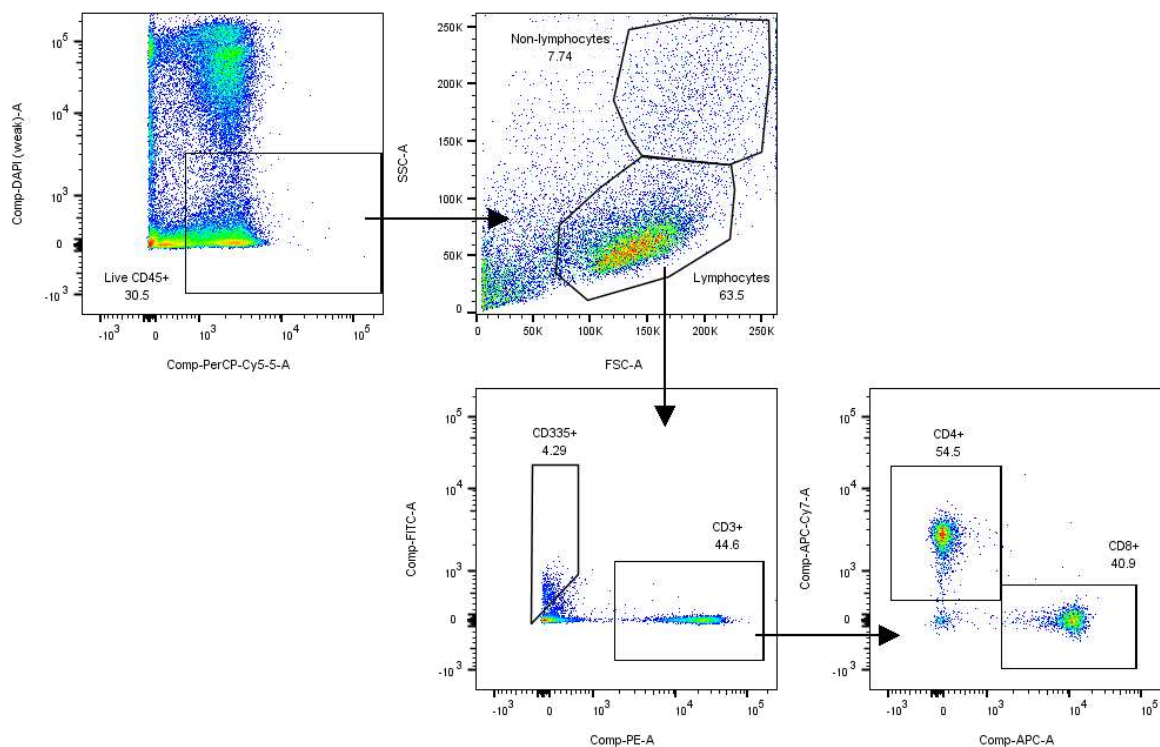


**Figure A30: Gating strategy for analysis of TILs after RVTx *in vivo*.** To analyze cell populations of interest, I first identified live leukocytes using DAPI and a PerCP-Cy<sup>TM</sup>5.5-conjugated anti-CD45 antibody. To discriminate the lymphocyte population from debris and non-lymphocytes, I used forward (FSC-A, -H) and side scatter (SSC-A) parameters. By plotting PE-conjugated CD3<sup>+</sup> against FITC-conjugated CD335<sup>+</sup> cells, I separated T cells from NK cells. The former could be further characterized into CD4<sup>+</sup> and CD8<sup>+</sup> cells by APC-Cy<sup>TM</sup>7- and APC-conjugated antibodies.

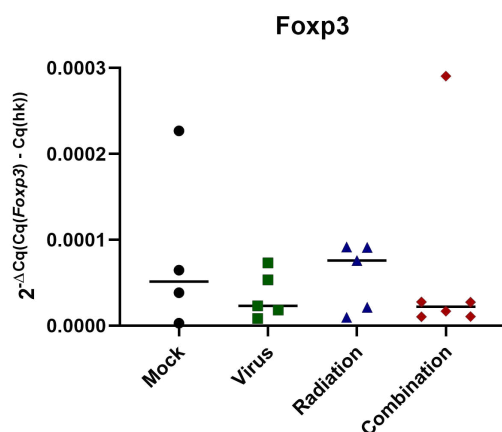


**Figure A31: *In vivo* expression of *Foxp3* after RVTx.** To analyze early T cell regulation, I investigated the expression of *Foxp3* on transcriptomic level in tumors of animals two days after the final treatment. The treatment overview is shown in Figure 4.20. After RNA extraction and cDNA synthesis, I performed qPCR analysis of the *Foxp3* gene. *Rpl13a* as well as *Actb* served as housekeeping controls. Statistical analysis was performed using one-way ANOVA with Tukey correction for multiple comparison testing. The graph shows mean data of technical replicates per mouse of  $n = 4$  animals per group for mock,  $n = 5$  for radio- as well as virotherapy and  $n = 6$  for combination. Cq — quantification cycle; hk — mean of housekeeping controls.

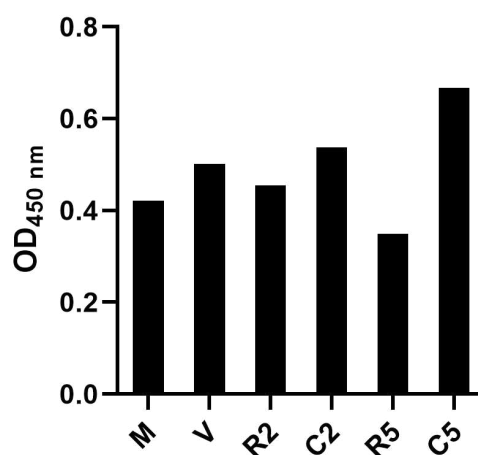


**Figure A32: HMGB1 release of RVTx-treated PDAC spheroids.** I analyzed the release of HMGB1 72 h after treating PDAC spheroids with RVTx. I collected supernatants and performed HMGB1 ELISA using pooled triplicates per sample. The graph shows data of a single experiment. OD<sub>450 nm</sub> — optical density at 450 nm; M — mock; V — virus; R2, R5 — radiation with 2 or 5 Gy; C2, C5 — combination with 2 or 5 Gy irradiation.

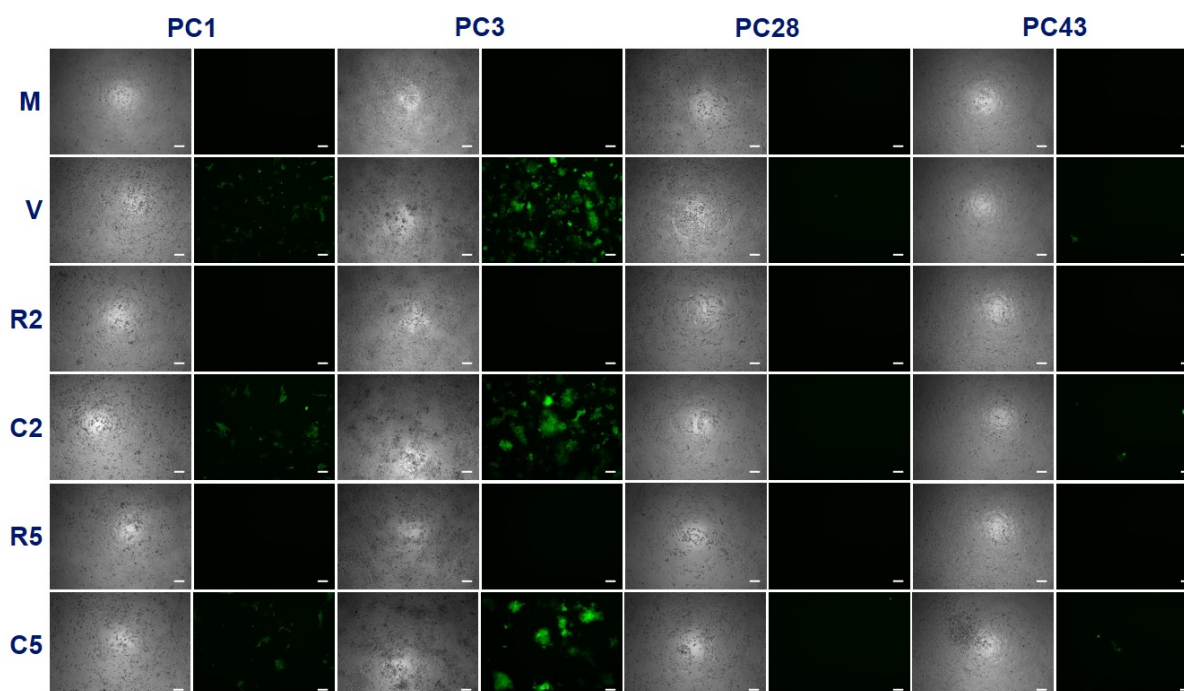


**Figure A33: RVTx treatment of patient-derived PDAC cultures.** As a second model to study RVTx *ex vivo*, I used patient-derived PDAC cultures, irradiated (2 or 5 Gy) and infected (MOI = 1) them according to the R24V schedule and monitored virus susceptibility and cell growth via fluorescence microscopy at 72 h p.tr.. Images were taken in phase contrast and green fluorescence channel. The images show representatives of triplicates per sample from one experiment. Scale bar: 50  $\mu\text{m}$ . M — mock; V — virus; R2, R5 — radiation with 2 or 5 Gy; C2, C5 — combination with 2 or 5 Gy irradiation.

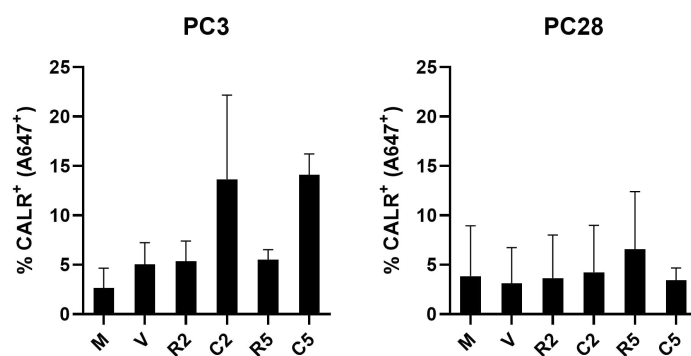


**Figure A34: Surface-exposed CALR after RVTx *ex vivo*.** I treated PC3 and PC28 cultures with RVTx and detected surface-CALR by FC analysis 48 h p.tr.. Statistical analysis was performed using one-way ANOVA with Tukey correction for multiple comparison testing. The graphs show mean and SD of  $n = 2$  independent experiments. CALR — calreticulin; M — mock; V — virus; R2, R5 — radiation with 2 or 5 Gy; C2, C5 — combination with 2 or 5 Gy irradiation.

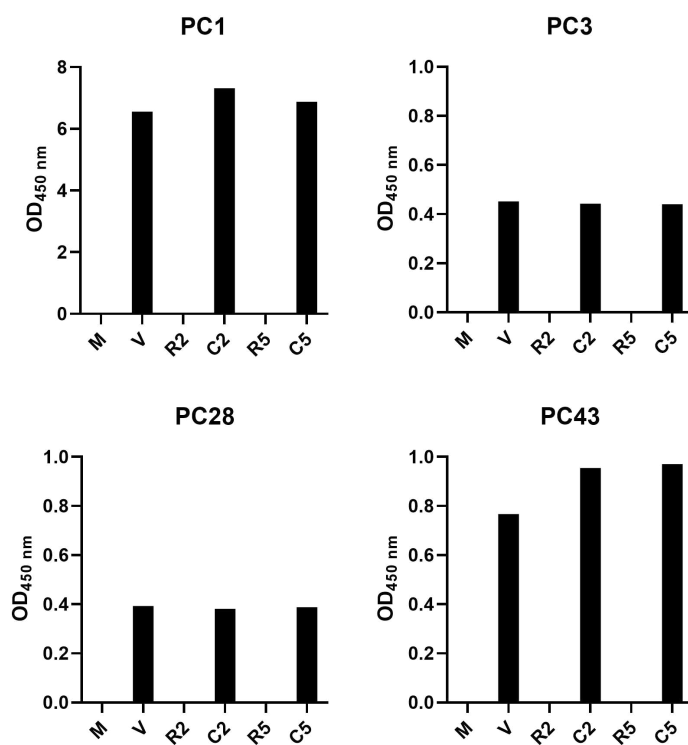


**Figure A35: IFN- $\beta$  release in treated PDAC cultures.** I treated patient-derived PDAC cultures with RVTx, collected supernatants 24 h p.tr. and detected released IFN- $\beta$  by ELISA. The graphs show data of pooled triplicates per condition of one experiment. OD<sub>450 nm</sub> — optical density at 450 nm; M — mock; V — virus; R2, R5 — radiation with 2 or 5 Gy; C2, C5 — combination with 2 or 5 Gy irradiation.

# Bibliography

- [1] I. B. Weinstein and K. Case. “The history of Cancer Research: introducing an AACR Centennial series”. In: *Cancer Res* 68.17 (Sept. 2008), pp. 6861–6862.
- [2] F. Bray, M. Laversanne, E. Weiderpass, and I. Soerjomataram. “The ever-increasing importance of cancer as a leading cause of premature death worldwide”. In: *Cancer* 127.16 (Aug. 2021), pp. 3029–3030.
- [3] H. Sung, J. Ferlay, R. L. Siegel, M. Laversanne, I. Soerjomataram, A. Jemal, and F. Bray. “Global Cancer Statistics 2020: GLOBOCAN Estimates of Incidence and Mortality Worldwide for 36 Cancers in 185 Countries”. In: *CA Cancer J Clin* 71.3 (May 2021), pp. 209–249.
- [4] B. Cao, F. Bray, A. Ilbawi, and I. Soerjomataram. “Effect on longevity of one-third reduction in premature mortality from non-communicable diseases by 2030: a global analysis of the Sustainable Development Goal health target”. In: *Lancet Glob Health* 6.12 (Dec. 2018), e1288–e1296.
- [5] J. Ferlay, M. Ervik, F. Lam, M. Colombet, L. Mery, M. Piñeros, A. Znaor, I. Soerjomataram, and F. Bray. *Global Cancer Observatory: Cancer Today*. Lyon, France: International Agency for Research on Cancer. 2020. URL: <https://gco.iarc.fr/today>.
- [6] R. L. Siegel, K. D. Miller, H. E. Fuchs, and A. Jemal. “Cancer statistics, 2022”. In: *CA Cancer J Clin* 72.1 (Jan. 2022), pp. 7–33.
- [7] F. Bray, J. Ferlay, I. Soerjomataram, R. L. Siegel, L. A. Torre, and A. Jemal. “Global cancer statistics 2018: GLOBOCAN estimates of incidence and mortality worldwide for 36 cancers in 185 countries”. In: *CA Cancer J Clin* 68.6 (Nov. 2018), pp. 394–424.
- [8] P. Hunter. “The fourth pillar: Despite some setbacks in the clinic, immunotherapy has made notable progress toward becoming an additional therapeutic option against cancer”. In: *EMBO Rep* 18.11 (Nov. 2017), pp. 1889–1892.
- [9] J. Ferlay, M. Colombet, I. Soerjomataram, D. M. Parkin, M. Piñeros, A. Znaor, and F. Bray. “Cancer statistics for the year 2020: An overview”. In: *Int J Cancer* (Apr. 2021).

- [10] T. J. Grant, K. Hua, and A. Singh. “Molecular Pathogenesis of Pancreatic Cancer”. In: *Prog Mol Biol Transl Sci* 144 (2016), pp. 241–275.
- [11] P. Rawla, T. Sunkara, and V. Gaduputi. “Epidemiology of Pancreatic Cancer: Global Trends, Etiology and Risk Factors”. In: *World J Oncol* 10.1 (Feb. 2019), pp. 10–27.
- [12] D. R. Principe, P. W. Underwood, M. Korc, J. G. Trevino, H. G. Munshi, and A. Rana. “The Current Treatment Paradigm for Pancreatic Ductal Adenocarcinoma and Barriers to Therapeutic Efficacy”. In: *Front Oncol* 11 (2021), p. 688377.
- [13] M. S. De La Cruz, A. P. Young, and M. T. Ruffin. “Diagnosis and management of pancreatic cancer”. In: *Am Fam Physician* 89.8 (Apr. 2014), pp. 626–632.
- [14] J. Werner, S. E. Combs, C. Springfield, W. Hartwig, T. Hackert, and M. W. Büchler. “Advanced-stage pancreatic cancer: therapy options”. In: *Nat Rev Clin Oncol* 10.6 (June 2013), pp. 323–333.
- [15] M. Orth, P. Metzger, S. Gerum, J. Mayerle, G. Schneider, C. Belka, M. Schnurr, and K. Lauber. “Pancreatic ductal adenocarcinoma: biological hallmarks, current status, and future perspectives of combined modality treatment approaches”. In: *Radiat Oncol* 14.1 (Aug. 2019), p. 141.
- [16] S. Mohammed, G. Van Buren, and W. E. Fisher. “Pancreatic cancer: advances in treatment”. In: *World J Gastroenterol* 20.28 (July 2014), pp. 9354–9360.
- [17] R. H. Nanda, B. El-Rayes, S. K. Maithel, and J. Landry. “Neoadjuvant modified FOLFIRINOX and chemoradiation therapy for locally advanced pancreatic cancer improves resectability”. In: *J Surg Oncol* 111.8 (June 2015), pp. 1028–1034.
- [18] F. Huguet, S. Mukherjee, and M. Javle. “Locally advanced pancreatic cancer: the role of definitive chemoradiotherapy”. In: *Clin Oncol (R Coll Radiol)* 26.9 (Sept. 2014), pp. 560–568.
- [19] U.S. National Library of Medicine. *ClinicalTrials.gov*. 2022. URL: <https://clinicaltrials.gov/ct2/home>.
- [20] D. S. Hong, M. G. Fakih, J. H. Strickler, J. Desai, G. A. Durm, G. I. Shapiro, G. S. Falchook, T. J. Price, A. Sacher, C. S. Denlinger, Y. J. Bang, G. K. Dy, J. C. Krauss, Y. Kuboki, J. C. Kuo, A. L. Coveler, K. Park, T. W. Kim, F. Barlesi, P. N. Munster, S. S. Ramalingam, T. F. Burns, F. Meric-Bernstam, H. Hensley, J. Ngang, G. Ngarmchamnanrith, J. Kim, B. E. Houk, J. Canon, J. R. Lipford, G. Friberg, P. Lito, R. Govindan, and B. T. Li. “KRAS(G12C) Inhibition with Sotorasib in Advanced Solid Tumors”. In: *N Engl J Med* 383.13 (Sept. 2020), pp. 1207–1217.

- 
- [21] D. Baumann, J. Drebant, T. Hägele, L. Burger, C. Serger, C. Lauenstein, P. Dudys, G. Erdmann, and R. Offringa. “p38 MAPK signaling in M1 macrophages results in selective elimination of M2 macrophages by MEK inhibition”. In: *J Immunother Cancer* 9.7 (July 2021).
- [22] A. V. Vaseva, D. R. Blake, T. S. K. Gilbert, S. Ng, G. Hostetter, S. H. Azam, I. Ozkan-Dagliyan, P. Gautam, K. L. Bryant, K. H. Pearce, L. E. Herring, H. Han, L. M. Graves, A. K. Witkiewicz, E. S. Knudsen, C. V. Pecot, N. Rashid, P. J. Houghton, K. Wennerberg, A. D. Cox, and C. J. Der. “KRAS Suppression-Induced Degradation of MYC Is Antagonized by a MEK5-ERK5 Compensatory Mechanism”. In: *Cancer Cell* 34.5 (Nov. 2018), pp. 807–822.
- [23] T. K. Hayes, N. F. Neel, C. Hu, P. Gautam, M. Chenard, B. Long, M. Aziz, M. Kassner, K. L. Bryant, M. Pierobon, R. Marayati, S. Kher, S. D. George, M. Xu, A. Wang-Gillam, A. A. Samatar, A. Maitra, K. Wennerberg, E. F. Petricoin, H. H. Yin, B. Nelkin, A. D. Cox, J. J. Yeh, and C. J. Der. “Long-Term ERK Inhibition in KRAS-Mutant Pancreatic Cancer Is Associated with MYC Degradation and Senescence-like Growth Suppression”. In: *Cancer Cell* 29.1 (Jan. 2016), pp. 75–89.
- [24] M. J. Moore, D. Goldstein, J. Hamm, A. Figer, J. R. Hecht, S. Gallinger, H. J. Au, P. Murawa, D. Walde, R. A. Wolff, D. Campos, R. Lim, K. Ding, G. Clark, T. Voskoglou-Nomikos, M. Ptasynski, and W. Parulekar. “Erlotinib plus gemcitabine compared with gemcitabine alone in patients with advanced pancreatic cancer: a phase III trial of the National Cancer Institute of Canada Clinical Trials Group”. In: *J Clin Oncol* 25.15 (May 2007), pp. 1960–1966.
- [25] J. R. Brahmer, S. S. Tykodi, L. Q. Chow, W. J. Hwu, S. L. Topalian, P. Hwu, C. G. Drake, L. H. Camacho, J. Kauh, K. Odunsi, H. C. Pitot, O. Hamid, S. Bhatia, R. Martins, K. Eaton, S. Chen, T. M. Salay, S. Alaparthi, J. F. Grosso, A. J. Korman, S. M. Parker, S. Agrawal, S. M. Goldberg, D. M. Pardoll, A. Gupta, and J. M. Wigginton. “Safety and activity of anti-PD-L1 antibody in patients with advanced cancer”. In: *N Engl J Med* 366.26 (June 2012), pp. 2455–2465.
- [26] R. E. Royal, C. Levy, K. Turner, A. Mathur, M. Hughes, U. S. Kammula, R. M. Sherry, S. L. Topalian, J. C. Yang, I. Lowy, and S. A. Rosenberg. “Phase 2 trial of single agent Ipilimumab (anti-CTLA-4) for locally advanced or metastatic pancreatic adenocarcinoma”. In: *J Immunother* 33.8 (Oct. 2010), pp. 828–833.
- [27] I. H. Sahin, G. Askan, Z. I. Hu, and E. M. O’Reilly. “Immunotherapy in pancreatic ductal adenocarcinoma: an emerging entity?” In: *Ann Oncol* 28.12 (Dec. 2017), pp. 2950–2961.

- [28] J. Kleeff, M. Korc, M. Apte, C. La Vecchia, C. D. Johnson, A. V. Biankin, R. E. Neale, M. Tempero, D. A. Tuveson, R. H. Hruban, and J. P. Neoptolemos. “Pancreatic cancer”. In: *Nat Rev Dis Primers* 2 (Apr. 2016), p. 16022.
- [29] D. E. Johnson, B. Burtneß, C. R. Leemans, V. W. Y. Lui, J. E. Bauman, and J. R. Grandis. “Head and neck squamous cell carcinoma”. In: *Nat Rev Dis Primers* 6.1 (Nov. 2020), p. 92.
- [30] A. P. Stein, S. Saha, J. L. Kraninger, A. D. Swick, M. Yu, P. F. Lambert, and R. J. Kimple. “Prevalence of Human Papillomavirus in Oropharyngeal Cancer: A Systematic Review”. In: *Cancer J* 21.3 (2015), pp. 138–146.
- [31] M. Taberna, M. Mena, M. A. Pavón, L. Alemany, M. L. Gillison, and R. Mesía. “Human papillomavirus-related oropharyngeal cancer”. In: *Ann Oncol* 28.10 (Oct. 2017), pp. 2386–2398.
- [32] P. Economopoulou, R. de Bree, I. Kotsantis, and A. Psyrri. “Diagnostic Tumor Markers in Head and Neck Squamous Cell Carcinoma (HNSCC) in the Clinical Setting”. In: *Front Oncol* 9 (2019), p. 827.
- [33] K. Munger, T. K. Gwin, and M. E. McLaughlin-Drubin. “p16 in HPV-associated cancers”. In: *Oncotarget* 4.11 (Nov. 2013), pp. 1864–1865.
- [34] D. T. Xing, R. Khor, H. Gan, M. Wada, T. Ermongkonchai, and S. P. Ng. “Recent Research on Combination of Radiotherapy with Targeted Therapy or Immunotherapy in Head and Neck Squamous Cell Carcinoma: A Review for Radiation Oncologists”. In: *Cancers (Basel)* 13.22 (Nov. 2021).
- [35] B. Lacas, A. Carmel, C. Landais, S. J. Wong, L. Licitra, J. S. Tobias, B. Burtneß, M. G. Ghi, E. E. W. Cohen, C. Grau, et al. “Meta-analysis of chemotherapy in head and neck cancer (MACH-NC): An update on 107 randomized trials and 19,805 patients, on behalf of MACH-NC Group”. In: *Radiother Oncol* 156 (Mar. 2021), pp. 281–293.
- [36] J. E. Bates and C. E. Steuer. “HPV as a Carcinomic Driver in Head and Neck Cancer: a De-escalated Future?” In: *Curr Treat Options Oncol* 23.3 (Mar. 2022), pp. 325–332.
- [37] J. A. Bonner, P. M. Harari, J. Giralt, N. Azarnia, D. M. Shin, R. B. Cohen, C. U. Jones, R. Sur, D. Raben, J. Jassem, R. Ove, M. S. Kies, J. Baselga, H. Youssoufian, N. Amellal, E. K. Rowinsky, and K. K. Ang. “Radiotherapy plus cetuximab for squamous-cell carcinoma of the head and neck”. In: *N Engl J Med* 354.6 (Feb. 2006), pp. 567–578.
- [38] M. L. Gillison, A. M. Trotti, J. Harris, A. Eisbruch, P. M. Harari, D. J. Adelstein, R. C. K. Jordan, W. Zhao, E. M. Sturgis, B. Burtneß, J. A. Ridge, J. Ringash, J. Galvin, M. Yao, S. A. Koyfman, D. M. Blakaj, M. A. Razaq, A. D. Colevas, J. J. Beitler, C. U. Jones, N. E. Dunlap, S. A. Seaward, S. Spencer, T. J. Galloway, J.

- Phan, J. J. Dignam, and Q. T. Le. “Radiotherapy plus cetuximab or cisplatin in human papillomavirus-positive oropharyngeal cancer (NRG Oncology RTOG 1016): a randomised, multicentre, non-inferiority trial”. In: *Lancet* 393.10166 (Jan. 2019), pp. 40–50.
- [39] H. Mehanna, M. Robinson, A. Hartley, A. Kong, B. Foran, T. Fulton-Lieuw, M. Dalby, P. Mistry, M. Sen, L. O’Toole, H. Al Booz, K. Dyker, R. Moleron, S. Whitaker, S. Brennan, A. Cook, M. Griffin, E. Aynsley, M. Rolles, E. De Winton, A. Chan, D. Srinivasan, I. Nixon, J. Grumett, C. R. Leemans, J. Buter, J. Henderson, K. Harrington, C. McConkey, A. Gray, J. Dunn, R. Moleron, O. McArdle, K. Dyker, H. Al Booz, L. O’Toole, A. Cook, D. Husband, V. Loo, W. Soe, E. Aynsley, T. Sridhar, P. Jankowska, M. Joseph, K. Geropantas, D. Vaidya, M. Griffin, A. Hartley, R. Vijayan, D. Hwang, K. Harrington, L. Pettit, S. Whitaker, E. De Winton, M. Rolles, S. Brennan, M. Sen, R. Mendes, M. Forster, A. Chan, M. Evans, J. Buter, D. Srinivasan, B. Foran, P. Nankivell, J. Bryant, N. Sharma, R. Spruce, J. Brooks, N. Batis, T. Roques, M. Bidmead, H. Yang, C. Nutting, J. Tyler, J. Henderson, H. Baines, A. Gasnier, E. Miles, C. Clark, and M. Evans. “Radiotherapy plus cisplatin or cetuximab in low-risk human papillomavirus-positive oropharyngeal cancer (De-ESCALaTE HPV): an open-label randomised controlled phase 3 trial”. In: *Lancet* 393.10166 (Jan. 2019), pp. 51–60.
- [40] M. Baumann, M. Krause, J. Overgaard, J. Debus, S. M. Bentzen, J. Daartz, C. Richter, D. Zips, and T. Bortfeld. “Radiation oncology in the era of precision medicine”. In: *Nat Rev Cancer* 16.4 (Apr. 2016), pp. 234–249.
- [41] F. Lohaus, A. Linge, I. Tinhofer, V. Budach, E. Gkika, M. Stuschke, P. Balermipas, C. Rödel, M. Avlar, A. L. Grosu, A. Abdollahi, J. Debus, C. Bayer, C. Belka, S. Pigorsch, S. E. Combs, D. Mönnich, D. Zips, C. von Neubeck, G. B. Baretton, S. Löck, H. D. Thames, M. Krause, and M. Baumann. “HPV16 DNA status is a strong prognosticator of loco-regional control after postoperative radiochemotherapy of locally advanced oropharyngeal carcinoma: results from a multicentre explorative study of the German Cancer Consortium Radiation Oncology Group (DKTK-ROG)”. In: *Radiother Oncol* 113.3 (Dec. 2014), pp. 317–323.
- [42] K. K. Ang, J. Harris, R. Wheeler, R. Weber, D. I. Rosenthal, P. F. Nguyen-Tân, W. H. Westra, C. H. Chung, R. C. Jordan, C. Lu, H. Kim, R. Axelrod, C. C. Silverman, K. P. Redmond, and M. L. Gillison. “Human papillomavirus and survival of patients with oropharyngeal cancer”. In: *N Engl J Med* 363.1 (July 2010), pp. 24–35.
- [43] P. Lassen, H. Primdahl, J. Johansen, C. A. Kristensen, E. Andersen, L. J. Andersen, J. F. Evensen, J. G. Eriksen, and J. Overgaard. “Impact of HPV-associated p16-expression on radiotherapy outcome in advanced oropharynx and non-oropharynx cancer”. In: *Radiother Oncol* 113.3 (Dec. 2014), pp. 310–316.

- [44] R. Mehra, T. Y. Seiwert, S. Gupta, J. Weiss, I. Gluck, J. P. Eder, B. Burtness, M. Tahara, B. Keam, H. Kang, K. Muro, R. Geva, H. C. Chung, C. C. Lin, D. Aurora-Garg, A. Ray, K. Pathiraja, J. Cheng, L. Q. M. Chow, and R. Haddad. “Efficacy and safety of pembrolizumab in recurrent/metastatic head and neck squamous cell carcinoma: pooled analyses after long-term follow-up in KEYNOTE-012”. In: *Br J Cancer* 119.2 (July 2018), pp. 153–159.
- [45] R. L. Ferris, G. Blumenschein, J. Fayette, J. Guigay, A. D. Colevas, L. Licitra, K. J. Harrington, S. Kasper, E. E. Vokes, C. Even, F. Worden, N. F. Saba, L. C. I. Docampo, R. Haddad, T. Rordorf, N. Kiyota, M. Tahara, M. Lynch, V. Jayaprakash, L. Li, and M. L. Gillison. “Nivolumab vs investigator’s choice in recurrent or metastatic squamous cell carcinoma of the head and neck: 2-year long-term survival update of CheckMate 141 with analyses by tumor PD-L1 expression”. In: *Oral Oncol* 81 (June 2018), pp. 45–51.
- [46] E. E. W. Cohen, D. Soulières, C. Le Tourneau, J. Dinis, L. Licitra, M. J. Ahn, A. Soria, J. P. Machiels, N. Mach, R. Mehra, et al. “Pembrolizumab versus methotrexate, docetaxel, or cetuximab for recurrent or metastatic head-and-neck squamous cell carcinoma (KEYNOTE-040): a randomised, open-label, phase 3 study”. In: *Lancet* 393.10167 (Jan. 2019), pp. 156–167.
- [47] B. Burtness, K. J. Harrington, R. Greil, D. Soulières, M. Tahara, G. de Castro, A. Psyrri, N. Basté, P. Neupane, Å. Bratland, et al. “Pembrolizumab alone or with chemotherapy versus cetuximab with chemotherapy for recurrent or metastatic squamous cell carcinoma of the head and neck (KEYNOTE-048): a randomised, open-label, phase 3 study”. In: *Lancet* 394.10212 (Nov. 2019), pp. 1915–1928.
- [48] J. B. Vermorken, R. Mesia, F. Rivera, E. Remenar, A. Kawecki, S. Rottey, J. Erfan, D. Zabolotnyy, H. R. Kienzer, D. Cupissol, F. Peyrade, M. Benasso, I. Vynnychenko, D. De Raucourt, C. Bokemeyer, A. Schueler, N. Amellal, and R. Hitt. “Platinum-based chemotherapy plus cetuximab in head and neck cancer”. In: *N Engl J Med* 359.11 (Sept. 2008), pp. 1116–1127.
- [49] Y. S. Lee, D. E. Johnson, and J. R. Grandis. “An update: emerging drugs to treat squamous cell carcinomas of the head and neck”. In: *Expert Opin Emerg Drugs* 23.4 (Dec. 2018), pp. 283–299.
- [50] Kenneth M. Murphy and Casey Weaver. *Janeway’s immunobiology*. 9th edition. New York, London: GS, Garland Science, Taylor and Francis Group, 2017.
- [51] J. Sia, P. J. Neeson, and N. M. Haynes. “Basic cancer immunology for radiation oncologists”. In: *J Med Imaging Radiat Oncol* 66.4 (June 2022), pp. 508–518.

- 
- [52] D. Hanahan and R. A. Weinberg. “Hallmarks of cancer: the next generation”. In: *Cell* 144.5 (Mar. 2011), pp. 646–674.
- [53] T. Li and Z. J. Chen. “The cGAS-cGAMP-STING pathway connects DNA damage to inflammation, senescence, and cancer”. In: *J Exp Med* 215.5 (May 2018), pp. 1287–1299.
- [54] R. E. Randall and S. Goodbourn. “Interferons and viruses: an interplay between induction, signalling, antiviral responses and virus countermeasures”. In: *J Gen Virol* 89.Pt 1 (Jan. 2008), pp. 1–47.
- [55] J. Wu and Z. J. Chen. “Innate immune sensing and signaling of cytosolic nucleic acids”. In: *Annu Rev Immunol* 32 (2014), pp. 461–488.
- [56] X. Feng, A. Tubbs, C. Zhang, M. Tang, S. Sridharan, C. Wang, D. Jiang, D. Su, H. Zhang, Z. Chen, L. Nie, Y. Xiong, M. Huang, A. Nussenzweig, and J. Chen. “ATR inhibition potentiates ionizing radiation-induced interferon response via cytosolic nucleic acid-sensing pathways”. In: *EMBO J* 39.14 (July 2020), e104036.
- [57] C. Lhuillier, N. P. Rudqvist, O. Elemento, S. C. Formenti, and S. Demaria. “Radiation therapy and anti-tumor immunity: exposing immunogenic mutations to the immune system”. In: *Genome Med* 11.1 (June 2019), p. 40.
- [58] L. Sun, J. Wu, F. Du, X. Chen, and Z. J. Chen. “Cyclic GMP-AMP synthase is a cytosolic DNA sensor that activates the type I interferon pathway”. In: *Science* 339.6121 (Feb. 2013), pp. 786–791.
- [59] M. Jiang, P. Chen, L. Wang, W. Li, B. Chen, Y. Liu, H. Wang, S. Zhao, L. Ye, Y. He, and C. Zhou. “cGAS-STING, an important pathway in cancer immunotherapy”. In: *J Hematol Oncol* 13.1 (June 2020), p. 81.
- [60] R. Yu, B. Zhu, and D. Chen. “Type I interferon-mediated tumor immunity and its role in immunotherapy”. In: *Cell Mol Life Sci* 79.3 (Mar. 2022), p. 191.
- [61] M. Yoneyama, M. Kikuchi, T. Natsukawa, N. Shinobu, T. Imaizumi, M. Miyagishi, K. Taira, S. Akira, and T. Fujita. “The RNA helicase RIG-I has an essential function in double-stranded RNA-induced innate antiviral responses”. In: *Nat Immunol* 5.7 (July 2004), pp. 730–737.
- [62] H. Kato, O. Takeuchi, S. Sato, M. Yoneyama, M. Yamamoto, K. Matsui, S. Uematsu, A. Jung, T. Kawai, K. J. Ishii, O. Yamaguchi, K. Otsu, T. Tsujimura, C. S. Koh, C. Reis e Sousa, Y. Matsuura, T. Fujita, and S. Akira. “Differential roles of MDA5 and RIG-I helicases in the recognition of RNA viruses”. In: *Nature* 441.7089 (May 2006), pp. 101–105.
-

- [63] J. Sprooten, P. Agostinis, and A. D. Garg. “Type I interferons and dendritic cells in cancer immunotherapy”. In: *Int Rev Cell Mol Biol* 348 (2019), pp. 217–262.
- [64] P. Matzinger. “Tolerance, danger, and the extended family”. In: *Annu Rev Immunol* 12 (1994), pp. 991–1045.
- [65] D. V. Krysko, A. D. Garg, A. Kaczmarek, O. Krysko, P. Agostinis, and P. Vandenabeele. “Immunogenic cell death and DAMPs in cancer therapy”. In: *Nat Rev Cancer* 12.12 (Dec. 2012), pp. 860–875.
- [66] A. D. Garg, D. Nowis, J. Golab, P. Vandenabeele, D. V. Krysko, and P. Agostinis. “Immunogenic cell death, DAMPs and anticancer therapeutics: an emerging amalgamation”. In: *Biochim Biophys Acta* 1805.1 (Jan. 2010), pp. 53–71.
- [67] M. E. Bianchi. “DAMPs, PAMPs and alarmins: all we need to know about danger”. In: *J Leukoc Biol* 81.1 (Jan. 2007), pp. 1–5.
- [68] W. Nickel. “The mystery of nonclassical protein secretion. A current view on cargo proteins and potential export routes”. In: *Eur J Biochem* 270.10 (May 2003), pp. 2109–2119.
- [69] A. Rubartelli and M. T. Lotze. “Inside, outside, upside down: damage-associated molecular-pattern molecules (DAMPs) and redox”. In: *Trends Immunol* 28.10 (Oct. 2007), pp. 429–436.
- [70] L. Galluzzi, I. Vitale, S. Warren, S. Adjemian, P. Agostinis, A. B. Martinez, T. A. Chan, G. Coukos, S. Demaria, E. Deutsch, D. Draganov, R. L. Edelson, S. C. Formenti, J. Fucikova, L. Gabriele, U. S. Gaipl, S. R. Gameiro, A. D. Garg, E. Golden, J. Han, K. J. Harrington, A. Hemminki, J. W. Hodge, D. M. S. Hossain, T. Illidge, M. Karin, H. L. Kaufman, O. Kepp, G. Kroemer, J. J. Lasarte, S. Loi, M. T. Lotze, G. Manic, T. Merghoub, A. A. Melcher, K. L. Mossman, F. Prosper, Ø. Rekdal, M. Rescigno, C. Riganti, A. Sistigu, M. J. Smyth, R. Spisek, J. Stagg, B. E. Strauss, D. Tang, K. Tatsuno, S. W. van Gool, P. Vandenabeele, T. Yamazaki, D. Zamarin, L. Zitvogel, A. Cesano, and F. M. Marincola. “Consensus guidelines for the definition, detection and interpretation of immunogenic cell death”. In: *J Immunother Cancer* 8.1 (Mar. 2020).
- [71] L. Galluzzi, A. Buqué, O. Kepp, L. Zitvogel, and G. Kroemer. “Immunogenic cell death in cancer and infectious disease”. In: *Nat Rev Immunol* 17.2 (Feb. 2017), pp. 97–111.
- [72] O. Krysko, T. Løve Aaes, C. Bachert, P. Vandenabeele, and D. V. Krysko. “Many faces of DAMPs in cancer therapy”. In: *Cell Death Dis* 4 (May 2013), e631.
- [73] J. Zhou, G. Wang, Y. Chen, H. Wang, Y. Hua, and Z. Cai. “Immunogenic cell death in cancer therapy: Present and emerging inducers”. In: *J Cell Mol Med* 23.8 (Aug. 2019), pp. 4854–4865.

- 
- [74] P. Gelebart, M. Opas, and M. Michalak. “Calreticulin, a Ca<sup>2+</sup>-binding chaperone of the endoplasmic reticulum”. In: *Int J Biochem Cell Biol* 37.2 (Feb. 2005), pp. 260–266.
- [75] L. Menger, E. Vacchelli, S. Adjemian, I. Martins, Y. Ma, S. Shen, T. Yamazaki, A. Q. Sukkurwala, M. Michaud, G. Mignot, F. Schlemmer, E. Sulpice, C. Locher, X. Gidrol, F. Ghiringhelli, N. Modjtahedi, L. Galluzzi, F. André, L. Zitvogel, O. Kepp, and G. Kroemer. “Cardiac glycosides exert anticancer effects by inducing immunogenic cell death”. In: *Sci Transl Med* 4.143 (July 2012), 143ra99.
- [76] M. Obeid, A. Tesniere, F. Ghiringhelli, G. M. Fimia, L. Apetoh, J. L. Perfettini, M. Castedo, G. Mignot, T. Panaretakis, N. Casares, D. Métivier, N. Larochette, P. van Endert, F. Ciccocanti, M. Piacentini, L. Zitvogel, and G. Kroemer. “Calreticulin exposure dictates the immunogenicity of cancer cell death”. In: *Nat Med* 13.1 (Jan. 2007), pp. 54–61.
- [77] M. Obeid, T. Panaretakis, A. Tesniere, N. Joza, R. Tufi, L. Apetoh, F. Ghiringhelli, L. Zitvogel, and G. Kroemer. “Leveraging the immune system during chemotherapy: moving calreticulin to the cell surface converts apoptotic death from “silent” to immunogenic”. In: *Cancer Res* 67.17 (Sept. 2007), pp. 7941–7944.
- [78] X. Chen, D. Fosco, D. E. Kline, and J. Kline. “Calreticulin promotes immunity and type I interferon-dependent survival in mice with acute myeloid leukemia”. In: *Oncoimmunology* 6.4 (2017), e1278332.
- [79] M. Michaud, I. Martins, A. Q. Sukkurwala, S. Adjemian, Y. Ma, P. Pellegatti, S. Shen, O. Kepp, M. Scoazec, G. Mignot, S. Rello-Varona, M. Tailler, L. Menger, E. Vacchelli, L. Galluzzi, F. Ghiringhelli, F. di Virgilio, L. Zitvogel, and G. Kroemer. “Autophagy-dependent anticancer immune responses induced by chemotherapeutic agents in mice”. In: *Science* 334.6062 (Dec. 2011), pp. 1573–1577.
- [80] M. R. Elliott, F. B. Chekeni, P. C. Trampont, E. R. Lazarowski, A. Kadl, S. F. Walk, D. Park, R. I. Woodson, M. Ostankovich, P. Sharma, J. J. Lysiak, T. K. Harden, N. Leitinger, and K. S. Ravichandran. “Nucleotides released by apoptotic cells act as a find-me signal to promote phagocytic clearance”. In: *Nature* 461.7261 (Sept. 2009), pp. 282–286.
- [81] F. Ghiringhelli, L. Apetoh, A. Tesniere, L. Aymeric, Y. Ma, C. Ortiz, K. Vermaelen, T. Panaretakis, G. Mignot, E. Ullrich, J. L. Perfettini, F. Schlemmer, E. Tasdemir, M. Uhl, P. Génin, A. Civas, B. Ryffel, J. Kanellopoulos, J. Tschopp, F. André, R. Lidereau, N. M. McLaughlin, N. M. Haynes, M. J. Smyth, G. Kroemer, and L. Zitvogel. “Activation of the NLRP3 inflammasome in dendritic cells induces IL-1beta-dependent adaptive immunity against tumors”. In: *Nat Med* 15.10 (Oct. 2009), pp. 1170–1178.

- [82] D. Tang, R. Kang, H. J. Zeh, and M. T. Lotze. “High-mobility group box 1 and cancer”. In: *Biochim Biophys Acta* 1799.1-2 (2010), pp. 131–140.
- [83] S. Wang and Y. Zhang. “HMGB1 in inflammation and cancer”. In: *J Hematol Oncol* 13.1 (Aug. 2020), p. 116.
- [84] C. W. Bell, W. Jiang, C. F. Reich, and D. S. Pisetsky. “The extracellular release of HMGB1 during apoptotic cell death”. In: *Am J Physiol Cell Physiol* 291.6 (Dec. 2006), pp. C1318–1325.
- [85] L. Apetoh, F. Ghiringhelli, A. Tesniere, M. Obeid, C. Ortiz, A. Criollo, G. Mignot, M. C. Maiuri, E. Ullrich, P. Saulnier, H. Yang, S. Amigorena, B. Ryffel, F. J. Barrat, P. Saftig, F. Levi, R. Lidereau, C. Nogues, J. P. Mira, A. Chompret, V. Joulin, F. Clavel-Chapelon, J. Bourhis, F. André, S. Delalogue, T. Tursz, G. Kroemer, and L. Zitvogel. “Toll-like receptor 4-dependent contribution of the immune system to anticancer chemotherapy and radiotherapy”. In: *Nat Med* 13.9 (Sept. 2007), pp. 1050–1059.
- [86] H. Yang, H. S. Hreggvidsdottir, K. Palmblad, H. Wang, M. Ochani, J. Li, B. Lu, S. Chavan, M. Rosas-Ballina, Y. Al-Abed, S. Akira, A. Bierhaus, H. Erlandsson-Harris, U. Andersson, and K. J. Tracey. “A critical cysteine is required for HMGB1 binding to Toll-like receptor 4 and activation of macrophage cytokine release”. In: *Proc Natl Acad Sci U S A* 107.26 (June 2010), pp. 11942–11947.
- [87] J. M. Curtsinger and M. F. Mescher. “Inflammatory cytokines as a third signal for T cell activation”. In: *Curr Opin Immunol* 22.3 (June 2010), pp. 333–340.
- [88] R. E. Tay, E. K. Richardson, and H. C. Toh. “T cells in cancer immunotherapy-new insights into old paradigms”. In: *Cancer Gene Ther* 28.1-2 (Feb. 2021), pp. 5–17.
- [89] Y. Togashi, K. Shitara, and H. Nishikawa. “Regulatory T cells in cancer immunosuppression - implications for anticancer therapy”. In: *Nat Rev Clin Oncol* 16.6 (June 2019), pp. 356–371.
- [90] L. Lu, J. Barbi, and F. Pan. “The regulation of immune tolerance by FOXP3”. In: *Nat Rev Immunol* 17.11 (Nov. 2017), pp. 703–717.
- [91] S. Sakaguchi, T. Yamaguchi, T. Nomura, and M. Ono. “Regulatory T cells and immune tolerance”. In: *Cell* 133.5 (May 2008), pp. 775–787.
- [92] D. S. Chen and I. Mellman. “Oncology meets immunology: the cancer-immunity cycle”. In: *Immunity* 39.1 (July 2013), pp. 1–10.
- [93] R. Baskar, J. Dai, N. Wenlong, R. Yeo, and K. W. Yeoh. “Biological response of cancer cells to radiation treatment”. In: *Front Mol Biosci* 1 (2014), p. 24.

- 
- [94] P. J. Hoskin and I. S. Bhattacharya. “Protons and more: state of the art in radiotherapy”. In: *Clin Med (Lond)* 14 Suppl 6 (Dec. 2014), s61–65.
- [95] E. J. Hall. “Cancer caused by x-rays—a random event?” In: *Lancet Oncol* 8.5 (May 2007), pp. 369–370.
- [96] M. Wannemacher, F. Wenz, and J. Debus. *Strahlentherapie*. 2., überarb. Aufl. 2013. Berlin, Heidelberg: Springer, 2013.
- [97] R. J. Sabin and R. M. Anderson. “Cellular Senescence - its role in cancer and the response to ionizing radiation”. In: *Genome Integr* 2.1 (Aug. 2011), p. 7.
- [98] M. Serrano. “The tumor suppressor protein p16INK4a”. In: *Exp Cell Res* 237.1 (Nov. 1997), pp. 7–13.
- [99] M. Shahidi, H. Mozdarani, and W. U. Mueller. “Radiosensitivity and repair kinetics of gamma-irradiated leukocytes from sporadic prostate cancer patients and healthy individuals assessed by alkaline comet assay”. In: *Iran Biomed J* 14.3 (July 2010), pp. 67–75.
- [100] Y. Lee, S. L. Auh, Y. Wang, B. Burnette, Y. Wang, Y. Meng, M. Beckett, R. Sharma, R. Chin, T. Tu, R. R. Weichselbaum, and Y. X. Fu. “Therapeutic effects of ablative radiation on local tumor require CD8+ T cells: changing strategies for cancer treatment”. In: *Blood* 114.3 (July 2009), pp. 589–595.
- [101] S. Demaria and S. C. Formenti. “Role of T lymphocytes in tumor response to radiotherapy”. In: *Front Oncol* 2 (2012), p. 95.
- [102] A. Gupta, H. C. Probst, V. Vuong, A. Landshammer, S. Muth, H. Yagita, R. Schwendener, M. Pruschy, A. Knuth, and M. van den Broek. “Radiotherapy promotes tumor-specific effector CD8+ T cells via dendritic cell activation”. In: *J Immunol* 189.2 (July 2012), pp. 558–566.
- [103] K. A. Pilonis, M. Charpentier, E. Garcia-Martinez, C. Daviaud, J. Kraynak, J. Aryankalayil, S. C. Formenti, and S. Demaria. “Radiotherapy Cooperates with IL15 to Induce Antitumor Immune Responses”. In: *Cancer Immunol Res* 8.8 (Aug. 2020), pp. 1054–1063.
- [104] B. C. Burnette, H. Liang, Y. Lee, L. Chlewicki, N. N. Khodarev, R. R. Weichselbaum, Y. X. Fu, and S. L. Auh. “The efficacy of radiotherapy relies upon induction of type I interferon-dependent innate and adaptive immunity”. In: *Cancer Res* 71.7 (Apr. 2011), pp. 2488–2496.
- [105] M. Charpentier, S. Spada, S. J. Van Nest, and S. Demaria. “Radiation therapy-induced remodeling of the tumor immune microenvironment”. In: *Semin Cancer Biol* (Apr. 2022).

- [106] R. R. Weichselbaum, H. Liang, L. Deng, and Y. X. Fu. “Radiotherapy and immunotherapy: a beneficial liaison?” In: *Nat Rev Clin Oncol* 14.6 (June 2017), pp. 365–379.
- [107] M. Zhu, M. Yang, J. Zhang, Y. Yin, X. Fan, Y. Zhang, S. Qin, H. Zhang, and F. Yu. “Immunogenic Cell Death Induction by Ionizing Radiation”. In: *Front Immunol* 12 (2021), p. 705361.
- [108] S. C. Formenti and S. Demaria. “Systemic effects of local radiotherapy”. In: *Lancet Oncol* 10.7 (July 2009), pp. 718–726.
- [109] G. Kroemer and L. Zitvogel. “Abscopal but desirable: The contribution of immune responses to the efficacy of radiotherapy”. In: *Oncoimmunology* 1.4 (July 2012), pp. 407–408.
- [110] K. Reynders, T. Illidge, S. Siva, J. Y. Chang, and D. De Ruyscher. “The abscopal effect of local radiotherapy: using immunotherapy to make a rare event clinically relevant”. In: *Cancer Treat Rev* 41.6 (June 2015), pp. 503–510.
- [111] D. Forner, P. Horwich, J. R. Trites, H. Hollenhorst, M. Bullock, and N. W. D. Lamond. “The abscopal effect in head-and-neck squamous cell carcinoma treated with radiotherapy and nivolumab: a case report and literature review”. In: *Curr Oncol* 27.6 (Dec. 2020), pp. 330–335.
- [112] N. Brix, A. Tiefenthaler, H. Anders, C. Belka, and K. Lauber. “Abscopal, immunological effects of radiotherapy: Narrowing the gap between clinical and preclinical experiences”. In: *Immunol Rev* 280.1 (Nov. 2017), pp. 249–279.
- [113] C. Allen, S. Her, and D. A. Jaffray. “Radiotherapy for Cancer: Present and Future”. In: *Adv Drug Deliv Rev* 109 (Jan. 2017), pp. 1–2.
- [114] M. Durante and J. S. Loeffler. “Charged particles in radiation oncology”. In: *Nat Rev Clin Oncol* 7.1 (Jan. 2010), pp. 37–43.
- [115] J. Staffurth, A. Barrett, J. Barrett, C. Beardmore, T. Cooper, S. Davies, S. Hood, R. Mackay, P. Mayles, A. Poynter, P. Price, D. Routsis, J. Staffurth, S. Thomas, and M. Williams. “A review of the clinical evidence for intensity-modulated radiotherapy”. In: *Clin Oncol (R Coll Radiol)* 22.8 (Oct. 2010), pp. 643–657.
- [116] K. Tipton, J. H. Launders, R. Inamdar, C. Miyamoto, and K. Schoelles. “Stereotactic body radiation therapy: scope of the literature”. In: *Ann Intern Med* 154.11 (June 2011), pp. 737–745.
- [117] M. Orth, K. Lauber, M. Niyazi, A. A. Friedl, M. Li, C. Maihöfer, L. Schüttrumpf, A. Ernst, O. M. Niemöller, and C. Belka. “Current concepts in clinical radiation oncology”. In: *Radiat Environ Biophys* 53.1 (Mar. 2014), pp. 1–29.

- 
- [118] W. Kim, S. Lee, D. Seo, D. Kim, K. Kim, E. Kim, J. Kang, K. M. Seong, H. Youn, and B. Youn. “Cellular Stress Responses in Radiotherapy”. In: *Cells* 8.9 (Sept. 2019).
- [119] S. Rey, L. Schito, M. Koritzinsky, and B. G. Wouters. “Molecular targeting of hypoxia in radiotherapy”. In: *Adv Drug Deliv Rev* 109 (Jan. 2017), pp. 45–62.
- [120] K. C. Bhuyan and D. K. Bhuyan. “Superoxide dismutase of the eye: relative functions of superoxide dismutase and catalase in protecting the ocular lens from oxidative damage”. In: *Biochim Biophys Acta* 542.1 (Aug. 1978), pp. 28–38.
- [121] C. Glorieux and P. B. Calderon. “Catalase, a remarkable enzyme: targeting the oldest antioxidant enzyme to find a new cancer treatment approach”. In: *Biol Chem* 398.10 (Sept. 2017), pp. 1095–1108.
- [122] B. Boulianne and N. Feldhahn. “Transcribing malignancy: transcription-associated genomic instability in cancer”. In: *Oncogene* 37.8 (Feb. 2018), pp. 971–981.
- [123] R. N. Rinkel, I. M. Verdonck-de Leeuw, P. Doornaert, J. Buter, R. de Bree, J. A. Langendijk, N. K. Aaronson, and C. R. Leemans. “Prevalence of swallowing and speech problems in daily life after chemoradiation for head and neck cancer based on cut-off scores of the patient-reported outcome measures SWAL-QOL and SHI”. In: *Eur Arch Otorhinolaryngol* 273.7 (July 2016), pp. 1849–1855.
- [124] S. A. Kraaijenga, I. M. Oskam, R. J. van Son, O. Hamming-Vrieze, F. J. Hilgers, M. W. van den Brekel, and L. van der Molen. “Assessment of voice, speech, and related quality of life in advanced head and neck cancer patients 10-years+ after chemoradiotherapy”. In: *Oral Oncol* 55 (Apr. 2016), pp. 24–30.
- [125] W. J. Moss and D. E. Griffin. “Global measles elimination”. In: *Nat Rev Microbiol* 4.12 (Dec. 2006), pp. 900–908.
- [126] A. Azap and F. Pehlivanoglu. “Chapter 26 - Measles”. In: *Emerging Infectious Diseases*. Ed. by Ö. Ergönül, F. Can, L. Madoff, and M. Akova. Amsterdam: Academic Press, 2014, pp. 347–357.
- [127] S. Delpeut, R. S. Noyce, R. W. Siu, and C. D. Richardson. “Host factors and measles virus replication”. In: *Curr Opin Virol* 2.6 (Dec. 2012), pp. 773–783.
- [128] C. L. Parks, R. A. Lerch, P. Walpita, H. P. Wang, M. S. Sidhu, and S. A. Udem. “Analysis of the noncoding regions of measles virus strains in the Edmonston vaccine lineage”. In: *J Virol* 75.2 (Jan. 2001), pp. 921–933.
- [129] T. F. Wild, E. Malvoisin, and R. Buckland. “Measles virus: both the haemagglutinin and fusion glycoproteins are required for fusion”. In: *J Gen Virol* 72 ( Pt 2) (Feb. 1991), pp. 439–442.
-

- [130] J. B. Patterson, D. Thomas, H. Lewicki, M. A. Billeter, and M. B. Oldstone. “V and C proteins of measles virus function as virulence factors in vivo”. In: *Virology* 267.1 (Feb. 2000), pp. 80–89.
- [131] P. Devaux, G. Hodge, M. B. McChesney, and R. Cattaneo. “Attenuation of V- or C-defective measles viruses: infection control by the inflammatory and interferon responses of rhesus monkeys”. In: *J Virol* 82.11 (June 2008), pp. 5359–5367.
- [132] J. M. Fontana, B. Bankamp, W. J. Bellini, and P. A. Rota. “Regulation of interferon signaling by the C and V proteins from attenuated and wild-type strains of measles virus”. In: *Virology* 374.1 (Apr. 2008), pp. 71–81.
- [133] Y. Nakatsu, M. Takeda, S. Ohno, Y. Shirogane, M. Iwasaki, and Y. Yanagi. “Measles virus circumvents the host interferon response by different actions of the C and V proteins”. In: *J Virol* 82.17 (Sept. 2008), pp. 8296–8306.
- [134] C. K. Pfaller, L. M. Bloyet, R. C. Donohue, A. L. Huff, W. P. Bartemes, I. Yousaf, E. Urzua, M. Clavière, M. Zachary, V. de Masson d’Autume, S. Carson, A. J. Schieferecke, A. J. Meyer, D. Gerlier, and R. Cattaneo. “The C Protein Is Recruited to Measles Virus Ribonucleocapsids by the Phosphoprotein”. In: *J Virol* 94.4 (Jan. 2020).
- [135] W. J. Moss. “Measles”. In: *Lancet* 390.10111 (Dec. 2017), pp. 2490–2502.
- [136] C. Erlenhoef, W. J. Wurzer, S. Löffler, S. Schneider-Schaulies, V. ter Meulen, and J. Schneider-Schaulies. “CD150 (SLAM) is a receptor for measles virus but is not involved in viral contact-mediated proliferation inhibition”. In: *J Virol* 75.10 (May 2001), pp. 4499–4505.
- [137] U. Schneider, V. von Messling, P. Devaux, and R. Cattaneo. “Efficiency of measles virus entry and dissemination through different receptors”. In: *J Virol* 76.15 (Aug. 2002), pp. 7460–7467.
- [138] M. D. Mühlebach, M. Mateo, P. L. Sinn, S. Prüfer, K. M. Uhlig, V. H. Leonard, C. K. Navaratnarajah, M. Frenzke, X. X. Wong, B. Sawatsky, S. Ramachandran, P. B. McCray, K. Cichutek, V. von Messling, M. Lopez, and R. Cattaneo. “Adherens junction protein nectin-4 is the epithelial receptor for measles virus”. In: *Nature* 480.7378 (Nov. 2011), pp. 530–533.
- [139] T. F. Wild, J. Fayolle, P. Beauverger, and R. Buckland. “Measles virus fusion: role of the cysteine-rich region of the fusion glycoprotein”. In: *J Virol* 68.11 (Nov. 1994), pp. 7546–7548.
- [140] T. Cathomen, H. Y. Naim, and R. Cattaneo. “Measles viruses with altered envelope protein cytoplasmic tails gain cell fusion competence”. In: *J Virol* 72.2 (Feb. 1998), pp. 1224–1234.

- 
- [141] R. Cox and R. K. Plemper. “The paramyxovirus polymerase complex as a target for next-generation anti-paramyxovirus therapeutics”. In: *Front Microbiol* 6 (2015), p. 459.
- [142] B. K. Rima and W. P. Duprex. “The measles virus replication cycle”. In: *Curr Top Microbiol Immunol* 329 (2009), pp. 77–102.
- [143] T. Nakamura and S. J. Russell. “Oncolytic measles viruses for cancer therapy”. In: *Expert Opin Biol Ther* 4.10 (Oct. 2004), pp. 1685–1692.
- [144] C. Burton and E. Bartee. “Syncytia Formation in Oncolytic Virotherapy”. In: *Mol Ther Oncolytics* 15 (Dec. 2019), pp. 131–139.
- [145] M. J. Sotir, D. H. Esposito, E. D. Barnett, K. Leder, P. E. Kozarsky, P. L. Lim, E. Gkrania-Klotsas, D. H. Hamer, S. Kuhn, B. A. Connor, R. Pradhan, and E. Caumes. “Measles in the 21st Century, a Continuing Preventable Risk to Travelers: Data From the GeoSentinel Global Network”. In: *Clin Infect Dis* 62.2 (Jan. 2016), pp. 210–212.
- [146] World Health Organization. “Measles vaccines: WHO position paper – April 2017”. In: *Wkly Epidemiol Rec* 92.17 (Apr. 2017), pp. 205–227.
- [147] W. J. Bellini, J. S. Rota, L. E. Lowe, R. S. Katz, P. R. Dyken, S. R. Zaki, W. J. Shieh, and P. A. Rota. “Subacute sclerosing panencephalitis: more cases of this fatal disease are prevented by measles immunization than was previously recognized”. In: *J Infect Dis* 192.10 (Nov. 2005), pp. 1686–1693.
- [148] M. G. Dixon, M. Ferrari, S. Antoni, X. Li, A. Portnoy, B. Lambert, S. Hauryski, C. Hatcher, Y. Nedelec, M. Patel, J. P. Alexander, C. Steulet, M. Gacic-Dobo, P. A. Rota, M. N. Mulders, A. S. Bose, A. Rosewell, K. Kretsinger, and N. S. Crowcroft. “Progress Toward Regional Measles Elimination - Worldwide, 2000-2020”. In: *MMWR Morb Mortal Wkly Rep* 70.45 (Nov. 2021), pp. 1563–1569.
- [149] J. F. Enders and T. C. Peebles. “Propagation in tissue cultures of cytopathogenic agents from patients with measles”. In: *Proc Soc Exp Biol Med* 86.2 (June 1954), pp. 277–286.
- [150] D. E. Griffin. “Measles Vaccine”. In: *Viral Immunol* 31.2 (Mar. 2018), pp. 86–95.
- [151] M. R. Hilleman. “Current overview of the pathogenesis and prophylaxis of measles with focus on practical implications”. In: *Vaccine* 20.5-6 (Dec. 2001), pp. 651–665.
- [152] C. Combredet, V. Labrousse, L. Mollet, C. Lorin, F. Delebecque, B. Hurtrel, H. McClure, M. B. Feinberg, M. Brahic, and F. Tangy. “A molecularly cloned Schwarz strain of measles virus vaccine induces strong immune responses in macaques and transgenic mice”. In: *J Virol* 77.21 (Nov. 2003), pp. 11546–11554.

- [153] R. E. Dörig, A. Marcil, A. Chopra, and C. D. Richardson. “The human CD46 molecule is a receptor for measles virus (Edmonston strain)”. In: *Cell* 75.2 (Oct. 1993), pp. 295–305.
- [154] R. Buckland and T. F. Wild. “Is CD46 the cellular receptor for measles virus?” In: *Virus Res* 48.1 (Apr. 1997), pp. 1–9.
- [155] Y. Yanagi, N. Ono, H. Tatsuo, K. Hashimoto, and H. Minagawa. “Measles virus receptor SLAM (CD150)”. In: *Virology* 299.2 (Aug. 2002), pp. 155–161.
- [156] B. D. Anderson, T. Nakamura, S. J. Russell, and K. W. Peng. “High CD46 receptor density determines preferential killing of tumor cells by oncolytic measles virus”. In: *Cancer Res* 64.14 (July 2004), pp. 4919–4926.
- [157] R. Buettner, M. Huang, T. Gritsko, J. Karras, S. Enkemann, T. Mesa, S. Nam, H. Yu, and R. Jove. “Activated signal transducers and activators of transcription 3 signaling induces CD46 expression and protects human cancer cells from complement-dependent cytotoxicity”. In: *Mol Cancer Res* 5.8 (Aug. 2007), pp. 823–832.
- [158] A. Maciejczyk, J. Szelachowska, B. Szynglarewicz, R. Szulc, A. Szulc, T. Wysocka, E. Jagoda, H. Lage, and P. Surowiak. “CD46 Expression is an unfavorable prognostic factor in breast cancer cases”. In: *Appl Immunohistochem Mol Morphol* 19.6 (Dec. 2011), pp. 540–546.
- [159] M. Elvington, M. K. Liszewski, and J. P. Atkinson. “CD46 and Oncologic Interactions: Friendly Fire against Cancer”. In: *Antibodies (Basel)* 9.4 (Nov. 2020).
- [160] A. Z. Bluming and J. L. Ziegler. “Regression of Burkitt’s lymphoma in association with measles infection”. In: *Lancet* 2.7715 (July 1971), pp. 105–106.
- [161] S. Gross. “Measles and leukaemia”. In: *Lancet* 1.7695 (Feb. 1971), pp. 397–398.
- [162] Z. Zygiert. “Hodgkin’s disease: remissions after measles”. In: *Lancet* 1.7699 (Mar. 1971), p. 593.
- [163] A. M. Taqi, M. B. Abdurrahman, A. M. Yakubu, and A. F. Fleming. “Regression of Hodgkin’s disease after measles”. In: *Lancet* 1.8229 (May 1981), p. 1112.
- [164] E. Kelly and S. J. Russell. “History of oncolytic viruses: genesis to genetic engineering”. In: *Mol Ther* 15.4 (Apr. 2007), pp. 651–659.
- [165] S. Robinson and E. Galanis. “Potential and clinical translation of oncolytic measles viruses”. In: *Expert Opin Biol Ther* 17.3 (Mar. 2017), pp. 353–363.
- [166] C. E. Engeland and G. Ungerechts. “Measles Virus as an Oncolytic Immunotherapy”. In: *Cancers (Basel)* 13.3 (Feb. 2021).
- [167] M. D. Mühlebach. “Measles virus in cancer therapy”. In: *Curr Opin Virol* 41 (Apr. 2020), pp. 85–97.

- 
- [168] F. Radecke, P. Spielhofer, H. Schneider, K. Kaelin, M. Huber, C. Dötsch, G. Christiansen, and M. A. Billeter. “Rescue of measles viruses from cloned DNA”. In: *EMBO J* 14.23 (Dec. 1995), pp. 5773–5784.
- [169] M. F. Leber, B. Hoyler, S. Prien, S. Neault, C. E. Engeland, J. M. Förster, S. Bossow, C. Springfield, C. von Kalle, D. Jäger, J. C. Bell, and G. Ungerechts. “Sequencing of serially passaged measles virus affirms its genomic stability and reveals a nonrandom distribution of consensus mutations”. In: *J Gen Virol* 101.4 (Apr. 2020), pp. 399–409.
- [170] A. Tsujimura, K. Shida, M. Kitamura, M. Nomura, J. Takeda, H. Tanaka, M. Matsumoto, K. Matsumiya, A. Okuyama, Y. Nishimune, M. Okabe, and T. Seya. “Molecular cloning of a murine homologue of membrane cofactor protein (CD46): preferential expression in testicular germ cells”. In: *Biochem J* 330 ( Pt 1) (Feb. 1998), pp. 163–168.
- [171] M. Manchester and G. F. Rall. “Model Systems: transgenic mouse models for measles pathogenesis”. In: *Trends Microbiol* 9.1 (Jan. 2001), pp. 19–23.
- [172] T. Nakamura, K. W. Peng, M. Harvey, S. Greiner, I. A. Lorimer, C. D. James, and S. J. Russell. “Rescue and propagation of fully retargeted oncolytic measles viruses”. In: *Nat Biotechnol* 23.2 (Feb. 2005), pp. 209–214.
- [173] G. Ungerechts, C. Springfield, M. E. Frenzke, J. Lampe, P. B. Johnston, W. B. Parker, E. J. Sorscher, and R. Cattaneo. “Lymphoma chemovirotherapy: CD20-targeted and convertase-armed measles virus can synergize with fludarabine”. In: *Cancer Res* 67.22 (Nov. 2007), pp. 10939–10947.
- [174] G. Ungerechts, M. E. Frenzke, K. C. Yaiw, T. Miest, P. B. Johnston, and R. Cattaneo. “Mantle cell lymphoma salvage regimen: synergy between a reprogrammed oncolytic virus and two chemotherapeutics”. In: *Gene Ther* 17.12 (Dec. 2010), pp. 1506–1516.
- [175] S. Bossow, C. Grossardt, A. Temme, M. F. Leber, S. Sawall, E. P. Rieber, R. Cattaneo, C. von Kalle, and G. Ungerechts. “Armed and targeted measles virus for chemovirotherapy of pancreatic cancer”. In: *Cancer Gene Ther* 18.8 (Aug. 2011), pp. 598–608.
- [176] K. Zaoui, S. Bossow, C. Grossardt, M. F. Leber, C. Springfield, P. K. Plinkert, C. v. Kalle, and G. Ungerechts. “Chemovirotherapy for head and neck squamous cell carcinoma with EGFR-targeted and CD/UPRT-armed oncolytic measles virus”. In: *Cancer Gene Ther* 19.3 (Mar. 2012), pp. 181–191.
- [177] M. F. Leber, M. A. Baertsch, S. C. Anker, L. Henkel, H. M. Singh, S. Bossow, C. E. Engeland, R. Barkley, B. Hoyler, J. Albert, C. Springfield, D. Jäger, C. von Kalle, and G. Ungerechts. “Enhanced Control of Oncolytic Measles Virus Using MicroRNA Target Sites”. In: *Mol Ther Oncolytics* 9 (June 2018), pp. 30–40.

- [178] M. F. Leber, S. Bossow, V. H. Leonard, K. Zaoui, C. Grossardt, M. Frenzke, T. Miest, S. Sawall, R. Cattaneo, C. von Kalle, and G. Ungerechts. “MicroRNA-sensitive oncolytic measles viruses for cancer-specific vector tropism”. In: *Mol Ther* 19.6 (June 2011), pp. 1097–1106.
- [179] M. A. Baertsch, M. F. Leber, S. Bossow, M. Singh, C. E. Engeland, J. Albert, C. Grossardt, D. Jäger, C. von Kalle, and G. Ungerechts. “MicroRNA-mediated multi-tissue detargeting of oncolytic measles virus”. In: *Cancer Gene Ther* 21.9 (Sept. 2014), pp. 373–380.
- [180] H. M. Singh, M. F. Leber, S. Bossow, C. E. Engeland, J. Dessila, C. Grossardt, K. Zaoui, J. C. Bell, D. Jäger, C. von Kalle, and G. Ungerechts. “MicroRNA-sensitive oncolytic measles virus for chemovirotherapy of pancreatic cancer”. In: *Mol Ther Oncolytics* 21 (June 2021), pp. 340–355.
- [181] C. Grossardt, C. E. Engeland, S. Bossow, N. Halama, K. Zaoui, M. F. Leber, C. Springfeld, D. Jaeger, C. von Kalle, and G. Ungerechts. “Granulocyte-macrophage colony-stimulating factor-armed oncolytic measles virus is an effective therapeutic cancer vaccine”. In: *Hum Gene Ther* 24.7 (July 2013), pp. 644–654.
- [182] C. E. Engeland, C. Grossardt, R. Veinalde, S. Bossow, D. Lutz, J. K. Kaufmann, I. Shevchenko, V. Umansky, D. M. Nettelbeck, W. Weichert, D. Jäger, C. von Kalle, and G. Ungerechts. “CTLA-4 and PD-L1 checkpoint blockade enhances oncolytic measles virus therapy”. In: *Mol Ther* 22.11 (Nov. 2014), pp. 1949–1959.
- [183] R. Veinalde, G. Pidelaserra-Martí, C. Moulin, L. M. Jeworowski, L. Küther, C. J. Buchholz, D. Jäger, G. Ungerechts, and C. E. Engeland. “Oncolytic measles vaccines encoding PD-1 and PD-L1 checkpoint blocking antibodies to increase tumor-specific T cell memory”. In: *Mol Ther Oncolytics* 24 (Mar. 2022), pp. 43–58.
- [184] R. Veinalde, C. Grossardt, L. Hartmann, M. C. Bourgeois-Daigneault, J. C. Bell, D. Jäger, C. von Kalle, G. Ungerechts, and C. E. Engeland. “Oncolytic measles virus encoding interleukin-12 mediates potent antitumor effects through T cell activation”. In: *Oncoimmunology* 6.4 (2017), e1285992.
- [185] P. S. Backhaus, R. Veinalde, L. Hartmann, J. E. Dunder, L. M. Jeworowski, J. Albert, B. Hoyler, T. Poth, D. Jäger, G. Ungerechts, and C. E. Engeland. “Immunological Effects and Viral Gene Expression Determine the Efficacy of Oncolytic Measles Vaccines Encoding IL-12 or IL-15 Agonists”. In: *Viruses* 11.10 (Oct. 2019).
- [186] T. Speck, J. P. W. Heidbuechel, R. Veinalde, D. Jaeger, C. von Kalle, C. R. Ball, G. Ungerechts, and C. E. Engeland. “Targeted BiTE Expression by an Oncolytic Vector Augments Therapeutic Efficacy Against Solid Tumors”. In: *Clin Cancer Res* 24.9 (May 2018), pp. 2128–2137.

- 
- [187] H. Li, K. W. Peng, D. Dingli, R. A. Kratzke, and S. J. Russell. “Oncolytic measles viruses encoding interferon beta and the thyroidal sodium iodide symporter gene for mesothelioma virotherapy”. In: *Cancer Gene Ther* 17.8 (Aug. 2010), pp. 550–558.
- [188] G. Pidelaserra-Martí and C. E. Engeland. “Mechanisms of measles virus oncolytic immunotherapy”. In: *Cytokine Growth Factor Rev* 56 (Dec. 2020), pp. 28–38.
- [189] O. G. Donnelly, F. Errington-Mais, L. Steele, E. Hadac, V. Jennings, K. Scott, H. Peach, R. M. Phillips, J. Bond, H. Pandha, K. Harrington, R. Vile, S. Russell, P. Selby, and A. A. Melcher. “Measles virus causes immunogenic cell death in human melanoma”. In: *Gene Ther* 20.1 (Jan. 2013), pp. 7–15.
- [190] A. Chen, Y. Zhang, G. Meng, D. Jiang, H. Zhang, M. Zheng, M. Xia, A. Jiang, J. Wu, C. Beltinger, and J. Wei. “Oncolytic measles virus enhances antitumour responses of adoptive CD8(+)NKG2D(+) cells in hepatocellular carcinoma treatment”. In: *Sci Rep* 7.1 (July 2017), p. 5170.
- [191] A. Marchini, C. S. Ilkow, and A. Melcher. “Oncolytic Virus Immunotherapy”. In: *Cancers (Basel)* 13.15 (July 2021).
- [192] M. M. Rahman and G. McFadden. “Oncolytic Viruses: Newest Frontier for Cancer Immunotherapy”. In: *Cancers (Basel)* 13.21 (Oct. 2021).
- [193] K. Garber. “China approves world’s first oncolytic virus therapy for cancer treatment”. In: *J Natl Cancer Inst* 98.5 (Mar. 2006), pp. 298–300.
- [194] R. H. Andtbacka, H. L. Kaufman, F. Collichio, T. Amatruda, N. Senzer, J. Chesney, K. A. Delman, L. E. Spitler, I. Puzanov, S. S. Agarwala, M. Milhem, L. Cranmer, B. Curti, K. Lewis, M. Ross, T. Guthrie, G. P. Linette, G. A. Daniels, K. Harrington, M. R. Middleton, W. H. Miller, J. S. Zager, Y. Ye, B. Yao, A. Li, S. Doleman, A. VanderWalde, J. Gansert, and R. S. Coffin. “Talimogene Laherparepvec Improves Durable Response Rate in Patients With Advanced Melanoma”. In: *J Clin Oncol* 33.25 (Sept. 2015), pp. 2780–2788.
- [195] K. Sugawara, M. Iwai, H. Ito, M. Tanaka, Y. Seto, and T. Todo. “Oncolytic herpes virus G47Delta works synergistically with CTLA-4 inhibition via dynamic intratumoral immune modulation”. In: *Mol Ther Oncolytics* 22 (Sept. 2021), pp. 129–142.
- [196] T. Todo, H. Ito, Y. Ino, H. Ohtsu, Y. Ota, J. Shibahara, and M. Tanaka. “Intratumoral oncolytic herpes virus G47Delta for residual or recurrent glioblastoma: a phase 2 trial”. In: *Nat Med* 28.8 (Aug. 2022), pp. 1630–1639.
- [197] L. Heinzerling, V. Künzi, P. A. Oberholzer, T. Kündig, H. Naim, and R. Dummer. “Oncolytic measles virus in cutaneous T-cell lymphomas mounts antitumor immune responses in vivo and targets interferon-resistant tumor cells”. In: *Blood* 106.7 (Oct. 2005), pp. 2287–2294.
-

- [198] K. W. Peng, S. Fecteau, T. Wegman, D. O’Kane, and S. J. Russell. “Non-invasive in vivo monitoring of trackable viruses expressing soluble marker peptides”. In: *Nat Med* 8.5 (May 2002), pp. 527–531.
- [199] D. Dingli, K. W. Peng, M. E. Harvey, P. R. Greipp, M. K. O’Connor, R. Cattaneo, J. C. Morris, and S. J. Russell. “Image-guided radiovirotherapy for multiple myeloma using a recombinant measles virus expressing the thyroidal sodium iodide symporter”. In: *Blood* 103.5 (Mar. 2004), pp. 1641–1646.
- [200] H. L. Kaufman, T. Amatruda, T. Reid, R. Gonzalez, J. Glaspy, E. Whitman, K. Harrington, J. Nemunaitis, A. Zloza, M. Wolf, and N. N. Senzer. “Systemic versus local responses in melanoma patients treated with talimogene laherparepvec from a multi-institutional phase II study”. In: *J Immunother Cancer* 4 (2016), p. 12.
- [201] H. Rehman, A. W. Silk, M. P. Kane, and H. L. Kaufman. “Into the clinic: Talimogene laherparepvec (T-VEC), a first-in-class intratumoral oncolytic viral therapy”. In: *J Immunother Cancer* 4 (2016), p. 53.
- [202] R. Havunen, J. M. Santos, S. Sorsa, T. Rantapero, D. Lumen, M. Siurala, A. J. Airaksinen, V. Cervera-Carrascon, S. Tähtinen, A. Kanerva, and A. Hemminki. “Abscopal Effect in Non-injected Tumors Achieved with Cytokine-Armed Oncolytic Adenovirus”. In: *Mol Ther Oncolytics* 11 (Dec. 2018), pp. 109–121.
- [203] G. Ungerechts, S. Bossow, B. Leuchs, P. S. Holm, J. Rommelaere, M. Coffey, R. Coffin, J. Bell, and D. M. Nettelbeck. “Moving oncolytic viruses into the clinic: clinical-grade production, purification, and characterization of diverse oncolytic viruses”. In: *Mol Ther Methods Clin Dev* 3 (2016), p. 16018.
- [204] M. F. Leber, S. Neault, E. Jirovec, R. Barkley, A. Said, J. C. Bell, and G. Ungerechts. “Engineering and combining oncolytic measles virus for cancer therapy”. In: *Cytokine Growth Factor Rev* 56 (Dec. 2020), pp. 39–48.
- [205] M. Morisada, M. Chamberlin, and C. Allen. “Exploring the rationale for combining ionizing radiation and immune checkpoint blockade in head and neck cancer”. In: *Head Neck* 40.6 (June 2018), pp. 1321–1334.
- [206] S. J. Antonia, A. Villegas, D. Daniel, D. Vicente, S. Murakami, R. Hui, T. Kurata, A. Chiappori, K. H. Lee, M. de Wit, et al. “Overall Survival with Durvalumab after Chemoradiotherapy in Stage III NSCLC”. In: *N Engl J Med* 379.24 (Dec. 2018), pp. 2342–2350.
- [207] J. M. Qian and J. D. Schoenfeld. “Radiotherapy and Immunotherapy for Head and Neck Cancer: Current Evidence and Challenges”. In: *Front Oncol* 10 (2020), p. 608772.

- 
- [208] F. G. Herrera, C. Ronet, M. Ochoa de Olza, D. Barras, I. Crespo, M. Andreatta, J. Corria-Osorio, A. Spill, F. Benedetti, R. Genolet, A. Orcurto, M. Imbimbo, E. Ghisoni, B. Navarro Rodrigo, D. R. Berthold, A. Sarivalasis, K. Zaman, R. Duran, C. Dromain, J. Prior, N. Schaefer, J. Bourhis, G. Dimopoulou, Z. Tsourti, M. Messemaker, T. Smith, S. E. Warren, P. Foukas, S. Rusakiewicz, M. J. Pittet, S. Zimmermann, C. Sempoux, U. Dafni, A. Harari, L. E. Kandalaft, S. J. Carmona, D. Dangaj Laniti, M. Irving, and G. Coukos. “Low-Dose Radiotherapy Reverses Tumor Immune Desertification and Resistance to Immunotherapy”. In: *Cancer Discov* 12.1 (Jan. 2022), pp. 108–133.
- [209] A. Melcher, K. Harrington, and R. Vile. “Oncolytic virotherapy as immunotherapy”. In: *Science* 374.6573 (Dec. 2021), pp. 1325–1326.
- [210] N. Macedo, D. M. Miller, R. Haq, and H. L. Kaufman. “Clinical landscape of oncolytic virus research in 2020”. In: *J Immunother Cancer* 8.2 (Oct. 2020).
- [211] A. Ribas, R. Dummer, I. Puzanov, A. VanderWalde, R. H. I. Andtbacka, O. Michielin, A. J. Olszanski, J. Malvehy, J. Cebon, E. Fernandez, J. M. Kirkwood, T. F. Gajewski, L. Chen, K. S. Gorski, A. A. Anderson, S. J. Diede, M. E. Lassman, J. Gansert, F. S. Hodi, and G. V. Long. “Oncolytic Virotherapy Promotes Intratumoral T Cell Infiltration and Improves Anti-PD-1 Immunotherapy”. In: *Cell* 170.6 (Sept. 2017), pp. 1109–1119.
- [212] V. May, S. Berchtold, A. Berger, S. Venturelli, M. Burkard, C. Leischner, N. P. Malek, and U. M. Lauer. “Chemovirotherapy for pancreatic cancer: Gemcitabine plus oncolytic measles vaccine virus”. In: *Oncol Lett* 18.5 (Nov. 2019), pp. 5534–5542.
- [213] Y. Toucheffeu, G. Vassaux, and K. J. Harrington. “Oncolytic viruses in radiation oncology”. In: *Radiother Oncol* 99.3 (June 2011), pp. 262–270.
- [214] M. H. Dai, S. L. Liu, N. G. Chen, T. P. Zhang, L. You, F. Q Zhang, T. C. Chou, A. A. Szalay, Y. Fong, and Y. P. Zhao. “Oncolytic vaccinia virus in combination with radiation shows synergistic antitumor efficacy in pancreatic cancer”. In: *Cancer Lett* 344.2 (Mar. 2014), pp. 282–290.
- [215] A. Angelova, T. Ferreira, C. Bretscher, J. Rommelaere, and A. Marchini. “Parvovirus-Based Combinatorial Immunotherapy: A Reinforced Therapeutic Strategy against Poor-Prognosis Solid Cancers”. In: *Cancers (Basel)* 13.2 (Jan. 2021).
- [216] K. Geletneky, A. D. Hartkopf, R. Krempien, J. Rommelaere, and J. R. Schlehofer. “Improved killing of human high-grade glioma cells by combining ionizing radiation with oncolytic parvovirus H-1 infection”. In: *J Biomed Biotechnol* 2010 (2010), p. 350748.

- [217] C. Liu, J. N. Sarkaria, C. A. Petell, G. Paraskevakou, P. J. Zollman, M. Schroeder, B. Carlson, P. A. Decker, W. Wu, C. D. James, S. J. Russell, and E. Galanis. “Combination of measles virus virotherapy and radiation therapy has synergistic activity in the treatment of glioblastoma multiforme”. In: *Clin Cancer Res* 13.23 (Dec. 2007), pp. 7155–7165.
- [218] C. Liu, K. Hasegawa, S. J. Russell, M. Sadelain, and K. W. Peng. “Prostate-specific membrane antigen retargeted measles virotherapy for the treatment of prostate cancer”. In: *Prostate* 69.10 (July 2009), pp. 1128–1141.
- [219] Y. Touchefeu, A. A. Khan, G. Borst, S. H. Zaidi, M. McLaughlin, V. Roulstone, D. Mansfield, J. Kyula, T. Pencavel, E. M. Karapanagiotou, J. Clayton, M. J. Federspiel, S. J. Russell, M. Garrett, I. Collins, and K. J. Harrington. “Optimising measles virus-guided radiovirotherapy with external beam radiotherapy and specific checkpoint kinase 1 inhibition”. In: *Radiother Oncol* 108.1 (July 2013), pp. 24–31.
- [220] S. Rajaraman, D. Canjuga, M. Ghosh, M. C. Codrea, R. Sieger, F. Wedekink, M. Tatagiba, M. Koch, U. M. Lauer, S. Nahnsen, H. G. Rammensee, M. D. Mühlebach, S. Stevanovic, and G. Tabatabai. “Measles Virus-Based Treatments Trigger a Pro-inflammatory Cascade and a Distinctive Immunopeptidome in Glioblastoma”. In: *Mol Ther Oncolytics* 12 (Mar. 2019), pp. 147–161.
- [221] A. Heller, A. L. Angelova, S. Bauer, S. P. Grekova, M. Aprahamian, J. Rommelaere, M. Volkmar, J. W. Janssen, N. Bauer, I. Herr, T. Giese, M. M. Gaida, F. Bergmann, T. Hackert, S. Fritz, and N. A. Giese. “Establishment and Characterization of a Novel Cell Line, ASAN-PaCa, Derived From Human Adenocarcinoma Arising in Intraductal Papillary Mucinous Neoplasm of the Pancreas”. In: *Pancreas* 45.10 (Nov. 2016), pp. 1452–1460.
- [222] M. H. Tan, N. J. Nowak, R. Loor, H. Ochi, A. A. Sandberg, C. Lopez, J. W. Pickren, R. Berjian, H. O. Douglass, and T. M. Chu. “Characterization of a new primary human pancreatic tumor line”. In: *Cancer Invest* 4.1 (1986), pp. 15–23.
- [223] M. Mermoud, A. Hiou-Feige, E. Bovay, V. Roh, J. Sponarova, M. Bongiovanni, D. W. Vermeer, J. H. Lee, T. V. Petrova, J. P. Rivals, Y. Monnier, G. V. Tolstonog, and C. Simon. “Mouse model of postsurgical primary tumor recurrence and regional lymph node metastasis progression in HPV-related head and neck cancer”. In: *Int J Cancer* 142.12 (June 2018), pp. 2518–2528.
- [224] N. P. Judd, A. E. Winkler, O. Murillo-Sauca, J. J. Brotman, J. H. Law, J. S. Lewis, G. P. Dunn, J. D. Bui, J. B. Sunwoo, and R. Uppaluri. “ERK1/2 regulation of CD44 modulates oral cancer aggressiveness”. In: *Cancer Res* 72.1 (Jan. 2012), pp. 365–374.

- 
- [225] J. P. Jacobs, C. M. Jones, and J. P. Baille. “Characteristics of a human diploid cell designated MRC-5”. In: *Nature* 227.5254 (July 1970), pp. 168–170.
- [226] T. H. Corbett, B. J. Roberts, W. R. Leopold, J. C. Peckham, L. J. Wilkoff, D. P. Griswold, and F. M. Schabel. “Induction and chemotherapeutic response of two transplantable ductal adenocarcinomas of the pancreas in C57BL/6 mice”. In: *Cancer Res* 44.2 (Feb. 1984), pp. 717–726.
- [227] K. R. Ehrenberg, J. Gao, F. Oppel, S. Frank, N. Kang, S. M. Dieter, F. Herbst, L. Möhrmann, T. D. Dubash, E. R. Schulz, H. Strakerjahn, K. M. Giessler, S. Weber, A. Oberlack, E. M. Rief, O. Strobel, F. Bergmann, F. Lasitschka, J. Weitz, H. Glimm, and C. R. Ball. “Systematic Generation of Patient-Derived Tumor Models in Pancreatic Cancer”. In: *Cells* 8.2 (Feb. 2019).
- [228] D. Baumann, T. Hägele, J. Mochayedi, J. Drebant, C. Vent, S. Blobner, J. H. Noll, I. Nickel, C. Schumacher, S. L. Boos, A. S. Daniel, S. Wendler, M. Volkmar, O. Strobel, and R. Offringa. “Proimmunogenic impact of MEK inhibition synergizes with agonist anti-CD40 immunostimulatory antibodies in tumor therapy”. In: *Nat Commun* 11.1 (May 2020), p. 2176.
- [229] T. Okabe, N. Yamaguchi, and N. Ohsawa. “Establishment and characterization of a carcinoembryonic antigen (CEA)-producing cell line from a human carcinoma of the exocrine pancreas”. In: *Cancer* 51.4 (Feb. 1983), pp. 662–668.
- [230] A. Follenzi and L. Naldini. “Generation of HIV-1 derived lentiviral vectors”. In: *Methods Enzymol* 346 (2002), pp. 454–465.
- [231] M. Bozza, E. W. Green, E. Espinet, A. De Roia, C. Klein, V. Vogel, R. Offringa, J. A. Williams, M. Sprick, and R. P. Harbottle. “Novel Non-integrating DNA Nano-S/MAR Vectors Restore Gene Function in Isogenic Patient-Derived Pancreatic Tumor Models”. In: *Mol Ther Methods Clin Dev* 17 (June 2020), pp. 957–968.
- [232] X. Wang, Z. Xu, Z. Tian, X. Zhang, D. Xu, Q. Li, J. Zhang, and T. Wang. “The EF-1 alpha promoter maintains high-level transgene expression from episomal vectors in transfected CHO-K1 cells”. In: *J Cell Mol Med* 21.11 (Nov. 2017), pp. 3044–3054.
- [233] J. Ye, G. Coulouris, I. Zaretskaya, I. Cutcutache, S. Rozen, and T. L. Madden. “Primer-BLAST: a tool to design target-specific primers for polymerase chain reaction”. In: *BMC Bioinformatics* 13 (June 2012), p. 134.
- [234] P. Stothard. “The sequence manipulation suite: JavaScript programs for analyzing and formatting protein and DNA sequences”. In: *Biotechniques* 28.6 (June 2000), pp. 1102, 1104.
-

- [235] W. J. Kent, C. W. Sugnet, T. S. Furey, K. M. Roskin, T. H. Pringle, A. M. Zahler, and D. Haussler. “The human genome browser at UCSC”. In: *Genome Res* 12.6 (June 2002), pp. 996–1006.
- [236] M. Schmitt and M. Pawlita. “High-throughput detection and multiplex identification of cell contaminations”. In: *Nucleic Acids Res* 37.18 (Oct. 2009), e119.
- [237] F. Castro, W. G. Dirks, S. Fährnich, A. Hotz-Wagenblatt, M. Pawlita, and M. Schmitt. “High-throughput SNP-based authentication of human cell lines”. In: *Int J Cancer* 132.2 (Jan. 2013), pp. 308–314.
- [238] New England Biolabs. *Tm Calculator, v1.15.0*. 2022. URL: <https://tmcalculator.neb.com/#!/main>.
- [239] A. Martin, P. Staeheli, and U. Schneider. “RNA polymerase II-controlled expression of antigenomic RNA enhances the rescue efficacies of two different members of the Mononegavirales independently of the site of viral genome replication”. In: *J Virol* 80.12 (June 2006), pp. 5708–5715.
- [240] J. Förster. “Combining Radiation and Oncolytic Measeles Virus for the Treatment of Pancreatic Cancer”. Master thesis. Heidelberg University, 2017.
- [241] J. Schindelin, I. Arganda-Carreras, E. Frise, V. Kaynig, M. Longair, T. Pietzsch, S. Preibisch, C. Rueden, S. Saalfeld, B. Schmid, J. Y. Tinevez, D. J. White, V. Hartenstein, K. Eliceiri, P. Tomancak, and A. Cardona. “Fiji: an open-source platform for biological-image analysis”. In: *Nat Methods* 9.7 (June 2012), pp. 676–682.
- [242] T. C. Chou and P. Talalay. “Quantitative analysis of dose-effect relationships: the combined effects of multiple drugs or enzyme inhibitors”. In: *Adv Enzyme Regul* 22 (1984), pp. 27–55.
- [243] M. Bozza, A. De Roia, M. P. Correia, A. Berger, A. Tuch, A. Schmidt, I. Zörnig, D. Jäger, P. Schmidt, and R. P. Harbottle. “A nonviral, nonintegrating DNA nanovector platform for the safe, rapid, and persistent manufacture of recombinant T cells”. In: *Sci Adv* 7.16 (Apr. 2021).
- [244] C. Vanpouille-Box, A. Alard, M. J. Aryankalayil, Y. Sarfraz, J. M. Diamond, R. J. Schneider, G. Inghirami, C. N. Coleman, S. C. Formenti, and S. Demaria. “DNA exonuclease Trex1 regulates radiotherapy-induced tumour immunogenicity”. In: *Nat Commun* 8 (June 2017), p. 15618.
- [245] C. Vanpouille-Box, S. C. Formenti, and S. Demaria. “TREX1 dictates the immune fate of irradiated cancer cells”. In: *Oncoimmunology* 6.9 (2017), e1339857.

- 
- [246] J. Fucikova, O. Kepp, L. Kasikova, G. Petroni, T. Yamazaki, P. Liu, L. Zhao, R. Spisek, G. Kroemer, and L. Galluzzi. “Detection of immunogenic cell death and its relevance for cancer therapy”. In: *Cell Death Dis* 11.11 (Nov. 2020), p. 1013.
- [247] L. Kasikova, I. Truxova, I. Cremer, C. Sautes-Fridman, O. Kepp, G. Kroemer, R. Spisek, and J. Fucikova. “Side-by-side comparison of flow cytometry and immunohistochemistry for detection of calreticulin exposure in the course of immunogenic cell death”. In: *Methods Enzymol* 632 (2020), pp. 15–25.
- [248] K. Geoffroy and M. C. Bourgeois-Daigneault. “The pros and cons of interferons for oncolytic virotherapy”. In: *Cytokine Growth Factor Rev* 56 (Dec. 2020), pp. 49–58.
- [249] M. J. Ware, K. Colbert, V. Keshishian, J. Ho, S. J. Corr, S. A. Curley, and B. Godin. “Generation of Homogenous Three-Dimensional Pancreatic Cancer Cell Spheroids Using an Improved Hanging Drop Technique”. In: *Tissue Eng Part C Methods* 22.4 (Apr. 2016), pp. 312–321.
- [250] J. Bell and G. McFadden. “Viruses for tumor therapy”. In: *Cell Host Microbe* 15.3 (Mar. 2014), pp. 260–265.
- [251] A. Bieler, K. Mantwill, R. Holzmüller, K. Jürchott, A. Kaszubiak, S. Stärk, G. Glockzin, H. Lage, A. L. Grosu, B. Gansbacher, and P. S. Holm. “Impact of radiation therapy on the oncolytic adenovirus dl520: implications on the treatment of glioblastoma”. In: *Radiother Oncol* 86.3 (Mar. 2008), pp. 419–427.
- [252] M. Zhang, S. Li, J. Li, W. D. Ensminger, and T. S. Lawrence. “Ionizing radiation increases adenovirus uptake and improves transgene expression in intrahepatic colon cancer xenografts”. In: *Mol Ther* 8.1 (July 2003), pp. 21–28.
- [253] T. Egami, K. Ohuchida, K. Mizumoto, M. Onimaru, H. Toma, S. Nishio, E. Nagai, K. Matsumoto, T. Nakamura, and M. Tanaka. “Radiation enhances adenoviral gene therapy in pancreatic cancer via activation of cytomegalovirus promoter and increased adenovirus uptake”. In: *Clin Cancer Res* 14.6 (Mar. 2008), pp. 1859–1867.
- [254] M. Hingorani, C. L. White, S. Zaidi, A. Merron, I. Peerlinck, M. E. Gore, C. M. Nutting, H. S. Pandha, A. A. Melcher, R. G. Vile, G. Vassaux, and K. J. Harrington. “Radiation-mediated up-regulation of gene expression from replication-defective adenoviral vectors: implications for sodium iodide symporter gene therapy”. In: *Clin Cancer Res* 14.15 (Aug. 2008), pp. 4915–4924.
- [255] P. K. Zhou, Y. Sun, and J. An. “Interaction between viral proteins and hosts and its disturbance in the cellular responses to ionising radiation”. In: *Int J Radiat Biol* 85.7 (July 2009), pp. 587–597.

- [256] H. Li, K. W. Peng, and S. J. Russell. “Oncolytic measles virus encoding thyroidal sodium iodide symporter for squamous cell cancer of the head and neck radiovirotherapy”. In: *Hum Gene Ther* 23.3 (Mar. 2012), pp. 295–301.
- [257] T. S. Miest, M. Frenzke, and R. Cattaneo. “Measles virus entry through the signaling lymphocyte activation molecule governs efficacy of mantle cell lymphoma radiovirotherapy”. In: *Mol Ther* 21.11 (Nov. 2013), pp. 2019–2031.
- [258] Y. Chen, T. DeWeese, J. Dilley, Y. Zhang, Y. Li, N. Ramesh, J. Lee, R. Pennathur-Das, J. Radzyminski, J. Wypych, D. Brignetti, S. Scott, J. Stephens, D. B. Karpf, D. R. Henderson, and D. C. Yu. “CV706, a prostate cancer-specific adenovirus variant, in combination with radiotherapy produces synergistic antitumor efficacy without increasing toxicity”. In: *Cancer Res* 61.14 (July 2001), pp. 5453–5460.
- [259] W. R. Jarnagin, J. S. Zager, M. Hezel, S. F. Stanziale, P. S. Adusumilli, M. Gonen, M. I. Ebricht, A. Culliford, N. J. Gusani, and Y. Fong. “Treatment of cholangiocarcinoma with oncolytic herpes simplex virus combined with external beam radiation therapy”. In: *Cancer Gene Ther* 13.3 (Mar. 2006), pp. 326–334.
- [260] J. Dilley, S. Reddy, D. Ko, N. Nguyen, G. Rojas, P. Working, and D. C. Yu. “Oncolytic adenovirus CG7870 in combination with radiation demonstrates synergistic enhancements of antitumor efficacy without loss of specificity”. In: *Cancer Gene Ther* 12.8 (Aug. 2005), pp. 715–722.
- [261] S. H. Kim, R. J. Wong, D. A. Kooby, J. F. Carew, P. S. Adusumilli, S. G. Patel, J. P. Shah, and Y. Fong. “Combination of mutated herpes simplex virus type 1 (G207 virus) with radiation for the treatment of squamous cell carcinoma of the head and neck”. In: *Eur J Cancer* 41.2 (Jan. 2005), pp. 313–322.
- [262] S. Nandi, I. V. Ulasov, M. A. Tyler, A. Q. Sugihara, L. Molinero, Y. Han, Z. B. Zhu, and M. S. Lesniak. “Low-dose radiation enhances survivin-mediated virotherapy against malignant glioma stem cells”. In: *Cancer Res* 68.14 (July 2008), pp. 5778–5784.
- [263] C. Liu, Y. Zhang, M. M. Liu, H. Zhou, W. Chowdhury, S. E. Lupold, T. L. Deweese, and R. Rodriguez. “Evaluation of continuous low dose rate versus acute single high dose rate radiation combined with oncolytic viral therapy for prostate cancer”. In: *Int J Radiat Biol* 86.3 (Mar. 2010), pp. 220–229.
- [264] G. Portella, R. Pacelli, S. Libertini, L. Cella, G. Vecchio, M. Salvatore, and A. Fusco. “ONYX-015 enhances radiation-induced death of human anaplastic thyroid carcinoma cells”. In: *J Clin Endocrinol Metab* 88.10 (Oct. 2003), pp. 5027–5032.

- 
- [265] K. Twigger, L. Vidal, C. L. White, J. S. De Bono, S. Bhide, M. Coffey, B. Thompson, R. G. Vile, L. Heinemann, H. S. Pandha, F. Errington, A. A. Melcher, and K. J. Harrington. “Enhanced in vitro and in vivo cytotoxicity of combined reovirus and radiotherapy”. In: *Clin Cancer Res* 14.3 (Feb. 2008), pp. 912–923.
- [266] G. G. Steel and M. J. Peckham. “Exploitable mechanisms in combined radiotherapy-chemotherapy: the concept of additivity”. In: *Int J Radiat Oncol Biol Phys* 5.1 (Jan. 1979), pp. 85–91.
- [267] Z. Asadzadeh, E. Safarzadeh, S. Safaei, A. Baradaran, A. Mohammadi, K. Hajiasgharzadeh, A. Derakhshani, A. Argentiero, N. Silvestris, and B. Baradaran. “Current Approaches for Combination Therapy of Cancer: The Role of Immunogenic Cell Death”. In: *Cancers (Basel)* 12.4 (Apr. 2020).
- [268] G. Kroemer, L. Galluzzi, O. Kepp, and L. Zitvogel. “Immunogenic cell death in cancer therapy”. In: *Annu Rev Immunol* 31 (2013), pp. 51–72.
- [269] I. Adkins, J. Fucikova, A. D. Garg, P. Agostinis, and R. Špíšek. “Physical modalities inducing immunogenic tumor cell death for cancer immunotherapy”. In: *Oncoimmunology* 3.12 (Dec. 2014), e968434.
- [270] S. Stangl, G. Themelis, L. Friedrich, V. Ntziachristos, A. Sarantopoulos, M. Molls, A. Skerra, and G. Multhoff. “Detection of irradiation-induced, membrane heat shock protein 70 (Hsp70) in mouse tumors using Hsp70 Fab fragment”. In: *Radiother Oncol* 99.3 (June 2011), pp. 313–316.
- [271] L. Apetoh, F. Ghiringhelli, A. Tesniere, A. Criollo, C. Ortiz, R. Lidereau, C. Mariette, N. Chaput, J. P. Mira, S. Delaloge, F. André, T. Tursz, G. Kroemer, and L. Zitvogel. “The interaction between HMGB1 and TLR4 dictates the outcome of anticancer chemotherapy and radiotherapy”. In: *Immunol Rev* 220 (Dec. 2007), pp. 47–59.
- [272] E. B. Golden, D. Frances, I. Pellicciotta, S. Demaria, M. Helen Barcellos-Hoff, and S. C. Formenti. “Radiation fosters dose-dependent and chemotherapy-induced immunogenic cell death”. In: *Oncoimmunology* 3 (2014), e28518.
- [273] M. J. Aryankalayil, A. Y. Makinde, S. R. Gameiro, J. W. Hodge, P. P. Rivera-Solis, S. T. Palayoor, M. M. Ahmed, and C. N. Coleman. “Defining molecular signature of pro-immunogenic radiotherapy targets in human prostate cancer cells”. In: *Radiat Res* 182.2 (Aug. 2014), pp. 139–148.
- [274] P. K. Bommareddy, A. Zloza, S. D. Rabkin, and H. L. Kaufman. “Oncolytic virus immunotherapy induces immunogenic cell death and overcomes STING deficiency in melanoma”. In: *Oncoimmunology* 8.7 (2019), p. 1591875.

- [275] A. L. Angelova, S. P. Grekova, A. Heller, O. Kuhlmann, E. Soyka, T. Giese, M. Aprahamian, G. Bour, S. Rüffer, C. Cziepluch, L. Daeffler, J. Rommelaere, J. Werner, Z. Raykov, and N. A. Giese. “Complementary induction of immunogenic cell death by oncolytic parvovirus H-1PV and gemcitabine in pancreatic cancer”. In: *J Virol* 88.10 (May 2014), pp. 5263–5276.
- [276] D. E. Griffin, W. H. Lin, and C. H. Pan. “Measles virus, immune control, and persistence”. In: *FEMS Microbiol Rev* 36.3 (May 2012), pp. 649–662.
- [277] I. E. Dumitriu, P. Baruah, B. Valentinis, R. E. Voll, M. Herrmann, P. P. Nawroth, B. Arnold, M. E. Bianchi, A. A. Manfredi, and P. Rovere-Querini. “Release of high mobility group box 1 by dendritic cells controls T cell activation via the receptor for advanced glycation end products”. In: *J Immunol* 174.12 (June 2005), pp. 7506–7515.
- [278] R. Saenz, D. Futralan, L. Leutenez, F. Eekhout, J. F. Fecteau, S. Sundelius, S. Sundqvist, M. Larsson, T. Hayashi, B. Minev, D. Carson, S. Esener, B. Messmer, and D. Messmer. “TLR4-dependent activation of dendritic cells by an HMGB1-derived peptide adjuvant”. In: *J Transl Med* 12 (Aug. 2014), p. 211.
- [279] A. Pichlmair, O. Schulz, C. P. Tan, T. I. Näslund, P. Liljeström, F. Weber, and C. Reis e Sousa. “RIG-I-mediated antiviral responses to single-stranded RNA bearing 5'-phosphates”. In: *Science* 314.5801 (Nov. 2006), pp. 997–1001.
- [280] S. R. Woo, M. B. Fuertes, L. Corrales, S. Spranger, M. J. Furdyna, M. Y. Leung, R. Duggan, Y. Wang, G. N. Barber, K. A. Fitzgerald, M. L. Alegre, and T. F. Gajewski. “STING-dependent cytosolic DNA sensing mediates innate immune recognition of immunogenic tumors”. In: *Immunity* 41.5 (Nov. 2014), pp. 830–842.
- [281] D. R. E. Ranoa, R. C. Widau, S. Mallon, A. D. Parekh, C. M. Nicolae, X. Huang, M. J. Bolt, A. Arina, R. Parry, S. J. Kron, G. L. Moldovan, N. N. Khodarev, and R. R. Weichselbaum. “STING Promotes Homeostasis via Regulation of Cell Proliferation and Chromosomal Stability”. In: *Cancer Res* 79.7 (Apr. 2019), pp. 1465–1479.
- [282] M. A. Suter, N. Y. Tan, C. H. Thiam, M. Khatoo, P. A. MacAry, V. Angeli, S. Gasser, and Y. L. Zhang. “cGAS-STING cytosolic DNA sensing pathway is suppressed by JAK2-STAT3 in tumor cells”. In: *Sci Rep* 11.1 (Mar. 2021), p. 7243.
- [283] N. Tanaka, M. Sato, M. S. Lamphier, H. Nozawa, E. Oda, S. Noguchi, R. D. Schreiber, Y. Tsujimoto, and T. Taniguchi. “Type I interferons are essential mediators of apoptotic death in virally infected cells”. In: *Genes Cells* 3.1 (Jan. 1998), pp. 29–37.
- [284] F. McNab, K. Mayer-Barber, A. Sher, A. Wack, and A. O’Garra. “Type I interferons in infectious disease”. In: *Nat Rev Immunol* 15.2 (Feb. 2015), pp. 87–103.
- [285] E. C. Borden. “Interferons alpha and beta in cancer: therapeutic opportunities from new insights”. In: *Nat Rev Drug Discov* 18.3 (Mar. 2019), pp. 219–234.

- 
- [286] R. F. V. Medrano, A. Hunger, S. A. Mendonça, J. A. M. Barbuto, and B. E. Strauss. “Immunomodulatory and antitumor effects of type I interferons and their application in cancer therapy”. In: *Oncotarget* 8.41 (Sept. 2017), pp. 71249–71284.
- [287] L. Zitvogel, L. Galluzzi, O. Kepp, M. J. Smyth, and G. Kroemer. “Type I interferons in anticancer immunity”. In: *Nat Rev Immunol* 15.7 (July 2015), pp. 405–414.
- [288] X. Wang, J. E. Schoenhals, A. Li, D. R. Valdecanas, H. Ye, F. Zang, C. Tang, M. Tang, C. G. Liu, X. Liu, S. Krishnan, J. P. Allison, P. Sharma, P. Hwu, R. Komaki, W. W. Overwijk, D. R. Gomez, J. Y. Chang, S. M. Hahn, M. A. Cortez, and J. W. Welsh. “Suppression of Type I IFN Signaling in Tumors Mediates Resistance to Anti-PD-1 Treatment That Can Be Overcome by Radiotherapy”. In: *Cancer Res* 77.4 (Feb. 2017), pp. 839–850.
- [289] I. Melero, J. I. Quetglas, M. Reboredo, J. Dubrot, J. R. Rodriguez-Madoz, U. Mancheño, E. Casales, J. I. Riezu-Boj, M. Ruiz-Guillen, M. C. Ochoa, M. F. Sanmamed, N. Thieblemont, C. Smerdou, and S. Hervas-Stubbs. “Strict requirement for vector-induced type I interferon in efficacious antitumor responses to virally encoded IL12”. In: *Cancer Res* 75.3 (Feb. 2015), pp. 497–507.
- [290] W. Ouyang and A. O’Garra. “IL-10 Family Cytokines IL-10 and IL-22: from Basic Science to Clinical Translation”. In: *Immunity* 50.4 (Apr. 2019), pp. 871–891.
- [291] M. Saraiva, P. Vieira, and A. O’Garra. “Biology and therapeutic potential of interleukin-10”. In: *J Exp Med* 217.1 (Jan. 2020).
- [292] A. Facciabene, G. T. Motz, and G. Coukos. “T-regulatory cells: key players in tumor immune escape and angiogenesis”. In: *Cancer Res* 72.9 (May 2012), pp. 2162–2171.
- [293] N. P. Judd, C. T. Allen, A. E. Winkler, and R. Uppaluri. “Comparative analysis of tumor-infiltrating lymphocytes in a syngeneic mouse model of oral cancer”. In: *Otolaryngol Head Neck Surg* 147.3 (Sept. 2012), pp. 493–500.
- [294] E. Moore, P. E. Clavijo, R. Davis, H. Cash, C. Van Waes, Y. Kim, and C. Allen. “Established T Cell-Inflamed Tumors Rejected after Adaptive Resistance Was Reversed by Combination STING Activation and PD-1 Pathway Blockade”. In: *Cancer Immunol Res* 4.12 (Dec. 2016), pp. 1061–1071.
- [295] A. Oweida, M. K. Hararah, A. Phan, D. Binder, S. Bhatia, S. Lennon, S. Bukkapatnam, B. Van Court, N. Uyanga, L. Darragh, H. M. Kim, D. Raben, A. C. Tan, L. Heasley, E. Clambey, R. Nemenoff, and S. D. Karam. “Resistance to Radiotherapy and PD-L1 Blockade Is Mediated by TIM-3 Upregulation and Regulatory T-Cell Infiltration”. In: *Clin Cancer Res* 24.21 (Nov. 2018), pp. 5368–5380.
- [296] M. D. Mühlebach. “Vaccine platform recombinant measles virus”. In: *Virus Genes* 53.5 (Oct. 2017), pp. 733–740.
-

- [297] S. Hutzler, S. Erbar, R. A. Jabulowsky, J. R. H. Hanauer, J. H. Schnotz, T. Beissert, B. S. Bodmer, R. Eberle, K. Boller, T. Klamp, U. Sahin, and M. D. Mühlebach. “Antigen-specific oncolytic MV-based tumor vaccines through presentation of selected tumor-associated antigens on infected cells or virus-like particles”. In: *Sci Rep* 7.1 (Dec. 2017), p. 16892.
- [298] S. P. Wong, O. Argyros, C. Coutelle, and R. P. Harbottle. “Non-viral S/MAR vectors replicate episomally in vivo when provided with a selective advantage”. In: *Gene Ther* 18.1 (Jan. 2011), pp. 82–87.
- [299] L. D. Kloker, C. Yurttas, and U. M. Lauer. “Three-dimensional tumor cell cultures employed in virotherapy research”. In: *Oncolytic Virother* 7 (2018), pp. 79–93.
- [300] B. Seliger, A. Al-Samadi, B. Yang, T. Salo, and C. Wickenhauser. “In vitro models as tools for screening treatment options of head and neck cancer”. In: *Front Med (Lausanne)* 9 (2022), p. 971726.
- [301] A. Teijeira Crespo, S. Burnell, L. Capitani, R. Bayliss, E. Moses, G. H. Mason, J. A. Davies, A. J. Godkin, A. M. Gallimore, and A. L. Parker. “Pouring petrol on the flames: Using oncolytic virotherapies to enhance tumour immunogenicity”. In: *Immunology* 163.4 (Aug. 2021), pp. 389–398.
- [302] L. Engelmann, J. Thierauf, N. Koerich Laureano, H. J. Stark, E. S. Prigge, D. Horn, K. Freier, N. Grabe, C. Rong, P. Federspil, K. Zaoui, P. K. Plinkert, N. Rotter, M. von Knebel Doeberitz, J. Hess, and A. Affolter. “Organotypic Co-Cultures as a Novel 3D Model for Head and Neck Squamous Cell Carcinoma”. In: *Cancers (Basel)* 12.8 (Aug. 2020).
- [303] M. M. Gerlach, F. Merz, G. Wichmann, C. Kubick, C. Wittekind, F. Lordick, A. Dietz, and I. Bechmann. “Slice cultures from head and neck squamous cell carcinoma: a novel test system for drug susceptibility and mechanisms of resistance”. In: *Br J Cancer* 110.2 (Jan. 2014), pp. 479–488.
- [304] A. Runge, M. Mayr, T. Schwaiger, S. Sprung, P. Chetta, T. Gottfried, J. Dudas, M. C. Greier, M. C. Glatz, J. Haybaeck, K. Elbers, H. Riechelmann, P. Erlmann, and M. Petersson. “Patient-derived head and neck tumor slice cultures: a versatile tool to study oncolytic virus action”. In: *Sci Rep* 12.1 (Sept. 2022), p. 15334.
- [305] P. O. Frappart and T. G. Hofmann. “Pancreatic Ductal Adenocarcinoma (PDAC) Organoids: The Shining Light at the End of the Tunnel for Drug Response Prediction and Personalized Medicine”. In: *Cancers (Basel)* 12.10 (Sept. 2020).

- 
- [306] X. Jiang, Y. D. Seo, J. H. Chang, A. Coveler, E. N. Nigjeh, S. Pan, F. Jalikis, R. S. Yeung, I. N. Crispe, and V. G. Pillarisetty. “Long-lived pancreatic ductal adenocarcinoma slice cultures enable precise study of the immune microenvironment”. In: *Oncoimmunology* 6.7 (2017), e1333210.
- [307] S. Misra, C. F. Moro, M. Del Chiaro, S. Pouso, A. Sebestyén, M. Löhr, M. Björnstedt, and C. S. Verbeke. “Ex vivo organotypic culture system of precision-cut slices of human pancreatic ductal adenocarcinoma”. In: *Sci Rep* 9.1 (Feb. 2019), p. 2133.
- [308] K. J. Harrington, M. Hingorani, M. A. Tanay, J. Hickey, S. A. Bhide, P. M. Clarke, L. C. Renouf, K. Thway, A. Sibtain, I. A. McNeish, K. L. Newbold, H. Goldsweig, R. Coffin, and C. M. Nutting. “Phase I/II study of oncolytic HSV GM-CSF in combination with radiotherapy and cisplatin in untreated stage III/IV squamous cell cancer of the head and neck”. In: *Clin Cancer Res* 16.15 (Aug. 2010), pp. 4005–4015.
- [309] K. J. Harrington, E. M. Karapanagiotou, V. Roulstone, K. R. Twigger, C. L. White, L. Vidal, D. Beirne, R. Prestwich, K. Newbold, M. Ahmed, K. Thway, C. M. Nutting, M. Coffey, D. Harris, R. G. Vile, H. S. Pandha, J. S. Debono, and A. A. Melcher. “Two-stage phase I dose-escalation study of intratumoral reovirus type 3 dearing and palliative radiotherapy in patients with advanced cancers”. In: *Clin Cancer Res* 16.11 (June 2010), pp. 3067–3077.
- [310] L. K. Mell, K. T. Brumund, G. A. Daniels, S. J. Advani, K. Zakeri, M. E. Wright, S. J. Onyeama, R. A. Weisman, P. R. Sanghvi, P. J. Martin, and A. A. Szalay. “Phase I Trial of Intravenous Oncolytic Vaccinia Virus (GL-ONC1) with Cisplatin and Radiotherapy in Patients with Locoregionally Advanced Head and Neck Carcinoma”. In: *Clin Cancer Res* 23.19 (Oct. 2017), pp. 5696–5702.
- [311] A. R. Penheiter, T. R. Wegman, K. L. Classic, D. Dingli, C. E. Bender, S. J. Russell, and S. K. Carlson. “Sodium iodide symporter (NIS)-mediated radiotherapy for pancreatic cancer”. In: *AJR Am J Roentgenol* 195.2 (Aug. 2010), pp. 341–349.
- [312] S. Aref, K. Bailey, and A. Fielding. “Measles to the Rescue: A Review of Oncolytic Measles Virus”. In: *Viruses* 8.10 (Oct. 2016).
- [313] L. Belgioia, C. Becherini, A. Bacigalupo, and P. Bonomo. “Chemo- immunotherapy and radiation in locally advanced head and neck cancer: Where do we stand?” In: *Oral Oncol* 127 (Apr. 2022), p. 105773.
- [314] M. Hamada and Y. Yura. “Efficient Delivery and Replication of Oncolytic Virus for Successful Treatment of Head and Neck Cancer”. In: *Int J Mol Sci* 21.19 (Sept. 2020).

- [315] K. J. Harrington, A. Kong, N. Mach, J. A. Chesney, B. C. Fernandez, D. Rischin, E. E. W. Cohen, H. S. Radcliffe, B. Gumuscu, J. Cheng, W. Snyder, and L. L. Siu. “Talimogene Laherparepvec and Pembrolizumab in Recurrent or Metastatic Squamous Cell Carcinoma of the Head and Neck (MASTERKEY-232): A Multicenter, Phase 1b Study”. In: *Clin Cancer Res* 26.19 (Oct. 2020), pp. 5153–5161.
- [316] M. Özcan-Wahlbrink, C. Schifflers, and A. B. Riemer. “Enhanced Radiation Sensitivity of Human Papillomavirus-Driven Head and Neck Cancer: Focus on Immunological Aspects”. In: *Front Immunol* 10 (2019), p. 2831.
- [317] S. D. Haller, M. L. Monaco, and K. Essani. “The Present Status of Immuno-Oncolytic Viruses in the Treatment of Pancreatic Cancer”. In: *Viruses* 12.11 (Nov. 2020).
- [318] V. Hamidi-Sofiani, R. Rakhshi, N. Moradi, P. Zeynali, M. Nakhaie, and E. Behboudi. “Oncolytic viruses and pancreatic cancer”. In: *Cancer Treat Res Commun* 31 (2022), p. 100563.
- [319] B. Bockorny, J. E. Grossman, and M. Hidalgo. “Facts and Hopes in Immunotherapy of Pancreatic Cancer”. In: *Clin Cancer Res* 28.21 (Nov. 2022), pp. 4606–4617.
- [320] S. D. Kamath, A. Kalyan, S. Kircher, H. Nimeiri, A. J. Fought, A. Benson, and M. Mulcahy. “Ipilimumab and Gemcitabine for Advanced Pancreatic Cancer: A Phase Ib Study”. In: *Oncologist* 25.5 (May 2020), e808–e815.
- [321] D. Mahalingam, G. A. Wilkinson, K. H. Eng, P. Fields, P. Raber, J. L. Moseley, K. Cheetham, M. Coffey, G. Nuovo, P. Kalinski, B. Zhang, S. P. Arora, and C. Fountzilias. “Pembrolizumab in Combination with the Oncolytic Virus Pelareorep and Chemotherapy in Patients with Advanced Pancreatic Adenocarcinoma: A Phase Ib Study”. In: *Clin Cancer Res* 26.1 (Jan. 2020), pp. 71–81.
- [322] M. Bazan-Peregrino, R. Garcia-Carbonero, B. Laquente, R. Álvarez, A. Mato-Berciano, M. Gimenez-Alejandro, S. Morgado, A. Rodríguez-García, M. V. Maliandi, M. C. Riesco, R. Moreno, M. M. Ginestà, M. Perez-Carreras, J. B. Gornals, S. Prados, S. Perea, G. Capella, R. Alemany, R. Salazar, E. Blasi, C. Blasco, M. Cascallo, and M. Hidalgo. “VCN-01 disrupts pancreatic cancer stroma and exerts antitumor effects”. In: *J Immunother Cancer* 9.11 (Nov. 2021).

# List of Figures

1.1	DNA damage and virus sensing activate innate immune signaling . . . . .	5
1.2	Markers of immunogenic cell death . . . . .	7
1.3	Schematic representation of measles virus particle and genome . . . . .	12
2.1	Investigating combined radiovirotherapy (RVTx) . . . . .	19
3.1	Experimental overview for RVTx analysis <i>in vitro</i> and <i>ex vivo</i> . . . . .	35
4.1	Radiosensitivity of human tumor cell lines . . . . .	50
4.2	Virus sensitivity of human tumor cell lines . . . . .	51
4.3	Irradiation of MeV solutions . . . . .	52
4.4	Multi-step growth curves after RVTx treatment . . . . .	53
4.5	Cell viability after RVTx <i>in vitro</i> . . . . .	54
4.6	Cell viability of BxPC-3 after RVTx treatment in ATPlite assay . . . . .	56
4.7	Heatmap of synergy analysis of RVTx in ATPlite assay . . . . .	58
4.8	Heatmap of schedule counts for analysis of RVTx treatment schedules . . . . .	60
4.9	HMGB1 release after RVTx <i>in vitro</i> . . . . .	62
4.10	Surface-exposed CALR after RVTx <i>in vitro</i> . . . . .	63
4.11	Surface-exposed CALR in HNO410 after RVTx visualized by IF . . . . .	65
4.12	Protein expression of RIG-I after RVTx . . . . .	67
4.13	IFN- $\beta$ release after RVTx <i>in vitro</i> . . . . .	68
4.14	<i>In vitro</i> characterization of newly generated murine tumor cells . . . . .	70
4.15	Growth of transgenic murine tumors <i>in vivo</i> . . . . .	72
4.16	Analysis of virus susceptibility and puromycin resistance of 30364-hCD46 tumor samples . . . . .	73
4.17	Expression of <i>CD46</i> in murine tumors on genomic and transcriptomic level . . . . .	75
4.18	Efficacy of radio- or virotherapy <i>in vivo</i> . . . . .	77
4.19	Efficacy of radiovirotherapy <i>in vivo</i> . . . . .	78
4.20	Treatment overview for RVTx immune analysis . . . . .	80
4.21	<i>In vivo</i> expression of <i>Ifnb1</i> after RVTx . . . . .	81
4.22	Analysis of tumor-infiltrating lymphocytes in treated tumors . . . . .	82
4.23	Analysis of cytokine release after RVTx <i>in vivo</i> . . . . .	84
4.24	RVTx treatment of 3D PDAC spheroids . . . . .	86
4.25	Cell viability of patient-derived PDAC cultures after RVTx . . . . .	87
4.26	HMGB1 release after RVTx <i>ex vivo</i> . . . . .	89
4.27	Expression of <i>IFNB1</i> on transcriptomic level in PDAC cultures . . . . .	90
A1	Cell viability after RVTx <i>in vitro</i> . . . . .	116

---

A2	Cell viability of BxPC-3 after RVTx treatment in XTT assay . . . . .	117
A3	Cell viability of T3M4 after RVTx treatment in ATPlite assay . . . . .	118
A4	Cell viability of T3M4 after RVTx treatment in XTT assay . . . . .	119
A5	Cell viability of HNO210 after RVTx treatment in ATPlite assay . . . . .	120
A6	Cell viability of HNO210 after RVTx treatment in XTT assay . . . . .	121
A7	Cell viability of HNO410 after RVTx treatment in ATPlite assay . . . . .	122
A8	Cell viability of HNO410 after RVTx treatment in XTT assay . . . . .	123
A9	Heatmap of synergy analysis of RVTx in XTT assay . . . . .	124
A10	Heatmap of schedule counts for analysis of RVTx treatment schedules . . . . .	129
A11	Gating strategy for analysis of surface-exposed CALR after RVTx . . . . .	130
A12	Protein expression of cGAS after RVTx . . . . .	131
A13	Western blot of cGAS and STING . . . . .	132
A14	Protein expression of STING after RVTx . . . . .	133
A15	Western blot of RIG-I . . . . .	134
A16	Expression of <i>IFNB1</i> after RVTx . . . . .	135
A17	Radiosensitivity of murine tumor cell lines . . . . .	136
A18	<i>In vitro</i> characterization of newly generated murine tumor cells . . . . .	137
A19	Surface expression of hCD46 at tumor implantation and gating strategy . . . . .	138
A20	Growth of 30364-hCD46 tumors <i>in vivo</i> . . . . .	139
A21	Human CD46 expression in murine tumors . . . . .	140
A22	Analysis of virus susceptibility and puromycin resistance of MOC2-hCD46 tumor samples . . . . .	141
A23	Expression of <i>Actb</i> in murine tumors on genomic and transcriptomic level . . . . .	142
A24	Assessment of secondary tumor growth <i>in vivo</i> . . . . .	143
A25	Tumor growth after radio- or virotherapy <i>in vivo</i> . . . . .	144
A26	Tumor growth after radiovirotherapy <i>in vivo</i> . . . . .	145
A27	Analysis of abscopal effects after RVTx <i>in vivo</i> . . . . .	146
A28	Cq values for <i>in vivo</i> analysis of IFN- $\beta$ and Foxp3 after RVTx . . . . .	147
A29	Amplification and melting curves for qPCR analysis of IFN- $\beta$ and Foxp3 after RVTx . . . . .	148
A30	Gating strategy for analysis of TILs after RVTx <i>in vivo</i> . . . . .	149
A31	<i>In vivo</i> expression of <i>Foxp3</i> after RVTx . . . . .	150
A32	HMGB1 release of RVTx-treated PDAC spheroids . . . . .	151
A33	RVTx treatment of patient-derived PDAC cultures . . . . .	152
A34	Surface-exposed CALR after RVTx <i>ex vivo</i> . . . . .	153
A35	IFN- $\beta$ release in treated PDAC cultures . . . . .	154

# List of Tables

- 3.7 Polymerase chain reaction conditions . . . . . 31
- 4.1 Categories for treatment schedule assessment . . . . . 59
- A1 Combination indices of synergy analysis . . . . . 125
- A2 Summary of schedule assessment with cut-off at 20 and 80% . . . . . 127
- A3 Summary of schedule assessment with cut-off at 25 and 75% . . . . . 128



# Publications

E. Foord, C. Klynning, E. Schoutrop, **J. M. Förster**, J. Krieg, A. Mörtberg, M. R. Müller, C. Herzog, D. Schiegg, D. Villemagne, U. Fiedler, D. Snell, B. Kebble, J. Mattsson, V. Levitsky, and M. Uhlin.

**Profound Functional Suppression of Tumor-Infiltrating T-Cells in Ovarian Cancer Patients Can Be Reversed Using PD-1-Blocking Antibodies or DARPin® Proteins.** *J Immunol Res.* 2020 (2020), p. 7375947.

M. F. Leber, B. Hoyler, S. Prien, S. Neault, C. E. Engeland, **J. M. Förster**, S. Bossow, C. Springfeld, C. von Kalle, D. Jäger, J. C. Bell, and G. Ungerechts.

**Sequencing of serially passaged measles virus affirms its genomic stability and reveals a nonrandom distribution of consensus mutations.** *J Gen Virol*, 101.4 (2020 Apr), pp. 399–409.

C. E. Engeland, S. Bossow, A. W. Hudacek, B. Hoyler, **J. Förster**, R. Veinalde, D. Jäger, R. Cattaneo, G. Ungerechts, and C. Springfeld.

**A Tupaia paramyxovirus vector system for targeting and transgene expression.** *J Gen Virol*, 98.9 (2017 Sep), pp. 2248–2257.



# Congress Contributions

**J. M. Förster**, K. Günther, K. Zaoui, C. Ball, A. L. Angelova, H. Glimm, J. Debus, D. Jäger, A. Abdollahi, A. Nowrouzi, C. E. Engeland, M. F. Leber, and G. Ungerechts.

**Combining radiation and oncolytic measles virus for treatment of refractory tumors.**

Poster presentation. 13<sup>th</sup> International Oncolytic Virus Conference, November 5–7, 2021, Sedona, AZ/USA.

**J. M. Förster**, C. E. Engeland, M. F. Leber, K. Gupta, A. Nowrouzi, K. Zaoui, J. Debus, D. Jäger, A. Abdollahi, and G. Ungerechts.

**Combining radiation and oncolytic measles virus for treatment of refractory tumors.**

Poster presentation. Fourth International Conference on Immunotherapy Radiotherapy Combinations, September 12–14, 2019, New York City, NJ/USA.

**J. M. Förster**, M. F., Leber, C. E. Engeland, A. Nowrouzi, C. von Kalle, J. Debus, D. Jäger, A. Abdollahi, and G. Ungerechts.

**Combining radiation and oncolytic measles virus for treatment of pancreatic adenocarcinoma.**

Poster presentation. 25<sup>th</sup> ESGCT Annual Congress, October 17–20, 2017, Berlin, Germany.



# Acknowledgments

At last, I would like to express my gratitude to everyone who supported me throughout the preparation of this thesis:

Prof. Dr. Dr. Guy Ungerechts for his trust, giving me the opportunity to work on this exciting project in the past years and as member of my examining committee.

Prof. Dr. Martin Müller as faculty supervisor and first examiner of my thesis.

Prof. Dr. Ralf Bartenschlager as reviewer of my thesis and chairperson of my examining committee.

PD Dr. Karin Müller-Decker as member of my examining committee and Prof. Dr. Matthias Uhl as member of my thesis advisory committee.

Prof. Dr. Dr. Christine E. Engeland and Dr. Dr. Mathias F. Leber for their excellent and unlimited support throughout the preparation of this thesis. Thank you for sharing your expertise, valuable advice even beyond the project, constructive criticism and motivating optimism in the past years with all their ups and downs. Your supervision made the success of this thesis possible.

The Alois Hirdt-Erben und Wieland Stiftung as well as the Evangelisches Studienwerk Villigst for the funding of this project and my PhD position.

Prof. Dr. Rienk Offringa for providing the PDA30364 cell line, PD Dr. Genrich Tolstonog for providing the mEERL95 cell line, Dr. Claudia Ball for providing the patient-derived PDAC cultures and Dr. Richard Harbottle for designing and providing the nanovectors.

Dr. Assia L. Angelova, Alexandra Just and Milena Barf for generating the PDAC spheroids used in this project. Thank you for your great help and expertise.

Dr. Ina Kurth, Mareike Roscher, Armin Runz, Dr. Peter Häring, Clemens Lang, Christiane Stahl-Arnsberger and Mona Lifferth for their great support with the irradiation of cells, viruses or animals and providing all the necessary tools and advice. Dr. Kerstin Dell, Anette Berdel and the entire team of ATV 101 for the tremendous support with the animal experiments. Thank you for sharing your expertise, providing advice, technical support and excellent animal care. The FACS Core Facility and Florian Müller for providing the machinery and support for flow cytometry analyses. Silvia Martin for her help with the cell sorting, Manuela Brohm

for her great support with the slide scanner and Ingrid Hülsmeier for her selfless help with the ELISpot readout.

Jessica Albert, Stefanie Sawall and Birgit Hoyler for their excellent help in countless experiments. I don't know how this project should have worked without you! Jesse and Steffi, you are the queens of western blots and masters of animal experiments. You have magic hands not only for making fantastic virus titers and your organizing skills are worth an award. Birgit, you rock RNA isolations and PCRs, independent of the sample size. Thank you all so much for your contributions. You are the stars of this department!

Katia Günther for her amazing support in the animal experiments, taking over important project parts, proof-reading this thesis and so many other tasks besides her own agenda. Thank you so so much! The continuation of the RVTx project could not be in better hands!

Kinam Gupta, Katia Günther and Silja Schlue for joining me in this project during their internships. Thank you for sharing the excitement on this research topic and investing so much into it! It was such an honor to work with you and a great privilege to mentor you. I wish you all the best for your own PhD projects!

All past and present members of AG Ungerechts, CCU Virotherapy and the AdMe Club for the productive and friendly working atmosphere in the past seven years. It was an honor and much fun to work with you, develop our research projects and refill our energy levels at lunch, cake or coffee breaks and other occasions.

A special thanks to Jesse, Steffi, Katia and Natalie for your great friendship and unconditional support. Going through deep valleys or climbing on high mountains throughout these years, thriving together, shooting with aqua guns or just helping each other to get through the day. It would not have been possible without you. I will be eternally grateful for you!

And last but most definitely not least, my family and friends for all their support in the past years. Whatever life brought along the way, you were the ones who made it worth to enjoy and move forward! My husband, Hayel, what would life be without you! Words are not enough to express how thankful I am for who you are and what you do to make life better! And finally, my Lord and creator, you are my life-giver, joy-bringer, peace-provider and future-holder. Thank you for making me who I am and providing a wonderful path of life.

For it is Christ, in whom are hidden all treasures of wisdom and knowledge.

Colossians 2:3

# Thesis Declaration

I hereby declare that I have written the submitted dissertation myself and in this process I have used no other sources or materials than those specifically indicated. I hereby declare that I have not applied to be examined at any other institution, nor have I used the dissertation in this or any other form at any other institution as an examination paper, nor submitted it to any other faculty as a dissertation.

Heidelberg, November 24<sup>th</sup>, 2022

Judith Magdalena Derani